ANALYSIS OF FIXED AND FLOATING STRUCTURES IN RANDOM MULTI-DIRECTIONAL WAVES

by

Okey Nwogu

B.A.Sc., University of Ottawa, 1983

M.A.Sc., University of British Columbia, 1985

A THESIS SUBMITTED IN PARTIAL FULFILLMENT OF

THE REQUIREMENTS FOR THE DEGREE OF

DOCTOR OF PHILOSOPHY

in

THE FACULTY OF GRADUATE STUDIES

DEPARTMENT OF CIVIL ENGINEERING

We accept this thesis as conforming

to the required standard

THE UNIVERSITY OF BRITISH COLUMBIA

April 1989

In presenting this thesis in partial fulfilment of the requirements for an advanced degree at the University of British Columbia, I agree that the Library shall make it freely available for reference and study. I further agree that permission for extensive copying of this thesis for scholarly purposes may be granted by the head of my department or by his or her representatives. It is understood that copying or publication of this thesis for financial gain shall not be allowed without my written permission.

Department of CIVIL ENGINEERING

The University of British Columbia
Vancouver, Canada

Date APRIL 19, 1989

Abstract

Offshore structures have traditionally been designed on the assumption of long-crested or uni-directional incident waves. Realistic sea states are however short-crested or multi-directional with a distribution of wave energy over both frequency and direction. The present thesis investigates the influence of the directional spreading of wave energy on the forces on fixed structures and motions of floating structures. The work is both theoretical and experimental, with the experiments carried out at the multi-directional wave basin of the Hydraulics Laboratory at the National Research Council in Ottawa.

Different methods of estimating directional wave spectra are evaluated using numerically synthesized time series of the water surface elevation and horizontal orbital velocities at a single location, and the maximum entropy method is found to provide the best directional resolution. The maximum entropy method is developed further to estimate directional wave spectra from an array of wave probes.

Expressions are developed for the spectral densities of the inline and transverse components of the force on a slender cylinder in random multi-directional waves, and for the probability distribution of the peaks of the corresponding resultant force. The former are based on a linearization of the Morison equation, while the latter is based on the assumption of a narrow-band spectrum. Experiments were carried out to measure the forces on a segmented vertical cylinder in random multi-directional waves. The theoretical expressions for the force spectral density and probability distribution match the measured data reasonably well. Reduction factors relating the forces in short-crested seas to the forces in long-crested seas are also presented.

Experiments were also carried out with a moored floating barge in regular and random multi-directional waves. The experiments show an increase of the sway, roll, and yaw motions due to directional spreading, and a slight reduction of the pitch and first order surge motions. The second order, low frequency surge motions are however significantly reduced in multi-directional waves. Linear diffraction theory is used to predict the transfer functions for the first order surge, heave, and pitch motions of the barge. Reasonable agreement was obtained between the measured and predicted first order transfer functions. A procedure to compute the spectral density of the second order drift forces in multi-directional waves based on the concept of a bi-frequency, bi-directional quadratic transfer function is also presented.

Table of Contents

List of Tables

List of Figures

Acknowledgement

This thesis is the result of a collaborative research effort between the University of British Columbia and the National Research Council of Canada and the author is grateful to many individuals who assisted in various phases of the project.

The author would like to thank his advisor, Dr. Michael Isaacson, for his help and encouragement throughout the research project, and his invaluable suggestions in the preparation of the thesis. The author would also like to express his immense gratitude to the Hydraulics Laboratory of the National Research Council of Canada for giving him the opportunity to carry out the research project in their excellent facilities. The support of the entire staff of the Hydraulics Laboratory is greatly appreciated. In particular, the author wishes to thank Mr. E.R. Funke, Dr. E.P.D Mansard, and Mr. M.D. Miles for their numerous contributions to various aspects of the study, and Mr. A. Cornett and Mr. R. Clarke for their assistance with the experimental work.

This study was funded by the Natural Sciences and Engineering Research Council and National Research Council of Canada. Financial support in the form of fellowships from the University of British Columbia, International Center for Ocean Development, and Natural Sciences and Engineering Research Council is gratefully acknowledged.

Chapter 1

INTRODUCTION

1.1 General

As oil exploration moves into deeper waters, offshore structures represent large financial investments and require a more accurate estimation of the design loads. Traditionally, offshore structures have been designed based on the assumption of a two-dimensional or long-crested incident wave field. Realistic sea states are however three-dimensional or short-crested with wave components propagating in different directions. This led to the concept of representing the energy in a sea state by a directional wave spectrum. The directional wave spectrum can be expressed as the product of a directional spreading function and a one-dimensional frequency spectrum. The directional spreading function represents the directional distribution of wave energy at a given frequency over direction.

The directional spreading of wave energy may have a significant influence on the loads and motions experienced by an offshore structure. In some cases, it leads to a reduction of the loads, and consequently savings in fabrication costs. It could also lead to a significant increase of the estimated fatigue life of an offshore structure. Marshall (1976) reported a more than doubling of the estimated fatigue life of a structure by considering the angular spread of wave energy. The use of a directional sea state in numerical or physical modelling might also be the only way to estimate certain effects such as torsional loads, excessive rolling and yawing motions, and lateral forces on structural members.

Directional spectra models have not however been commonly used in the design of offshore structures. This has been partly due to an inadequate measurement of directional spreading characteristics in the ocean environment, reliable methods of resolving directional spreading, and the lack of laboratories capable of generating short-crested sea states for the testing of physical models.

Recently, a number of laboratories have built wave basins equipped with segmented wave generators capable of producing directional sea states. These include the University of Edinburgh in 1978, the Hydraulics Research Station, Wallingford, U.K. in 1980, the Norwegian Hydrodynamics Laboratory (MARINTEK) in 1981, the Offshore Technology Corporation, U.S.A., in 1983, the Danish Hydraulic Institute in 1984, the National Research Council of Canada Hydraulics Laboratory in 1986, and a few others not listed here. Buoys capable of resolving wave directionality have also been deployed at various locations around the world. This should all lead to directional wave spectra models becoming a part of the offshore structure design process.

In a random long-crested wave field, measurement of the water surface elevation at a single location can be transformed into a one-dimensional frequency energy spectrum. Knowledge of a directional wave field however requires simultaneous measurement of either the water surface elevation at a number of locations, or the water surface elevation and orthogonal water surface slopes or horizontal orthogonal water particle velocities. Different approaches such as the Maximum Likelihood Method (MLM) (see Capon, 1969) or the Maximum Entropy Method (MEM) (see Jaynes, 1957) can be used to estimate the directional distribution of wave energy.

The Morison equation (Morison et al., 1950) is often used to estimate the wave forces on a slender structural member where the presence of the body does not significantly affect the incident wave kinematics. The wave force consists of a linear inertial and a nonlinear drag component. When the structure is large enough to diffract the incident wave field, flow separation effects are generally ignored and the problem is solved using potential flow theory (Kellogg, 1929). The complete problem is nonlinear and is usually linearized by assuming a small amplitude wave train.

In regular waves, a large floating body experiences first order motions at the frequency of the exciting waves and a steady drift force due a change in the momentum of the fluid. In random seas, the different wave frequencies interact to produce a slowly varying force at the difference frequencies. The magnitudes of the second order forces are generally smaller than those of the first order forces, but they tend to occur at frequencies close to the natural frequencies of the mooring system resulting in large horizontal excursions of moored vessels. The drift forces are also important in the dynamic positioning of vessels in the open sea and the added resistance of ships moving through waves.

In trying to determine the effect of wave directionality on offshore structures, it is useful to compare the differences between the forces experienced by the structure in long-crested and short-crested wave fields with the same total energy. When there is a linear relationship between the forces and motions and water surface elevation, linear superposition principles can be used to establish transfer functions for long-crested and short-crested seas. There are however various nonlinear problems for which the linear transfer function approach can no longer be used. These include the nonlinear drag forces on slender structural members, slowly varying second order drift forces and motions of moored floating structures, mooring lines with nonlinear stiffness, and severe roll motions with nonlinear viscous damping. Other techniques would have to be developed to relate the response in short-crested seas to the incident wave spectrum.

This thesis compares different methods of analyzing directional wave fields, and develops techniques for the computation of the spectral densities and probability distributions of the nonlinear forces on a slender cylinder, and the slowly varying second order motions of a moored floating barge in directional seas. The numerical results are compared with the results from experiments carried out in the multi-directional wave basin of the Hydraulics Laboratory at the National Research Council in Ottawa.

1.2 Literature Review

1.2.1 Analysis of Directional Wave Fields

The directional wave spectrum is often used to describe the wave energy in a given sea state as a function of both wave frequency and direction of propagation. Most methods of directional wave analysis are based on the cross-spectra of simultaneous measurements of various quantities such as the water surface elevation, water surface slopes, and water particle velocities. The most common methods of estimating directional spreading functions include the Direct Fourier Transform (DFT) method, parametric methods, the maximum likelihood method (MLM), and the maximum entropy method (MEM).

The direct Fourier transform method first proposed by Barber (1963) estimates the directional wave spectrum from the double integral of the cross-spectrum of two arbitrary points in the wave field. A large number of wave probes is however needed to provide reasonable directional resolution.

Parametric methods involve modelling the angular spreading function as either a truncated Fourier series or other distributions such as the cosine power or circular normal. The parameters or coefficients of the distributions are estimated from the relationship between the directional wave spectrum and the cross-spectral density matrix of the measured signals. Longuet-Higgins et al. (1963) applied the Fourier series approach to the heave and slope signals of a floating buoy while Panicker and Borgman (1970) applied it to an array of wave guages.

Due to limited amount of information available from measurement arrays, the Fourier series approach is unable to adequately resolve sharp-peaked spreading functions. It also sometimes estimates spreading functions with unrealistic negative values. Panicker and Borgman (1970) used a smoothing function to ensure a positive spreading function but this results in further loss of directional resolution. Mitsuyasu et al. (1975) improved the resolution slightly by measuring the curvature of the water surface in addition to the slopes.

The assumption of a parametric distribution such as the cosine power or circular normal distributions *a priori* might be useful in cases such as laboratories where the target distributions are fairly well known. The estimated distributions are however biased, and when there are substantial deviations from the assumed distribution such as in the case of a bi-directional sea state with a double peaked spreading function, the approach becomes flawed.

The maximum likelihood method is a standard method used in statistics to estimate the parameters of a probability distribution by maximizing the likelihood of obtaining the observed data set. Capon (1969) used the MLM for the analysis of seismic waves. Barnard (1969), and Oakley and Lozow (1977) applied the method to directional wave resolution from an array of wave guages. Isobe et al. (1984) extended the method to include measurements of other wave properties such as velocities and slopes. Jeffreys (1986) compared the MLM with two parametric methods (cosine power and Fourier series) and found the MLM gave the best directional resolution. The MLM estimated spreading function is not forced to satisfy constraints imposed by the relationship between the spreading function and the cross-spectral density matrix, resulting in the estimation of broader distributions.

The concept of entropy has been used in thermodynamics as a measure of the amount of energy in a system not available for doing work. Jaynes (1957) introduced maximum entropy ideas to probability theory. Entropy in probability theory can be thought of as a measure of uncertainty or lack of information. Maximizing the entropy subject to constraints imposed by the available information yields the probability distribution. The MEM has since been used (e.g. Dowson and Wragg (1973), Mead and Papanicolaou (1984)) to estimate probability distributions from a limited amount of data.

Burg (1967) applied the MEM to spectral analysis. Barnard (1969) attempted to extend Burg's approach to the computation of wavenumber spectra, but an analytical solution could only be found for an equally spaced linear array. The linear array, however, does not resolve directional seas adequately. Barnard's formulation uses the change in entropy associated with the spreading function (i.e. the integral of the logarithm of the spreading function, $D(\theta)$). This differs from the definition of entropy used in probability theory ($-\int D(\theta) log D(\theta) d\theta$). The directional spreading function can however be thought of as the probability distribution of wave energy at a given frequency over direction. The definition of entropy used in probability theory is thus more justifiable for use in the analysis of directional wave fields.

Kobune and Hashimoto (1986) used the probability theory definition of entropy in an MEM procedure to estimate directional wave spectra from measurements of the water surface elevation and either the orthogonal slopes or orthogonal velocities at a single location. The MEM was found to resolve directional seas even better than the MLM. The only drawback of the MEM is that it is an iterative procedure and does not converge for very narrow spreading functions.

1.2.2 Forces on a Slender Cylinder

The Morison equation is normally used to estimate the wave forces on small diameter members of an offshore structure. Numerous experiments, many of which are summarized in Sarpkaya and Isaacson (1981), have been carried out to validate the equation and determine appropriate values of drag and inertia force coefficients. Dimensional analysis and experimental results show that the coefficients depend primarily on the Reynolds number, the Keulegan-Carpenter number, and the relative roughness of the cylinder.

Most of the experimental data is however based on one-dimensional oscillatory flow past a circular section.

For a random, long-crested wave field, the nonlinearity in the Morison equation results in a non-Gaussian wave force. Borgman (1967a) derived an expression for the force spectrum by linearizing the drag component. While the linearized force spectrum gives a good estimate of the standard deviation of the force, Tickell (1977) showed the corresponding Gaussian distribution underestimates the extreme values of the force.

Pierson and Holmes (1965) derived an expression for the probability density of the force for a unidirectional random wave field. The expression is exact and takes into account the nonlinearity of the drag force. It is however in integral form and has to be evaluated numerically. An alternate distribution involving parabolic cylinder functions was derived by Borgman (1967b).

For reliability based design and fatigue analysis of offshore structures, the probability distribution of the peaks of the force and the upcrossing frequency of different force levels are required. The derivation of this distribution for any arbitrary random process is quite difficult. Borgman (1972) derived an expression for the probability distribution of the peak forces, assuming a narrow-band wave spectrum. Moe and Crandall (1978) extended the results to account for a small current and derived asymptotic expressions for a wide-band process.

Borgman (1972) also reviewed various methods of estimating force coefficients for random wave conditions. When the force coefficients are assumed constant, two methods can be used. One approach is the method of moments where the second and fourth moments of the measured force distribution are equated to those of the theoretical distribution. An alternate approach is a least-squares fit of the measured force spectrum to the theoretical linearized force spectrum. Frequency dependent force coefficients can also be determined from the real and imaginary parts of the cross-spectrum of the measured force and water surface elevation.

The spectral density and probability distribution of the force in short-crested seas has received relatively less attention in the literature. Hackley (1979) and Shinozuka et al. (1979) used a time domain approach to simulate the loading and response of slender cylinders in short-crested seas. The Fast Fourier Transform (FFT) technique was used to simulate the kinematics for use in the Morison equation. Both studies found a reduction of the standard deviation and maximum values of the inline force and an increased transverse force.

Borgman and Yfantis (1981) derived linearized expressions for the spectra and cross-spectra of the horizontal components of the total force in directional seas. Tickell and Elwany (1979) used the transformation of variables technique to derive expressions for the joint distribution of the inline and transverse forces, retaining the nonlinearity of the drag force. The expression is however in integral form and has to be evaluated numerically. The distribution of the peaks of the resultant force is of more importance in the design process, and is derived in the present thesis.

Most of the previous studies have ignored the effect of the lift (transverse) force due to vortex shedding in estimating the total force in short-crested seas. This is due to the difficulty of modelling the lift force phenomenom. It is however expected that the three-dimensional nature of the wave field might reduce the correlation of vortex shedding and hence diminish the magnitude and effect of the lift force in directional seas.

1.2.3 Second Order Forces and Motions of Floating Structures

As stated earlier, the wave loads on large floating bodies in random seas consists of a first order component at the frequency of the individual waves, and a second order low frequency component at the difference frequencies of the waves.

The first order wave forces and motions in regular unidirectional waves can usually be determined from well established procedures based on three-dimensional linear diffraction theory (Faltinsen and Michelsen (1974), Garrison (1978), Isaacson (1985a)). The first order results can be extended to random, short-crested waves by using linear superposition principles (Huntington and Thompson (1976), Isaacson and Sinha (1986)). Huntington and Thompson (1976) found the predicted results to be in good agreement with the experimental results.

The prediction of the second order wave drift force on floating bodies has received a lot of attention in the literature. Maruo (1960) developed expressions for the inline and transverse components of the mean drift force in regular waves. The mean drift force is estimated from changes in the momentum of the fluid. The approach is sometimes termed the 'far field' approach since the behaviour of the fluid potentials in the far field is used to evaluate the forces.

Newman (1967) extended Maruo's method to include computation of the mean yaw moment. The results were evaluated using slender body theory assumptions for an infinite water depth. Faltinsen and Michelsen (1974) generalized the expressions for finite water depth and used the three-dimensional source distribution method to evaluate the potentials.

Pinkster (1976) presented expressions for the mean drift forces and moments by a near field method based on direct integration of the pressures over the wetted surfaces of the structure. The near field approach shows explicitly the different components of the drift force and can also be used to evaluate vertical drift forces.

In random seas, the drift force is no longer steady but slowly varying in time. Due to the nonlinear nature of the drift force, linear superposition of the contributions from different wave frequencies and directions can no longer be used to extend the results to random waves. The second order drift force in random long-crested seas can however be modelled as a two term Volterra or functional power series. The functional power series which is a Taylor series expansion of a functional, was originally introduced by

Volterra (1930). The Volterra series representation of the drift force has been used by a number of authors such as Neal (1974) and Kim and Dalzell (1981). A quadratic impulse response function is used to relate the drift force to the water surface elevation. The impulse response function can be Fourier transformed to obtain a frequency dependent, quadratic transfer function.

The quadratic transfer function can be determined from a solution of the complete second order hydrodynamic problem, including determination of the second order diffraction potential. This is quite difficult and could prove to be rather cumbersome since the transfer function has to be computed for all the different frequency combinations in a given sea state. Different approximations have been used by various authors to simplify the problem.

Hsu and Blenkarn (1970) presented an approximate method that uses only the mean drift force in regular waves. The method considers an irregular wave train to be made up of a sequence in time of regular waves of varying heights, with periods equal to twice the time between two zero-crossings. Each regular wave is considered to impart a steady drift force resulting in a slowly varying drift force.

Newman (1974) presented a method that approximates the quadratic transfer function with the mean drift force in regular waves. The method ignores certain interaction terms and is only valid for sea states with a narrow-band spectrum. Marthinsen (1983a) also presented an approximate method which is valid for narrow-banded seas. The method relates the slowly varying drift force to the envelope of the wave train, obtained from a Hilbert transform of the water surface elevation.

Pinkster (1980) approximated the second order potential in his computations and found his results compared favourably with experimental measurements. Lighthill (1979), and Faltinsen and Loken (1979) avoided having to solve for the second order potential by using Green's second identity to relate the second order diffraction potential to the first order potentials. Faltinsen and Loken found Newman's method represented a reasonable engineering approach. Matsui (1986) used Lighthill's method to estimate the overturning moment on an articulated column and found the second order potential contribution to be most significant at the very low frequencies.

The low frequency damping coefficients are critical for the estimation of the low frequency motions. Wichers and van Sluijs (1979) carried out free oscillation tests for the surge motion of a tanker in still water and regular waves. The results revealed an additional low frequency damping term due to the presence of the waves, often referred to as wave drift damping. Nakamura et al. (1986), Hearn et al. (1987), and Standing et al. (1987) examined different numerical methods of estimating the wave drift damping coefficient.

There are relatively fewer studies on the computation and experimental measurements of wave drift forces and motions of large structures in directional seas. Marthinsen (1983b) extended his approximate method of computing wave drift forces in long-crested seas to short-crested seas. The results showed a considerable reduction of the mean values of the forces. The results were however not compared with any experimental results. Molin and Fauveau (1984) studied the effect of wave directionality on set-down component of the drift force and found significant reductions in short-crested seas. The set-down component is due to the second order potentials and is in many cases a negligible component of the total drift force.

The functional polynomial approach can be extended to short-crested seas (e.g. Hasselmann, 1966). The second order impulse response function is now dependent on spatial variables and time. The approach results in a bi-frequency, bi-directional quadratic transfer function. Dalzell (1985) used Hasselmann's formulation to express the mean and spectral moments of the second order forces but no numerical or experimental results were presented. Pinkster (1985) also discussed the computation of drift forces in directional seas using the bi-directional, bi-frequency quadratic transfer function. The computed mean drift force on a tanker in regular crossing waves were found to be generally in good agreement with the experimental measurements.

Experiments have also been carried out to measure the response of structures in short-crested seas. Teigen (1983) carried out model tests with a Tension Leg Platform (TLP) in random short-crested seas. The experiments showed a considerable reduction of the mean and standard deviation of the surge motions in short-crested seas compared to long-crested seas.

Houlie et al. (1983) carried out tests on a single point moored tanker in long-crested and short-crested seas. The experiments showed that the short-crestedness of the waves led to increased yaw, sway, roll and heave motions and also increased loads at the hinge connection. Romeling et al. (1984) tested an articulated column with a yoke moored tanker in directional waves. The results also showed a more than doubling of the loads at the tanker/yoke hinge connection possibly due to increased bow motions.

Maeda et al. (1986) carried out tests with a semisubmersible in regular crossing waves in order to validate the extension of the Volterra series approach to regular short-crested waves. Sand et al. (1987) tested a moored semisubmersible in two- and three-dimensional waves. For head seas, there were considerable reductions of the low frequency components of the heave and pitch motions and an increased roll response.

The statistics of the second order forces and motions are of ultimate interest in the design of mooring systems. Kac and Siegert (1947) formulated the method for the calculation of the exact probability distribution of the second order response based on a two term Volterra series. Neal (1974) used Kac and Siegert's method to develop a closed form expression for the characteristic function but concluded the probability density function would have to be evaluated numerically.

Vinje (1983) derived various closed form expressions for the probability distribution based on different assumptions. Langley (1984) presented expressions for the distribution of the second order forces consistent with the Newman approximation. Naess (1986) was finally able to derive a closed form solution for the probability density function based on Kac and Siegert's method.

It has however been shown by Vinje (1983) that the probability density of the response of a lightly damped system is almost independent of the probability distribution of the exciting force, and should approach a Gaussian distribution by the central limit theorem. Roberts (1981) also found the probability density of the response of a lightly damped linear system to nonlinear forces to be 'near' Gaussian. Experimentally, Pinkster and Wichers (1987) measured the low frequency surge motions of a linearly moored tanker in head seas and found the statistical distribution of the surge motions were fairly well represented by a Gaussian distribution.

1.3 Scope of Present Investigation

Previous studies have dealt mainly with wave-structure interaction in regular and random long-crested waves. There is however a need to simulate the loading and response of offshore stuctures in the three-dimensional sea state encountered in the ocean environment. The present investigation seeks to fulfill that need.

The overall objective of the present investigation is to study the effect of wave directionality on the nonlinear forces on a slender cylinder and the second order horizontal drift motions of a moored floating structure. In particular, the present investigation

1. compares different methods of measuring and resolving directional wave spectra in order to determine the most accurate and efficient method for use in laboratories and in the field. The maximum entropy method is particularly examined in great detail.

2. derives expressions for the spectral densities of the inline and transverse forces on

a slender cylinder, and the probability distribution of the peaks of the resultant force in short-crested seas. Numerical and experimental data are used to validate the models, and the forces in long-crested and short-crested seas with the same frequency spectrum are compared.

3. develops a numerical model based on the functional polynomial approach for the prediction of the horizontal drift forces and motions of large floating structures in random short-crested seas, and compares the results with experimental measurements. The measured mooring line forces and motions of a barge in long-crested and short-crested seas are also compared.

4. examines different approximations for the probability distributions of the drift motions and mooring line forces.

It is hoped that this thesis will help provide designers of offshore structures a better understanding of the problems associated with wave-structure interaction in random, multi-directional waves.

Chapter 2

DESCRIPTION AND ANALYSIS OF DIRECTIONAL WAVE FIELDS

Ocean waves exhibit a pattern which is highly irregular and short-crested. In order to understand the behaviour of offshore structures in such wave fields, information about the directional distribution of wave energy is required. This chapter first presents a mathematical description of directional seas, then describes a method of numerically simulating the time series of the water surface elevation and wave kinematics. Finally, the Fourier series, MLM, and MEM methods of estimating directional spreading functions are described.

Whilst the Fourier series and MLM techniques are extensively used in the literature and are thus briefly reviewed here, the application of the MEM to the estimation of directional wave spectra is relatively recent and is discussed in great detail. The section on the use of the MEM to analyze directional wave fields using measurements from an array of wave probes is an original development of this thesis.

2.1 Mathematical Description of Directional Seas

The water surface elevation, $\eta(\mathbf{x}, t)$, at location $\mathbf{x}$=(x,y) and time, t, is assumed to be a zero mean, stationary, ergodic, random Gaussian process. The wave field is also assumed to be spatially homogenous. The assumptions of stationarity and spatial homogeneity imply that the statistical properties of η are independent of the time and location of measurement. In a typical ocean environment, these assumptions are usually valid only for a localized area and limited duration. The assumption of a Gaussian process implies a symmetric distribution of the water surface elevation about the still water level. This is however only realistic for small amplitude waves.

In the present study, the waves are assumed to be of small amplitude relative to the water depth and wavelength, enabling one to use the results of linear wave theory. The Gaussian assumption represents a reasonable approximation for moderate sea states under deep water conditions. The coordinate system is fixed and Cartesian with z measured upwards from the still water level and the x-y plane horizontal. A regular long-crested wave train propagating at an angle θ relative to the positive x axis (see Figure 2.1) may be represented by

$$\eta(x, y, t) = \mathrm{Re}[A \exp\{i(kx\cos\theta + ky\sin\theta - \omega t)\}] \tag{2.1}$$

where A is the complex wave amplitude, $i = \sqrt{-1}$, and k is the wavenumber related to the angular wave frequency, ω, by the linear dispersion relation

$$\omega^2 = gk\tanh kd \tag{2.2}$$

The water depth is d, and g is the gravitational acceleration. An irregular, short-crested wave train can be modelled as a linear superposition of regular long-crested waves with different frequencies propagating in different directions, that is

$$\eta(x, y, t) = Re\left[\sum_{j=1}^{\infty} A_j \exp\{i(k_j x\cos\theta_j + k_j y\sin\theta_j - \omega_j t)\}\right] \tag{2.3}$$

The phases associated with the complex amplitudes A_j are assumed to be randomly distributed from 0 to 2π. The above single summation model is only one of several models used to represent a directional wave field. An integral form representation of a

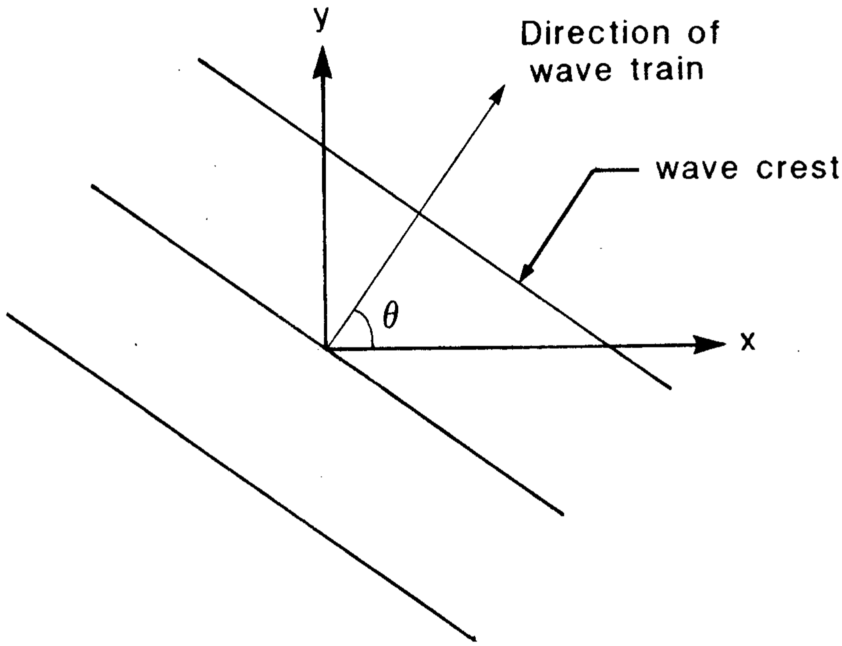

Figure 2.1: Definition sketch for incident wave direction

short-crested wave train can be expressed as

$$\eta(\mathbf{x}, t) = Re\left[\int\!\!\int \exp\{i(\mathbf{k}\cdot\mathbf{x} - \omega t)\}\, dA(\mathbf{k})\right] \tag{2.4}$$

where $\mathbf{k} = (k\cos\theta, k\sin\theta)$ and dA represents a differential wave amplitude. A directional wave spectrum $S_\eta(\omega, \theta)$ can be defined as

$$S_\eta(\omega, \theta) = \frac{\overline{dAdA^*}}{2\Delta\omega\Delta\theta} \tag{2.5}$$

where the symbol * denotes the complex conjugate and the overbar denotes an ensemble mean. The mean square value of the water surface elevation at any location can be expressed as

$$\overline{\eta^2} = \int_0^\infty \int_{-\pi}^{\pi} S_\eta(\omega, \theta)\, d\theta d\omega \tag{2.6}$$

Since the average energy density of the waves is proportional to the square of the wave amplitude, the product $S_\eta(\omega, \theta)d\omega d\theta$ can be considered to be the relative contribution

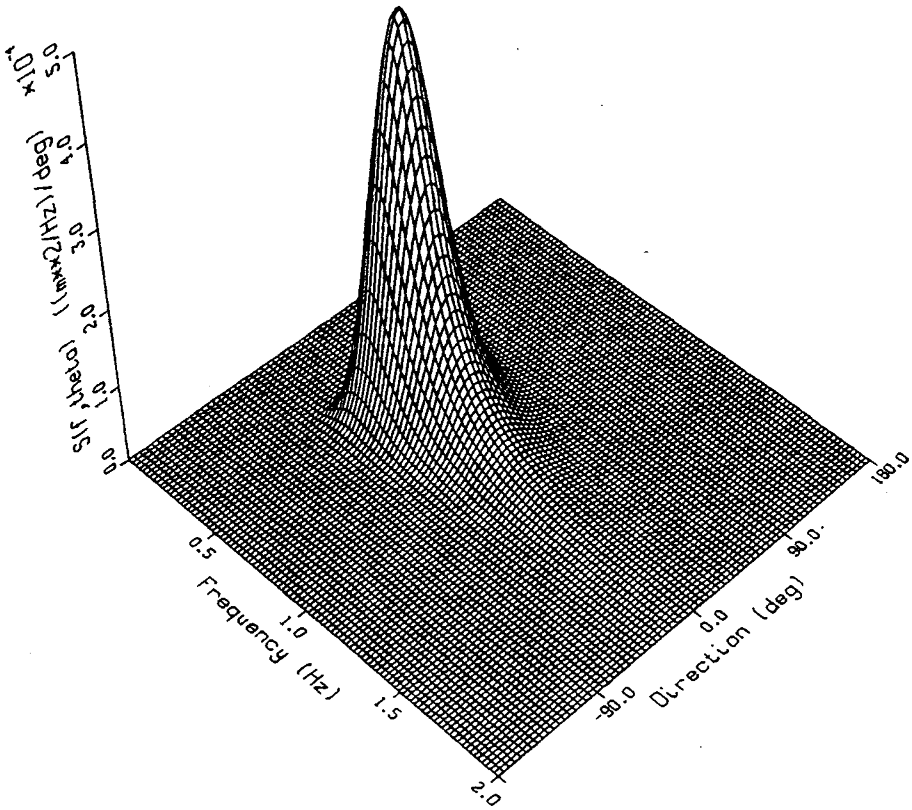

Figure 2.2: Sketch of a typical directional wave spectrum

to the wave energy from wave components with frequencies between ω and $\omega + d\omega$, propagating in directions between θ and $\theta + d\theta$. A sketch of a typical directional wave spectrum is shown in Figure 2.2 . The conventional one-dimensional frequency spectrum can be obtained by integrating the directional wave spectrum over all directions

$$S_\eta(\omega) = \int_{-\pi}^{\pi} S_\eta(\omega, \theta)\, d\theta \tag{2.7}$$

It is convenient to separate out the frequency and directional dependence of wave energy by expressing directional wave spectrum as the product of a directional spreading function $D(\omega, \theta)$ and a frequency spectrum, that is

$$S_\eta(\omega, \theta) = S_\eta(\omega) D(\omega, \theta) \tag{2.8}$$

The directional spreading function represents the directional distribution of wave energy and should be non-negative. It follows from equations (2.7) and (2.8) that $D(\omega, \theta)$ should

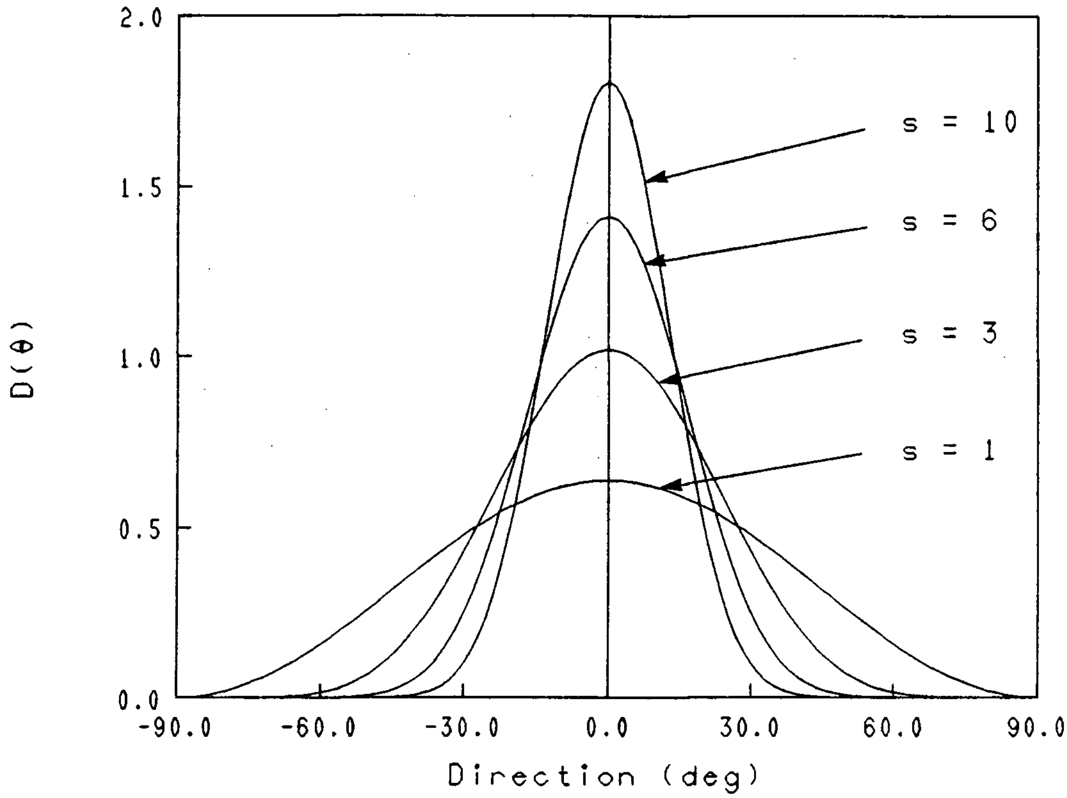

Figure 2.3: Cosine power spreading function for different values of the index s

satisfy

$$\int_{-\pi}^{\pi} D(\omega,\theta)\, d\theta = 1 \tag{2.9}$$

One of the most commonly used models for the directional spreading function is the frequency independent cosine power function defined as

$$D(\theta) = \begin{cases} C(s)\cos^{2s}(\theta-\theta_0) & \text{for } |\theta-\theta_0| < \pi/2 \\ 0 & \text{otherwise} \end{cases} \tag{2.10}$$

where θ_0 is the principal direction of wave propagation, and C(s) is a normalizing coefficient that ensures that equation (2.9) is satisfied, given by

$$C(s) = \frac{\Gamma(s+1)}{\sqrt{\pi}\,\Gamma(s+\frac{1}{2})} \tag{2.11}$$

Γ is the gamma function. The parameter s is a spreading index describing the degree of wave short-crestedness with $s \rightarrow \infty$ representing a long-crested wave field. Figure 2.3

shows a plot of the cosine power spreading function for different values of the spreading index, s.

2.2 Numerical Simulation of Directional Seas

In evaluating different methods of estimating directional wave spectra, most previous studies (Isobe et al., (1984), Jeffreys (1986), Kobune and Hashimoto (1986)) simulate directly a cross-spectral density matrix representing a specified directional sea state. In real situations however, the data is usually available in the form of a time series and is often corrupted to a certain degree by the presence of noise. It was therefore part of the intent of the present study to simulate directly the time series of the water surface elevation, water particle velocities, and accelerations in order to evaluate different methods of directional wave analysis and also for use in wave force simulation studies.

Miles and Funke (1987) have compared different numerical models used for the simulation of directional sea states. Most earlier studies (Hackley(1979), Forristall (1981), Pinkster (1984)) used the double summation model in which the water surface elevation is given by

$$\eta(x,y,t) = \sum_{i=1}^{N}\sum_{j=1}^{M} a_{ij}\cos[\omega_i t - k_i(x\cos\theta_j + y\sin\theta_j) + \varepsilon_{ij}] \tag{2.12}$$

The double summation model however produces a wave field which is neither ergodic nor spatially homogeneous for finite values of N and M (see Jeffreys, 1987). This is due to the fact that any two wave components with identical frequencies, but travelling in different directions are 'phase-locked'. In other words, the phases of the different wave components in the wave field are no longer totally random.

An alternate model which produces a spatially homogeneous wave field is the single direction per frequency or single summation model. The water surface elevation is given by equation (2.3) as

$$\eta(x,y,t) = \sum_{j=1}^{N} a_j\cos[k_j(x\cos\theta_j + y\sin\theta_j) - \omega_j t + \varepsilon_j] \tag{2.13}$$

where N is the total number of frequency components used to model the sea state. The wave amplitudes a_j and phases ε_j can be chosen by different methods. One of the more commonly used methods is the random phase method in which the amplitudes are set deterministically by the desired spectral density and the phases are randomly selected from 0 to 2π . The amplitudes and phases are given by the random phase method as

$$a_j = \sqrt{2S(\omega_j)D(\omega_j,\theta_j)\Delta\omega\Delta\theta} \tag{2.14}$$

$$\varepsilon_j = 2\pi U[0,1] \tag{2.15}$$

where $U[0,1]$ is a uniform distribution over the interval [0,1]. For any specified interval of the the time series Δt, constant width frequency bands can be obtained as

$$\Delta\omega = \frac{2\pi}{L\Delta t} \tag{2.16}$$

where $L = N/M$ is the total number of frequency bands. In each frequency band $\Delta\omega$, the directional spreading function is calculated at M wave angles. There are thus M sub-frequencies within each frequency bandwidth $\Delta\omega$, each corresponding to a different angle of propagation. The wave frequencies are thus given by

$$\omega_j = j\frac{\Delta\omega}{M} \tag{2.17}$$

The angles corresponding to each frequency component can be chosen by different methods. One approach is to chose the angles randomly for each frequency component, while another approach is a linear variation of wave angle with frequency. The latter can be expressed as

$$\theta_j = \theta_0 + (j-1)\Delta\theta - \theta_{max} \tag{2.18}$$

where θ_{max} is the maximum angle of wave propagation relative to θ_0, set equal to 90° in the present study, and $\Delta\theta = 2\theta_{max}/(M-1)$. By choosing N and M to be powers of 2, the inverse Fast Fourier Transform (FFT) technique can be used to obtain the time series of the water surface elevation, with the record length of the simulated time series equal to $2N\Delta t$.

The wave kinematics can be computed using transfer functions given by linear wave theory. The horizontal orbital velocities are in phase with the water surface elevation and are given by

$$
\begin{aligned}
u(x,y,z,t) &= \sum_{j=1}^{N} h_u(\omega_j) a_j \cos\theta_j \cos[k_j(x\cos\theta_j + y\sin\theta_j) - \omega_j t + \varepsilon_j] \quad (2.19)\\
v(x,y,z,t) &= \sum_{j=1}^{N} h_u(\omega_j) a_j \sin\theta_j \cos[k_j(x\cos\theta_j + y\sin\theta_j) - \omega_j t + \varepsilon_j] \quad (2.20)
\end{aligned}
$$

where u and v are the x and y components of the horizontal velocities, and $h_u(\omega)$ is a transfer function given in Table 2.1. The horizontal accelerations are out of phase with the water surface elevation and are given by

$$
\begin{aligned}
a_x(x,y,z,t) &= \sum_{j=1}^{N} \omega_j h_u(\omega_j) a_j \cos\theta_j \sin[k_j(x\cos\theta_j + y\sin\theta_j) - \omega_j t + \varepsilon_j] \quad (2.21)\\
a_y(x,y,z,t) &= \sum_{j=1}^{N} \omega_j h_u(\omega_j) a_j \sin\theta_j \sin[k_j(x\cos\theta_j + y\sin\theta_j) - \omega_j t + \varepsilon_j] \quad (2.22)
\end{aligned}
$$

where a_x and a_y are the x and y components of the horizontal water particle acceleration.

2.3 Analysis of Directional Wave Fields

The directional spreading function can be estimated from measured or simulated data using various methods. Data is usually available in the form of the time series of different wave properties such as water surface elevation, slopes or velocities. In order to obtain information about wave directionality, the measured time series are first Fourier transformed to yield a frequency dependent, cross-spectral density matrix. Most current methods of analysis then utilize the relationship between the cross-spectral density matrix of the measured data and the directional wave spectrum to estimate the directional

Table 2.1: Transfer functions for various wave properties based on linear wave theory

Wave Property	Symbol	$h(\omega)$	α	β
Water Surface Elevation	η	1	0	0
Pressure	p	$\rho g \frac{\cosh kz}{\sinh kd}$	0	0
Surface Slope (x)	η_x	ik	1	0
Surface Slope (y)	η_y	ik	0	1
Surface Curvature (x)	η_{xx}	$-k^2$	2	0
Surface Curvature (y)	η_{yy}	$-k^2$	0	2
Surface Curvature (xy)	η_{xy}	$-k^2$	1	1
Water Particle Velocity (x)	u	$\omega \frac{\cosh kz}{\sinh kd}$	1	0
Water Particle Velocity (y)	v	$\omega \frac{\cosh kz}{\sinh kd}$	0	1
Water Particle Velocity (z)	w	$-i\omega \frac{\sinh kz}{\sinh kd}$	0	0
Water Particle Acceleration (x)	a_x	$-i\omega^2 \frac{\cosh kz}{\sinh kd}$	1	0
Water Particle Acceleration (y)	a_y	$-i\omega^2 \frac{\cosh kz}{\sinh kd}$	0	1
Water Particle Acceleration (z)	a_z	$-\omega^2 \frac{\sinh kz}{\sinh kd}$	1	0

spreading function. This relationship can be expressed in general form as (see Isobe et al., 1984)

$$S_{mn}(\omega) = \int_{\mathbf{k}} H_m(\mathbf{k},\omega) H_n^*(\mathbf{k},\omega) \exp\{-i\mathbf{k}\cdot(\mathbf{x}_n - \mathbf{x}_m)\} S(\mathbf{k},\omega)\, d\mathbf{k} \qquad (2.23)$$

where the subscripts m and n represent any two measured quantities, $H(\mathbf{k},\omega)$ is a complex transfer function that relates a measured quantity to the water surface elevation, and $\mathbf{x}_m$, $\mathbf{x}_n$ are the location of the measurements. The above relationship is only valid for a spatially homogeneous wave field where there is no correlation of the wave components travelling in different directions. The transfer function can be expressed as

$$H_m(\mathbf{k},\omega) = (\cos\theta)^{\alpha}(\sin\theta)^{\beta} h_m(\omega) \qquad (2.24)$$

where $h(\omega)$ is a direction independent transfer function. The values of h, α, and β for various wave properties based on linear wave theory are listed in Table 2.1. While measurements of various combinations of wave properties can be used for the analysis of directional waves, attention will now be focussed on measurements using a wave probe-biaxial current meter array and a wave probe array.

2.3.1 Analysis Using Measurements from a Wave Probe - Current Meter Array

When the measurements of the water surface elevation and the two orthogonal components of the horizontal velocity are made at a single location, equation (2.23) reduces to

$$\int_{-\pi}^{\pi} D(\omega,\theta)\, q_j(\theta)\, d\theta = P_j(\omega) \qquad j = 1,\ldots,5 \qquad (2.25)$$

where

$$\left.\begin{aligned}
P_1(\omega) &= 1 &&;\quad q_1(\theta) = 1\\
P_2(\omega) &= \frac{C_{\eta u}}{h_u(\omega)S_\eta(\omega)} &&;\quad q_2(\theta) = \cos\theta\\
P_3(\omega) &= \frac{C_{\eta v}}{h_u(\omega)S_\eta(\omega)} &&;\quad q_3(\theta) = \sin\theta\\
P_4(\omega) &= \frac{C_{uu} - C_{vv}}{h_u^2(\omega)S_\eta(\omega)} &&;\quad q_4(\theta) = \cos 2\theta\\
P_5(\omega) &= \frac{2C_{uv}}{h_u^2(\omega)S_\eta(\omega)} &&;\quad q_5(\theta) = \sin 2\theta
\end{aligned}\right\} \tag{2.26}$$

where $C_{mn}(\omega)$ is the real part of the cross-spectrum $S_{mn}(\omega)$, often referred to as the coincident spectrum. Instead of using linear wave theory, the transfer function $h_u(\omega)$ can be estimated from the co-spectra of the measured quantities as

$$h_u(\omega) = \sqrt{\frac{C_{uu} + C_{vv}}{C_{\eta\eta}}} \tag{2.27}$$

The use of the above equation to estimate the transfer function minimizes the effect of the errors introduced in the calibration of current meters. The Fourier series, MLM, and MEM all use the above relationship between the cross-spectra and the spreading function to estimate the spreading function.

The Fourier Series Approach

The directional spreading function can be expanded as a Fourier series in direction θ as

$$D(\omega, \theta) = a_0 + \sum_{n=1}^{\infty}(a_n \cos n\theta + b_n \sin n\theta) \tag{2.28}$$

where a_n and b_n are Fourier coefficients. Because of the limited number of measured quantities for a wave probe - current meter array, the expansion can only be carried out to obtain the first five Fourier coefficients. Substituting equation (2.28) into equation (2.25) and using the orthogonality of the cosine and sine functions gives the Fourier coefficients as

$$a_0 = P_1/(2\pi);\ a_1 = P_2/\pi;\ a_2 = P_4/\pi;\ b_1 = P_3/\pi;\ b_2 = P_5/\pi \tag{2.29}$$

There are no constraints on the values of the Fourier coefficients so unrealistic negative values of the directional spreading function can appear. Smoothing functions can be used (see Panicker and Borgman, 1970) to ensure a positive spreading function but this however results in a further decrease in directional resolution.

The Maximum Likelihood Method

The MLM is described in great detail by Isobe et al. (1984), and is thus briefly summarized here. The MLM is normally used in probability theory to estimate parameters of a probability distribution which maximize the likelihood of obtaining the observed data set. In directional wave analysis, the MLM estimate of the spreading function minimizes the error of the weighted sum of Fourier coefficients, with the weighting function dependent on the direction of wave propagation. The MLM estimate of the directional spreading function can be expressed as (see Isobe et al. , 1984)

$$D(\omega,\theta) = \frac{a_0}{\{\gamma\}^T\,[P]^{-1}\,\{\gamma\}} \tag{2.30}$$

where a_0 is a normalizing coefficient that ensures equation (2.9) is satisfied, and $\{\gamma\}$ is the weighting function given by

$$\{\gamma\} = \begin{bmatrix} 1 \\ \cos\theta \\ \sin\theta \end{bmatrix} \tag{2.31}$$

$[P]$ is the normalized cross-spectral density matrix of η, u, and v, and is given by

$$[P] = \begin{bmatrix} P_1 & P_2 & P_3 \\ P_2 & \frac{1+P_4}{2} & \frac{P_5}{2} \\ P_3 & \frac{P_5}{2} & \frac{1-P_4}{2} \end{bmatrix} \tag{2.32}$$

The cross-spectral density matrix at each frequency, obtained from an FFT analysis of the measured time series can be substituted into equation (2.30) to yield a discrete directional distribution.

The Maximum Entropy Method

The maximum entropy method used in this thesis is based on a similar concept used in probability theory (Jaynes, 1957), where probability distributions are estimated from a limited amount of information. The probability approach was first applied to directional wave analysis by Kobune and Hashimoto (1986). The application of the MEM to directional wave analysis is now presented in detail.

The spreading function can be considered to be the probability distribution of wave energy at a given frequency over direction. The problem of estimating the spreading function thus becomes one of estimating a probability distribution from a limited amount of data. Information is available in the form of the integral equation (2.25), in which the kernel functions $q_j(\theta)$ and the cross spectra components $P_j(\omega)$ are known, and the directional spreading function is unknown. There are different directional distributions that can satisfy the integral equation. Based on maximum entropy ideas, the least biased distribution is the one which maximizes the entropy I associated with the directional distribution. The entropy I is defined as

$$I = -\int_{-\pi}^{\pi} D(\omega,\theta)\, \ln\, D(\omega,\theta)\, d\theta \tag{2.33}$$

When there is no information available, the distribution with the largest entropy is the uniform distribution. Maximum entropy thus predicts an equal probability of wave energy propagating in all possible directions. All other non-uniform distributions result in a decrease in entropy.

Since there is information provided by the relationship between the measured cross-spectral density matrix and the directional distribution, the maximum entropy solution is chosen to satisfy that relationship. Maximizing the entropy, I, subject to the constraints imposed by equation (2.25) produces the solution

$$D(\omega,\theta) = \exp\left[-1 - \sum_{j=1}^{5} \mu_j q_j(\theta)\right] \tag{2.34}$$

where μ_j are Lagrange multipliers that ensure the constraints are satisfied. Since $q_1(\theta) = 1$, the multiplier μ_1 is just a constant and can be modified to absorb the extra constant -1 in the above equation. Substitution of the MEM solution (2.34) into equation (2.25) results in a nonlinear set of equations

$$\int_{-\pi}^{\pi} \exp\left[-\sum_{i=1}^{5} \mu_i q_i(\theta)\right] q_j(\theta)\, d\theta = P_j(\omega) \qquad j = 1,\ldots,5 \tag{2.35}$$

The problem now becomes one of determining the Lagrange multipliers μ_j which satisfy the above integral equation. The integral equation cannot be analytically solved to determine μ_j so one has to resort to an iterative procedure such as the Newton-Raphson procedure. Starting with initial guesses for μ_j, $j = 1,\ldots,5$, updated values μ_j' are obtained by solving the following equation

$$\sum_{j=1}^{5} \frac{\partial f_i}{\partial \mu_j}(\mu_j' - \mu_j) = -f_i \qquad i = 1,\ldots,5 \tag{2.36}$$

where

$$f_i = P_i - \int_{-\pi}^{\pi} q_i(\theta)\, \exp\left\{-\sum_{k=1}^{5} \mu_k q_k(\theta)\right\} d\theta \tag{2.37}$$

$$\frac{\partial f_i}{\partial \mu_j} = \int_{-\pi}^{\pi} q_i(\theta) q_j(\theta)\, \exp\left\{-\sum_{k=1}^{5} \mu_k q_k(\theta)\right\} d\theta \tag{2.38}$$

The iterative procedure is stopped by a convergence criterion which requires that the differences between the current and updated values of μ_j be less than a specified tolerance. A suitable initial guess for the parameters μ_j can be determined from the MLM solution for $D(\theta)$ as

$$\mu_1 = -\frac{1}{\pi} \int_{-\pi}^{\pi} \ln D(\theta)\, d\theta \tag{2.39}$$

$$\mu_j = -\frac{2}{\pi}\int_{-\pi}^{\pi} \ln D(\theta)\, q_j(\theta)\, d\theta \qquad j = 2, \ldots, 5 \tag{2.40}$$

While Kobune and Hashimoto (1986) eliminated μ_1 from the iterative procedure and solved for four instead of five parameters, μ_1 is retained here to improve convergence for narrow spreading functions.

2.3.2 Analysis Using Measurements from a Wave Probe Array

When measurements of the water surface elevation are made with a wave probe array, the relationship between the cross-spectral density matrix and directional spreading function changes. The normalized cross-spectrum of the measurements of the water surface elevation at locations $\mathbf{x}_j$ and $\mathbf{x}_l$ can be obtained from equation (2.23) as

$$P_{jl}(\omega) = \int_{-\pi}^{\pi} \exp\{-i\mathbf{k}\cdot(\mathbf{x}_l - \mathbf{x}_j)\} D(\omega, \theta)\, d\theta \tag{2.41}$$

where $P_{jl}(\omega) = S_{jl}(\omega)/\sqrt{S_j(\omega)S_l(\omega)}$. The above equation can be rewritten as

$$P_{jl}(\omega) = \int_{-\pi}^{\pi} \exp\{ikr_{jl}\cos(\beta_{jl} - \theta)\} D(\omega, \theta)\, d\theta \tag{2.42}$$

where

$$\begin{aligned} r_{jl} &= \sqrt{(x_j - x_l)^2 + (y_j - y_l)^2} \\ \beta_{jl} &= \arctan[(y_j - y_l)/(x_j - x_l)] \end{aligned}$$

The Fourier series, MLM, and MEM methods of estimating the directional spreading function will now have to be modified to take into account the above relationship between the cross-spectra and the spreading function.

The Fourier Series Method

The Fourier Series representation of the directional spreading function (equation (2.28)) can be substituted into equation (2.42) to yield (see Panicker and Borgman, 1970)

$$
\begin{aligned}
P_{jl}(\omega) &= \int_{-\pi}^{\pi} \left[a_0 + \sum_{n=1}^{\infty} (a_n \cos n\theta + b_n \sin n\theta) \right] \exp\{ikr_{jl} \cos(\beta_{jl} - \theta)\}\, d\theta \\
&= \pi \left[a_0 A_0 + \sum_{n=1}^{\infty} i^n (a_n A_n + b_n B_n) \right] \qquad (2.43)
\end{aligned}
$$

where

$$
\begin{aligned}
A_0 &= 2J_0(kr_{jl}) \\
A_n &= 2\cos(n\beta_{jl})\, J_n(kr_{jl}) \\
B_n &= 2\sin(n\beta_{jl})\, J_n(kr_{jl})
\end{aligned}
$$

J_n is the Bessel function of the first kind of order n. The real and imaginary parts of the cross-spectrum can be expressed as

$$C_{jl} = \pi[a_0 A_0 - (a_2 A_2 + b_2 B_2) + (a_4 A_4 + b_4 B_4) - \cdots] \qquad (2.44)$$

$$Q_{jl} = \pi[(a_1 A_1 + b_1 B_1) - (a_3 A_3 + b_3 B_3) + \cdots] \qquad (2.45)$$

The imaginary part of the cross-spectrum Q_{jl} is often referred to as the quadrature spectrum. There are two equations for each combination of probes and two unknown Fourier coefficients for every harmonic. The number of equations can be made to exceed the number of unknown coefficients by choosing an appropriate number of harmonics for any specified number of probes. Panicker and Borgman (1970) used the least squares method to estimate the coefficients. The Fourier series method for a wave probe array also resolves directional seas poorly due to the finite number of coefficients used in the analysis.

The Maximum Likelihood Method

The MLM estimate of the directional spreading function for a wave probe array is similar to that of a wave probe - current meter array, and is given by Barnard (1969) as

$$D(\omega, \theta) = \frac{a_0}{\{\gamma\}^{*T}[P]^{-1}\{\gamma\}} \qquad (2.46)$$

where [P] is the normalized cross-spectral density matrix given by

$$[P] = \begin{bmatrix} P_{11} & P_{12} & \cdots & P_{1N} \\ P_{21} & P_{22} & \cdots & P_{2N} \\ \vdots & \vdots & \ddots & \vdots \\ P_{N1} & P_{N2} & \cdots & P_{NN} \end{bmatrix} \tag{2.47}$$

and

$$\{\gamma\} = \begin{bmatrix} \exp\{i\mathbf{k}\cdot\mathbf{x}_1\} \\ \exp\{i\mathbf{k}\cdot\mathbf{x}_2\} \\ \vdots \\ \exp\{i\mathbf{k}\cdot\mathbf{x}_N\} \end{bmatrix} \tag{2.48}$$

a_0 is a normalizing constant that ensures equation (2.9) is satisfied, and N is the number of wave probes. The estimation of the directional distribution by the MLM is relatively straightforward and just requires the determination of the cross-spectral density matrix from the measured elevation time series, and the evaluation of equation (2.46).

The Maximum Entropy Method

Barnard (1969) used the spectral analysis definition of entropy to obtain an analytical solution for the spreading function from an equally spaced linear array. The approach however estimates double peaked spreading functions when unimodal sea states are simulated, and is consequently not used in this thesis. The MEM based on the probability definition of entropy, used for the wave probe-current meter array will now be applied to a wave probe array.

The application of the MEM is a lot more complicated for the wave probe array than for the wave probe-current meter array. While the formulation of the method is essentially the same, the implementation of the method is different because of the non-orthogonality of the kernel functions $q_j(\theta)$ for a wave probe array.

The maximum entropy solution has to satisfy the relationship between the cross-spectral density matrix and the directional spreading function (equation (2.42)), which can be rewritten as

$$R_j(\omega) = \int_{-\pi}^{\pi} q_j(\theta)\, D(\omega,\theta)\, d\theta \qquad j = 1,\ldots,M+1 \tag{2.49}$$

where $M = N(N-1)$, N is the number of wave probes, and

$$q_j(\theta) = \begin{cases} \cos(kr_j \cos(\beta_j - \theta)) & j = 1,\ldots,M/2 \\ \sin(kr_j \cos(\beta_j - \theta)) & j = M/2+1,\ldots,M \\ 1 & j = M+1 \end{cases} \tag{2.50}$$

$$R_j(\omega) = \begin{cases} \mathrm{Re}[P_{mn}(\omega)] & j = 1,\ldots,M/2 \\ \mathrm{Im}[P_{mn}(\omega)] & j = M/2+1,\ldots,M \\ 1 & j = M+1 \end{cases} \tag{2.51}$$

The maximum entropy solution is given by equation (2.34) as

$$D(\omega,\theta) = \exp\left[-1 - \sum_{j=1}^{M+1} \mu_j q_j(\theta)\right] \tag{2.52}$$

Substitution of the above equation into equation (2.49) results in a nonlinear set of equations

$$\int_{-\pi}^{\pi} \exp\left[-\sum_{j=1}^{M+1} \mu_j q_j(\theta)\right] q_i(\theta)\, d\theta = R_i(\omega) \qquad i = 1,\ldots,M+1 \tag{2.53}$$

Most iterative procedures to determine the unknown Lagrange multipliers μ_j would have problems with convergence since some of the kernel functions $q_i(\theta)$ and $q_j(\theta)$ are correlated, depending on the relative spacing of the wave probes. The problem would have to be reformulated in terms of an orthogonal set of kernel functions.

According to well known theorems of linear algebra, a set of orthogonal functions $g_i(\theta)$ can be formed from $q_i(\theta)$ as

$$\{g\} = [T]^T\{q\} \tag{2.54}$$

where $[T]$ is a matrix with column vectors equal to the orthonormal eigenvectors of the covariance matrix defined by

$$Q_{ij} = \int_{-\pi}^{\pi} q_i(\theta) q_j(\theta)\, d\theta \tag{2.55}$$

The covariance matrix components can be evaluated explicitly by substituting the different expressions for the functions $q_j(\theta)$ in equation (2.50) into the above equation and carrying out the integration, resulting in

$$Q_{ij} = \begin{cases} \pi[J_0(z_1) + J_0(z_2)] & i = 1, \ldots, M/2; \quad j = 1, \ldots, M/2 \\ \pi[J_0(z_1) - J_0(z_2)] & i = M/2+1, \ldots, M; \quad j = M/2+1, \ldots, M \\ 2\pi J_0(kr_j) & i = M+1; \quad j = 1, \ldots, M/2 \\ 2\pi J_0(kr_i) & i = 1, \ldots, M/2; \quad j = M+1 \\ 2\pi & i = M+1; \quad j = M+1 \end{cases} \tag{2.56}$$

where

$$\begin{aligned} z_1 &= k[(r_i \cos\beta_i - r_j \cos\beta_j)^2 + (r_i \sin\beta_i - r_j \sin\beta_j)^2]^{\frac{1}{2}} \\ z_2 &= k[(r_i \cos\beta_i + r_j \cos\beta_j)^2 + (r_i \sin\beta_i + r_j \sin\beta_j)^2]^{\frac{1}{2}} \end{aligned}$$

All other components of the covariance matrix are identically zero.

The existence of a zero eigenvalue of $[Q]$ indicates that one of the functions $q_i(\theta)$ is either identically zero or correlated with the other functions $q_j(\theta)$. Eigenvalues close to zero also indicate a correlation of the functions which implies redundancies in the provided information. In order to take advantage of the redundancies in the data and stabilize the solution, the smallest eigenvalues are dropped and the solution is computed for L 'important' eigenvalues. A suitable criterion would have to be established for determining the number of important eigenvalues. The problem now reduces to determining the parameters ν_j, $j = 1, \ldots, L$ which satisfy the following set of equations

$$\int_{-\pi}^{\pi} \exp\left[-\sum_{j=1}^{L} \nu_j g_j(\theta)\right] g_i(\theta)\, d\theta = G_i(\omega) \qquad i = 1, \ldots, L \tag{2.57}$$

where

$$\{G\} = [T]^T \{R\} \tag{2.58}$$

The Newton-Raphson method is used to solve the nonlinear system of equations for the parameters ν_j. The directional spreading function is then obtained as

$$D(\omega, \theta) = \exp\left[-1 - \sum_{j=1}^{L} \nu_j g_j(\theta)\right] \tag{2.59}$$

A suitable initial guess for the parameters ν_j can be determined by considering the linear approximation of the exponential function

$$\exp\left[-1 - \sum_{j=1}^{L} \nu_j g_j(\theta)\right] \simeq \sum_{j=1}^{L} \nu_j g_j(\theta) \tag{2.60}$$

Substitution of the linear approximation into equation (2.57) leads to initial guesses

$$\nu_j = G_j \qquad\qquad j = 1, \ldots, L \tag{2.61}$$

The convergence criteria used to stop the iterative procedure requires that either the updated values of the ν's agree with the current values of the ν's to a specified accuracy, or that differences between the left and right hand sides of equation (2.57) be less than a specified tolerance. Due to the presence of noise and truncation of the information provided by the original data set, the above two criteria cannot be met in some cases and the solution is determined as that which minimized the square error in the iterative procedure. The square error, E_Q is given as

$$E_Q = \sum_{i=1}^{L} \left[G_i(\omega) - \int_{-\pi}^{\pi} \exp\left[-\sum_{j=1}^{L} \nu_j g_j(\theta)\right] g_i(\theta)\, d\theta\right]^2 \tag{2.62}$$

The eigenvalue analysis is also useful for investigating different array spacings and configurations. As an example, if a five probe array and a ten probe array have the same number of important eigenvalues for a given wavelength, then the information provided by the additional five probes can be considered to be redundant at that particular wavelength.

Chapter 3

WAVE FORCES ON A SLENDER VERTICAL CYLINDER

In this chapter, we examine the random wave forces on a slender structural member where the presence of the body does not significantly affect the incident wave field. This is generally assumed to be the case when the structure's diameter is less than one-fifth of the wavelength. The Morison equation is used to compute the wave forces on such members.

Due to the nonlinearity of the drag component of the force predicted by the Morison equation, the standard linear spectral approach cannot be used to model the force in the frequency domain. By linearizing the drag component of the force, Borgman (1967a) derived an expression for the force spectral density for long-crested waves. The approach was later extended to short-crested waves by Borgman and Yfantis (1981). In this chapter, a different approach is used to derive the spectral density of the inline and transverse forces in directional seas.

Although linearization is useful for estimating the force spectral density and standard deviation, the corresponding Gaussian distribution of the wave force severely underestimates the extreme force values when the drag force is dominant. The nonlinearity of the drag force would thus have to be considered in predicting extreme events. By considering a transformation of variables, Pierson and Holmes (1965) derived the probability distribution of the nonlinear force for long-crested waves.

The probability distribution of the peaks of the force is however required for the prediction of extreme events. The derivation of the peak force distribution is rather complicated for any arbitrary sea state, so a narrow-band assumption is often made. Borgman(1972) used the narrow-band assumption to derive the peak distribution for long-crested waves. The probability distribution of the peaks of the resultant force in short-crested waves which has not been previously derived elsewhere in the literature is derived in this chapter.

3.1 The Morison Equation

The horizontal force per unit length acting in the direction of wave propagation on a fixed slender vertical structural member of diameter, D, in a regular long-crested wave field is given by the Morison equation (see Morison et al., 1950) as

$$F(z,t) = K_D u(z,t)|u(z,t)| + K_M a(z,t) \tag{3.1}$$

where $K_D = \rho C_D D/2$, $K_M = \rho \pi D^2 C_M/4$, ρ is the mass density of water, C_D, C_M are empirical drag and inertia coefficients, and u, a are the horizontal water particle velocity and acceleration respectively. The force comprises of a linear inertial component, analagous to the force due to an accelerating flow of an inviscid fluid past a stationary body, and a nonlinear drag component, analagous to the force due to the steady flow of a real fluid past a body.

Numerous experiments, many of which are summarized in Sarpkaya and Isaacson (1981), have been carried out to validate the Morison equation and determine appropriate values of the force coefficients. The force coefficients have been found to depend primarily on the Reynolds number, R_N, the Keulegan-Carpenter number, K_C, and the relative roughness of the cylinder. The Reynolds number is the ratio of inertia to viscous forces and is defined for a regular long-crested wave field as

$$R_N = \frac{u_m(z)D}{\nu} \tag{3.2}$$

where $u_m(z)$ is the maximum orbital velocity and ν is the kinematic viscosity. The Keulegan-Carpenter number is proportional to the ratio of the horizontal water particle displacement to the cylinder diameter and is given by

$$K_C = \frac{u_m(z)T}{D} \tag{3.3}$$

where $T = 2\pi/\omega$ is the wave period. For random wave conditions, the parameters are defined using the significant velocity amplitude $u_m(z) = 2\sigma_u$, and the average zero-crossing period, T_z, where σ_u is the standard deviation of the water particle velocity. Figures 3.1 and 3.2 show typical C_D and C_M values as a function of K_C and R_N based on the U-tube experimental data of Sarpkaya (1975). The force coefficients vary from 0.6 to 2.0 for a wide range of R_N and K_C. Sarpkaya and Isaacson (1981) recommend using $C_D = 0.6$ and $C_M = 1.8$ as typical values for $R_N > 1.5 \times 10^6$.

3.2 The Lift Force

In addition to the force acting in the direction of wave propagation due to the drag and inertia effects in a long-crested wave field, there is also a lift force perpendicular to the flow associated with the alternate shedding of vortices. The lift force can be particularly critical if the lift force frequency 'locks-in' with the natural frequency of the structure.

The amplitude of the lift force and the frequency of vortex shedding are dependent primarily on R_N and K_C. The amplitude of the lift force for regular waves can be expressed in terms of a lift force coefficient as

$$F_{Lm} = \frac{1}{2}\rho C_L D u_m^2 \tag{3.4}$$

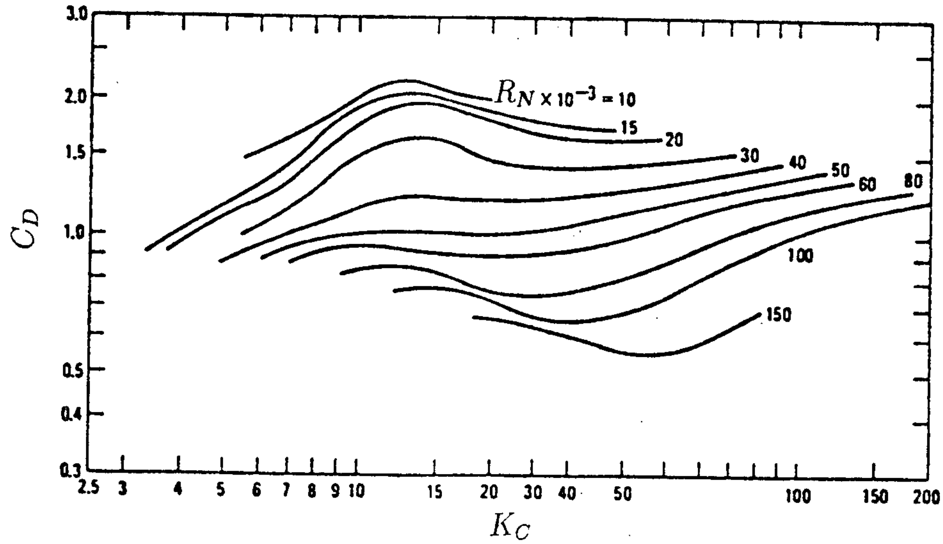

Figure 3.1: Drag coefficient versus K_C and R_N (from Sarpkaya, 1975)

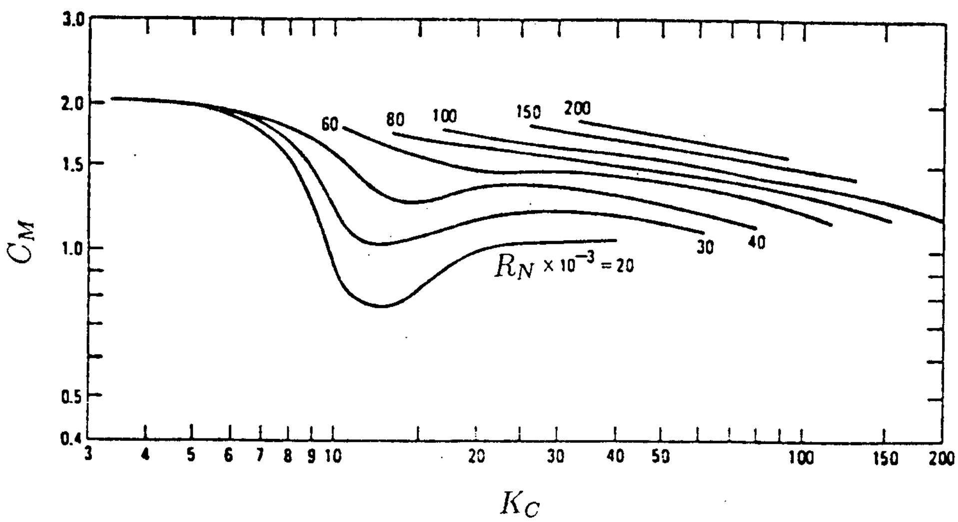

Figure 3.2: Inertia coefficient versus K_C and R_N (from Sarpkaya, 1975)

where C_L is the lift force coefficient. Sarpkaya and Isaacson (1981) also summarize different experimental measurements of the lift force for a harmonically oscillating flow. The lift force is generally irregular and sensitive to the experimental conditions. The experimental measurements indicate that the lift force coefficient reaches its maximum in the neighborhood of $K_C = 12$ with the associated frequency of the force twice the frequency of oscillation of the flow.

3.3 Long-Crested Random Wave Forces

3.3.1 Force Spectral Density

Even though the Morison equation was originally developed for a harmonically oscillating flow, it is generally assumed applicable for random wave conditions. Because of the nonlinearity of the drag force, the procedure for determining the force spectrum from the water surface elevation spectrum is no longer as straightforward as for linear systems. Borgman (1967a) derived the linearized force spectral density by expanding the covariance function in a power series and retaining the first term. The covariance function of the force can be expressed as (see Borgman, 1967a)

$$\begin{aligned} R_F(\tau) &= \overline{F(t)F(t+\tau)} \\ &= K_D^2 \sigma_u^4 G\left(\frac{R_u(\tau)}{\sigma_u^2}\right) + K_M^2 R_a(\tau) \end{aligned} \tag{3.5}$$

where R_F, R_u, R_a are the covariance or autocorrelation functions of the force, velocity, and acceleration respectively. The function $G(x)$ is given by

$$G(x) = [(4x^2+2)\arcsin(x) + 6x\sqrt{1-x^2}]/\pi \tag{3.6}$$

where $x = R_u(\tau)/\sigma_u^2$. $G(x)$ can be expanded as a power series in x

$$G(x) = \frac{1}{\pi}\left[8x + \frac{4}{3}x^3 + \frac{x^5}{15} + \cdots\right] \tag{3.7}$$

The spectral density of the force $S_F(\omega)$ is given as the Fourier transform of the covariance function

$$S_F(\omega) = 2\int_0^{\infty} R_F(\tau)\exp(-i\omega\tau)\, d\tau \tag{3.8}$$

The spectral density of the nonlinear force can thus be expressed as

$$\begin{aligned} S_F(\omega) &= 2K_D^2\sigma_u^4 \int_0^{\infty} \frac{1}{\pi}\left[8\frac{R_u(\tau)}{\sigma_u^2} + \frac{4R_u^3(\tau)}{3\sigma_u^6} + \frac{R_u^5}{15\sigma_u^{10}} + \cdots\right] \exp(-i\omega\tau)\, d\tau \\ &+ 2K_M^2 \int_0^{\infty} R_a(\tau)\exp(-i\omega\tau)\, d\tau \end{aligned} \tag{3.9}$$

Since powers of $R_u(\tau)$ appear in the expression for $S_F(\omega)$, the force spectrum will involve a series of self-convolutions of the velocity spectrum, requiring an intensive computational effort. The drag force component can be linearized by considering only the first term of $G(x)$ in equation (3.7) resulting in

$$S_F(\omega) = \frac{8}{\pi}K_D^2\sigma_u^2 S_u(\omega) + K_M^2 S_a(\omega) \tag{3.10}$$

where $S_u(\omega)$ and $S_a(\omega)$ are the velocity and acceleration spectrum respectively, given by linear wave theory as

$$S_u(\omega) = |h_u(\omega)|^2 S_\eta(\omega) \tag{3.11}$$

$$S_a(\omega) = \omega^2 |h_u(\omega)|^2 S_\eta(\omega) \tag{3.12}$$

$S_\eta(\omega)$ is the water surface elevation spectrum and $h_u(\omega)$ is a transfer function given in Table 2.1.

A simpler approach to deriving the linearized force spectrum is to consider a linear approximation of the velocity squared term

$$u(z,t)|u(z,t)| \simeq \gamma_u u(z,t) \tag{3.13}$$

Since $u(z,t)$ is a random process, the best estimate of the constant γ_u is the one which minimizes the expected value of the square error of the linearization. The square error E_Q is given by

$$E_Q = \int_{-\infty}^{\infty} [u|u| - \gamma_u u]^2 p(u)\, du \tag{3.14}$$

where $p(u)$ is the probability density function of the water particle velocity which is assumed Gaussian. Substituting a normal distribution for $p(u)$ into equation (3.14) and differentiating E_Q with respect to γ_u results in

$$\gamma_u = \sqrt{\frac{8}{\pi}}\,\sigma_u \tag{3.15}$$

The spectral density of the force can now be obtained by the usual linear transfer function approach and is identical to equation (3.10).

3.3.2 Estimation of Force Coefficients

There are a few different methods used to estimate the force coefficients under random wave conditions from measured data. The various methods are reviewed in Borgman (1972). The force coefficients can be assumed to be either constant or dependent on the wave frequency. When the force coefficients are assumed constant, the coefficients can be estimated by the method of moments where the second and fourth moments of the measured distribution are equated to those of the theoretical distribution. An alternate approach is to determine the coefficients which minimize the difference between the measured force spectrum $S_{FM}(\omega)$ and the theoretical linearized force spectrum in a least squares sense. The square error, E_Q, is given by

$$E_Q = \sum_j [S_{FM}(\omega_j) - S_F(\omega_j)]^2 \tag{3.16}$$

The coefficients K_D and K_M which minimize E_Q are given by

$$K_D = \left[\frac{f_3 f_4 - f_1 f_6}{f_3 f_5 - f_2 f_6}\right]^{\frac{1}{2}} \tag{3.17}$$

$$K_M = \left[\frac{f_1 f_5 - f_2 f_4}{f_3 f_5 - f_2 f_6}\right]^{\frac{1}{2}} \tag{3.18}$$

where

$$f_1 = \sum_j S_{FM}(\omega_j) S_u(\omega_j)$$

$$
\begin{aligned}
f_2 &= \sum_j \frac{8}{\pi}\sigma_u^2 S_u^2(\omega_j) \\
f_3 &= \sum_j S_u(\omega_j) S_a(\omega_j) \\
f_4 &= \sum_j S_{FM}(\omega_j) S_a(\omega_j) \\
f_5 &= \frac{8}{\pi}\sigma_u^2 f_3 \\
f_6 &= \sum_j S_a^2(\omega_j)
\end{aligned}
$$

Frequency dependent force coefficients can be estimated from the cross-spectra of the time series of the measured force, the product of the velocity and its absolute value, and the acceleration. The time series $u(t)|u(t)|$ and $a(t)$ are derived from the time series of the measured water surface elevation. The cross-spectral density components can be expressed as

$$
S_{Fu|u|}(\omega) = K_D S_{u|u|u|u|}(\omega) + K_M S_{au|u|}(\omega) \tag{3.19}
$$

$$
S_{Fa}(\omega) = K_D S_{au|u|}(\omega) + K_M S_a(\omega) \tag{3.20}
$$

where $S_{mn}(\omega)$ is the complex cross-spectrum of quantities m and n. Considering only the real part of the cross-spectra, $C_{mn}(\omega)$, and solving for the force coefficients results in

$$
K_D(\omega) = \frac{C_{Fu|u|}(\omega) S_a(\omega) - C_{Fa}(\omega) C_{au|u|}(\omega)}{S_{u|u|u|u|}(\omega) S_a(\omega) - C^2_{au|u|}(\omega)} \tag{3.21}
$$

$$
K_M(\omega) = \frac{C_{Fa}(\omega) S_{u|u|u|u|}(\omega) - C_{Fu|u|}(\omega) C_{au|u|}(\omega)}{S_{u|u|u|u|}(\omega) S_a(\omega) - C^2_{au|u|}(\omega)} \tag{3.22}
$$

The frequency dependent coefficients are usually only reasonable over the range of frequencies where there is a significant amount of wave energy.

3.3.3 Probability Distribution of the Force

If the drag force is linearized, the probability distribution of the force becomes Gaussian since the sea state is assumed to be a Gaussian process. A Gaussian distribution of the force however underestimates the extreme force values when the drag force is important. The probability density function of the nonlinear wave force can however be derived from the joint distribution of the water particle velocity and acceleration by the transformation of variables procedure. This approach was originally used by Pierson and Holmes (1965). The water particle velocity and acceleration are assumed to be statistically independent with each possessing a Gaussian distribution. Their joint distribution can thus be expressed as

$$p(u,a) = \frac{1}{2\pi\sigma_u\sigma_a}\exp\left\{-\frac{1}{2}\left(\frac{u^2}{\sigma_u^2}+\frac{a^2}{\sigma_a^2}\right)\right\} \tag{3.23}$$

The joint probability distribution of the force, F, and an auxilary variable, ψ, can be obtained from $p(u,a)$ as

$$p(F,\psi) = \frac{p(u,a)}{|J|} \tag{3.24}$$

where $|J|$ is the determinant of the Jacobian of the transformation between (F,ψ) variables and (u,a) variables, defined by

$$\begin{aligned} [J] &= \frac{\partial(F,\psi)}{\partial(u,a)} \\ &= \begin{bmatrix} \frac{\partial F}{\partial u} & \frac{\partial F}{\partial a} \\ \frac{\partial \psi}{\partial u} & \frac{\partial \psi}{\partial a} \end{bmatrix} \end{aligned} \tag{3.25}$$

By choosing the auxilary variable $\psi = u$, the determinant of [J] turns out to be equal to K_M. The probability distribution of F can be obtained by integrating over the auxilary variable resulting in

$$p(F) = \frac{1}{2\pi K_M\sigma_u\sigma_a}\int_{-\infty}^{\infty}\exp\left[-\frac{1}{2}\left(\frac{u^2}{\sigma_u^2}+\frac{(F-K_D u|u|)^2)}{K_M^2\sigma_a^2}\right)\right]\,du \tag{3.26}$$

The above distribution is in integral form and has to be evaluated numerically. Borgman (1967b) alternately expressed the probability distribution of the nondimensional force, ζ in terms of the parabolic cylinder function $U(0,x)$ as

$$\begin{aligned} p(\zeta) &= \left(\frac{\zeta_0}{8\pi}\right)^{\frac{1}{2}}\exp\left(-\frac{\zeta^2}{2}\right)\{\exp[(\zeta_0+\zeta)^2/4]U(0,\zeta_0+\zeta) \\ &\quad + \exp[(\zeta_0-\zeta)^2/4]U(0,\zeta_0-\zeta)\} \end{aligned} \tag{3.27}$$

where

$$\zeta = \frac{F}{K_M \sigma_a} \tag{3.28}$$

$$\zeta_0 = \frac{K_M \sigma_a}{2K_D \sigma_u^2} \tag{3.29}$$

The variable ζ_0 is proportional to the ratio of the inertia to drag components of the force. For very large values of ζ_0, the force is predominantly inertial and the probability distribution approaches a Gaussian distribution. For smaller values of ζ_0, a Gaussian distribution with the correct standard deviation would underestimate the value of the force at the tail of the distribution.

The force probability distribution is symmetric with zero mean. The second and fourth moments of a distribution are defined as

$$m_2 = \int_{-\infty}^{\infty} \zeta^2 p(\zeta)\, d\zeta \tag{3.30}$$

$$m_4 = \int_{-\infty}^{\infty} \zeta^4 p(\zeta)\, d\zeta \tag{3.31}$$

For a zero mean process, the second moment is equal to the variance of the process. The second and fourth moments of the force can be evaluated to give

$$m_2 = 1 + \frac{3}{4\zeta_0^2} \tag{3.32}$$

$$m_4 = 3 + \frac{9}{2\zeta_0^2} + \frac{105}{16\zeta_0^4} \tag{3.33}$$

The variance of the dimensional force can thus be expressed as

$$\sigma_F^2 = K_M^2 \sigma_a^2 + 3K_D^2 \sigma_u^4 \tag{3.34}$$

By comparison, the linearized force spectrum predicts the variance of the force as

$$\sigma_F^2 = K_M^2 \sigma_a^2 + \frac{8}{\pi} K_D^2 \sigma_u^4 \tag{3.35}$$

In a totally drag regime, use of the linearized force spectrum would underestimate the standard deviation of the force by about 8% . Depending on the relative contribution of the drag and inertia components, the linearized force spectrum can give quite a good estimate of the standard deviation of the force.

The probability distribution of the maxima of the force and the frequency of upcrossing of various force levels are however of more importance in the reliability based design and fatigue analysis of offshore structures, and are presented next.

3.3.4 Force Upcrossing Frequency

The frequency of upcrossing of a certain force level, F, is given by Lin (1967) as

$$\nu^+(F) = \int_0^\infty \dot{F} p(F, \dot{F})\, d\dot{F} \tag{3.36}$$

where the overdot denotes a derivative with respect to time, and $p(F, \dot{F})$ is the joint distribution of the force and its time derivative $\dot{F}$, given by

$$\dot{F} = 2K_D|u|a + K_M\dot{a} \tag{3.37}$$

The problem of estimating the upcrossing frequency of the force now becomes one of deriving an expression for $p(F, \dot{F})$. Using the transformation of variables procedure, the distribution can be expressed as

$$p(F, \dot{F}, u) = \frac{p(u, a, \dot{a})}{|J|} \tag{3.38}$$

where

$$\begin{aligned} |J| &= \begin{vmatrix} 2K_D|u| & K_M & 0 \\ 2K_D a \; sign(u) & 2K_D|u| & K_M \\ 1 & 0 & 0 \end{vmatrix} \\ &= K_M^2 \end{aligned} \tag{3.39}$$

and $p(u, a, \dot{a})$ is the joint distribution of the water particle velocity, acceleration, and the time derivative of the acceleration, given by

$$p(u, a, \dot{a}) = \frac{1}{(\sqrt{2\pi})^3 |C|^{\frac{1}{2}}} \exp\left[-\frac{1}{2}\{u\}^T[C]\{u\}\right] \tag{3.40}$$

[C] is a covariance matrix given by

$$[C] = \begin{bmatrix} \sigma_u^2 & 0 & -\sigma_a^2 \\ 0 & \sigma_a^2 & 0 \\ -\sigma_a^2 & 0 & \sigma_{\dot{a}}^2 \end{bmatrix} \tag{3.41}$$

and

$$\{u\} = \begin{bmatrix} u \\ a \\ \dot{a} \end{bmatrix} \tag{3.42}$$

The joint distribution of F and $\dot{F}$ can be obtained by integrating over the auxilary variable u

$$p(F, \dot{F}) = \int_{-\infty}^{\infty} p(F, \dot{F}, u)\, du \tag{3.43}$$

An evaluation of the above integral to provide a closed form expression for $p(F, \dot{F})$ is quite difficult. Moe and Crandall (1978) used Laplace's procedure for asymptotic integration to obtain an asymptotic distribution

$$p(F, \dot{F}) = \frac{1}{8\pi\sigma_a\sigma_u K_D F} \exp\left\{-\frac{1}{2K_D\sigma_u^2}\left[F - \frac{F_0}{2} + \frac{\sigma_u^2\dot{F}^2}{4\sigma_a^2 F}\right]\right\} \tag{3.44}$$

where $F_0 = K_M^2\sigma_a^2/(2K_D\sigma_u^2)$. Substitution of the above expression into equation (3.36) results in an asymptotic expression for the upcrossing frequency

$$\nu^+(F) = \frac{\omega_u}{2\pi} \exp\left[-\frac{1}{2K_D\sigma_u^2}\left(F - \frac{F_0}{2}\right)\right] \tag{3.45}$$

where $\omega_u = \sigma_a/\sigma_u$ is the average zero upcrossing frequency of the water particle velocity. The asymptotic expression for the force upcrossing frequency is valid for high force levels, and can be seen to be influenced by the nonlinear drag component. If the force is predominantly inertia ($K_D \to 0$), the joint distribution of the force and its time derivative is Gaussian and can be expressed as

$$p(F, \dot{F}) = \frac{1}{2\pi\sigma_a\sigma_{\dot{a}}K_M^2} \exp\left\{-\frac{1}{2K_M^2\sigma_a^2}\left(F^2 + \frac{\sigma_a^2\dot{F}^2}{\sigma_{\dot{a}}^2}\right)\right\} \tag{3.46}$$

The force upcrossing frequency can thus be obtained as

$$\nu^+(F) = \frac{\omega_a}{2\pi} \exp\left\{ -\frac{F^2}{2K_M^2 \sigma_a^2} \right\} \tag{3.47}$$

where $\omega_a = \sigma_{\dot{a}}/\sigma_a$ is the average zero upcrossing frequency of the water particle acceleration.

3.3.5 Probability Distribution of the Force Peaks

Let us now consider the probability distribution of the peaks or maxima of the force, $\hat{F}$. A maximum of a random process $F(t)$ occurs when $\dot{F}(t) = 0$ and $\ddot{F}(t) < 0$. The expected number of peaks per unit time above level ξ is given by Lin (1967) as

$$\mu(\xi) = -\int_{\xi}^{\infty} \int_{-\infty}^{\infty} \ddot{F} p(F, 0, \ddot{F}) \, d\ddot{F} dF \tag{3.48}$$

The probability that a peak lies above a certain force level ξ is equal to the ratio of the expected number of peaks per unit time above ξ to the expected total number of peaks per unit time, that is

$$1 - P_{\hat{F}}(\xi) = \frac{\mu(\xi)}{\mu(0)} \tag{3.49}$$

where $P_{\hat{F}}(\xi)$ is the cumulative distribution function of the force peaks, defined as

$$P_{\hat{F}}(\xi) = \int_0^{\xi} p(\hat{F}) \, d\hat{F} \tag{3.50}$$

A closed form expression for $p(F, \dot{F}, \ddot{F})$ is also quite difficult to obtain and certain assumptions are usually made in order derive an expression for the probability distribution of the force peaks.

A common assumption usually made for ocean waves is one of narrow-bandedness, implying a distribution of wave energy over a narrow range of frequencies. The water surface elevation is thus governed by a predominant frequency with the amplitude modulated by an envelope function. The water surface elevation can thus be expressed as

$$\eta(t) = a(t) \cos(\omega_0 t + \varepsilon(t)) \tag{3.51}$$

where $a(t)$ is the amplitude of the envelope, $\varepsilon(t)$ is a phase angle, and ω_0 is the predominant wave frequency, assumed equal to the average zero-crossing period of the water surface elevation, that is

$$\omega_0 = \frac{\sigma_{\dot{\eta}}}{\sigma_\eta} \tag{3.52}$$

The wave envelope and phase angle vary slowly in time. The force per unit length given by the Morison equation can be expressed as

$$F(t) = A\cos\beta|\cos\beta| + B\sin\beta \tag{3.53}$$

where $A = K_D\hat{u}^2$, $B = K_M\omega_0\hat{u}$, $\beta = \omega_0 t + \varepsilon(t)$, and $\hat{u} = h_u(\omega_0)a(t)$ is the slowly varying amplitude of the velocity process. The maximum force can be obtained by differentiating F with respect to β resulting in

$$\hat{F} = \begin{cases} A + \frac{B^2}{4A} & B < 2A \\ B & B \geq 2A \end{cases} \tag{3.54}$$

This can alternately be expressed as

$$\hat{F} = \begin{cases} K_D\hat{u}^2 + \frac{F_0}{2} & F_0 < B \\ K_M\omega_0\hat{u} & F_0 \geq B \end{cases} \tag{3.55}$$

It can be seen that the peak force is inertial if $F_0 \geq B$, and comprised of drag and inertial components for $F_0 < B$. In making the narrow-band assumption, the average zero upcrossing frequencies of the water surface elevation, water particle velocities and accelerations have all been assumed to be identical. There are however always differences for any process that is not infinitely narrow-banded. If the peak force is inertial, the frequency ω_0 should express the ratio of the acceleration amplitude to the velocity amplitude and a more appropriate value would be the average zero upcrossing frequency of the velocity process, ω_u.

Since the force peaks are directly related to the velocity peaks in equation (3.55), the probability distribution of the force peaks can be obtained from the probability distribution of the velocity peaks by the transformation of variables technique. Longuet-Higgins (1952) showed that the peaks of a narrow-band Gaussian process are governed by the Rayleigh distribution. The probability distribution of the positive peaks of the velocity can thus be expressed as

$$p(\hat{u}) = \frac{\hat{u}}{\sigma_u^2} \exp\left\{-\frac{\hat{u}^2}{2\sigma_u^2}\right\} \qquad 0 < \hat{u} < \infty \tag{3.56}$$

The probability distribution of the peaks of the force can be obtained from $p(\hat{u})$ as

$$p(\hat{F}) = \frac{p(\hat{u})}{d\hat{F}/d\hat{u}} \tag{3.57}$$

Substitution of equation (3.55) into equation (3.57)results in

$$p(\hat{F}) = \begin{cases} \dfrac{\hat{F}}{K_M^2\sigma_a^2} \exp\left[-\dfrac{\hat{F}^2}{2K_M^2\sigma_a^2}\right] & 0 < \hat{F} < F_0 \\ \\ \dfrac{1}{2K_D\sigma_u^2} \exp\left[-\dfrac{[\hat{F} - F_0/2]}{2K_D\sigma_u^2}\right] & \hat{F} > F_0 \end{cases} \tag{3.58}$$

When $\hat{F} < F_0$, the peak force is inertial and the probability distribution of the force peaks is Rayleigh. For $\hat{F} > F_0$, the effects of the drag force become more pronounced and the distribution becomes exponential.

The peak force distribution can alternately be obtained from the upcrossing frequency of the force for a narrow-band process. The expected number of peaks per unit time between force levels $\hat{F}$ and $\hat{F}+d\hat{F}$ is assumed equal to the difference between the number of upcrossings of levels $\hat{F}$ and $\hat{F}+d\hat{F}$. The probability of having a peak between $\hat{F}$ and $\hat{F}+d\hat{F}$ is equal to the ratio of the number of peaks per unit time between $\hat{F}$ and $\hat{F}+d\hat{F}$ to the total number of peaks per unit time. For a narrow band process, each zero upcrossing is assumed to lead to a peak so the total number of peaks per unit time is equal to the total number of zero upcrossings. The probability distribution of the peak force can be expressed as

$$p(\hat{F}) = -\frac{1}{\nu^+(0)} \frac{d}{d\hat{F}} \left[\nu^+(\hat{F})\right] \tag{3.59}$$

Since the high levels of the peak force are predominantly inertial for $\hat{F} < \hat{F}_0$, the upcrossing frequency of the peak force is given by equations (3.45) and (3.47) as

$$\nu^+(\hat{F}) = \begin{cases} \nu^+(0)\exp\left\{-\frac{\hat{F}^2}{2K_M^2\sigma_a^2}\right\} & 0 < \hat{F} < F_0 \\ \\ \nu^+(0)\exp\left[-\frac{1}{2K_D\sigma_u^2}\left(\hat{F} - \frac{F_0}{2}\right)\right] & \hat{F} > F_0 \end{cases} \tag{3.60}$$

It is implicit in the narrow-band assumption that the zero upcossing frequencies of the velocity and acceleration are almost identical so $\nu^+(0)$ may be taken as $\omega_u/2\pi$. Substitution of equation (3.60) into equation (3.59) results in the previously derived equation (3.58).

3.3.6 Distribution of the Single Largest Peak Force

The expected maximum peak force, $E[\hat{F}_{max}]$, in a storm of a given duration, T_D is of ultimate interest in the design of offshore structures. The problem can be expressed equivalently as one of finding the expected $max\{\hat{F}_i; i = 1, \ldots, N\}$ in a sample of N consecutive peaks in $(0, T_D)$. Assuming that all the peaks are statistically independent and identically distributed, the cumulative distribution of the largest one can be expressed as

$$\begin{aligned} P_{\hat{F}_{max}}(\xi) &= P[max(\hat{F}_1, \hat{F}_2, \ldots, \hat{F}_N) \leq \xi] \\ &= [P_{\hat{F}}(\xi)]^N \end{aligned} \tag{3.61}$$

The assumption of statistical independence of the peaks has been shown by Longuet-Higgins (1952) to lead to conservative estimates of the maximum peak force for a narrow-band process. The expected value and variance of the largest peak force can thus be expressed as

$$E[\hat{F}_{max}] = \int_0^\infty \xi \frac{d}{d\xi}\left[P_{\hat{F}_{max}}(\xi)\right] d\xi \tag{3.62}$$

$$\sigma^2_{\hat{F}_{max}} = \int_0^\infty \xi^2 \frac{d}{d\xi}\left[P_{\hat{F}_{max}}(\xi)\right] d\xi - \left\{E[\hat{F}_{max}]\right\}^2 \tag{3.63}$$

The above integrals cannot in general be evaluated to give closed form expressions so one has to resort to numerical integration.

An alternate approach to estimating the single largest peak force is based on the upcrossing frequency analysis. If the upcrossings of level ξ by $F(t)$ are assumed to be statistically independent, the upcrossings are then governed by the Poisson distribution. This can be shown to be the case (see Cramer and Leadbetter, 1967) in the asymptotic limit, i. e. as $\xi \to \infty$, $T_D \to \infty$. The cumulative distribution of the maximum peak force can thus be expressed as

$$\begin{aligned} P_{\hat{F}_{max}}(\xi) &= P[max\{F(t); 0 \le t \le T_D\} \le \xi] \\ &= \exp\{-\nu^+(\xi)T_D\} \end{aligned} \tag{3.64}$$

The expected maximum peak force and standard deviation of the maximum peak force can be obtained by substituting the expression for the upcrossing frequency (3.60) and the cumulative distribution of the peak force (3.64) into equations (3.62) and (3.63).

3.4 Short-Crested Random Wave Forces

The Morison equation can be extended to predict the horizontal component of the force on a vertical member in a three-dimensional wave field as

$$\mathbf{F} = K_D\mathbf{w}|\mathbf{w}| + K_M\mathbf{a} \tag{3.65}$$

where $\mathbf{F} = (F_x, F_y)$, $\mathbf{w} = (u, v)$, and $\mathbf{a} = (a_x, a_y)$. The above force model assumes the force coefficients in the inline (x) and transverse (y) directions are the same and ignores the presence of lift forces associated with vortex shedding. The contribution of the lift force to the total force in multi-directional seas is investigated experimentally and discussed later in Chapter 6.

3.4.1 Force Spectral Density

As with the two-dimensional force model, the exact expressions for the spectral density of the inline and transverse forces would involve several self-convolutions of the velocity spectrum due to the nonlinear drag component. Simplified expressions can be derived by linearizing the drag force component. The inline component of the drag force can be linearized as

$$u|\mathrm{w}| \simeq \gamma_u u \tag{3.66}$$

The parameter γ_u is chosen to minimize the expected value of the square error of the linearization, E_Q, given by

$$E_Q = E[\{u|\mathrm{w}| - \gamma_u u\}^2] \tag{3.67}$$

Minimizing the square error with respect to the parameter γ_u leads to

$$\gamma_u = \frac{E[u^2\sqrt{u^2+v^2}]}{E[u^2]} \tag{3.68}$$

The evaluation of the above equation requires knowledge of the joint distribution of the inline and transverse velocities, which can be expressed as

$$p(u,v) = \frac{1}{2\pi\sigma_u\sigma_v\sqrt{1-\lambda_{uv}^2}} \exp\left\{-\frac{1}{2\sqrt{1-\lambda_{uv}^2}}\left[\frac{u^2}{\sigma_u^2} + \frac{v^2}{\sigma_v^2} - \frac{2\lambda_{uv}uv}{\sigma_u\sigma_v}\right]\right\} \tag{3.69}$$

where λ_{uv} is the correlation coefficient of the u and v velocities, given by

$$\lambda_{uv}^2 = \frac{1}{\sigma_u\sigma_v}\int_0^\infty S_{uv}(\omega)\, d\omega \tag{3.70}$$

where $S_{uv}(\omega)$ is the cross spectrum of u and v. If the directional spreading function is assumed to be frequency independent, the correlation coefficient can be expressed as

$$\lambda_{uv}^2 = \frac{q_{uv}}{q_u q_v} \tag{3.71}$$

where

$$q_{uv} = \int_{-\pi}^{\pi} D(\theta)\sin\theta\cos\theta\, d\theta \tag{3.72}$$

$$q_u^2 = \int_{-\pi}^{\pi} D(\theta) \cos^2\theta \, d\theta \tag{3.73}$$

$$q_v^2 = \int_{-\pi}^{\pi} D(\theta) \sin^2\theta \, d\theta \tag{3.74}$$

If the mean direction of wave propagation is zero and the spreading function is symmetric, the correlation coefficient is zero and the velocity components are independent. The joint distribution thus reduces to

$$p(u,v) = \frac{1}{2\pi\sigma_u\sigma_v} \exp\left\{-\frac{1}{2}\left(\frac{u^2}{\sigma_u^2} + \frac{v^2}{\sigma_v^2}\right)\right\} \tag{3.75}$$

By defining the following non-dimensional variables

$$u_1 = \frac{u}{\sigma_u}; \quad u_2 = \frac{v}{\sigma_v} \tag{3.76}$$

the expression for the linearization constant γ_u (equation (3.68)) can be written as

$$\gamma_u = \frac{\sigma_u}{2\pi} \int_{-\infty}^{\infty}\int_{-\infty}^{\infty} u_1^2\sqrt{u_1^2 + ru_2^2} \, \exp\left\{-\frac{1}{2}(u_1^2 + u_2^2)\right\} \, du_1 du_2 \tag{3.77}$$

where $r = \sigma_v^2/\sigma_u^2$, is a measure of the degree of directional spreading of the waves. For long-crested waves, $r = 0$, while for a $\cos^2\theta$ directional distribution, $r = 1/3$. The integral in equation (3.77) is easier to evaluate in polar coordinates. The variables can be expressed in polar coordinates as

$$u_1 = w_1 \cos\beta \tag{3.78}$$

$$u_2 = w_1 \sin\beta \tag{3.79}$$

Equation (3.77) thus reduces to

$$\begin{aligned} \gamma_u &= \frac{\sigma_u}{2\pi} \int_{-\infty}^{\infty} w_1^4 \exp\left(-\frac{w_1^2}{2}\right) dw_1 \; \int_{-\pi}^{\pi} \cos^2\beta\sqrt{\cos^2\beta + r\sin^2\beta} \, d\beta \\ &= 3\sigma_u\sqrt{\frac{2}{\pi}} I_{20}(r) \end{aligned} \tag{3.80}$$

where

$$I_{20}(r) = \int_0^{\pi/2} \cos^2\beta\sqrt{\cos^2\beta + r\sin^2\beta}\, d\beta$$

$$= \frac{m+1}{3m}E(m) + \frac{m-1}{3m}K(m) \tag{3.81}$$

$m = 1 - r$, and $E(m)$ and $K(m)$ are Jacobian elliptic integrals (see Abramowitz and Stegun, 1965)

Applying a similar treatment to the transverse direction, with a linear approximation of $v|\mathbf{w}|$ taken as $\gamma_v v$ results in

$$\gamma_v = 3\sigma_u\sqrt{\frac{2}{\pi}}I_{02}(r) \tag{3.82}$$

where

$$I_{02}(r) = \int_0^{\pi/2} \sin^2\beta\sqrt{\cos^2\beta + r\sin^2\beta}\, d\beta$$

$$= \frac{2m-1}{3m}E(m) - \frac{m-1}{3m}K(m) \tag{3.83}$$

The linearized spectral density of the inline and transverse components of the horizontal force in multi-directional seas can thus be expressed as

$$S_{FX}(\omega) = \frac{18}{\pi}[I_{20}(r)]^2K_D^2\sigma_u^2S_u(\omega) + K_M^2S_{a_x}(\omega) \tag{3.84}$$

$$S_{FY}(\omega) = \frac{18}{\pi}[I_{02}(r)]^2K_D^2\sigma_u^2S_v(\omega) + K_M^2S_{a_y}(\omega) \tag{3.85}$$

If the waves are long-crested, $r = 0$ and $I_{20}(r) = 2/3$. The force spectral density for long-crested waves (equation (3.10)) is thus recovered.

The velocity and acceleration spectra in short-crested waves can be expressed in terms of the wave spectrum as

$$S_u(\omega) = |h_u(\omega)|^2S_\eta(\omega)q_u^2 \tag{3.86}$$

$$S_v(\omega) = |h_u(\omega)|^2 S_\eta(\omega) q_v^2 \tag{3.87}$$

$$S_{a_x}(\omega) = \omega^2 |h_u(\omega)|^2 S_\eta(\omega) q_u^2 \tag{3.88}$$

$$S_{a_y}(\omega) = \omega^2 |h_u(\omega)|^2 S_\eta(\omega) q_v^2 \tag{3.89}$$

The transfer function $h_u(\omega)$ is given in Table 2.1, while q_u and q_v are calculated from the directional spreading function by equations (3.73) and (3.74).

3.4.2 Probability Distribution of the Inline and Transverse Forces

While linearization of the drag force component is satisfactory for estimating the force spectral densities, it results in a Gaussian distribution of the forces. As was the case with long-crested waves, it is important to retain the nonlinearity of the force in deriving the distribution of forces in directional seas. The joint probability density function of the inline and transverse forces can be derived from the joint distribution of the inline and transverse velocities and accelerations as

$$p(F_X, F_Y, \psi_1, \psi_2) = \frac{p(u, v, a_x, a_y)}{|J|} \tag{3.90}$$

where

$$\begin{aligned} |J| &= \begin{vmatrix} \frac{K_D(2u^2+v^2)}{\sqrt{u^2+v^2}} & \frac{K_D uv}{\sqrt{u^2+v^2}} & K_M & 0 \\ \frac{K_D uv}{\sqrt{u^2+v^2}} & \frac{K_D(u^2+2v^2)}{\sqrt{u^2+v^2}} & 0 & K_M \\ 1 & 0 & 0 & 0 \\ 0 & 1 & 0 & 0 \end{vmatrix} \\ &= K_M^2 \end{aligned} \tag{3.91}$$

and the auxilary variables are chosen as $\psi_1 = u$, and $\psi_2 = v$. For a symmetric, frequency independent directional spreading function centred about the inline direction, u, v, a_x, and a_y are all statistically independent and their joint probability density function is given by

$$p(u, v, a_x, a_y) = \frac{1}{4\pi^2 \sigma_u \sigma_v \sigma_{a_x} \sigma_{a_y}} \exp\left\{-\frac{1}{2}\left(\frac{u^2}{\sigma_u^2} + \frac{v^2}{\sigma_v^2} + \frac{a_x^2}{\sigma_{a_x}^2} + \frac{a_y^2}{\sigma_{a_y}^2}\right)\right\} \tag{3.92}$$

The joint distribution of F_X and F_Y can thus be expressed as

$$p(F_X, F_Y) = \frac{1}{4\pi^2 \sigma_u \sigma_v \sigma_{a_x} \sigma_{a_y} K_M^2} \int_{-\infty}^{\infty}\int_{-\infty}^{\infty} \exp\left\{-\frac{1}{2}\left(\frac{u^2}{\sigma_u^2} + \frac{v^2}{\sigma_v^2} + \frac{a_x^2}{\sigma_{a_x}^2} + \frac{a_y^2}{\sigma_{a_y}^2}\right)\right\} du dv \tag{3.93}$$

where $a_x = (F_X - K_D u\sqrt{u^2+v^2})/K_M$ and $a_y = (F_Y - K_D v\sqrt{u^2+v^2})/K_M$. The marginal distributions of the inline and transverse force may be obtained from the joint distribution as

$$p(F_X) = \int_{-\infty}^{\infty} p(F_X, F_Y)\, dF_Y \tag{3.94}$$

$$p(F_Y) = \int_{-\infty}^{\infty} p(F_X, F_Y)\, dF_X \tag{3.95}$$

The variance of the inline and transverse forces can be obtained from the probability distributions as

$$\sigma_{F_X}^2 = \int_{-\infty}^{\infty} F_X^2\, p(F_X)\, dF_X \tag{3.96}$$

$$\sigma_{F_Y}^2 = \int_{-\infty}^{\infty} F_Y^2\, p(F_Y)\, dF_Y \tag{3.97}$$

By defining the following nondimensional variables,

$$u_1 = \frac{u}{\sigma_u}; \quad u_2 = \frac{v}{\sigma_v}; \quad u_3 = \frac{a_x}{\sigma_{a_x}}; \quad u_4 = \frac{a_y}{\sigma_{a_y}} \tag{3.98}$$

the variance of the forces can be expressed as

$$\sigma_{F_X}^2 = \frac{K_M^2 \sigma_{a_x}^2}{4\pi^2} \iiiint \left(u_3 + \frac{u_1}{2\zeta_0}\sqrt{u_1^2 + r u_2^2}\right)^2 \exp\left\{-\frac{1}{2}w_1^2\right\} du_1 du_2 du_3 du_4 \tag{3.99}$$

$$\sigma_{F_Y}^2 = \frac{K_M^2 \sigma_{a_y}^2}{4\pi^2} \iiiint \left(u_4 + \frac{u_2}{2\zeta_0}\sqrt{u_1^2 + r u_2^2}\right)^2 \exp\left\{-\frac{1}{2}w_1^2\right\} du_1 du_2 du_3 du_4 \tag{3.100}$$

where $w_1^2 = u_1^2 + u_2^2 + u_3^2 + u_4^2$, ζ_0 is defined in equation (3.29), and the integrals are defined over the range 0 to ∞. The above integrals can be evaluated to give

$$\sigma_{F_X}^2 = K_M^2\sigma_{a_x}^2 + 3K_D^2\sigma_u^4 + K_D^2\sigma_u^2\sigma_v^2 \tag{3.101}$$

$$\sigma_{F_Y}^2 = K_M^2\sigma_{a_y}^2 + 3K_D^2\sigma_v^4 + K_D^2\sigma_u^2\sigma_v^2 \tag{3.102}$$

By comparison, the linearized spectral densities of the inline and transverse forces predict the variances of the forces as

$$\sigma_{F_X}^2 = K_M^2\sigma_{a_x}^2 + \frac{18}{\pi}\left[I_{20}(r)\right]^2 K_D^2\sigma_u^4 \tag{3.103}$$

$$\sigma_{F_Y}^2 = K_M^2\sigma_{a_y}^2 + \frac{18r}{\pi}\left[I_{02}(r)\right]^2 K_D^2\sigma_v^4 \tag{3.104}$$

In a totally drag regime with $r = 0.33$ corresponding to a $\cos^2\theta$ directional distribution, use of the linearized spectra results in an underprediction of the variances of the inline and transverse forces by 12% and 22% respectively. This is higher than the 8% error introduced for the long-crested case.

3.4.3 Distribution of the Resultant Force Peaks

In order to derive an explicit expression for the probability distribution of the resultant force peaks in short-crested waves, the assumption of a narrow-band wave spectrum is made. The inline and transverse forces predicted by the Morison equation can be expressed for a narrow-band sea state as

$$F_X = A_x \cos\beta|\cos\beta| + B_x \sin\beta \tag{3.105}$$

$$F_Y = A_y \cos\beta|\cos\beta| + B_y \sin\beta \tag{3.106}$$

where

$$A_x = K_D\hat{u}\sqrt{\hat{u}^2 + \hat{v}^2}$$

$$A_y = K_D\hat{v}\sqrt{\hat{u}^2 + \hat{v}^2}$$

$$\begin{aligned} B_x &= K_M \hat{a}_x \\ B_y &= K_M \hat{a}_y \\ \beta &= \omega_0 t + \varepsilon(t) \end{aligned}$$

and $\hat{u}$, $\hat{v}$, $\hat{a_x}$, and $\hat{a_y}$ represent the slowly varying amplitude envelope of the inline and transverse velocities and accelerations respectively. The peaks of the inline and transverse force are obtained by differentiating with respect to β, resulting in

$$\hat{F}_X = \begin{cases} K_D \hat{u}\sqrt{\hat{u}^2+\hat{v}^2} + \frac{F_{X0}}{2} & F_{X0} < B_x \\ \\ K_M \hat{a}_x & F_{X0} \geq B_x \end{cases} \tag{3.107}$$

and

$$\hat{F}_Y = \begin{cases} K_D \hat{v}\sqrt{\hat{u}^2+\hat{v}^2} + \frac{F_{Y0}}{2} & F_{Y0} < B_y \\ \\ K_M \hat{a}_y & F_{Y0} \geq B_y \end{cases} \tag{3.108}$$

where $F_{X0} = K_M^2 \hat{a}_x^2 / 2K_D \hat{u}\sqrt{\hat{u}^2+\hat{v}^2}$, and $F_{Y0} = K_M^2 \hat{a}_y^2 / 2K_D \hat{v}\sqrt{\hat{u}^2+\hat{v}^2}$. The joint distribution of the peaks of the inline and transverse force can be obtained from the joint distribution of the peaks of the inline and transverse velocities by transformation of variables. The probability distribution of the peaks of the resultant force is however of more importance since the largest peaks of the inline and transverse forces might not occur at the same time. The resultant force is given by

$$\begin{aligned} F_R &= \sqrt{F_X^2 + F_Y^2} & (3.109) \\ &= \sqrt{(A_x^2 + A_y^2)\cos^4\beta + (B_x^2 + B_y^2)\sin^2\beta + 2(A_x B_x + A_y B_y)\sin\beta\cos\beta|\cos\beta|} \end{aligned}$$

By making use of the following inequality,

$$2ab \leq a^2 + b^2 \tag{3.110}$$

it can be shown that

$$F_R \leq \sqrt{A_x^2 + A_y^2}\cos^2\beta + \sqrt{B_x^2 + B_y^2}\sin\beta \tag{3.111}$$

Differentiating with respect to β gives the peak of the resultant force as

$$\hat{F}_R = \begin{cases} K_D\hat{w} + \frac{F_{R0}}{2} & F_{R0} < \sqrt{B_x^2 + B_y^2} \\ \\ K_M\omega_r\hat{w} & F_{R0} \geq \sqrt{B_x^2 + B_y^2} \end{cases} \tag{3.112}$$

where $\hat{w} = \sqrt{\hat{u}^2 + \hat{v}^2}$, $\omega_r^2 = (\sigma_{a_x}^2 + \sigma_{a_y}^2)/(\sigma_u^2 + \sigma_v^2)$, and $F_{R0} = K_M^2\omega_r^2/2K_D$. The probability distribution of the peak of the resultant force can be obtained from the probability distribution of the peak of the resultant velocity as

$$p(\hat{F}_R) = \frac{p(\hat{w})}{d\hat{F}_R/d\hat{w}} \tag{3.113}$$

The joint distribution of the peaks of the velocities for a narrow-band process is given by the joint Rayleigh distribution

$$p(\hat{u}, \hat{v}) = \frac{\hat{u}\hat{v}}{\sigma_u^2\sigma_v^2} \exp\left[-\frac{1}{2}\left(\frac{\hat{u}^2}{\sigma_u^2} + \frac{\hat{v}^2}{\sigma_v^2}\right)\right] \tag{3.114}$$

where $\hat{u}$, $\hat{v} > 0$. The distribution of the resultant velocity $\hat{w}$ and an auxilary variable $\psi = \arctan(\hat{v}/\hat{u})$ can be obtained from the above equation as

$$p(\hat{w}, \psi) = \frac{\hat{w}^3 \sin(2\psi)}{2\sigma_u^2\sigma_v^2} \exp\left[-\frac{\hat{w}^2}{4\sigma_v^2}\left(k_1 - k_2\cos(2\psi)\right)\right] \tag{3.115}$$

where $k_1 = 1 + r$ and $k_2 = 1 - r$. The probability density of the peaks of the resultant force can be derived from equations (3.112), (3.113), and (3.115) as

$$p(\hat{F}_R) = \begin{cases} \frac{8r\hat{F}_R^3}{\alpha^2} \exp\left(-\frac{k_1\hat{F}_R^2}{\alpha}\right) I_1\left[\frac{k_2\hat{F}_R^2}{\alpha}\right] & 0 < \hat{F}_R < F_{R0} \\ \\ \frac{4r\hat{F}'_R}{\beta^2} \exp\left(-\frac{k_1\hat{F}'_R}{\beta}\right) I_1\left[\frac{k_2\hat{F}'_R}{\beta}\right] & \hat{F}_R > F_{R0} \end{cases} \tag{3.116}$$

where $\hat{F}'_R = \hat{F}_R - F_{R0}/2$, $\alpha = 4\sigma_v^2 K_M^2\omega_r^2$, $\beta = 4\sigma_v^2 K_D$, and

$$I_1(x) = \int_0^{\pi/2} \sin(2\psi) \exp[x\cos(2\psi)]\, d\psi \tag{3.117}$$

The distribution of the force peaks may be used to obtain the cumulative distribution of $\hat{F}_R$, the distribution of the largest peak of the resultant force in a storm with N consecutive peaks $\hat{F}_{Rmax}$, and finally the expected value of $\hat{F}_{Rmax}$ in N peaks with equations (3.50), (3.61), and (3.62) respectively.

Chapter 4

FORCES AND MOTIONS OF LARGE FLOATING STRUCTURES

A structure floating in a random sea state experiences first order motions at the frequencies of the exciting waves, and second order motions at the difference frequencies of the waves. The second order exciting forces often occur at frequencies close to the natural frequency of the mooring system resulting in large horizontal motions due to the low damping present at such low frequencies. Knowledge of the magnitude of such motions is very critical in the design of mooring systems. The first and second order forces are usually computed using potential flow theory if the structure is considered large enough to diffract the incident wave field.

This chapter first reviews the computation of first order forces and motions using linear diffraction theory. Expressions are presented for the computation of the steady drift force in regular long-crested waves using the far-field method. A frequency domain approach to the estimation of the slowly varying second order forces in random long-crested seas based on the concept of a quadratic transfer function is presented. The frequency domain approach is then extended to random multi-directional waves with the quadratic transfer function now dependent on two frequency and two direction variables. Different methods of estimating the probability distribution of the drift forces and motions are presented. Finally, the effect of wave grouping on the second order motions is discussed.

4.1 First Order Diffraction Theory

4.1.1 Formulation

The problem of determining the first order exciting forces and motions of a floating structure in regular long-crested waves has been dealt with by a number of authors (Faltinsen and Michelsen (1974), Garrison (1978), Isaacson (1985a)). It is however reviewed here since it is important for the computation of the second order forces and motions.

Consider the oscillatory motions of a freely floating structure in response to a regular small amplitude wave train as shown in Figure 4.1. The coordinate system is right-handed and fixed with respect to the initial position of the body. The origin of the coordinate system is at the still water level with z measured upwards through the centre of gravity. The oscillatory motions of the body consists of three translational motions parallel to the (x, y, z) axes referred to as surge (Ξ_1), sway (Ξ_2), and heave (Ξ_3) respectively, and three rotational motions about the same axes referred to as roll (Ξ_4), pitch (Ξ_5), and yaw (Ξ_6) respectively. Each mode of motion is periodic in time, t, with the same frequency ω as the incident waves and can be expressed as

$$\Xi_j(t) = \xi_j \exp(-i\omega t) \tag{4.1}$$

where ξ_j is the complex amplitude of the jth mode of motion. The incident waves are of height, H, and propagate at an angle θ relative to the positive x axis in water of depth d. The fluid is assumed inviscid and incompressible and the flow irrotational so that the fluid motion $\mathbf{u}$ may be described by a velocity potential Φ

$$\mathbf{u} = \nabla\Phi(x, y, z, t) \tag{4.2}$$

where $\nabla = (\partial/\partial x, \partial/\partial y, \partial/\partial z)$. If the oscillatory motions of the structure are considered

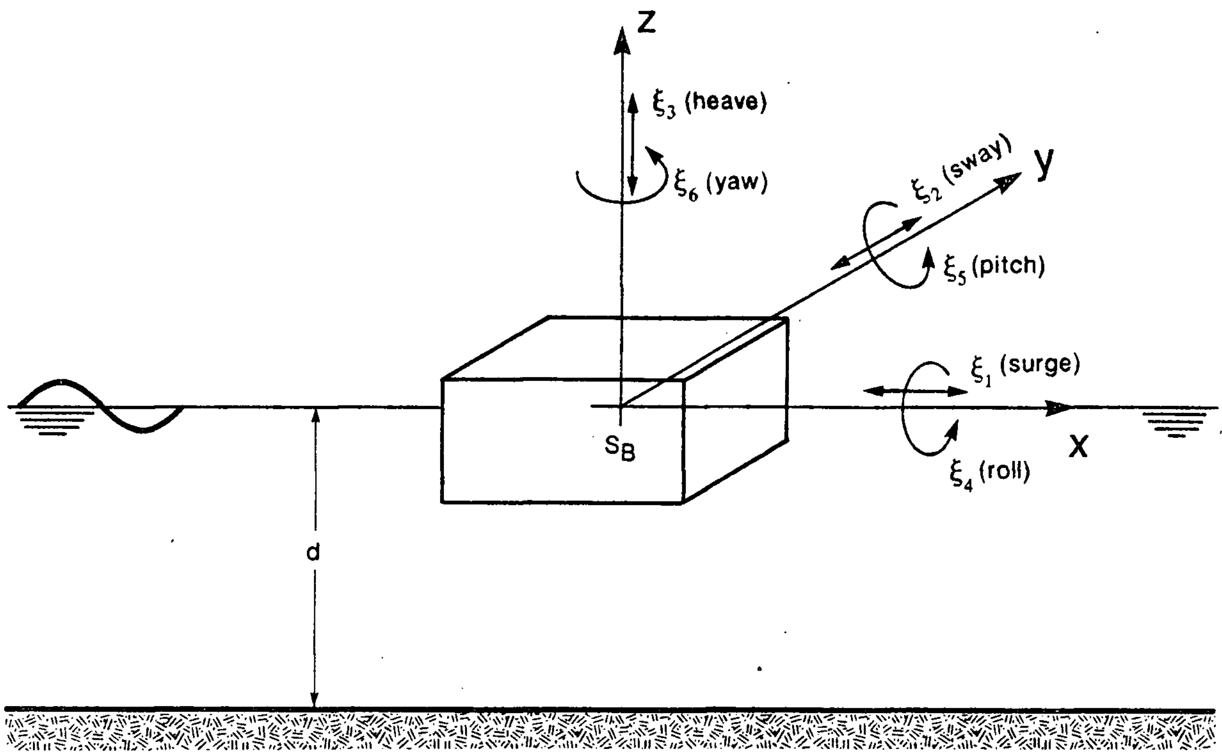

Figure 4.1: Definition sketch for floating body

small, the flow potential can be considered to be a linear superposition of components due to the incident waves (ϕ_0), the diffracted waves (ϕ_7), and radiated waves associated with the body motions ($\phi_j, j = 1, 2, \ldots, 6$). The total velocity potential may thus be expressed as

$$\Phi(x,y,z,t) = \left[-\frac{i\omega H}{2}(\phi_0(x,y,z) + \phi_7(x,y,z)) - \sum_{j=1}^{6} i\omega\xi_j\phi_j(x,y,z)\right]\exp(-i\omega t) \quad (4.3)$$

where ϕ_0 is given by linear wave theory as

$$\phi_0(x,y,z) = \frac{\cosh[k(z+d)]}{k\sinh(kd)}\exp\{ik(x\cos\theta + y\sin\theta)\} \quad (4.4)$$

Each of the potentials must satisfy the equation of continuity or Laplace's equation in the fluid

$$\nabla^2\phi_j(x,y,z) = 0 \qquad j = 1, 2, \ldots, 7 \quad (4.5)$$

The potentials must also satisfy appropriate boundary conditions on the free surface, seabed, body surface and radiation surface. There are two nonlinear boundary conditions on the free surface. The first one sets the dynamic pressure given by the Bernoulli equation to zero on the free surface, that is

$$\frac{\partial \Phi}{\partial t} + g\eta + \frac{1}{2}(\nabla \Phi)^2 = 0 \tag{4.6}$$

The second boundary condition on the free surface is a kinematic one and requires the substantial derivative of the free surface elevation equal the vertical component of the fluid particle velocity at the free surface. This can be expressed as

$$\begin{aligned} \frac{\partial \Phi}{\partial z} &= \frac{D\eta}{Dt} \\ &= \frac{\partial \eta}{\partial t} + \frac{\partial \Phi}{\partial x}\frac{\partial \eta}{\partial x} + \frac{\partial \Phi}{\partial y}\frac{\partial \eta}{\partial y} \end{aligned} \tag{4.7}$$

where D/Dt is the substantial derivative. The two nonlinear free surface boundary conditions can be linearized and combined to give a boundary condition applied at the still water level $z = 0$ rather than at the instantaneous water surface elevation. The linearized free surface boundary conditions for the potentials $\phi_j, j = 1, 2, \ldots, 7$ can be expressed as

$$\frac{\partial \phi_j}{\partial z} - \frac{\omega^2}{g}\phi_j = 0 \qquad j = 1, 2, \ldots, 7 \tag{4.8}$$

The seabed is assumed horizontal and impermeable and hence the normal velocity of the fluid on the seabed must equal zero

$$\frac{\partial \phi_j}{\partial z} = 0 \qquad j = 1, 2, \ldots, 7 \tag{4.9}$$

The boundary condition on the immersed body surface requires that the normal velocity of fluid on the body surface must equal the normal velocity of the body surface. The normal velocity of the body surface can be expressed as

$$V_n = \sum_{j=1}^{6} \frac{\partial \Xi_j}{\partial t} n_j = \sum_{j=1}^{6} -i\omega \xi_j n_j \exp(-i\omega t) \tag{4.10}$$

where n_j, $j = 1, 2, \ldots, 6$ are defined as

$$\mathbf{n} = (n_1, n_2, n_3) \tag{4.11}$$

$$\mathbf{x} \times \mathbf{n} = (n_4, n_5, n_6) \tag{4.12}$$

$\mathbf{n}$ is the unit normal vector on the body surface, directed outward from the body, and $\mathbf{x}$ is the position vector (x, y, z). The linearized body surface boundary condition is applied at the equilibrium position of the body and can be expressed as

$$\frac{\partial \phi_j}{\partial n} = \begin{cases} n_j & j = 1, 2, \ldots, 6 \\ -\frac{\partial \phi_0}{\partial n} & j = 7 \end{cases} \tag{4.13}$$

A radiation condition is also applied to the potentials at a radiation surface at infinity to ensure that the diffracted and radiated waves are travelling away from the body. The condition is given by

$$\lim_{R \to \infty} R^{\frac{1}{2}} \left[\frac{\partial \phi_j}{\partial R} - ik\phi_j \right] = 0 \tag{4.14}$$

where $R = \sqrt{x^2 + y^2}$ is a radial distance.

4.1.2 Source Distribution Method of Solution

The unknown potentials $\phi_j (j = 1, 2, \ldots, 7)$ are evaluated numerically using a source distribution method. The potential $\phi_j(\mathrm{x})$ at any general point $\mathbf{x}$ in the fluid can be represented as a distribution of point sources over the immersed body surface S_B (see Lamb, 1945)

$$\phi_j(\mathrm{x}) = \frac{1}{4\pi} \int_{S_B} f_j(\mathrm{x}') G(\mathrm{x}; \mathrm{x}') \, dS \tag{4.15}$$

where $G(\mathrm{x}; \mathrm{x}')$ is a Green's function for point $\mathbf{x}$ due to a point source of unit strength at location $\mathrm{x}' = (x', y', z')$ and $f_j(\mathrm{x}')$ is an unknown source strength distribution function. The Green's function is chosen to satisfy the Laplace equation and the boundary conditions at the seabed, free surface and radiation surface. Such a Green's function was originally derived by John (1950) and alternative expressions for it are presented in Appendix A. The source strength distribution function is chosen to satisfy the body surface boundary condition. This can be expressed in integral form as

$$-f_j(\mathbf{x}) + \frac{1}{2\pi}\int_{S_B} f_j(\mathbf{x})\frac{\partial G}{\partial n}(\mathbf{x};\mathbf{x}')\,dS = \begin{cases} n_j(\mathbf{x}) & j = 1,2,\ldots,6 \\ \\ -\frac{\partial \phi_0}{\partial n}(\mathbf{x}) & j = 7 \end{cases} \tag{4.16}$$

where $\mathbf{x}$ now represents a point on the body surface where the boundary condition is applied. A numerical procedure is used to determine the source strengths in which the body surface is discretized into a finite number of facets with $f_j(\mathbf{x})$ taken to be uniform over each facet. The integral equations (4.16) are then applied at the centre of each facet, thus reducing to a set of linear algebraic equations. The algebraic equations are solved to obtain the source strengths and the unknown potentials $\phi_j (j = 1, 2, \ldots, 7)$ are determined using equation (4.15).

4.1.3 Exciting Force, Added Mass and Damping Coefficients

Once the velocity potential is known, the hydrodynamic pressure can be computed from the linearized form of the Bernoulli equation as

$$p(x,y,z,t) = -\rho\frac{\partial \Phi}{\partial t}(x,y,z,t) \tag{4.17}$$

The forces and moments are then determined by integrating the hydrodynamic pressure over the immersed body surface

$$F_j(t) = \left[\int_{S_B}\left(\frac{\rho\omega^2 H}{2}(\phi_0 + \phi_7) + \rho\omega^2\sum_{k=1}^{6}\xi_k\phi_k\right) n_j\, dS\right]\exp(-i\omega t) \tag{4.18}$$

where (F_1, F_2, F_3) are forces in the (x, y, z) directions and (F_4, F_5, F_6) are moments about the same axes. Each force or moment consists of an exciting force component, F_j^e, associated with the incident and diffracted waves, and components due to the forced motions of the body. The exciting wave force is given by

$$F_j^e(t) = \frac{\rho\omega^2 H}{2}\left[\int_{S_B}(\phi_0 + \phi_7)n_j\, dS\right]\exp(-i\omega t) \tag{4.19}$$

The jth force due to the kth mode of motion can be expressed in terms of components in phase with the velocity and acceleration of the body as

$$F_{jk}(t) = -\mu_{jk}\ddot{\Xi}_k - \lambda_{jk}\dot{\Xi}_k \tag{4.20}$$

where μ_{jk} and λ_{jk} are added mass and damping coefficients respectively given by equations (4.1), (4.18), and (4.20) as

$$\mu_{jk} = \rho \, \mathrm{Re}\left[\int_{S_B} \phi_k n_j \, dS\right] \tag{4.21}$$

$$\lambda_{jk} = \rho\omega \, \mathrm{Im}\left[\int_{S_B} \phi_k n_j \, dS\right] \tag{4.22}$$

Re() and Im() denote the real and imaginary parts of a complex argument respectively.

4.1.4 Equations of Motion

The complex amplitudes of the oscillatory motions of the structure can be determined by solving the equations of motion which can be expressed as

$$\sum_{k=1}^{6}\left[(m_{jk}+\mu_{jk})\ddot{\Xi}_k + (\lambda_{jk}+\lambda^v_{jk})\dot{\Xi}_k + (c_{jk}+c'_{jk})\Xi_k\right] = F^e_j(t) \;\; j = 1,2,\ldots,6 \tag{4.23}$$

where m_{jk}, λ^v_{jk}, c_{jk}, and c'_{jk} are the mass, viscous damping, hydrostatic stiffness, and mooring stiffness matrix coefficients respectively. Viscous damping is important particularly for surge, roll, and pitch motions and is determined empirically from free oscillation tests in still water. The viscous damping force is often nonlinearly dependent on the body's velocity and an equivalent linear coefficient would have to be used in equation (4.23).

The mass matrix components are given by Newman (1977) as

$$[m] = \begin{bmatrix} m & 0 & 0 & 0 & mz_G & 0 \\ 0 & m & 0 & -mz_G & 0 & 0 \\ 0 & 0 & m & 0 & 0 & 0 \\ 0 & -mz_G & 0 & I_{xx} & I_{xy} & I_{xz} \\ mz_G & 0 & 0 & I_{xy} & I_{yy} & I_{yz} \\ 0 & 0 & 0 & I_{xz} & I_{yz} & I_{zz} \end{bmatrix} \tag{4.24}$$

where m is the mass of the body, z_G is the z coordinate of the centre of gravity, and the moments and products of inertia are defined as

$$I_{xx} = \int_{V_B} \rho_B(y^2 + z^2)\, dV = m(r_x^2 + z_G^2) \tag{4.25}$$

$$I_{yy} = \int_{V_B} \rho_B(x^2 + z^2)\, dV = m(r_y^2 + z_G^2) \tag{4.26}$$

$$I_{zz} = \int_{V_B} \rho_B(x^2 + y^2)\, dV = mr_z^2 \tag{4.27}$$

$$I_{xy} = -\int_{V_B} \rho_B xy\, dV \tag{4.28}$$

$$I_{xz} = -\int_{V_B} \rho_B xz\, dV \tag{4.29}$$

$$I_{yz} = -\int_{V_B} \rho_B yz\, dV \tag{4.30}$$

where ρ_B is the mass density of the body, V_B is the displaced volume of the body, and r_x, r_y, and r_z are the radii of gyration of the body about the x, y, and z axes respectively. For a body symmetrical about the x-z and y-z planes, $I_{xy} = I_{xz} = I_{yz} = 0$.

The hydrostatic stiffness matrix is determined by calculating the hydrostatic forces required to restore the body to its equilibrium position for small amplitude displacements and is given as

$$[c] = \begin{bmatrix} 0 & 0 & 0 & 0 & 0 & 0 \\ 0 & 0 & 0 & 0 & 0 & 0 \\ 0 & 0 & c_{33} & c_{34} & c_{35} & 0 \\ 0 & 0 & c_{34} & c_{44} & 0 & 0 \\ 0 & 0 & c_{35} & 0 & c_{55} & 0 \\ 0 & 0 & 0 & 0 & 0 & 0 \end{bmatrix} \tag{4.31}$$

where

$$c_{33} = \rho g S_{wp}$$

$$c_{34} = -\rho g S_2$$

$$c_{35} = -\rho g S_1$$

$$c_{44} = mg\left[S_{22}/V_B + z_B - z_G\right]$$

$$c_{55} = mg\left[S_{11}/V_B + z_B - z_G\right]$$

S_{wp} is the waterplane area, z_B is the z coordinate of the centre of buoyancy, and the waterplane area moments are defined as

$$S_1 = \int_{S_{wp}} x \, dS \tag{4.32}$$

$$S_2 = \int_{S_{wp}} y \, dS \tag{4.33}$$

$$S_{11} = \int_{S_{wp}} x^2 \, dS \tag{4.34}$$

$$S_{22} = \int_{S_{wp}} y^2 \, dS \tag{4.35}$$

For the body to be statically stable, the hydrostatic restoring force coefficients have to be greater than zero. This condition is always satisfied for the heave motion since the waterplane area is nonzero. For the roll and pitch motions, the *metacentres* $S_{jj}/V_B + z_B$ would have to be higher than the centre of gravity.

The stiffness matrix coefficients for the mooring system are calculated from the net mooring line forces produced by small amplitude displacements or rotation of the body. The coefficients depend on the individual mooring line pretensions, stiffnesses, and configuration of the mooring system. Mooring systems are used to restrict the horizontal plane motions of surge, sway and yaw and the mooring stiffness matrix would only have components for such motions.

The equations of motion (4.23) can be solved to obtain the complex amplitudes of oscillation ξ_j for any given incident wave frequency and direction using a complex matrix inversion technique. The amplitudes of motion are often expressed in terms of a response amplitude operator $Z_j(\omega, \theta)$ defined as

$$Z_j(\omega, \theta) = \begin{cases} \dfrac{\xi_j}{H/2} & j = 1, 2, 3 \\ \\ \dfrac{B\xi_j}{H/2} & j = 4, 5, 6 \end{cases} \tag{4.36}$$

where B is a characteristic dimension of the body. The response amplitude operator is a complex valued transfer function that represents the amplitude of body motion due to a unit amplitude wave of frequency ω travelling in direction θ. It can be used to relate the linear motions of a structure in random short-crested seas to the incident wave spectrum.

4.2 First Order Motions in Random Seas

As discussed earlier in Chapter 2, a random short-crested sea state can be represented by a linear superposition of regular unidirectional wave trains with different frequencies, propagating in different directions. The wave field can be described in terms of a directional wave spectrum $S_\eta(\omega,\theta)$ which represents the distribution of wave energy over frequency and direction. The directional wave spectrum may be expressed as the product of the one-dimensional frequency spectrum $S_\eta(\omega)$ and a directional spreading function $D(\omega,\theta)$.

For a regular oblique wave train, the amplitude of body motion is linearly related to the wave amplitude by the complex transfer function $Z_j(\omega,\theta)$. The motion of the body in a short-crested sea state at any frequency will be due to component wave trains approaching the body from all possible directions. The spectrum of the jth mode of motion is thus related to the incident wave spectrum by

$$S_{\xi_j}(\omega) = \int_{-\pi}^{\pi} |Z_j(\omega,\theta)|^2 S_\eta(\omega,\theta)\, d\theta \tag{4.37}$$

The variance or mean square value of the jth mode of motion is given by

$$\sigma^2_{\xi_j} = \int_0^\infty S_{\xi_j}(\omega)\, d\omega \tag{4.38}$$

The probability distribution of the first order body motions will be Gaussian with zero mean since a linear relationship exists between the wave field and the body motions and the water surface elevation is assumed to be a Gaussian process. Of particular interest in the design of offshore structures is the expected value of the maximum motion ξ_{max} of the body in a storm. The expected maximum motion in a storm of duration T_D is given by Davenport (1964) as

$$\frac{E[\xi_{max}]}{\sigma_\xi} \simeq [2\ln(\nu_0^+ T_D)]^{\frac{1}{2}} + \frac{\gamma}{[2\ln(\nu_0^+ T_D)]^{\frac{1}{2}}} \tag{4.39}$$

where ν_0^+ is the average zero upcrossing frequency and γ is Eulers constant (0.5772). The above expression is based on the assumption of statistical independence of the upcrossings of any response level, and is valid for both narrow-band and wide-band processes. The average zero upcrossing frequency is given by

$$\nu_0^+ = \frac{1}{2\pi}\frac{\sigma_{\dot{\xi}}}{\sigma_\xi} \tag{4.40}$$

where

$$\sigma_{\dot{\xi}}^2 = \int_0^\infty \omega^2 S_\xi(\omega)\, d\omega \tag{4.41}$$

In trying to determine the effect of wave directionality on the first order motions of floating structures, it is useful to compare the standard deviations of the motions in long-crested and short-crested sea states with an identical frequency spectrum. In a long-crested sea state with a zero angle of incidence, a floating body can surge, heave, and pitch. In a short-crested sea state, the body experiences in addition the sway, roll and yaw motions. If the long-crested and short-crested waves have an identical frequency spectrum, the amplitudes of the surge, heave and pitch motions in short-crested waves will generally be reduced. The effect of wave short-crestedness can thus be expressed as reduction factor, R_F, relating the standard deviations of the motions in short-crested seas to long-crested seas

$$R_F^2 = \frac{\int_0^\infty \int_{-\pi}^{\pi} |Z_j(\omega,\theta)|^2 S_\eta(\omega) D(\omega,\theta)\, d\theta d\omega}{\int_0^\infty |Z_j(\omega,\theta_0)|^2 S_\eta(\omega)\, d\omega} \tag{4.42}$$

where θ_0 is the direction of propagation of the long-crested wave train.

4.3 Steady Drift Forces in Regular Long-crested Waves

The first order theory just presented predicts a zero mean displacement of the body. The body however experiences a steady horizontal drift due to second order effects. The near-field and far-field methods are usually used to estimate the steady drift forces on a body in regular waves.

The far-field approach first presented by Maruo (1960) uses the equations of conservation of momentum of the fluid to relate the drift forces to the fluid potentials in the far field. Alternatively, the near-field approach presented by Pinkster (1976) is a perturbation procedure that integrates the second order contributions around the immersed body surface. The near-field method is computationally more intensive than the far-field method since it involves calculation of the normals of the potentials on the body surface in addition to the potentials. The far-field method is used in the present investigation and is now briefly reviewed.

Consider a closed surface S comprised of the immersed body surface S_B, the free surface S_F, the radiation surface S_R and the seabed S_D as shown in Figure 4.2. The rate of change of linear and angular momentum M_j is given by Newman (1967) as

$$\frac{dM_j}{dt} = -\int_S [pn_j + \rho u_j(u_n - V_n)]\, dS \qquad j = 1,2,6 \tag{4.43}$$

where V_n is the normal velocity of the surface, u_j are components of the fluid velocity vector $\mathbf{u}$ and are defined as

$$\mathbf{u} = (u_1, u_2, u_3) \tag{4.44}$$

$$\mathbf{x} \times \mathbf{u} = (u_4, u_5, u_6) \tag{4.45}$$

and u_n is the normal component of the fluid velocity on the surface given by

$$u_n = \mathbf{u} \cdot \mathbf{n} \tag{4.46}$$

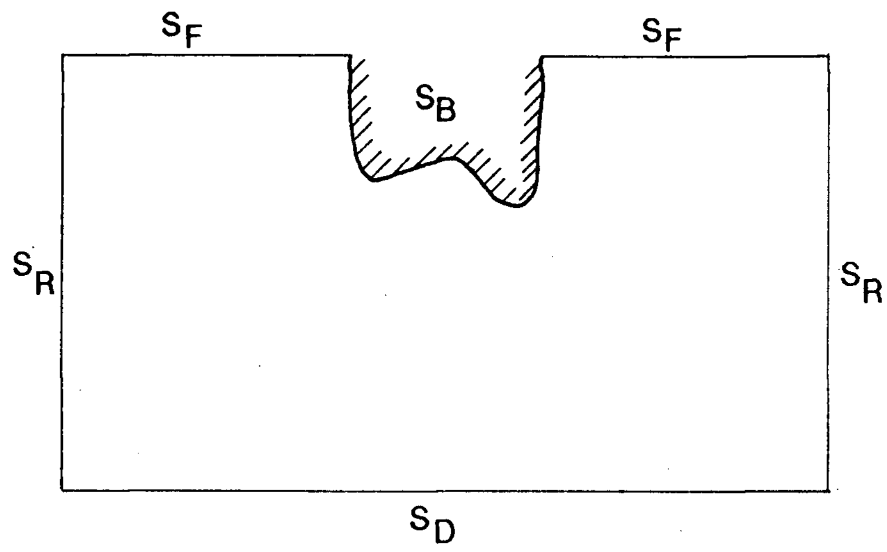

Figure 4.2: Sketch of closed control surface

The horizontal plane motions consists of surge, sway and yaw, and are denoted by subscripts 1, 2, and 6 respectively. The forces and moment on the body are given by

$$F_j(t) = -\int_{S_B} pn_j \, dS \tag{4.47}$$

Equation (4.43) can be rewritten as

$$F_j(t) = -\int_{S_F+S_R+S_D} [pn_j + \rho u_j(u_n - V_n)] \, dS - \frac{dM_j}{dt} \tag{4.48}$$

since $u_n = V_n$ on the immersed body surface. By considering various other boundary conditions on the different surfaces

$$\begin{aligned} \text{On } S_F &: \; p = 0, u_n = V_n \\ \text{On } S_R &: \; V_n = 0 \\ \text{On } S_D &: \; n_1 = n_2 = n_6 = 0, \;\; u_n = V_n = 0 \end{aligned} \tag{4.49}$$

and taking a time average of equation (4.48) gives the steady horizontal drift forces and moment as

$$\overline{F_j} = \overline{-\int_{S_R} (pn_j + \rho u_j u_n)\, dS} \qquad j = 1,2,6 \tag{4.50}$$

The time average of the rate of change of linear and angular momentum are zero since the amount of momentum inside a closed surface is bounded. The radiation surface is a large cylindrical surface at a far radial distance from the body. The integrals are easier to evaluate using cylindrical polar coordinates with $x = R\cos\beta$, $y = R\sin\beta$, and $z = z$. The steady drift forces and moment can then be expressed as

$$\overline{F_1} = \overline{-\int_{-d}^{\eta}\int_{-\pi}^{\pi} [p\cos\beta + \rho u_R(u_R\cos\beta - u_\beta\sin\beta)]\, Rd\beta dz} \tag{4.51}$$

$$\overline{F_2} = \overline{-\int_{-d}^{\eta}\int_{-\pi}^{\pi} [p\sin\beta + \rho u_R(u_R\sin\beta + u_\beta\cos\beta)]\, Rd\beta dz} \tag{4.52}$$

$$\overline{F_6} = \overline{-\int_{-d}^{\eta}\int_{-\pi}^{\pi} \rho u_R u_\beta\, R^2 d\beta dz} \tag{4.53}$$

where u_R and u_β are the radial and tangential components of the fluid velocity repectively, defined by

$$u_R = \frac{\partial\Phi}{\partial R}(R,\beta,z,t)\ ;\ \ u_\beta = \frac{1}{R}\frac{\partial\Phi}{\partial\beta}(R,\beta,z,t) \tag{4.54}$$

The above equations (4.51)-(4.53) for the drift force have involved no linearization. In order to compute the drift forces, it is convenient to separate the first and second order quantities by carrying out a perturbation expansion for Φ

$$\Phi = \varepsilon\Phi^{(1)} + \varepsilon^2\Phi^{(2)} + O(\varepsilon^3) \tag{4.55}$$

where ε is a small perturbation parameter such as the wave steepness. The pressure p is given by the Bernoulli equation as

$$\begin{aligned} p &= -\rho\left[gz + \frac{\partial\Phi}{\partial t} + \frac{1}{2}|\nabla\Phi|^2\right] \\ &= -\rho gz - \rho\varepsilon\frac{\partial\Phi^{(1)}}{\partial t} - \rho\varepsilon^2\left[\frac{\partial\Phi^{(2)}}{\partial t} + \frac{1}{2}|\nabla\Phi^{(1)}|^2\right] + O(\varepsilon^3) \end{aligned} \tag{4.56}$$

Salvesen (1974) showed that the second order potential is responsible for a set-down of the wave but makes no contribution to the mean horizontal drift forces and moment. The periodic components of the pressure average out to zero. The mean drift forces and moment can now be expressed as

$$\begin{aligned}\overline{F_1} &= -\frac{1}{2}\rho g \int_{-\pi}^{\pi} \overline{\eta^2} \cos\beta \; Rd\beta \\ &+ \int_{-d}^{0}\int_{-\pi}^{\pi} \left[(\overline{u_R^2} - \overline{u_\beta^2} - \overline{u_z^2}) \cos\beta - 2\overline{u_R u_\beta} \sin\beta\right] \; Rd\beta dz \end{aligned} \tag{4.57}$$

$$\begin{aligned}\overline{F_2} &= -\frac{1}{2}\rho g \int_{-\pi}^{\pi} \overline{\eta^2} \sin\beta \; Rd\beta \\ &+ \int_{-d}^{0}\int_{-\pi}^{\pi} \left[(\overline{u_R^2} - \overline{u_\beta^2} - \overline{u_z^2}) \sin\beta + 2\overline{u_R u_\beta} \cos\beta\right] \; Rd\beta dz \end{aligned} \tag{4.58}$$

$$\overline{F_6} = -\rho \int_{-d}^{0}\int_{-\pi}^{\pi} \overline{u_R u_\beta} \; R^2 d\beta dz \tag{4.59}$$

where $\overline{\eta^2}$ is the mean square water surface elevation on the radiation surface and consists of contributions from the incident wave, diffracted wave, and radiated waves. It can be expressed in terms of the first order potential as

$$\overline{\eta^2} = \frac{\omega^2}{g^2} \overline{|\Phi^{(1)}(R \to \infty, \beta, 0, t)|^2} \tag{4.60}$$

The terms involving the velocities in equations (4.57)-(4.59) are all evaluated using the first order potential. It can thus be seen that the steady drift forces in regular waves involve second order quantities arising from first order terms, and have no contribution from the second order potential.

The first order potential in the far-field is needed to evaluate the expressions for the drift forces and moment. By using the asymptotic behaviour of the Green's function at large radial distances, Faltinsen and Michelsen (1974) expressed the far field first order potential in terms of the source strength distribution function as

$$\Phi^{(1)} = -\frac{i\omega H}{2}\phi_0 - \frac{i\omega}{4\pi\sqrt{R}} \cosh[k(z+d)] \exp\{i(kR - 3\pi/4 - \omega t)\}\psi(\beta) \tag{4.61}$$

where $\psi(\beta)$ is a complex valued function given by

$$\psi(\beta) = G_0\sqrt{\frac{2}{\pi k}}\int_{S_B}\left[\frac{H}{2}f_7(\mathbf{x}') + \sum_{j=1}^{6}\xi_j f_j(\mathbf{x}')\right]$$
$$\exp\{-ik(x'\cos\beta + y'\sin\beta)\}\cosh[k(z'+d)]\,dS \qquad (4.62)$$

G_0 is defined in Appendix A. All the terms in the expressions for the drift forces and moment (4.57)-(4.59) are linearly proportional to the square of the incident wave amplitude. The drift forces can thus be expressed in terms of mean drift force coefficient $P(\omega, \theta)$ as

$$\overline{F_j} = P_j(\omega, \theta)\frac{H^2}{4} \qquad j = 1, 2, 6 \qquad (4.63)$$

4.4 Second Order Forces in Random Seas

In a random sea, the drift forces and moments are no longer steady but slowly varying in time. There are a few different approaches used to relate the drift forces in random seas to the incident wave field. Due to the nonlinearity of the drift force, the linear spectral approach can no longer be used.

An approximate time domain method used by Marthinsen (1983a) relates the slowly varying drift force to the envelope of the wave train obtained from a Hilbert transform of the water surface elevation. The transfer function is obtained from the mean drift force in regular waves and the approach is valid for narrow-band seas.

An alternate approach is based on the concept of the Taylor series expansion of a functional, an idea originally introduced by Volterra (1930). The wave drift force is a function of the wave field, which in turn is a function of space and time. It is thus by definition a functional. The nonlinear force can be expanded as a functional power (Volterra) series which is truncated after the second term to model a second order force.

The functional polynomial representation of the wave drift force has been used by a number of authors including Neal (1974), and Kim and Dalzell (1981). In the frequency domain, the functional polynomial approach results in the drift force spectrum being related to the wave spectrum by a quadratic transfer function. Both time and frequency domain representations of the slowly varying drift force based on the functional polynomial approach will now be presented.

4.4.1 Time Domain Representation of Second Order Force

The total exciting wave force on a structure can be modelled as a functional power series

$$F(t) = F^{(1)}(t) + F^{(2)}(t) + \cdots \tag{4.64}$$

where

$$F^{(1)}(t) = \int_{-\infty}^{\infty} h_1(\tau)\eta(t-\tau)\, d\tau \tag{4.65}$$

$$F^{(2)}(t) = \int_{-\infty}^{\infty}\int_{-\infty}^{\infty} h_2(\tau_1,\tau_2)\eta(t-\tau_1)\eta(t-\tau_2)\, d\tau_1 d\tau_2 \tag{4.66}$$

$h_1(\tau)$ and $h_2(\tau_1, \tau_2)$ are the first and second order impulse response functions respectively, and τ, τ_1, and τ_2 are time shifts. In the above equations, the wave train is assumed to be long-crested so the water surface elevation is independent of the spatial location. The functional power series has been truncated after the second term to model nonlinearities up to second order. The first order term is usually determined using linear superposition principles discussed in Section 4.2, and attention is now focussed on the second order term. The two-dimensional Fourier transform of the second order impulse response function yields a quadratic transfer function $H(\omega_1, \omega_2)$ as

$$H_2(\omega_1,\omega_2) = \int_{-\infty}^{\infty}\int_{-\infty}^{\infty} h_2(\tau_1,\tau_2)\exp(-i(\omega_1\tau_1+\omega_2\tau_2))\, d\tau_1 d\tau_2 \tag{4.67}$$

where ω_1 and ω_2 are frequency variables. The above equation is valid provided the function $h_2(\tau_1, \tau_2)$ is continuous and absolutely integrable, that is

$$\int_{-\infty}^{\infty}\int_{-\infty}^{\infty} |h_2(\tau_1,\tau_2)|\, d\tau_1 d\tau_2 < \infty \tag{4.68}$$

The inverse Fourier transform of the quadratic transfer function yields the second order impulse response function as

$$h(\tau_1, \tau_2) = \frac{1}{4\pi^2} \int_{-\infty}^{\infty} \int_{-\infty}^{\infty} H_2(\omega_1, \omega_2) \exp(i(\omega_1 \tau_1 + \omega_2 \tau_2))\, d\omega_1 d\omega_2 \tag{4.69}$$

The second order impulse response function may be considered symmetric, that is

$$h_2(\tau_1, \tau_2) = h_2(\tau_2, \tau_1) \tag{4.70}$$

This results in the following symmetry conditions for the quadratic transfer function

$$H_2(\omega_1, \omega_2) = H_2(\omega_2, \omega_1) \tag{4.71}$$

$$H_2^*(\omega_1, \omega_2) = H_2(-\omega_2, -\omega_1) \tag{4.72}$$

The physical significance of the quadratic transfer function can be investigated by considering the second order forces in wave fields composed of one and two regular long-crested waves. Consider initially a regular unidirectional wave train given by

$$\begin{aligned} \eta(t) &= a_1 \cos(\omega t) \\ &= \frac{a_1}{2} [\exp(i\omega t) + \exp(-i\omega t)] \end{aligned} \tag{4.73}$$

The second order force in regular waves can be obtained from equations (4.66), (4.67), and (4.73) as

$$F^{(2)}(t) = \frac{a_1^2}{2} \{\mathrm{Re}[H_2(\omega, -\omega)] + \mathrm{Re}[H(\omega, \omega) \exp(2i\omega t)]\} \tag{4.74}$$

The force consists of a mean component and a second harmonic oscillatory term. The value of the quadratic transfer function at frequencies of ω and $-\omega$ can be related to the mean drift force coefficient in regular waves $P(\omega)$ by

$$H_2(\omega, -\omega) = 2P(\omega) \tag{4.75}$$

$H_2(\omega, -\omega)$ is real since the symmetry condition (4.72) can only be satisfied if the imaginary part of $H_2(\omega, -\omega)$ is identically zero.

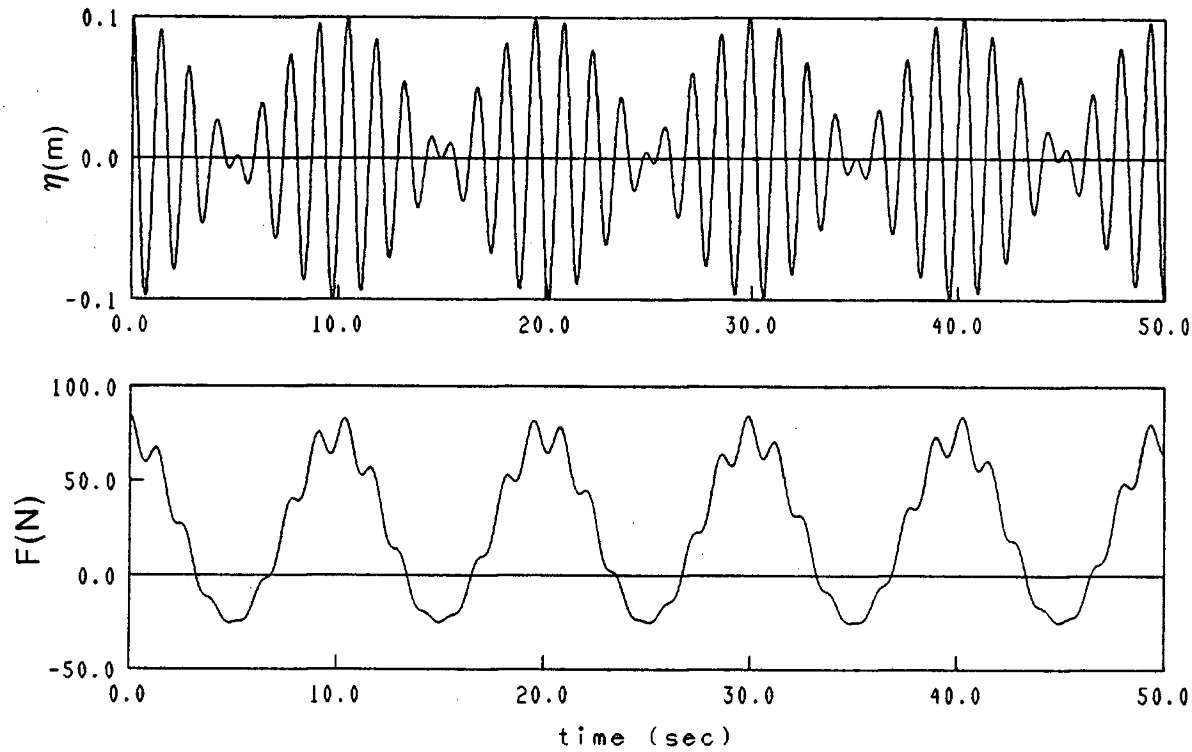

Figure 4.3: Sketch of bichromatic wave train and corresponding drift force

Consider a bichromatic wave train consisting of two regular waves with different frequencies, given by

$$\begin{aligned} \eta(t) &= a_1 \cos(\omega_1 t + \varepsilon_1) + a_2 \cos(\omega_2 t + \varepsilon_2) \\ &= a(t) \cos(\omega_1 t + \varepsilon_1) \end{aligned} \tag{4.76}$$

where

$$a(t) = a_1 \left[1 + \frac{a_2}{a_1} \cos[(\omega_1 - \omega_2)t + (\varepsilon_1 - \varepsilon_2) + \pi/2] \right] \tag{4.77}$$

When the difference between the component wave frequencies are small, the amplitude $a(t)$ represents a slowly varying wave envelope at the difference frequency $\omega_1 - \omega_2$ of the waves. The wave train which is rapidly varying at frequency ω_1 is thus modulated by a slowly varying envelope as shown in Figure 4.3. The second order force is obtained by substituting equation (4.76) into equation (4.66) resulting in

$$
\begin{aligned}
F^{(2)}(t) &= \mathrm{Re}\left[\frac{a_1^2}{2}H_2(\omega_1,-\omega_1)+\frac{a_2^2}{2}H_2(\omega_2,-\omega_2)\right] \\
&+ \mathrm{Re}\left[\frac{a_1^2}{2}H(\omega_1,\omega_1)\exp\{2i(\omega_1 t+\varepsilon_1)\}\right. \\
&\qquad \left. + \frac{a_2^2}{2}H(\omega_2,\omega_2)\exp\{2i(\omega_2 t+\varepsilon_2)\}\right] \\
&+ a_1 a_2\,\mathrm{Re}\left[H(\omega_1,\omega_2)\exp\{i(\omega_1+\omega_2)t+i(\varepsilon_1+\varepsilon_2)\}\right. \\
&\qquad \left. + H(\omega_1,-\omega_2)\exp\{i(\omega_1-\omega_2)t+i(\varepsilon_1-\varepsilon_2)\}\right] \qquad (4.78)
\end{aligned}
$$

The force consists of a summation of the mean components of the individual wave trains, a slowly varying component at the difference frequency of the waves, and high frequency components at the sum frequencies of the waves. The high frequency components are of some interest in the fatigue analysis of structures such as Tension Leg Platforms (TLPs) but are not considered in the present study. The mean and slowly varying drift force shown in Figure 4.3 are responsible for the large horizontal excursions of moored vessels. The mean and slowly varying components of the second order force $\tilde{F}^{(2)}(t)$ can be rewritten as

$$
\begin{aligned}
\tilde{F}^{(2)}(t) &= \sum_{n=1}^{2}\sum_{m=1}^{2} a_n a_m\{P_{nm}\cos[(\omega_n-\omega_m)t+(\varepsilon_n-\varepsilon_m)] \\
&\qquad + Q_{nm}\sin[(\omega_n-\omega_m)t+(\varepsilon_n-\varepsilon_m)]\} \qquad (4.79)
\end{aligned}
$$

where P_{nm} and Q_{nm} are given by the real and imaginary parts of the quadratic transfer function as

$$
\begin{aligned}
P_{nm} &= P(\omega_n,\omega_m) = \frac{1}{2}\mathrm{Re}[H(\omega_n,-\omega_m)] \\
Q_{nm} &= Q(\omega_n,\omega_m) = -\frac{1}{2}\mathrm{Im}[H(\omega_n,-\omega_m)]
\end{aligned}
$$

The quadratic transfer function can be seen to represent the amplitude and phase of second order force due to the presence of two unit amplitude waves with different frequencies. The symmetry conditions imposed on the quadratic transfer function are necessary to ensure that the transfer function does not depend on the order in which the waves are specified. The mean drift force coefficient of a regular wave with frequency ω_n is given by $P(\omega_n, \omega_n)$. A new complex quadratic transfer function can be defined for positive frequencies ω_n and ω_m as

$$T(\omega_n, \omega_m) = P_{nm} + iQ_{nm} \tag{4.80}$$

Let us now consider a random long-crested wave train represented by a superposition of N regular waves with random phases

$$\eta(t) = \sum_{n=1}^{N} a_n \cos(\omega_n t + \varepsilon_n) \tag{4.81}$$

The amplitudes are related to the wave spectrum by the random phase method as

$$a_n = \sqrt{2S_\eta(\omega_n)\Delta\omega} \tag{4.82}$$

The mean and slowly varying components of the second order force in random waves are due to the interaction between all the different frequency components in the wave train and are obtained from equations (4.66), (4.67), and (4.81) as

$$\begin{aligned} \tilde{F}^{(2)}(t) &= \sum_{n=1}^{N} \sum_{m=1}^{N} a_n a_m \{P_{nm} \cos[(\omega_n - \omega_m)t + (\varepsilon_n - \varepsilon_m)] \\ &\qquad + Q_{nm} \sin[(\omega_n - \omega_m)t + (\varepsilon_n - \varepsilon_m)]\} \end{aligned} \tag{4.83}$$

The mean drift force in random seas can be obtained from the above equation as

$$\overline{F^{(2)}(t)} = \sum_n a_n^2 P_{nn} \tag{4.84}$$

The mean drift force in irregular waves can thus be determined from the drift force coefficients in regular waves.

4.4.2 Frequency Domain Representation of Second Order Force

In the frequency domain, we would like to estimate the spectral density of the second order force from the incident wave spectrum. The spectral density of the force can be determined from the auto-correlation function of the force as

$$S_{F^{(2)}}(\omega) = 2\int_0^\infty R_{F^{(2)}}(\tau)\exp(-i\omega\tau)\,d\tau \tag{4.85}$$

The auto-correlation function of the force $R_{F^{(2)}}$ is given by

$$\begin{aligned} R_{F^{(2)}}(\tau) &= \overline{F^{(2)}(t)F^{(2)}(t+\tau)} \\ &= \iiiint h_2(\tau_1,\tau_2)h_2(\tau_3,\tau_4) \\ &\quad \overline{\eta(t-\tau_1)\eta(t-\tau_2)\eta(t-\tau_3+\tau)\eta(t-\tau_4+\tau)}\,d\tau_1 d\tau_2 d\tau_3 d\tau_4 \end{aligned} \tag{4.86}$$

By carrying out various manipulations, it can be shown (see Neal, 1974) that the spectral density of the low frequency component of the second order force is given by

$$\begin{aligned} S_{F^{(2)}}(\omega) &= 2\int_0^\infty H_2(-\omega',\omega+\omega')H_2^*(-\omega',\omega+\omega')S_\eta(\omega')S_\eta(\omega+\omega')\,d\omega' \\ &= 8\int_0^\infty |T(\omega',\omega+\omega')|^2 S_\eta(\omega')S_\eta(\omega+\omega')\,d\omega' \end{aligned} \tag{4.87}$$

Once the quadratic transfer function $T(\omega',\omega+\omega')$ is known, the spectral density of the second order force can be determined from the above equation. The mean drift force can be obtained from the wave spectrum as

$$\overline{F^{(2)}(t)} = 2\int_0^\infty S_\eta(\omega)P(\omega,\omega)\,d\omega \tag{4.88}$$

The above equation represents the continuous form of equation (4.84).

4.4.3 Extension to Short-Crested Seas

In a random short-crested wave field, the water surface elevation is a function of not only time, but also spatial coordinates. The assumptions of stationarity and spatial homogeneity imply that the impulse response functions would depend on time and space differences. The second order drift force can be modelled as the second term of the functional power series as (see Hasselmann, 1966)

$$F^{(2)}(t) = \iiiint h_2(\mathbf{x}_1,\tau_1,\mathbf{x}_2,\tau_2)\eta(\mathbf{x}_1,t-\tau_1)\eta(\mathbf{x}_2,t-\tau_2)\,d\mathbf{x}_1 d\tau_1 d\mathbf{x}_2 d\tau_2 \tag{4.89}$$

where $\mathbf{x} = (x, y)$, and $h_2(\mathbf{x}_1, \tau_1, \mathbf{x}_2, \tau_2)$ is a second order impulse response function dependent on spatial and time variables. A quadratic transfer function dependent on two frequency and two direction variables can be defined as

$$\begin{aligned} T(\omega_1, \omega_2, \theta_1, \theta_2) &= \\ \frac{1}{2} \iiiint h_2(\mathbf{x}_1, \tau_1, \mathbf{x}_2, \tau_2) & \exp\{-i(\mathbf{k}_1 \cdot \mathbf{x}_1 + \omega_1\tau_1 - \mathbf{k}_2 \cdot \mathbf{x}_2 - \omega_2\tau_2)\} \, d\mathbf{x}_1 d\tau_1 d\mathbf{x}_2 d\tau_2 \end{aligned} \tag{4.90}$$

where $\mathbf{k} = (k\cos\theta, k\sin\theta)$. The second order impulse response function may be considered symmetric, that is

$$h_2(\mathbf{x}_1, \tau_1, \mathbf{x}_2, \tau_2) = h_2(\mathbf{x}_2, \tau_2, \mathbf{x}_1, \tau_1) \tag{4.91}$$

This results in the following symmetry condition for the quadratic transfer function

$$T(\omega_1, \omega_2, \theta_1, \theta_2) = T^*(\omega_2, \omega_1, \theta_2, \theta_1) \tag{4.92}$$

The physical significance of the bidirectional quadratic transfer function can be investigated by considering a short-crested wave field composed of two long-crested wave trains, propagating in different directions, given by

$$\begin{aligned} \eta(x, y, t) &= a_1 \cos(k_1 x \cos\theta_1 + k_1 y \sin\theta_1 - \omega_1 t + \varepsilon_1) \\ &+ a_2 \cos(k_2 x \cos\theta_2 + k_2 y \sin\theta_2 - \omega_2 t + \varepsilon_2) \end{aligned} \tag{4.93}$$

where a_1, a_2 and $\varepsilon_1, \varepsilon_2$ are respectively the amplitudes and phases of the component wave trains. The second order force can be obtained by substituting equation (4.93) into equation (4.89). The mean and low frequency components of the second order force can be expressed as

$$\begin{aligned} \tilde{F}^{(2)}(t) &= a_1^2 T(\omega_1, \omega_1, \theta_1, \theta_1) + a_2^2 T(\omega_2, \omega_2, \theta_2, \theta_2) \\ &+ 2a_1 a_2 \operatorname{Re}\left[T(\omega_1, \omega_2, \theta_1, \theta_2) \exp\{i((\omega_1 - \omega_2)t - (\varepsilon_1 - \varepsilon_2))\}\right] \end{aligned} \tag{4.94}$$

The force consists of the mean components due to the individual wave trains and a slowly varying component due to the nonlinear interaction of the two waves. The symmetry condition (4.92) ensures that the force is independent of how the waves are specified. It can be seen that the quadratic transfer function for short-crested waves represents the amplitude and phase of the drift force due to two unit amplitude long-crested wave trains with different frequencies, propagating in different directions. Equation (4.94) can be rewritten as

$$\begin{aligned} \tilde{F}^{(2)}(t) &= \sum_{n=1}^{2}\sum_{m=1}^{2} a_n a_m \{P_{nm}\cos[(\omega_n-\omega_m)t+(\varepsilon_n-\varepsilon_m)] \\ &\qquad + Q_{nm}\sin[(\omega_n-\omega_m)t+(\varepsilon_n-\varepsilon_m)]\} \end{aligned} \tag{4.95}$$

where P_{nm} and Q_{nm} are the real and imaginary parts of the bidirectional quadratic transfer function, that is

$$\begin{aligned} T(\omega_n,\omega_m,\theta_n,\theta_m) &= P(\omega_n,\omega_m,\theta_n,\theta_m)+iQ(\omega_n,\omega_m,\theta_n,\theta_m) \\ &= P_{nm}+iQ_{nm} \end{aligned} \tag{4.96}$$

P_{nn} is the steady drift force coefficient of a regular oblique wave train, while Q_{nn} has to be identically zero in order to satisfy equation (4.92). Consider the special case of a regular short-crested wave train where the component wave frequencies are the same. The mean drift force is obtained from equation (4.94) as

$$\begin{aligned} \overline{F^{(2)}(t)} &= a_1^2 P(\omega,\omega,\theta_1,\theta_1)+a_2^2 P(\omega,\omega,\theta_2,\theta_2) \\ &\quad + 2a_1a_2[P(\omega,\omega,\theta_1,\theta_2)\cos(\varepsilon_1-\varepsilon_2)+Q(\omega,\omega,\theta_1,\theta_2)\sin(\varepsilon_1-\varepsilon_2)] \end{aligned} \tag{4.97}$$

It can be seen from the above equation that the mean drift force in regular short-crested waves is not just a direct summation of the mean drift forces of the component long-crested waves, but contains an additional term due to the interaction of the two waves. The interaction term is dependent on the relative phase between the two waves.

A directional sea state can be represented by a summation of regular long-crested waves of different frequencies, propagating in different directions

$$\eta(x,y,t)=\sum_{n=1}^{N} a_n\cos[k_n(x\cos\theta_n+y\sin\theta_n)-\omega_n t+\varepsilon_n] \tag{4.98}$$

where the amplitudes a_n are related to the directional wave spectrum by

$$a_n = \sqrt{2S_\eta(\omega_n, \theta_n)\Delta\omega\Delta\theta} \tag{4.99}$$

and the phases are randomly distributed. The mean and slowly varying drift force in random short-crested seas are due to the interaction of all the wave components with different frequencies and directions in the sea state and can be generalized from equation (4.94)

$$\begin{aligned} \tilde{F}^{(2)}(t) &= \sum_{n=1}^{N}\sum_{m=1}^{N} a_n a_m \{P_{nm}\cos[(\omega_n - \omega_m)t + (\varepsilon_n - \varepsilon_m)] \\ &\qquad + Q_{nm}\sin[(\omega_n - \omega_m)t + (\varepsilon_n - \varepsilon_m)]\} \end{aligned} \tag{4.100}$$

The above equation is consistent with the single summation model used to represent the directional sea state and is similar to the expression for the drift force in unidirectional waves. The coefficients P_{nm} and Q_{nm} are however dependent on the direction of propagation of the waves. Pinkster's (1985) expression for the drift force in directional seas involves a quadruple summation, consistent with a double summation representation of the sea state.

The mean drift force can be obtained from equation (4.100) as

$$\overline{F^{(2)}(t)} = \sum_{n=1}^{N} a_n^2 P_{nn} \tag{4.101}$$

The mean force depends on the drift force coefficients for regular oblique waves and can be written in continuous form as

$$\begin{aligned} \overline{F^{(2)}(t)} &= 2\int_0^\infty \int_{-\pi}^{\pi} P(\omega,\omega,\theta,\theta) S_\eta(\omega,\theta)\, d\theta d\omega \\ &= 2\int_0^\infty P(\omega) S_\eta(\omega)\, d\omega \end{aligned} \tag{4.102}$$

where $P(\omega)$ is a frequency dependent, directionally averaged drift force coefficient given by

$$P(\omega) = \int_{-\pi}^{\pi} P(\omega,\omega,\theta,\theta) D(\omega,\theta)\, d\theta \tag{4.103}$$

It can be seen from equation (4.101) that the mean drift force is no more difficult to compute in short-crested seas than in long-crested seas.

The procedure for the derivation of the spectral density of the drift force in short-crested seas is similar to that followed for long-crested seas and results in

$$S_{F^{(2)}}(\omega) = 8\int_0^{\infty}\int_{-\pi}^{\pi}\int_{-\pi}^{\pi} |T(\omega',\omega+\omega',\theta_1,\theta_2)|^2 S_\eta(\omega',\theta_1)S_\eta(\omega+\omega',\theta_2)\, d\theta_1 d\theta_2 d\omega' \quad (4.104)$$

The above equation can be rewritten in terms of a directionally averaged quadratic transfer function $|T(\omega',\omega+\omega')|^2$ as

$$S_{F^{(2)}}(\omega) = 8\int_0^{\infty} |T(\omega',\omega+\omega')|^2 S_\eta(\omega')S_\eta(\omega+\omega')d\omega' \quad (4.105)$$

where

$$|T(\omega',\omega+\omega')| = \left[\int_{-\pi}^{\pi}\int_{-\pi}^{\pi} |T(\omega',\omega+\omega',\theta_1,\theta_2)|^2 D(\omega',\theta_1)D(\omega+\omega',\theta_2)\, d\theta_1 d\theta_2\right]^{\frac{1}{2}} \quad (4.106)$$

The expressions for the directional averaged drift force coefficient and the directionally averaged quadratic transfer function should provide some insight into the effect of wave directionality on the mean and low frequency components of the second order force.

4.4.4 Evaluation of the Quadratic Transfer Function

The computation of the drift forces in random seas requires the computation of the quadratic transfer function for all the different two frequency, two direction combinations in the sea state. This requires the solution of the complete second order problem including determination of second order diffraction potential for all the combinations. In a typical sea state which is simulated with about 256 frequency bands and 32 directions per frequency band, this would require an excessively large computational effort.

Newman (1974) presented an aproximate method for the case of long-crested waves which has found widespread use. The approach is based on the assumption that the contribution to the slowly varying force associated with the off diagonal coefficients

$T(\omega_n, \omega_m)$, $\omega_n \neq \omega_m$ are very close to the diagonal coefficients for small differences in frequency, that is

$$T(\omega_n, \omega_m) = T(\omega_n, \omega_n) + O(\omega_n - \omega_m) \tag{4.107}$$

for

$$|\omega_n - \omega_m| \ll \frac{1}{2}(\omega_n + \omega_m) \tag{4.108}$$

Use of the above approximation simplifies the problem considerably in that the drift force in random seas can now be determined from the regular drift force coefficients in regular waves, which is obtained from the solution of the first order problem. It is however valid for narrow-band wave spectra. The approximation has been used in slightly different forms in practice such as

$$T(\omega_n, \omega_m) = P\left(\frac{\omega_n + \omega_m}{2}, \frac{\omega_n + \omega_m}{2}\right) \tag{4.109}$$

or

$$T(\omega_n, \omega_m) = \frac{1}{2}[P(\omega_n, \omega_n) + P(\omega_m, \omega_m)] \tag{4.110}$$

The difference between the above two approximations depends on the type of structure considered but is usually small in practice.

The validity of Newman's approximation was investigated by Faltinsen and Loken (1979) who compared the exact and approximate solutions for a two-dimensional case and found the approximate method gave reasonable results for a wide range of frequencies. The major differences were found to be due to the contribution of the second order potential at very low frequencies. Major differences were also found close to the resonance frequencies of first order motions such as roll.

It should also be noted that the final objective of the calculations is to determine the drift motions. Since such motions are usually lightly damped, the spectrum of the drift motions become narrow-banded even though the drift force spectrum might be wide-band, making the Newman approximation more valid. There are also various factors which affect the accuracy of the calculation of the drift motions such as the low frequency damping, which is primarily due to viscosity effects and difficult to estimate accurately.

In order to make the calculation of the drift forces practical for directional seas, the following intuitive approximation is proposed for the bidirectional quadratic transfer function

$$T(\omega_n, \omega_m, \theta_n, \theta_m) = \frac{1}{2}[P(\omega_n, \omega_n, \theta_n, \theta_n) + P(\omega_m, \omega_m, \theta_m, \theta_m)] \qquad (4.111)$$

The above equation implies that the drift force in a regular short-crested wave field composed of two long-crested waves with different frequencies and directions can be approximated by the summation of the mean drift forces due to the component waves. It thus neglects the additional interaction term due to the different directions of propagation of the two waves with nearly the same frequency which might be of the form $P(\frac{\omega_n + \omega_m}{2}, \frac{\omega_n + \omega_m}{2}, \theta_n, \theta_m)$. It can however be argued that the interaction term is also dependent on the relative phases between the waves as can be seen from equation (4.97) and it is expected that for a sea state with random phases, the influence of the interaction term is expected to diminish.

4.4.5 Equations of Motion

Assuming that the low frequency surge, sway, and yaw can be approximately decoupled from the first order motions, the equations of motion for low frequency motions can be written as

$$[[m] + [\mu]]\{\ddot{\Xi}^{(2)}\} + [\lambda^v]\{\dot{\Xi}^{(2)}\} + [c']\{\Xi^{(2)}\} \;=\; \{\tilde{F}^{(2)}(t)\} \qquad (4.112)$$

where $[m]$, $[\mu]$, $[\lambda^v]$, and $[c']$ are the mass, added mass, viscous damping, and mooring stiffness matrices respectively, and $\{\Xi^{(2)}\} = \{\Xi_1^{(2)}, \Xi_2^{(2)}, \Xi_6^{(2)}\}^T$. The added mass matrix is not constant but frequency dependent. The viscous damping and mooring stiffness matrices are in general nonlinear, but equivalent linear coefficients have been assumed in the above equation.

The radiation damping obtained from the forced motion potential is usually very small at the low frequencies. The primary source of damping for the low frequency motions is due to viscosity effects. The viscous damping coefficients can be estimated from free oscillation tests in still water. Free oscillation tests by Wichers and van Sluijs (1979) in still water and regular waves indicated an increase in the low frequency damping due to the presence of the waves. The additional damping is often referred to as wave drift damping. Considerable research has been carried out on various methods of estimating the wave drift damping coefficient. There is however only a partly satisfactory correlation of the models with experimental data. In the present investigation, damping estimates are made from the free oscillation tests in still water and the wave drift damping term is neglected.

As with the second order forces, the drift motions consists of a mean component and a slowly varying component. The mean component can be determined from the solution of the static problem

$$[c']\{\overline{\Xi^{(2)}(t)}\} = \{\overline{F^{(2)}(t)}\} \tag{4.113}$$

For symmetric mooring line configurations, the low frequency surge, sway and yaw motions will usually be uncoupled and since the equations of motion are assumed linear, the spectral density for the jth mode of motion can be written as

$$S_{\Xi_j^{(2)}}(\omega) = |H_{\Xi_j}(\omega)|^2 S_{F_j^{(2)}}(\omega) \qquad j = 1, 2, 6 \tag{4.114}$$

where $H_{\Xi_j}(\omega)$ is a complex transfer function given by

$$H_{\Xi_j}(\omega) = \left[-\omega^2(m_{jj} + \mu_{jj}) - i\omega\lambda_{jj}^v + c'_{jj}\right]^{-1} \tag{4.115}$$

The variance of the slowly varying component of the jth mode of motion can then be obtained as

$$\sigma^2_{\Xi_j^{(2)}} = \int_0^\infty S_{\Xi_j^{(2)}}(\omega)\, d\omega \tag{4.116}$$

4.4.6 Probability Distribution of the Second Order Motions

Due to the nonlinearity of the drift force, the drift motions are in general non-Gaussian. The mean and variance of the motions are no longer enough to define the probability distribution of the second order motions. Since the equations of motion are assumed linear, the probability density of the drift motions can be found from the probability density of the drift forces.

Kac and Siegert (1947) formulated the method for the calculation of the probability distribution of a second order force modelled as a two term Volterra series. Naess (1986) derived a closed form expression for the probability distribution of the second order forces based on Kac and Siegert's formulation. The probability density function is given by Naess (1986) as

$$p(\Xi) = \begin{cases} \sum_{j=1}^{M} \frac{\alpha_j}{\lambda_j} \exp(-\Xi/\lambda_j) & \Xi \geq 0 \\ \sum_{j=M+1}^{N} \frac{\alpha_j}{|\lambda_j|} \exp(-\Xi/\lambda_j) & \Xi < 0 \end{cases} \tag{4.117}$$

where λ_j are the eigenvalues of the following integral equation

$$\int_0^\infty T(\omega,\omega')H_\Xi(\omega)\psi_j(\omega)\, d\omega = \lambda_j \psi_j(\omega') \tag{4.118}$$

$\psi_j(\omega)$ are the eigenfunctions of the integral equation. The term α_j is given by

$$\alpha_j = \prod_{\substack{k=1 \\ k \neq j}}^{N} \left(1 - \frac{\lambda_k}{\lambda_j}\right)^{-1} \tag{4.119}$$

The eigenvalues are determined from the discrete form of the integral equation (4.118)

$$\sum_{n=1}^{N} T(\omega_n,\omega_m)H_\Xi(\omega_n)\psi_j(\omega_n)\Delta\omega = \lambda_j \psi(\omega_m) \qquad m = 1,2,\ldots,N \tag{4.120}$$

where N is the number of frequency components used. The eigenvalues are arranged so that $\lambda_j, j = 1,2,\ldots,M$ are positive and $\lambda_j, j = M+1, M+2,\ldots,N$ are negative.

Vinje (1983) showed that for a linear system, the probability distribution of the response asymptotically approaches a Gaussian distribution as the damping approaches zero, irrespective of the nature of the forcing function. This suggests that the distribution of the drift motions which are lightly damped are 'near' Gaussian. Approximate methods such as an Edgeworth type expansion (see Cramer, 1966) or the maximum entropy method can be used with estimates of the first four moments or cumulants. Cumulants κ are an alternative representation of the moments of a probability distribution and are defined as

$$\kappa_n = \frac{d^n}{d\mu^n} \ln M(\mu)\bigg|_{\mu=0} \tag{4.121}$$

where $M(\mu)$ is the moment generating function given by

$$M(\mu) = \int_{-\infty}^{\infty} \exp(\mu\Xi)p(\Xi)\, d\Xi \tag{4.122}$$

The moments can also be obtained from the moment generating function as

$$m_n = \frac{d^n}{d\mu^n} M(\mu)\bigg|_{\mu=0} \tag{4.123}$$

The first four cumulants are related to the first four moments by (see Cramer, 1966)

$$\kappa_1 = m_1 \tag{4.124}$$

$$\kappa_2 = m_2 - m_1^2 \tag{4.125}$$

$$\kappa_3 = m_3 - 3m_1m_2 + 2m_1^3 \tag{4.126}$$

$$\kappa_4 = m_4 - 3m_2^2 - 4m_1m_3 + 12m_1^2m_2 - 6m_1^4 \tag{4.127}$$

The first cumulant is the mean of the distribution while the second cumulant is the variance. The third and fourth cumulants can be used to provide indications of deviations from a Gaussian distribution and can be expressed respectively as the skewness γ_3 and kurtosis γ_4

$$\gamma_3 = \kappa_3/\sqrt[3]{\kappa_2^2}\,; \quad \gamma_4 = \kappa_4/\kappa_2^2 \tag{4.128}$$

The skewness is a measure of the asymmetry of the distribution while the kurtosis is a measure of the peakedness of the distribution.

The cumulants of the drift motions can be obtained directly from the eigenvalues of the integral equation (4.120) as (see Langley, 1987)

$$\kappa_n = (n-1)! \sum_{j=1}^{N} \lambda_j^n \tag{4.129}$$

For weakly nonlinear systems, the probability distribution of the drift motions can be modelled as an Edgeworth series

$$\begin{aligned} p(\zeta) &= \frac{1}{\sqrt{2\pi\kappa_2}} \exp(-\zeta^2/2) \left[1 + \frac{1}{3!}\gamma_3 \, \mathrm{He}_3(\zeta) \right. \\ &\left. + \frac{1}{4!}\gamma_4 \, \mathrm{He}_4(\zeta) + \frac{10}{6!}\gamma_3^2 \, \mathrm{He}_6(\zeta) + \cdots \right] \end{aligned} \tag{4.130}$$

where $\zeta = (\Xi - \kappa_1)/\sqrt{\kappa_2}$ is the nondimensional drift motion amplitude, and $\mathrm{He}_n(\zeta)$ is a Hermite polynomial of order n given by

$$\mathrm{He}_n(\zeta) = (-1)^n \exp(\zeta^2/2) \frac{d^n}{d\zeta^n} [\exp(-\zeta^2/2)] \tag{4.131}$$

A truncated Egdeworth series sometimes predicts negative values or spurious peaks in the probability distribution (e.g. Draper and Tierney, 1972) leading to unrealistic extreme value estimates. An alternate distribution is the maximum entropy distribution given by (see for example Dowson and Wragg, 1973).

$$p(\Xi) = \exp\left(-\sum_{n=0}^{4} \mu_n \Xi^n \right) \tag{4.132}$$

where the parameters μ_n are obtained by solving the following integral equation iteratively

$$\int_{-\infty}^{\infty} \Xi^j \exp\left(-\sum_{n=0}^{4} \mu_n \Xi^n \right) d\Xi = m_j \qquad j = 0, 1, \ldots, 4 \tag{4.133}$$

The Newton-Raphson iterative procedure can be used to determine μ_n with the integrals evaluated numerically.

4.5 Effect of Wave Grouping

Wave grouping is a term used to refer to the occurrence of alternate groups of high and low waves in random wave trains. The simplest example of a highly grouped wave train is a bichromatic wave train consisting of two regular wave trains. When the difference between the frequencies of the component wave trains is small, the envelope of the combined wave train varies slowly in time at a frequency equal to the difference frequency of the component waves. Since the slowly varying drift forces respond to the envelope of the wave train, highly grouped wave trains cause a much larger horizontal excursion of moored vessels.

Different measures have been proposed to quantify the degree of groupiness in random sea states. The various wave grouping measures are summarized by Mansard et al. (1989). One such measure is the groupiness factor proposed by Funke and Mansard (1979). The groupiness factor G_F is defined as

$$G_F = \frac{\sigma_{\eta^{(2)}}}{\sigma_\eta^2} \tag{4.134}$$

where $\sigma_{\eta^{(2)}}$ is the standard deviation of the low frequency part of the square of the water surface elevation. Funke and Mansard (1979) use the concept of a Smoothed Instantaneous Wave Energy History (SIWEH) which is obtained by smoothing the square of the water surface elevation with a Bartlett filter.

By suitably selecting the phases of the wave components, different wave trains with different groupiness factors can be synthesized from the same wave spectrum. Spangenberg and Jacobsen (1980), and Mansard and Pratte (1982) found the horizontal motions of a moored vessel were significantly affected by the degree of groupiness in a sea state. Since different amplitudes of motion were obtained from the same wave spectrum, the issue of whether a wave spectrum was adequate to predict the low frequency motions of moored vessels was raised.

It can however be shown that the spectral density of the low frequency part of the square of the water surface elevation can be uniquely obtained from the wave spectrum as (see Pinkster, 1984)

$$S_{\eta^{(2)}}(\omega) = \int_0^{\infty} S_\eta(\omega')S_\eta(\omega + \omega')\, d\omega' \tag{4.135}$$

The level of grouping which is dependent on the spectrum of the squared elevation should thus be linearly related to the wave spectrum. This would however be valid for infinitely long simulation periods and finite record lengths would cause some statistical variability.

Finally, it should be also noted that the expression for the spectral density of the low frequency force (4.87) represents a convolution of the quadratic transfer function with the spectrum of the squared elevation. An intuitive attempt would be to try to directly relate the spectrum of the drift force to the spectrum of the squared elevation

$$S_{F^{(2)}}(\omega) = T(\omega)S_{\eta^{(2)}}(\omega) \tag{4.136}$$

where $T(\omega)$ is a transfer function. This approach would however be based on an even narrower band assumption than the Newman approximation which involves a convolution integral.

Chapter 5

EXPERIMENTS

Experiments were carried out to evaluate different methods of directional wave analysis, measure the wave forces on a fixed slender vertical cylinder in random long-crested and short-crested waves, and measure the mooring line forces and motions of a floating barge in regular and random long-crested and short-crested waves. The tests were conducted in the multi-directional wave basin of the Hydraulics Laboratory at the National Research Council of Canada in Ottawa. The basin is equipped with a segmented wave generator capable of producing complex multi-directional sea states. The wave generator was commissioned recently (April, 1986) and the experiments described in this thesis were the first to be carried out in the new facility utilizing the full directional wave generation capabilities.

5.1 Test Facilities

5.1.1 The Wave Basin

The experiments were carried out in the wave basin shown in Figure 5.1. The basin is 50m wide, 30m long, and 3m deep. A relocatable partition reduced the working area for the present investigation to 30m by 19.2m as shown in Figure 5.2. Depending on the wave height, tests can be carried out in water depths up to 2.7m but the normal operating water depth is 2m.

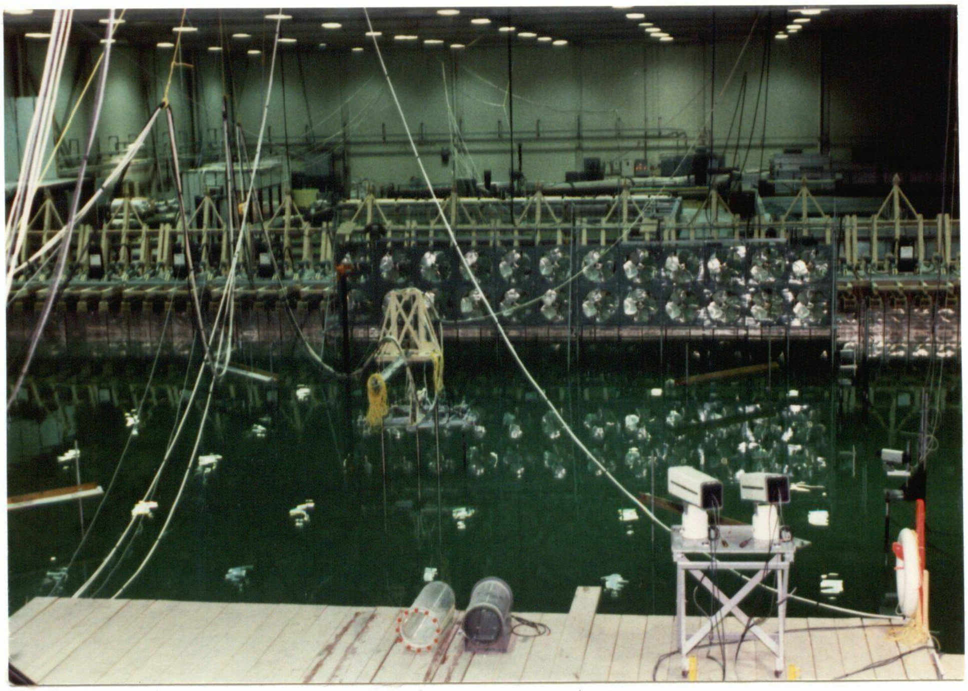

Figure 5.1: Overall view of wave basin

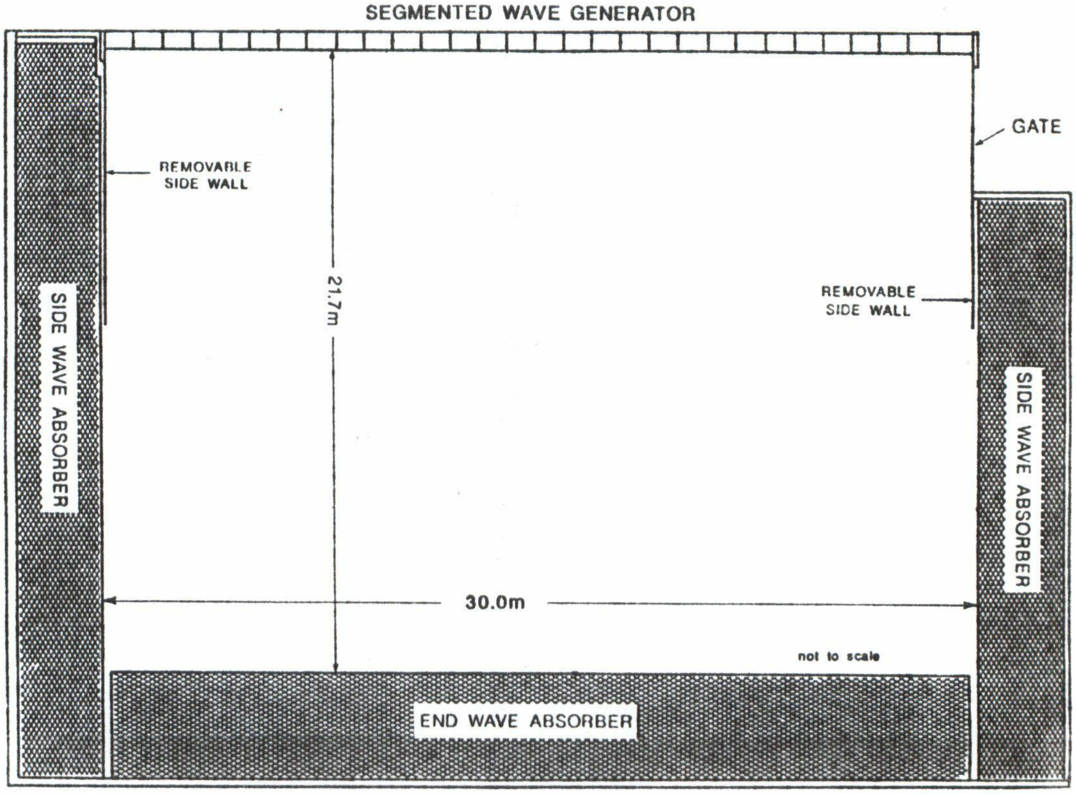

Figure 5.2: Plan view of wave basin

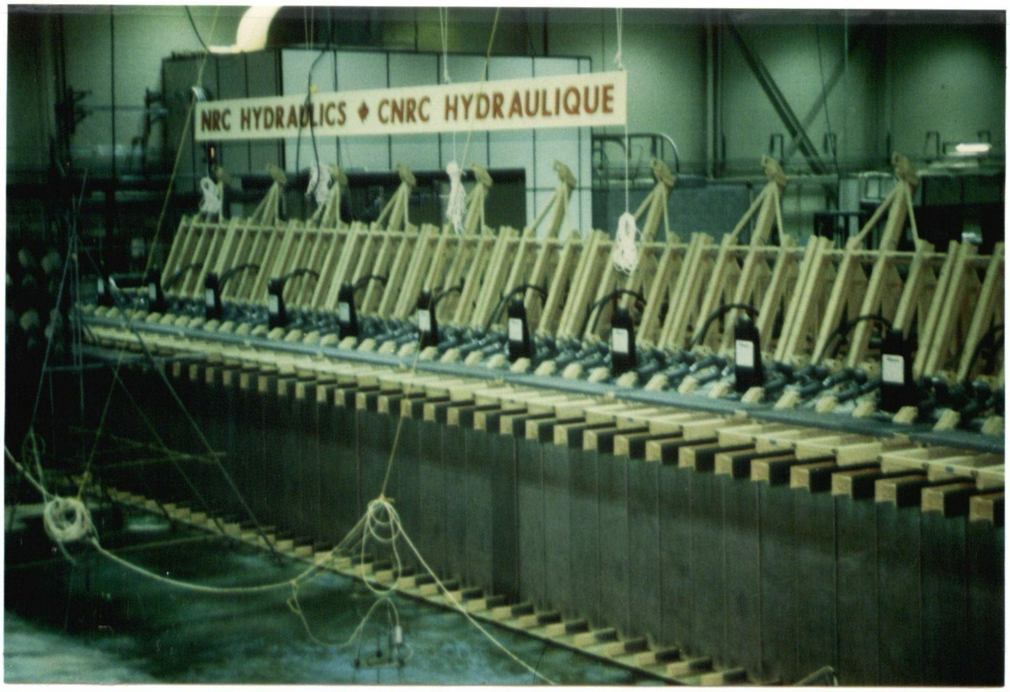

Figure 5.3: View of segmented wave generator

The segmented wave generator occupies one side of the basin while wave energy absorbers are placed along the other sides of the basin. The energy absorbers are made of perforated layers of metal sheeting. The absorbers were tested extensively by Jamieson and Mansard (1987) and have been shown to have reflection coefficients of less than 5% for waves up to 0.7m high, with wave periods ranging from 1 to 3 seconds.

5.1.2 The Wave Generator

The directional wave generator shown in Figure 5.3 consists of 60 segments driven individually by a servo controlled hydraulic system. The wave generator and its control system are described in detail by Miles et al. (1986) and is thus briefly described here.

The individual wave boards are 0.5m wide and 2.5m high, driven by a Moog hydraulic actuator with a maximum stroke of 0.2m at a rated static force of 45kN. The maximum displacement of the waveboards are mechanically amplified by means of a lever arm.

The hydraulic power supply consists of six pumps, each rated at $3.16\ell/s$ (50 USgpm) and driven by an electric motor rated at 75kW. A servo system controls the flow of pressurized oil to the hydraulic actuators and hence the motion of the waveboards.

The wave generator can operate either in the piston (translational) mode, flapper (rotational) mode, or a combined translational and rotational mode. The piston mode is used for shallow water waves while the flapper mode is used for deep water waves. The use of different articulation modes for the different wave conditions ensures that the profile of the board motion approximately matches the water particle velocity profile for the various conditions, thus minimizing an excessive or inadequate energy input into the progressive wave.

The control system for the directional wave generator is a microprocessor based digital system with a four unit modular design. The control signals for the waveboard displacements (drive signals) are initially synthesized on an HP1000 computer. The signals are then downloaded to an Intel 186/51 communication computer. The communication computer passes the information to four module control units (MCU) which act as nodes on an Ethernet network. Each MCU is responsible for the control of 16 segments and performs real time tasks such as acquisition of feedback data on lever arm rotation and actuator displacement, calculation of the analog drive voltage signal using the feedback data and the desired drive signal, and output of the control signal to the servo system. The control loop is implemented entirely in software.

Synthesis of Wave Generator Drive Signals

In order to reproduce a given water surface elevation time series with specific directional spreading characteristics at a test location in the basin, control signals for the 60 individual waveboards have to be synthesized. The drive signals are usually in the form of waveboard displacement or rotation. A comprehensive software package for the generation of long-crested random waves was developed by Funke and Mansard (1984). For the segmented wave generator, Miles et al. (1987) discuss the software used for the generation of multi-directional waves.

The computer programs for the synthesis of the wave generator control signals are all based on the basic linear theory that relates the waveboard rotation or displacement to the water surface elevation in front of the waveboard formulated originally by Havelock (1929). Factors such as propagation of the wave from the waveboard to the test section, articulation mode of the wave generator, and the dynamics of the servo system are all taken into account in the creation of the drive signal.

The multi-directional wave generation signals are based on the 'snake' principal. A regular oblique wave train can be generated by a sinusoidal or snakelike motion along the length of the generator as shown in Figure 5.4. By a suitable linear superposition of different wave frequencies and directions, the drive signals for the 60 waveboards can be produced (see Isaacson, 1985b).

5.1.3 Data Acquisition System

The data acquisition system enables the sampling of continuous analog signals produced by the test instrumentation (such as wave probes, current meters, and load cells) and converts the data to digital form for storage on magnetic tape and later analysis on the computer.

The analog signals from the instrumentation enter a Series 100 analog to digital (A/D) conversion unit manufactured by the Neff Corporation. The unit optionally provides for conditioning of the analog signals and a 15 bit analog to digital conversion. Signal conditioning is usually in the form of low level amplification and/or low pass filtering. The Neff unit and associated hardware are placed in a specially manufactured rack. After the data is converted to digital form, it is transmitted to the HP1000 computer where it is stored in memory. Figure 5.5 shows the flow of information in the data acquisition

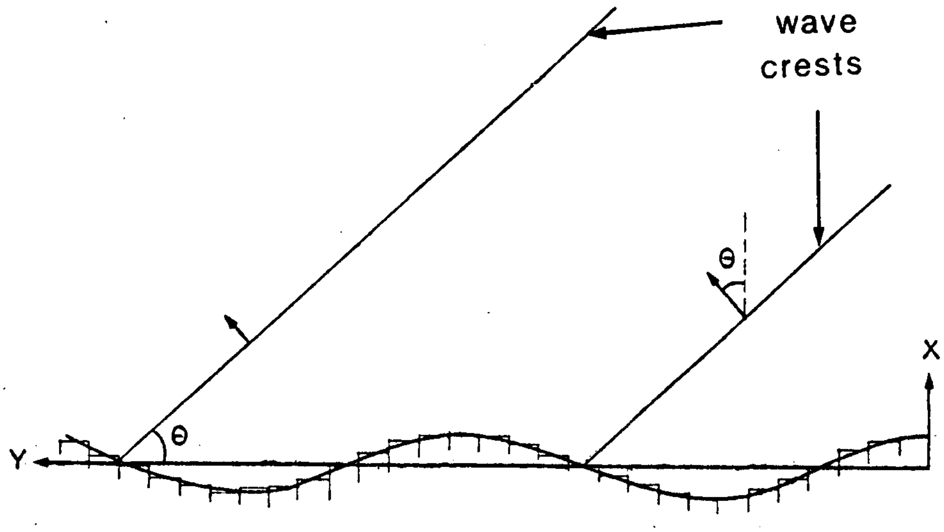

Figure 5.4: Sketch showing the 'snake' principle

system.

A software package developed at the NRC Hydraulics Laboratory called the Generalized Data Acquistion Package (GEDAP) is responsible for the initialization of the sampling and writing of the measured data to GEDAP data files. The data acquisition system can sample at frequencies of up to 1000Hz for 16 recording channels, or at lower rates for a maximum of 64 channels. There are usually 16 channels for each port with a separate Neff card. Since the A/D converter is shared by 16 channels, there is initially a single multiplexed data file containing information from all 16 channels.

The sampling frequency is chosen by the user but normally varies from 10 to 20Hz for the measurement of regular and random wave forces on structures and the motions of floating vessels, but can be as high as 1000Hz for impact type wave loads. The sampling frequency is chosen to be about 5 to 10 times the highest expected significant frequency component in the measured signal to minimize aliasing problems.

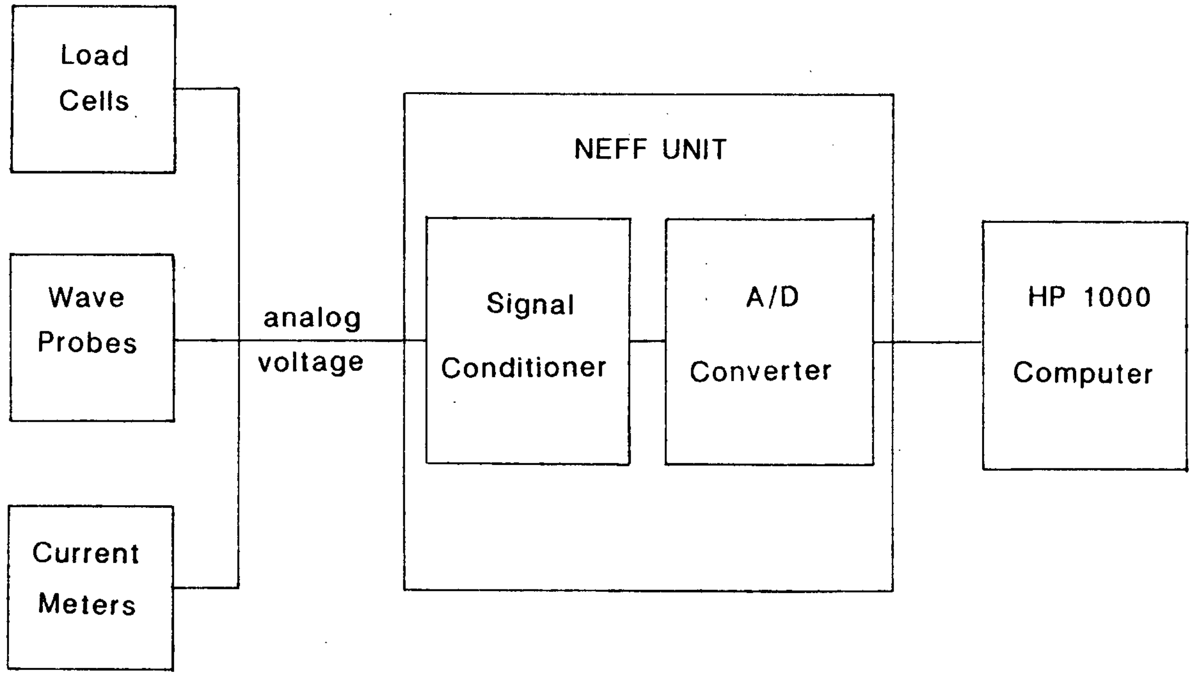

Figure 5.5: Flow diagram for data acquisition system

Low pass filtering of the analog signals is usually performed to eliminate high frequency noise components. A low pass filter passes signal frequencies below a specified cutoff frequency and rejects those above the cutoff frequency. In the present experiments, interchangeable 2-pole Butterworth filters were plugged into the Neff cards with the cutoff frequency always chosen to be half the sampling frequency. Low level amplification of some analog signals is also needed in order to match the maximum voltage output of the instrumentation to the full scale voltage range of the A/D converter as was the case with the load cells used in the present investigation which had to be amplified with a gain of 200.

A control room located across from the wave generator housed the data acquisition hardware and the HP1000 computer terminals used for operating the wave generator and acquiring data. Figure 5.6 shows a view of racks housing the Neff data acquisition hardware.

Figure 5.6: View of control room

5.2 Directional Wave Measurement

The analysis of the directional wave fields generated in the wave basin was based on data from 1) the simultaneous measurement of the water surface elevation at a number of locations in the basin using a wave probe array, and 2) simultaneous measurement of the water surface elevation and orthogonal water particle velocities at a single location in the basin.

5.2.1 The Wave Probe Array

A wave probe array was specifically designed to provide information about wave directionality in the offshore wave basin. The array has nine twin wire capacitance type wave probes mounted on a rigid frame. The frame is attached to a support structure consisting of three vertical rods fixed to a steel base structure. A view of the array is

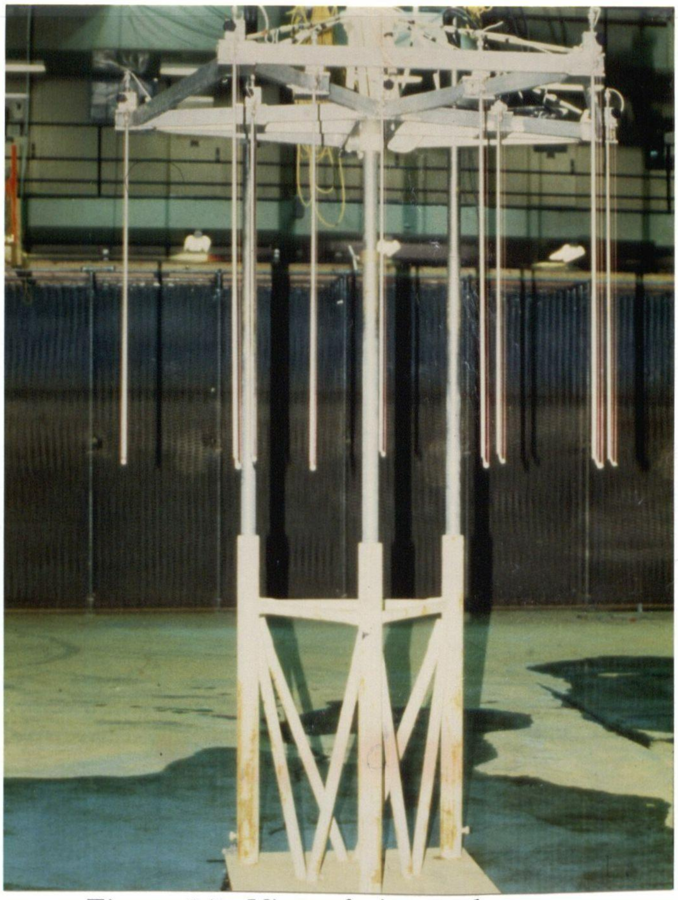

Figure 5.7: View of nine probe array

shown in Figure 5.7.

Each wave probe measures the water surface elevation by outputing a voltage induced by an imbalance in its circuit due to immersion of the probe in water. The output voltage is proportional to the change of the depth of immersion relative to its balanced position. The wave probes are approximately 1m high.

The configuration of the array is similar to the one designed for the Coastal Engineering Research centre (CERC) by Panicker and Borgman (1970). Figure 5.8 shows the layout of array. The outer four probes are all on a circle and the inner four probes are placed on a circle half the radius of the outer circle.

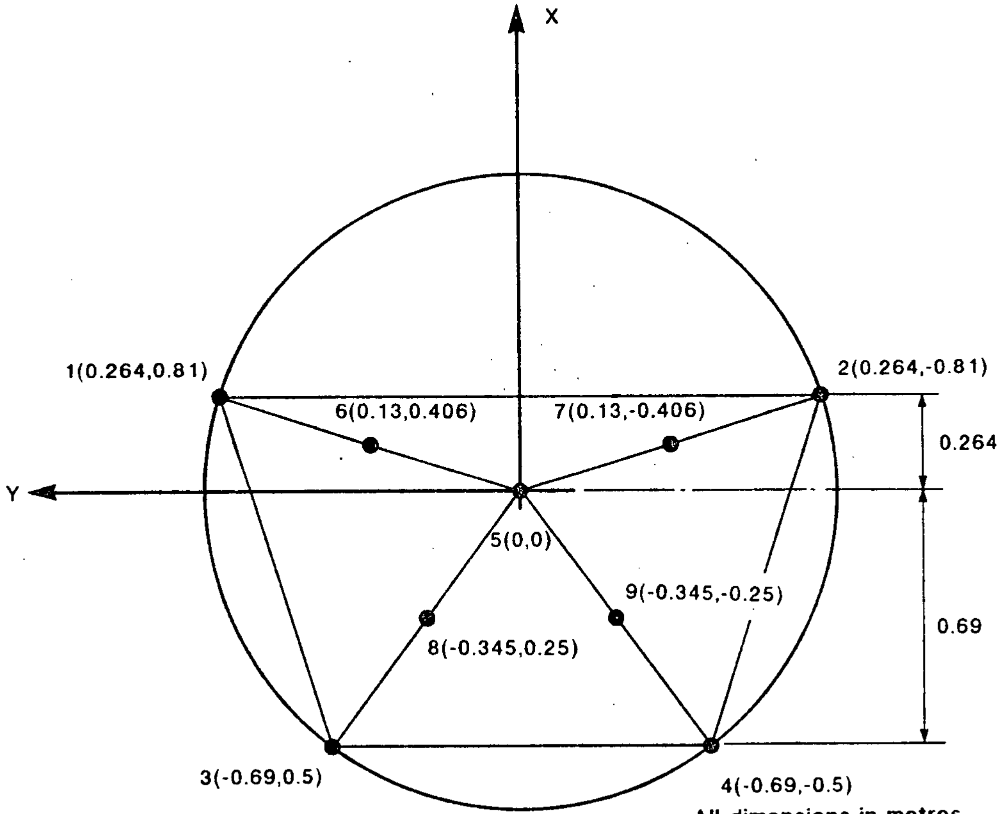

Figure 5.8: Layout of nine probe array

Calibration

All nine probes can be calibrated at the same time by remotely moving the rigid frame containing the probes specified distances along the vertical support posts. A calibration program is run to sample the voltages at distances of -0.3m, 0.0m, and 0.3m in still water. The program then fits a second order polynomial to the measured voltages. The second order contribution is usually less than 0.1% of the first order term indicating a high degree of linearity.

5.2.2 The Current Meters

Two Marsh McBirney biaxial electromagnetic current meters were used to measure the two dimensional horizontal water particle velocities. One of the current meters is shown in Figure 5.9. The current meters use the Faraday principle of electromagnetic induction to measure the velocities in the flow field. A solenoid in the current meter

Figure 5.9: View of Marsh-McBirney current meter

generates a magnetic field and flow of water past the magnetic field induces a voltage potential since water is a conductor. The induced voltage potential is proportional to the vector components of the flow velocity. Two pairs of carbon electrodes measure the orthogonal components of the voltage caused by the two dimensional flow and output the signals to the data acquisition system.

The presence of metallic objects near the current meters interfere with the generated magnetic field, producing noise components in the output signal. Special mounting brackets made of nonconducting material were built to support the current meters and minimize the interference. The presence of wave probes near the current meters still produced significant levels of noise in the output signals. Some of the noise frequencies were within the range of the wave frequencies and could not be filtered out using analog or digital methods.

Calibration

The current meters were calibrated in a 1.25m × 1.25m × 64m steel wave flume. Small amplitude waves generated in the flume at a water depth of 0.6m with wave periods ranging from 0.7 to 2.8 seconds. The water particle velocities in a glass section of the flume were measured using the Marsh-McBirney current meters and a Laser-Doppler anemometer. The Laser-Doppler anemometer measurements correlated fairly well with predictions by linear wave theory while the electromagnetic current meters showed a higher degree of variability. The variability had no particular dependence on wave frequency, and was only slightly dependent on the velocity magnitude. After investigating various polynomial fits of the calibration data, a linear fit was finally used. The maximum deviation of the measured data from the predicted value based on the linear fit was about 4%.

5.3 Segmented Cylinder Tests

Tests were carried out to measure the forces on a slender vertical cylinder for different wave conditions. The test conditions included regular and random, long-crested and short-crested waves.

5.3.1 The Segmented Cylinder

The test cylinder is 0.17m in diameter and 2.4m high with the upper 1.5m divided into 9 independent segments instrumented to measure the forces as shown in Figure 5.10. The bottom two segments were 0.35m high, the middle two segments were 0.15m high, and the top five segments were 0.10m high. The cylinder was segmented so as to provide data on the vertical distribution of wave forces, as well as the relative importance of the force components above the still water level. The cylinder segments had varying heights in order to keep the loading on each segment approximately the same.

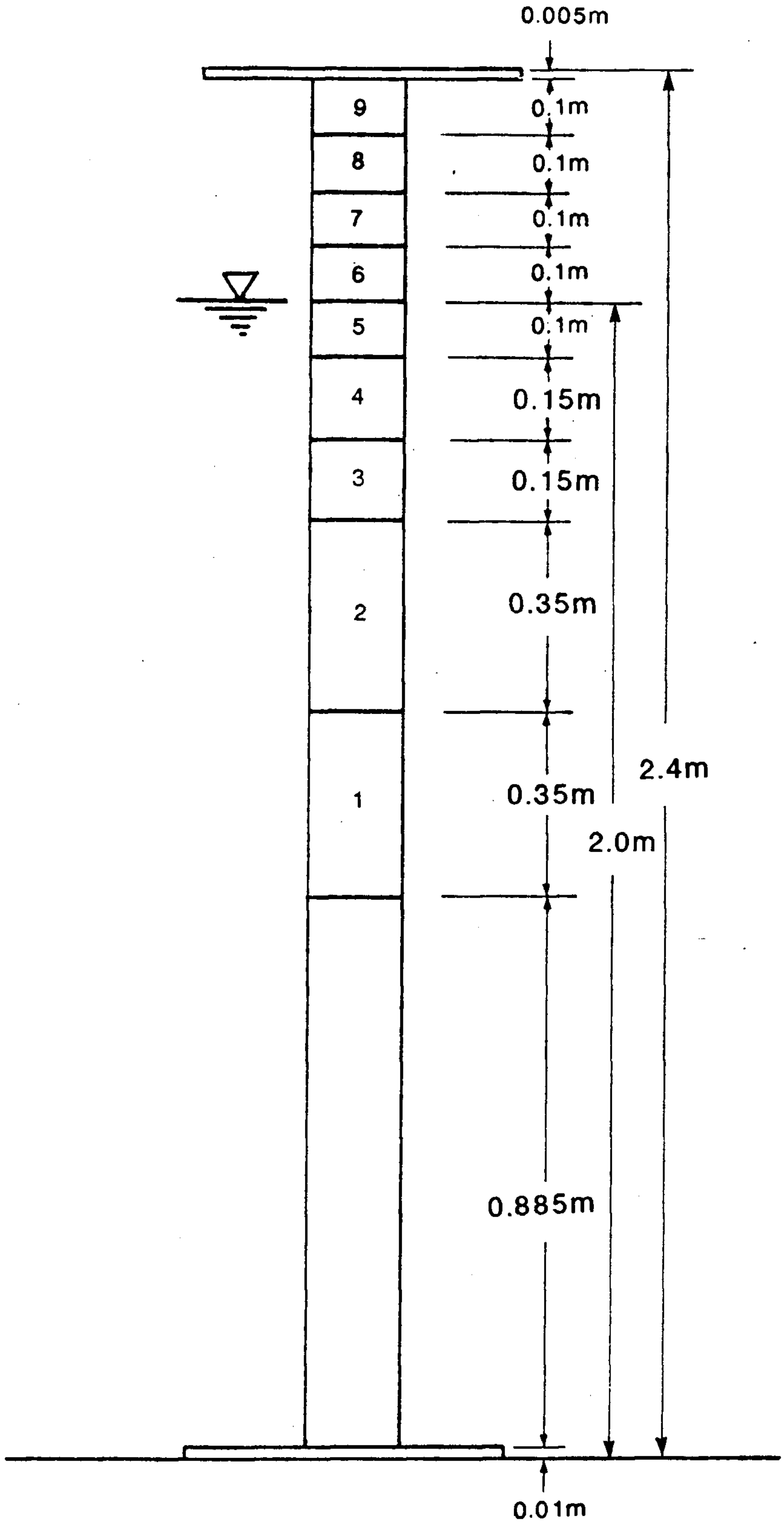

Figure 5.10: Sketch of test cylinder showing segment dimensions

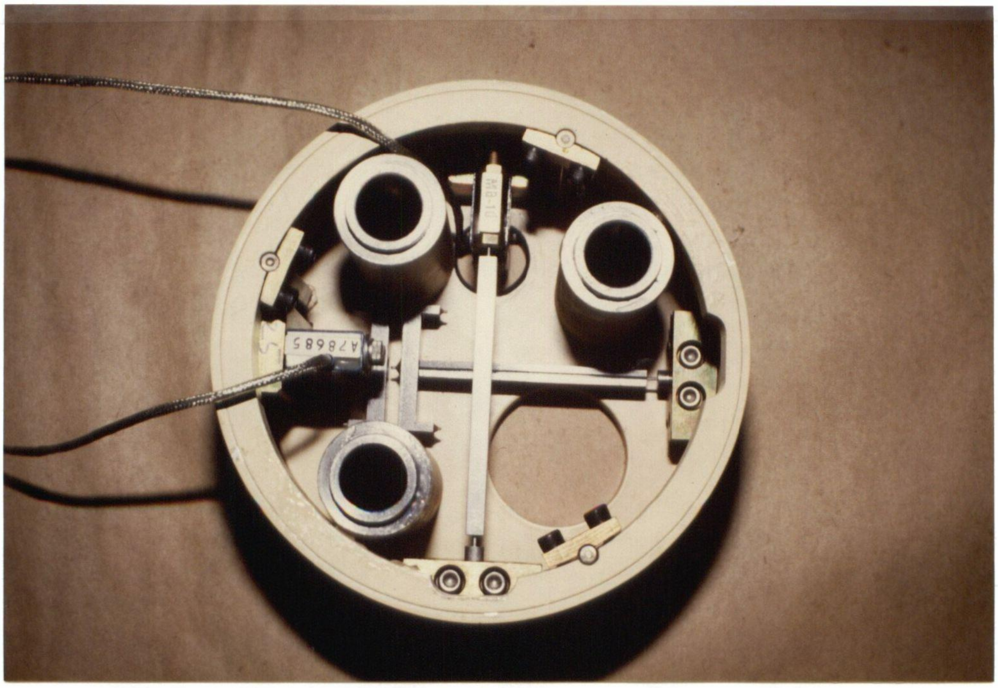

Figure 5.11: Top view of the interior of one segment

Each segment is fitted with two load cells oriented orthogonally so as to measure the vector components of the horizontal force in a three-dimensional wave field. Figure 5.11 shows a top view of the interior of a segment. The outer shell of the cylinder is made of aluminum. The load cells are manufactured by Innerpac and contain strain guages which form part of a Wheatstone bridge circuit. External forces produce strains which cause a change in the resistance of opposite arms of the bridge, producing an output voltage. The inline load cells were rated at 181N while the transverse load cells were rated at 72.5N.

Three steel rods fixed to the bottom non-instrumented part of the column were used to stack the segments on top of each other. The rods were bolted to a 0.61m square top steel plate in order to make the whole assembled structure rigid. The bottom section of the cylinder was also fixed to a 0.61m square steel plate. The entire cylinder was wrapped in polyvinyl to make it watertight and smooth. As a backup measure against accidental

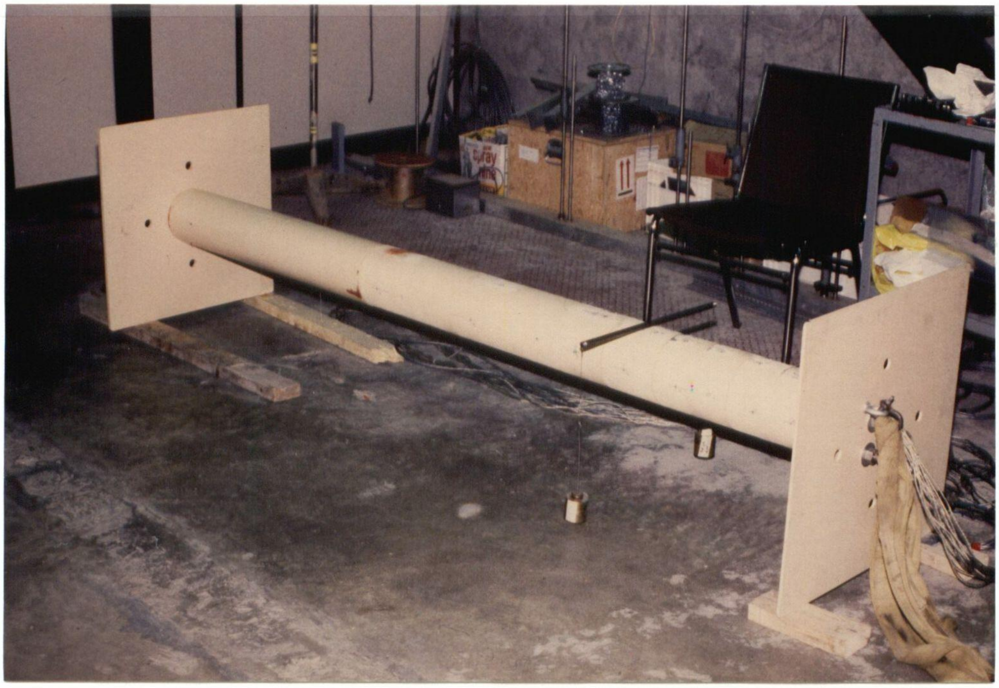

Figure 5.12: View of test cylinder during calibration tests

leakage, a tube attached to a pump was placed in the column.

5.3.2 Calibration

The load cells in the segmented cylinder were calibrated with the cylinder resting horizontally on the two end plates as shown in Figure 5.12. An aluminum frame was placed over the column from which weights were suspended. Loads of 0N, 10N, and 20N were applied and a second order polynomial was fitted to the measured voltages. An indication of the nonlinearity of the response of the load cells is the ratio of the second to first order contributions at the maximum load, and this was normally less than 0.5%.

Dynamic tests were also carried out to measure the natural frequencies of vibration of the segments and provide an indication of the degree of of coupling between the inline and transverse load cells, as well as between adjacent segments. A 1.8kg mass was suspended from the aluminum loading frame with a strand of piano wire. A torch flame was used to cut the wire instantly and unload the segment. The force response of both channels of the preloaded segment, as well as adjacent segments were sampled at a frequency of 400Hz for 5 seconds.

The measured inline and transverse force response of the fourth and fifth segments are shown in Figure 5.13 for the case where the fourth segment was initially loaded. It can be seen that the initial load of 20.1N was damped down the weight of the aluminum frame (2.2N) fairly rapidly. The natural frequency of vibration for this case was about 20Hz, well above the exciting wave frequencies of interest. Figure 5.13 also shows a maximum dynamic load of 0.6N on the transverse channel even though there was no applied load in that direction. The transverse load is also damped out fairly rapidly. The fifth segment recorded maximum dynamic loads of about 1.0N indicating a slight degree of coupling.

5.3.3 Experimental Set-Up

The assembled column was placed 9m away from the wave generator along the centreline of the basin. A wave probe was placed 20cm in front of the cylinder to record the water surface elevation at the cylinder location. Two Marsh-McBirney current meters were mounted directly underneath the wave probe at elevations of 1.08m and 1.68m, corresponding to the midpoints of the first and third segments respectively. The centre of the nine probe array was placed 4m in front of the cylinder. A total of 32 channels were used to record information from 10 wave probes, two biaxial current meters, and 18 load cells.

5.3.4 Test Conditions and Experimental Procedure

The test cylinder was subjected to various regular and random long-crested and short-crested waves in water of 2m depth. The results for regular waves are discussed by Cornett (1987) and the present investigation is limited to random wave conditions.

The random wave tests were carried out in two different phases. During the first set

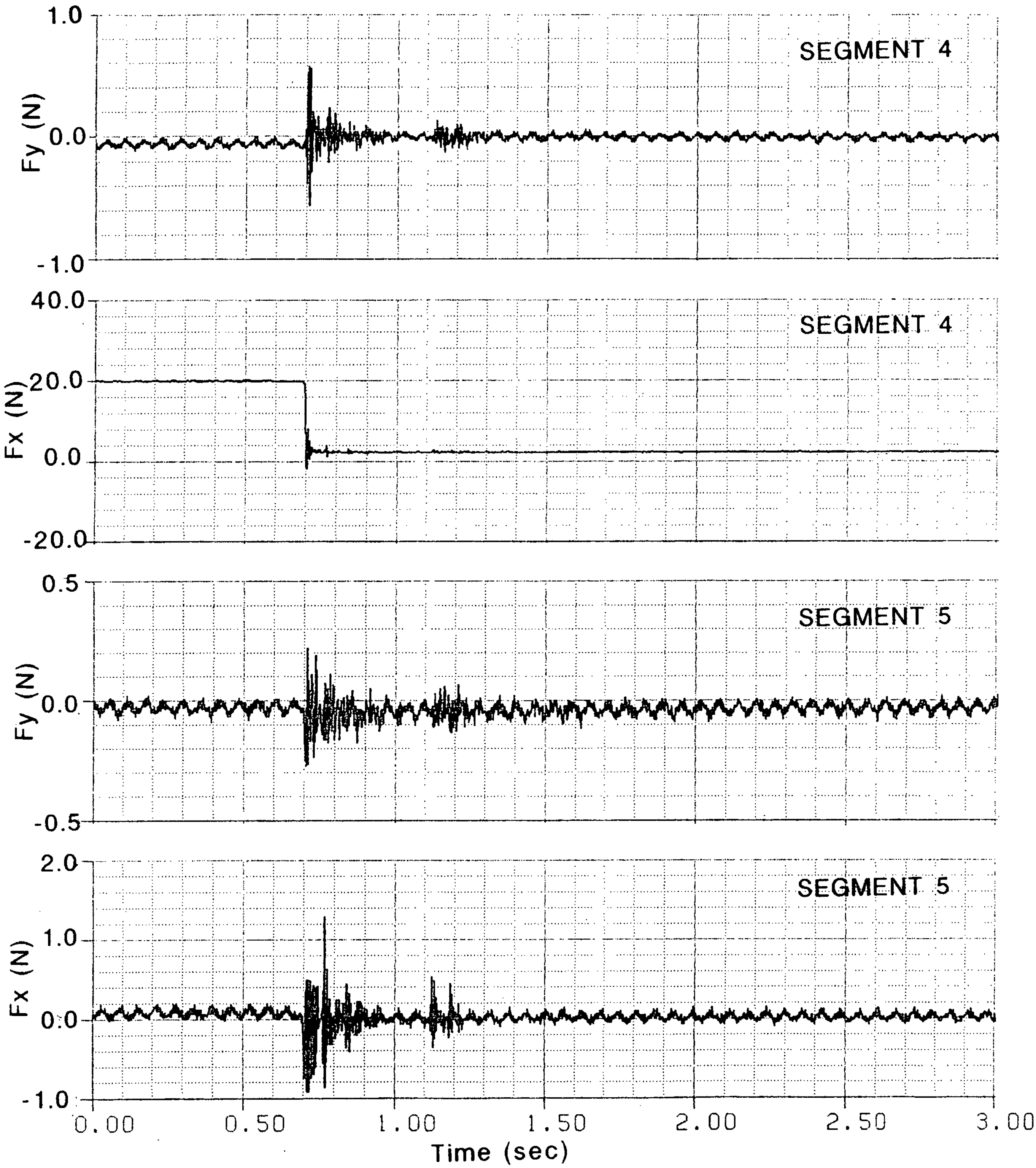

Figure 5.13: Free vibration response of cylinder segment

Table 5.1: Summary of test conditions for segmented cylinder

f_p (Hz)	H_{m0} (m)	
0.33	0.45	0.315
0.40	0.40	0.28
0.50	0.32	0.22

of tests, four of the nine transverse load cells failed, limiting the amount of analysis that could be carried out with the data. A second set of tests were later carried out during a different research project with the column.

For the first set of tests, the incident waves were described by a Bretschneider spectrum given by

$$S_\eta(\omega) = \frac{5H_{mo}^2}{16\omega_p}\frac{1}{(\omega/\omega_p)^5}\exp\left[-\frac{5}{4}\left(\frac{\omega}{\omega_p}\right)^{-4}\right] \tag{5.1}$$

where H_{mo} is the significant wave height, and ω_p is the peak frequency of the spectrum. Sea states with peak frequencies of 0.33, 0.4, and 0.5Hz were synthesized with two significant wave heights per peak frequency. A summary of the target significant wave heights is given in Table 5.1. In order to investigate the influence of the degree of wave short-crestedness on the forces, three multi-directional sea states with different spreading functions were generated for each long-crested wave train. Frequency independent cosine power spreading functions were used with target spreading indices $s = 1, 5$ and 10, and principal direction of wave propagation $\theta_0 = 0°$. There were thus a total of 24 different sea states for the first set of tests.

The directional sea states had approximately the same significant wave heights as the long-crested wave trains at the test location even though the time series were not identical. Attempts were made to synthesize long-crested and short-crested wave trains with an identical time series at the test location but the measured wave trains were always different.

The wave trains were synthesized at a time interval of 0.1s for a duration of 204.8s. The record length of the wave trains was chosen to facilitate an FFT analysis. The double summation model was used for directional wave synthesis since it was the only model available at the time of the tests.

The drive signals were first synthesized on the HP1000 computer, and then downloaded to the module control units of the wave generator. The wave generator was activated and after about 60s, wave conditions in the basin were assumed to have reached steady state conditions and the GEDAP data acquisition program was started. Data was sampled at a rate of 20Hz for 204.8s and stored on the online HP1000 computer. The data files were also backed up on magnetic tape.

Prior to the second set of tests, the order of the cylinder segments was rearranged. The bottom five segments were now 0.1m high, the middle two segments were 0.15m high, and the top two segments were 0.35m high as shown in Figure 5.14. The water depth was 1.94m. The rearrangement of the order of the segments was necessary for a different research project carried out with the column at the same time. The second set of random waves were described by the JONSWAP wave spectrum, given by

$$S_\eta(\omega) = \frac{A}{\omega_p^5} \exp\left[-\frac{5}{4}\left(\frac{\omega}{\omega_p}\right)^{-4}\right] \gamma^{\exp\left[-\frac{(\omega-\omega_p)^2}{2\sigma^2\omega_p^2}\right]} \tag{5.2}$$

where A is a normalizing factor that depends on the significant wave height, γ is a peak enhancement factor, and σ is given by

$$\sigma = \begin{cases} 0.07 & \omega \leq \omega_p \\ 0.09 & \omega > \omega_p \end{cases} \tag{5.3}$$

The phase II test conditions consisted of two long-crested and three short-crested sea states. The long-crested wave spectra had peak frequencies of 0.33Hz and 0.4Hz, significant wave heights of 0.3m, and peak enhancement factors of 3.3. Three multi-directional

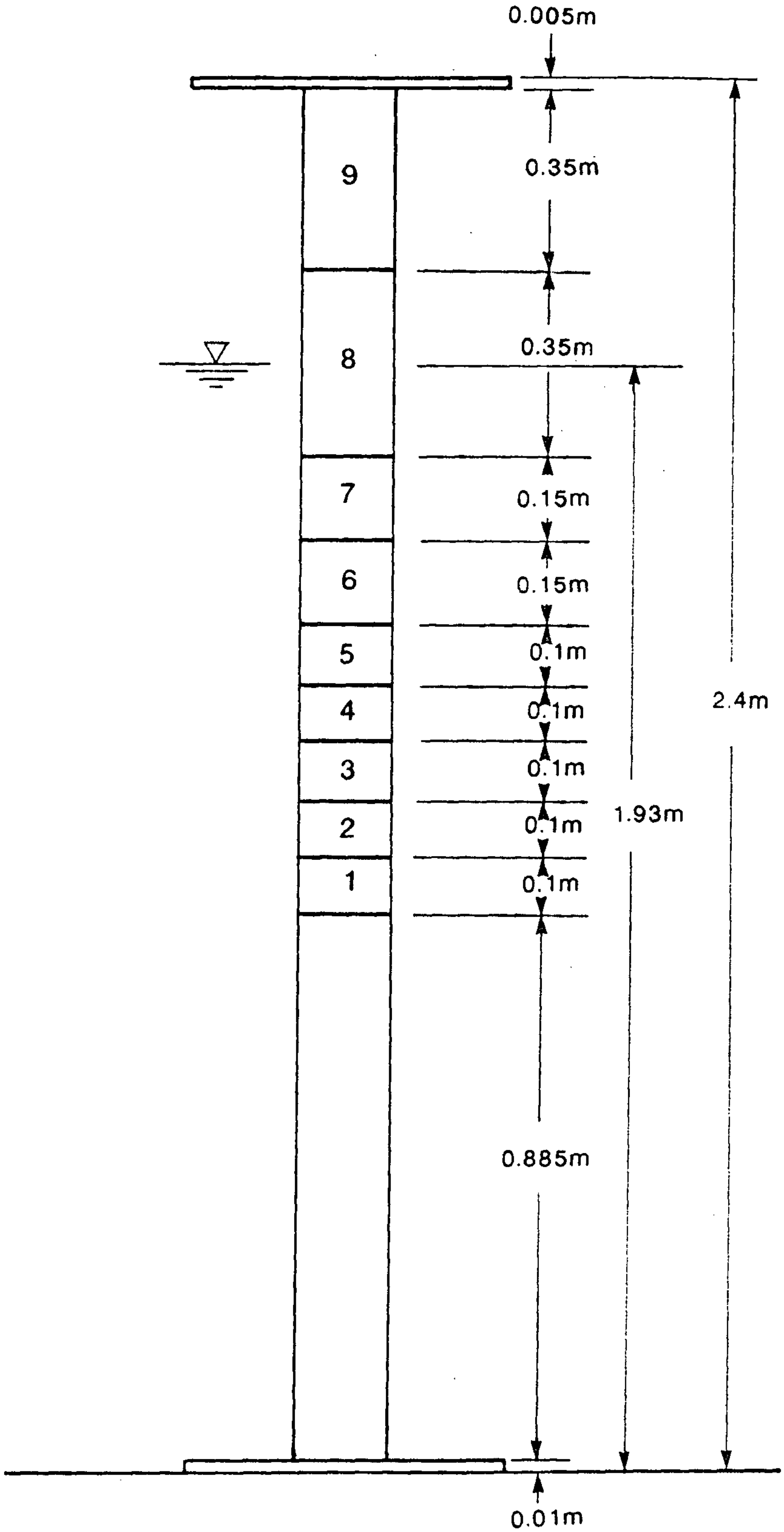

Figure 5.14: Sketch of segmented cylinder for the phase II tests

sea states were synthesized for the 0.33Hz wave spectrum, with target spreading indices s of 1, 3, and 6, and principal direction $\theta_0 = 0°$. The single summation model was used to synthesize the directional waves. Data was sampled using the GEDAP data acquisition system at a rate of 10Hz for a duration of 819.2s. The longer duration chosen for the phase II tests was necessary for the statistical analysis carried out on the data.

5.4 Floating Barge Model Tests

Experiments were also carried out to measure mooring line forces and six degree of freedom motions of a floating barge moored by a soft linear spring system in regular and random unidirectional and multi-directional waves.

5.4.1 The Barge Model

The rectangular barge model is 1.5m long, 1m wide, and 0.6m high. The draft of the model was 0.2m, and the water depth was 2m. Figure 5.15 shows the barge model floating in a multi-directional sea state. The model was constructed of plywood, 0.02m thick, and painted with fiberglass resin to make it watertight. A deck was placed at 15cm above the keel on which ballast weights were attached. The total weight of the barge was 300kg. The centre of gravity of the barge was at 0.04m above the still water level, while the radii of gyration were 0.345m, 0.503m, and 0.513m for roll, pitch and yaw respectively.

5.4.2 The Mooring System

The barge was restrained horizontally by a four point mooring system as shown in Figure 5.16. The mooring pattern is symmetric with each line aligned at $\pm 45°$ with respect to the x axis. The model was setup 11m away from the wave generator along the centreline of the basin, and was oriented for head seas for all the tests.

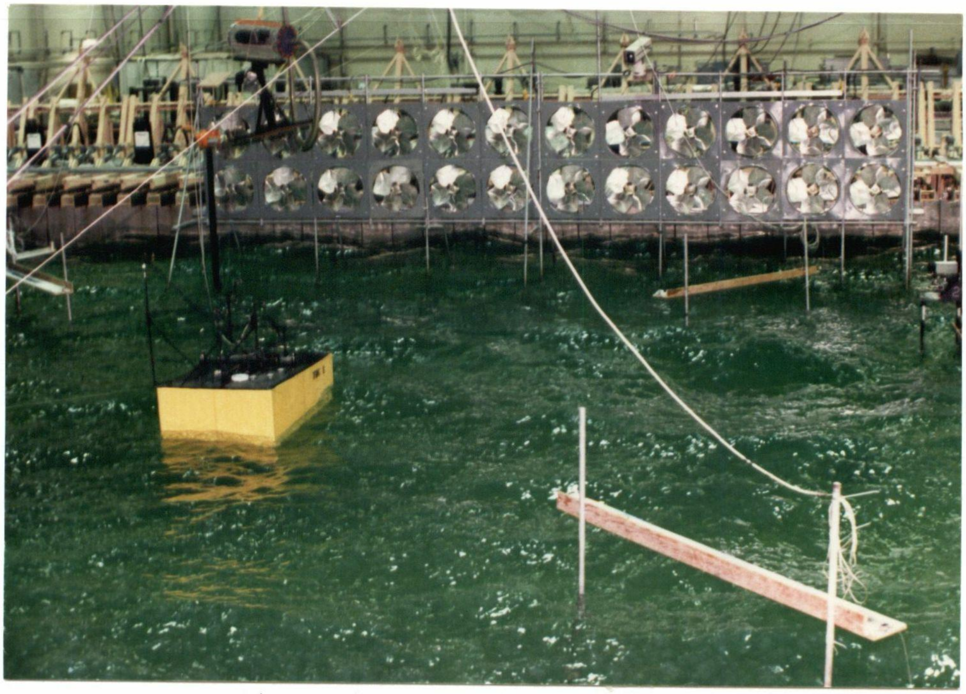

Figure 5.15: View of barge model floating in a multi-directional sea state

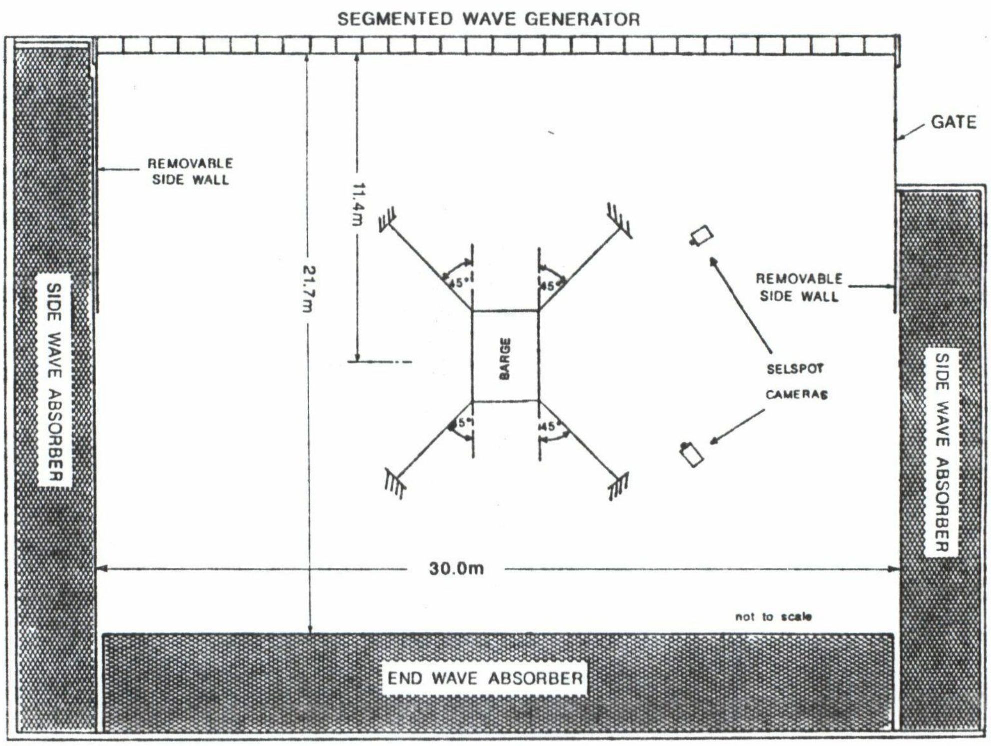

Figure 5.16: Layout of mooring system

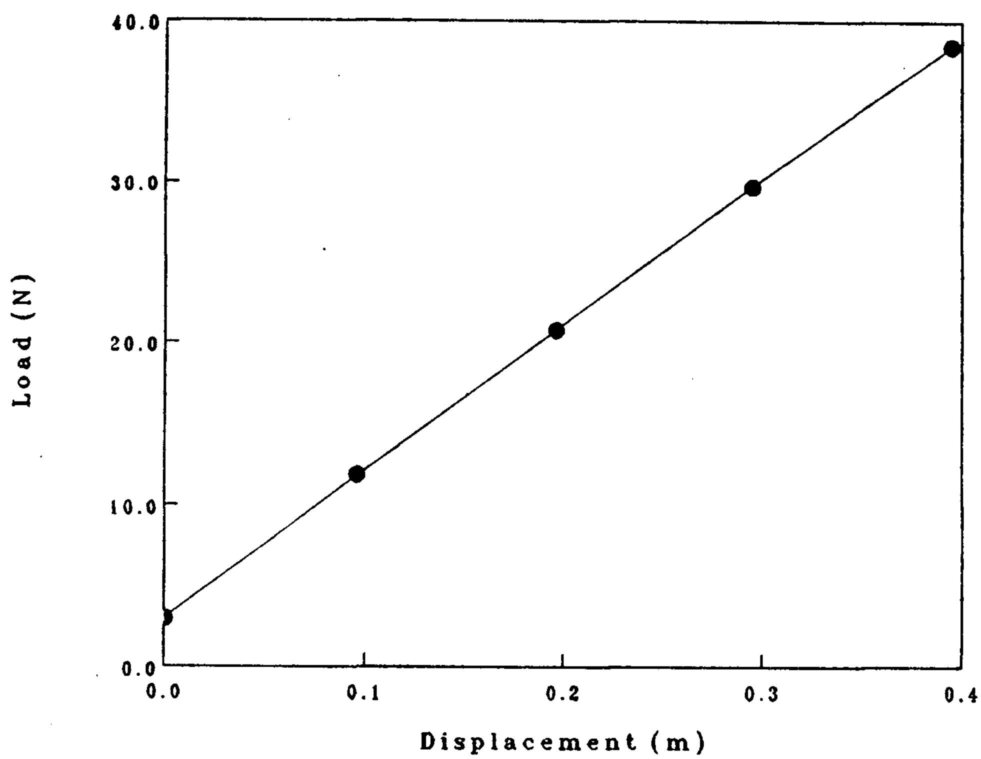

Figure 5.17: Typical load-displacement curve for mooring line

Each mooring line consists of fine steel wire and three linear extension springs, attached at one end to the top corners of the model, and at the other end to a load cell. Innerpac load cells rated at 362N were used. The springs were arranged in series and rested on a horizontal board supported by two vertical posts.

The spring stiffnesses were chosen to keep the natural frequencies for the horizontal motions well below the exciting wave frequencies. The springs were initially slackened to remove any pretensions. The combined stiffness for each set of three springs were obtained before installation in the basin by loading the springs vertically and measuring the displacement. Figure 5.17 shows a typical load-displacement curve for the springs. The figure shows that the mooring lines behaved in a linear manner, with an approximate stiffness value of 90N/m.

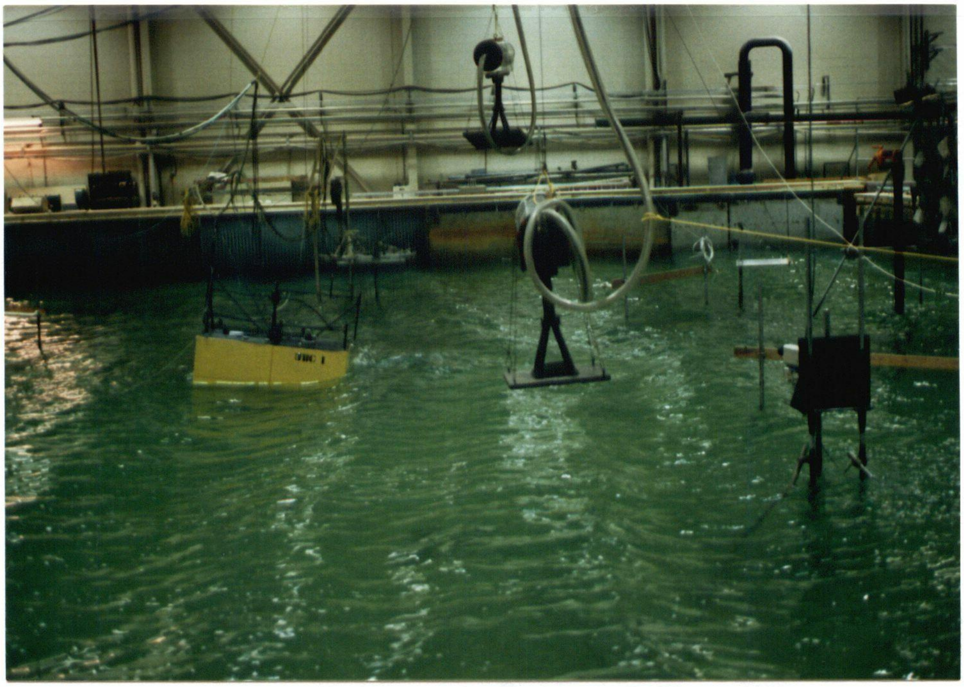

Figure 5.18: View showing LEDs mounted on top of barge model

5.4.3 Measurement of Barge Motions

The six rigid body motions of the barge were measured with an optical spotting system (SELSPOT) that tracks the displacement of eight infrared Light Emitting Diodes (LEDs) mounted on the model with two photosensitive cameras. Figure 5.18 shows the barge model floating with the LEDs on top of the model. The position of the LEDs with respect to a coordinate system fixed on the body were determined from a survey.

The two cameras were fixed on a support structure at an elevation of 0.8m above the still water level. Figure 5.19 shows the location and orientation of the cameras with respect to the initial position of the barge. The cameras are oriented at 60° with respect to each other and placed at approximately 6.0m away from the centreline of the barge. The layout was chosen to make sure that the cameras received an adequate intensity of light and could detect a majority of the LEDs at all times.

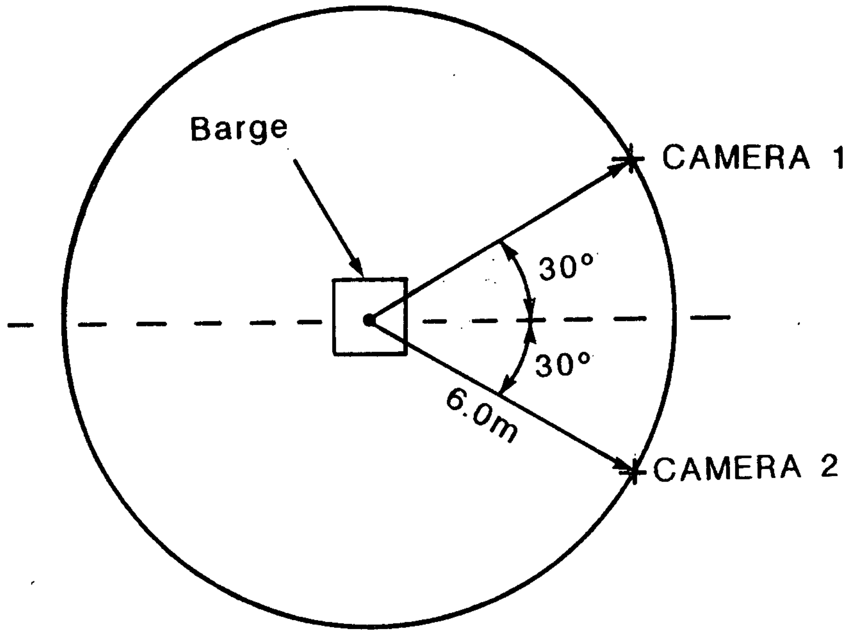

Figure 5.19: Layout of SELSPOT system

The cameras contain a microprocessor which digitizes the screen image to provide the coordinates of the LEDs on the screen. An analog signal of the LED positions is then output to the HP1000 computer. Appropriate software is used to convert the LED positions to six degree of freedom motions.

As a backup measure against sudden problems with the SELSPOT system, an accelerometer frame with seven accelerometers was mounted on the model. The accelerometers can be used to measure the first order motions, but not the low frequency drift motions. The SELSPOT system worked quite well during the tests and data from the accelerometers were not analyzed.

5.4.4 Estimation of Moments of Inertia

The moments of inertia (or radii of gyration) of the barge for the roll, pitch and yaw motions were determined from tests on a swing frame. The z coordinate of the centre

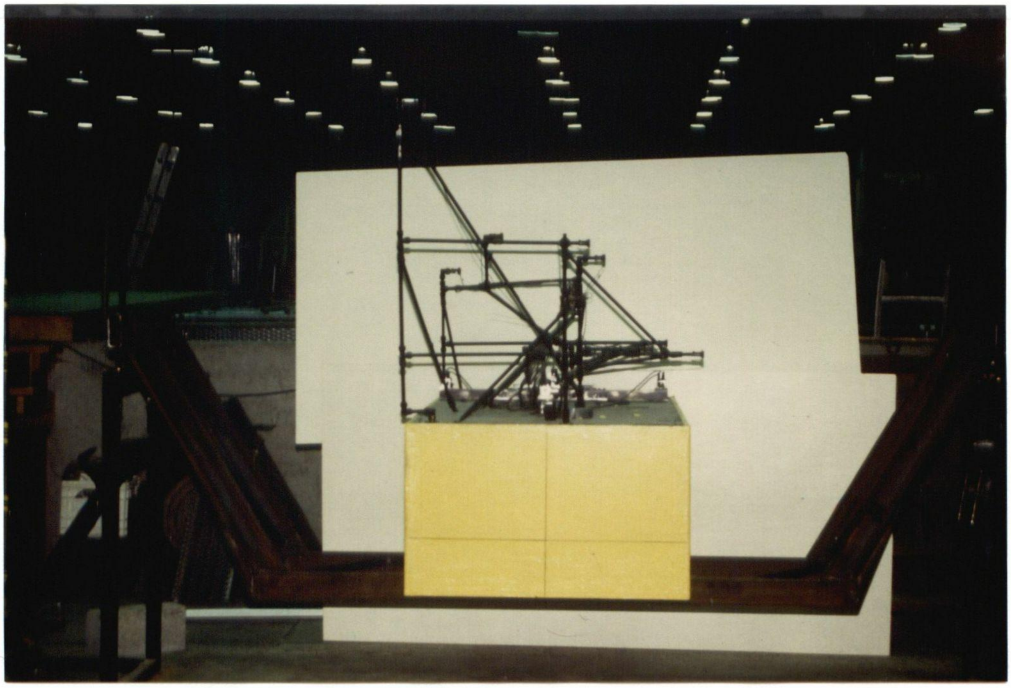

Figure 5.20: View of barge model on swing frame

of gravity z_G was also estimated from tests on the frame. The frame consists of steel I-beams resting on two knife edges as shown in Figure 5.20. The weight, moment of inertia, and centre of gravity of the frame are measured *a priori*.

The vertical centre of gravity of the barge was estimated by measuring the angle of tilt produced by an applied moment to the frame. The angle of tilt was measured with an accelerometer. By balancing the moments about the knife edge, z_G can be estimated as shown in Appendix B.

After the vertical centre of gravity was determined, the model was swung in roll, pitch, and yaw. The moments of inertia for the different motions are estimated from the periods of the angular motions of the frame, measured with a stopwatch. Details of the calculations are given in Appendix B.

5.4.5 Test Conditions and Experimental Procedure

Free oscillation tests in still water were initially carried out to provide estimates of the viscous damping coefficients and natural frequencies for the surge, sway, roll, pitch and yaw motions. The barge was initially displaced and then released. The time history of the free vibrations of the barge were recorded by the SELSPOT system. Data was sampled at the rate of 10Hz for a duration of 10s for the roll and pitch motions, and for 64s for the surge and sway motions. There were difficulties in getting the model to oscillate freely in yaw so no yaw free oscillation data was collected.

Plots of the measured free decay surge, sway, roll and pitch motions are shown in Figure 5.21. The natural frequencies were obtained from a zero-crossing analysis and are 11.8s, 12.1s, 1.51s, and 1.68s for surge, sway, pitch and roll respectively. Equivalent linear viscous damping coefficients were also obtained from the free oscillation tests, and are given in Appendix C. The degree of nonlinearity of viscous damping for the different motions is also discussed in Appendix C. The main particulars of the barge model are summarized in Table 5.2.

The test conditions for the barge included regular long-crested and crossing waves, long-crested bichromatic waves, and random unidirectional and multi-directional waves. The target waves were synthesized and run in the basin before the barge model was installed. The nine wave probe array with a biaxial current meter placed underneath one of the wave probes was used to measure the wave conditions at the test location. The sampling frequency was 10Hz for all the tests.

Regular Wave Tests

In order to obtain the response amplitude operators and steady drift motion amplitudes, tests were initially carried out with six regular long-crested wave trains with periods ranging from 1.2 to 3.0 seconds and wave heights ranging from 0.12m to 0.34m.

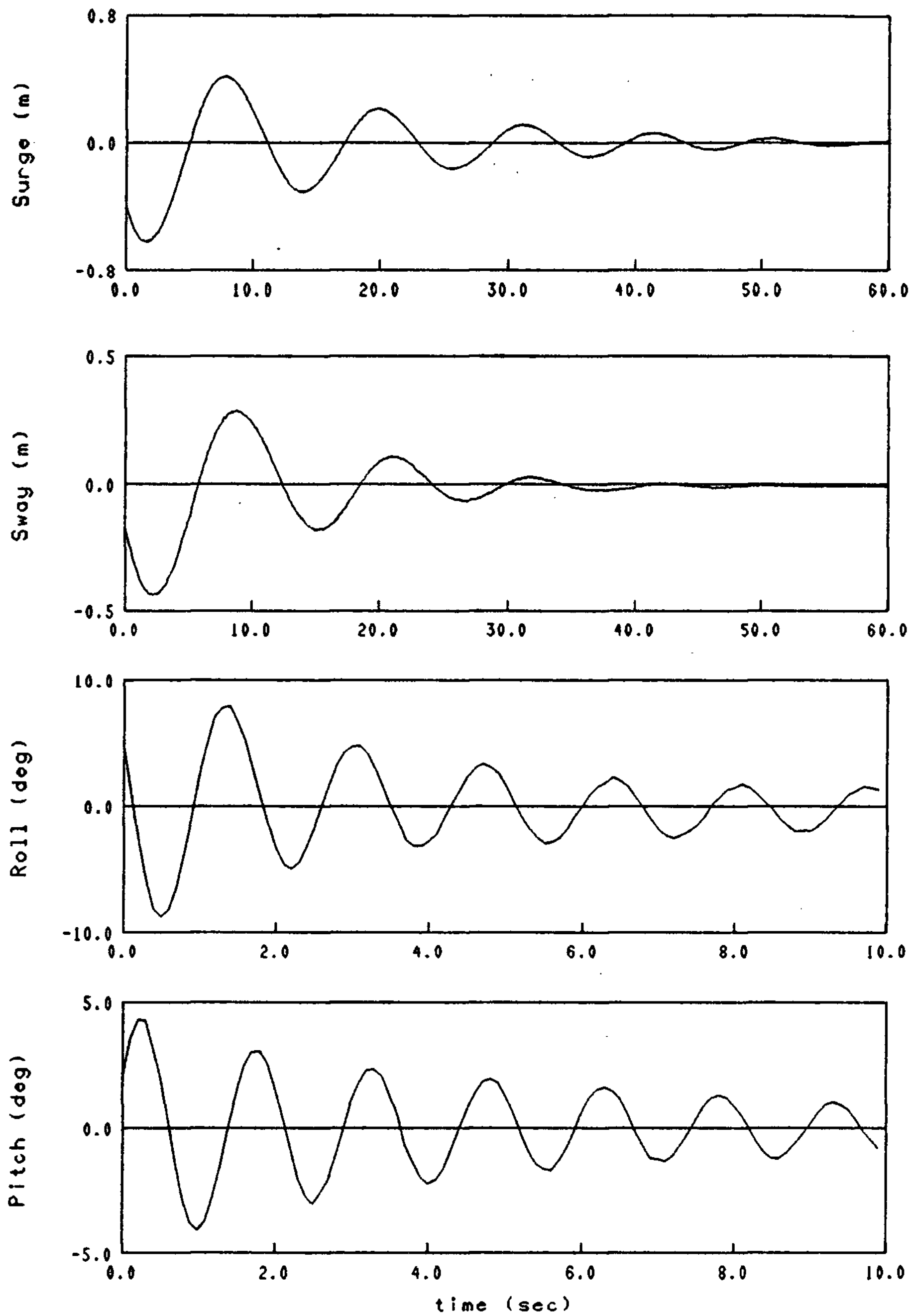

Figure 5.21: Time history of free oscillation tests

Table 5.2: Main particulars of barge model

Displacement volume	0.3m^3
Length	1.5m
Breadth	1.0m
Draft	0.2m
Centre of Gravity	(0.0, 0.0, 0.04m)
Roll radius of gyration	0.345m
Pitch radius of gyration	0.503m
Yaw radius of gyration	0.512m
Natural roll period	1.68s
Natural pitch period	1.51s
Natural heave period	1.55s
Natural surge period	11.8s
Natural sway period	12.1s

A summary of the test conditions is given in Table 5.3.

Before the start of each test, the LED positions are initially sampled. The wave generator was then activated and after the model reached its steady drift position, the GEDAP data acquisition program was started. Data from the four mooring line load cells and the SELSPOT system were collected for a duration of 64.0s. The GEDAP data files were backed up on magnetic tape.

The influence of crossing wave angle on the first and second order motions was investigated by generating two regular waves with the same frequency but propagating in directions $\pm\alpha$ about the x axis. Crossing angles α of $30°, 60°$, and $90°$ were specified for wave periods of 1.5 and 2.0 seconds. The phases of the wave components were chosen so that the crest of the short-crested wave train propagated along the centreline of the barge.

Table 5.3: Summary of regular wave test conditions for barge model

T(s)	H(m)
1.2	0.12
1.5	0.14
1.75	0.17
2.0	0.15
2.5	0.24
3.0	0.34

Long-crested Bichromatic Wave Tests

The barge was also subjected to bichromatic wave trains which are the superposition of two regular long-crested wave trains. The difference in the frequencies of the component wave trains was chosen to be close to the natural frequency for the surge motion. Three wave trains with component frequencies of 0.42 and 0.5Hz, 0.58 and 0.67Hz, and 0.67 and 0.74Hz were generated. The wave heights of the component wave trains were 0.16m, 0.1m, and 0.1m respectively. The sampling duration was also 64s.

Random Wave Tests

The last series of tests involved irregular long-crested and short-crested waves described by a JONSWAP spectrum. Two JONSWAP spectra with f_p of 0.5 and 0.67Hz, H_{m0} of 0.20m and 0.175m respectively, and $\gamma = 3.3$ were used. For each spectrum, one long-crested and three multi-directional sea states were generated. The multi-directional sea states were synthesized with the single summation model and had target cosine power spreading indices s of 1, 3, and 6 with the principal direction of wave propagation $\theta_0 = 0°$. Data was sampled for 819.2s.

The influence of wave groupiness on the slow drift oscillations was also investigated by synthesizing three long-crested wave trains with approximately the same spectrum but different groupiness factors. Two target JONSWAP spectra were used with peak frequencies of 0.5 and 0.67Hz, significant wave heights of 0.24m and 0.145m, and $\gamma = 3.3$. The target groupiness factors G_F were 0.4, 0.7, and 1.0. Data was sampled for a duration of 409.6s.

Chapter 6

RESULTS AND DISCUSSION

The results of the experimental and numerical investigations into the effect of wave directionality on the forces and motions of structures are presented and discussed in this chapter. The first part of this chapter focusses on the Fourier, maximum likelihood, and maximum entropy methods of estimating directional wave spectra, discussed earlier in Chapter 2. The methods are used to analyze numerically simulated data in order to assess the directional resolution capability of each method. Different multi-directional sea states with different degrees of directional spreading are analyzed, using data from both a wave probe-biaxial current meter array and a wave probe array.

The results of the laboratory measurements of the forces on a segmented cylinder in random long-crested and short-crested waves are next presented. Random force coefficients are estimated from the data and comparisons are made between measured and predicted force spectra. Reduction factors used to express the effect of wave directionality are presented for different multi-directional sea states. Finally, the theoretical probability distribution of the peaks of the inline force in long-crested waves and the resultant force in multi-directional waves, derived earlier in Chapter 3, are compared with distributions obtained from experimental and numerically simulated data.

The last section of this chapter discusses the measured mooring line forces, first order motions, and slow drift motions of a floating barge in multi-directional waves. Linear diffraction theory is used to compute the first order added mass, damping, exciting force, and drift force coefficients. The measured response amplitude operators and drift force coefficients are compared with numerical predictions. Comparisons are also made between measured and predicted spectra of the first order and second order motions. The effect of wave directionality on the drift motions and mooring line forces is investigated by comparing results for different degrees of directional spreading. Finally, the probability distributions of the measured low frequency motions are compared with the Gaussian distribution.

6.1 Analysis of Directional Wave Fields

The truncated Fourier series, maximum likelihood, and maximum entropy methods were used to estimate directional distributions from numerically simulated data in order to investigate the directional resolving power of each method. The methods are first compared using measurements of the water surface elevation and orthogonal velocities at the same location, and later with measurements of the water surface elevation at an array of points.

6.1.1 Wave Probe - Biaxial Current Meter Array

The random phase method was used to synthesize the water surface elevation and velocity time series for different multi-directional sea states with the same frequency spectrum. Frequency bands of width 0.02Hz were used in the synthesis with 32 directions per frequency band. This resulted in time series with record lengths of 1638.4s at a time interval of 0.2s.

The first set of simulated sea states were described by a JONSWAP spectrum with peak frequency $f_p = 0.5$Hz, significant wave height $H_{m0} = 0.3$m, and peak enhancement factor $\gamma = 3.3$. Three multi-directional sea states with spreading indices $s = 1$, 5, and 20, and mean direction $\theta_0 = 0°$ were synthesized. The velocity time series were synthesized

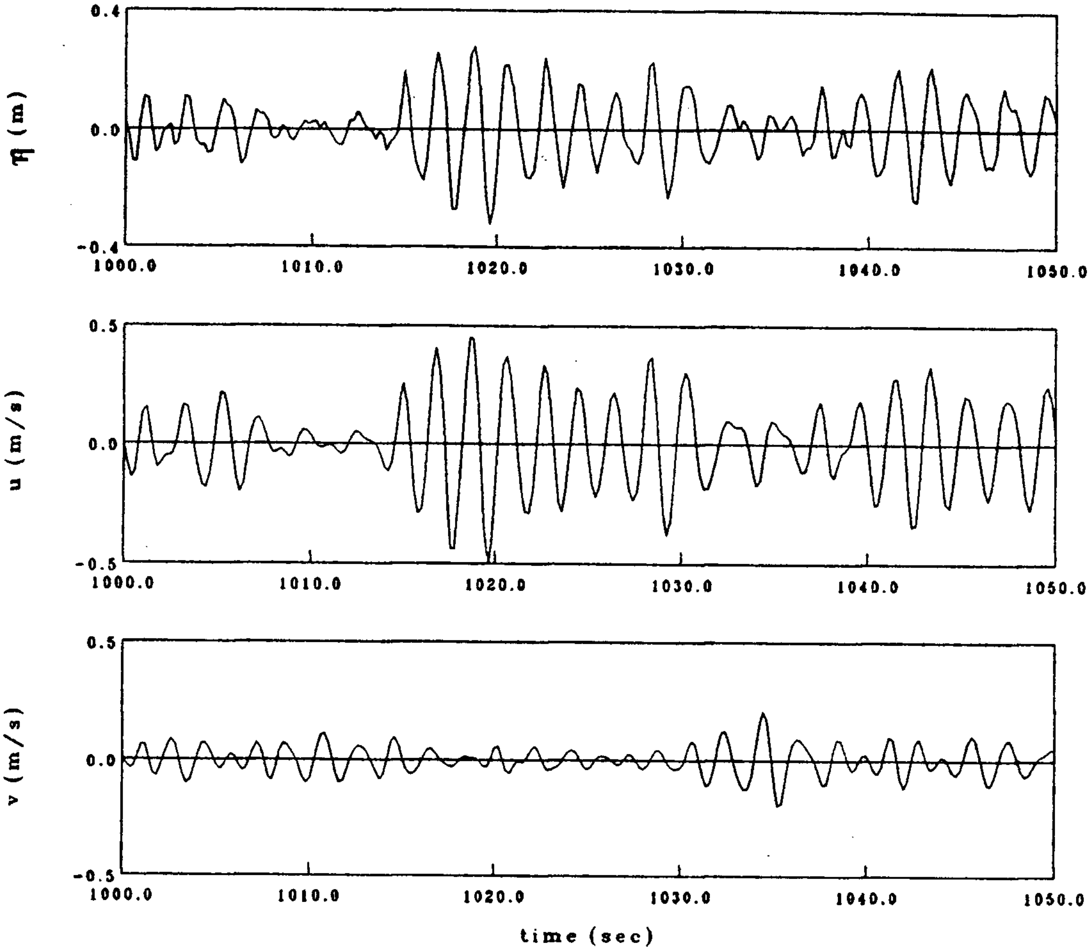

Figure 6.1: Typical time histories of simulated water surface elevation and kinematics

for an elevation of 1.5m above the basin floor in water of 2m depth. Typical time histories of the water surface elevation, inline and transverse velocities are shown in figure 6.1 for a 50s interval. The simulated long-crested and short-crested sea states have an identical water surface elevation time series, but different kinematics due to directional spreading. The synthesized water surface elevation time series of a long-crested and short-crested sea state (s = 1) are compared in figure 6.2.

Figure 6.3 shows a comparison of the target and synthesized water surface elevation spectra for the short-crested sea state (s =1). The synthesized spectrum matches the target spectrum quite well. The corresponding spectra of the inline and transverse velocities are shown in figure 6.4. The standard deviation of the transverse velocity σ_v is 58%

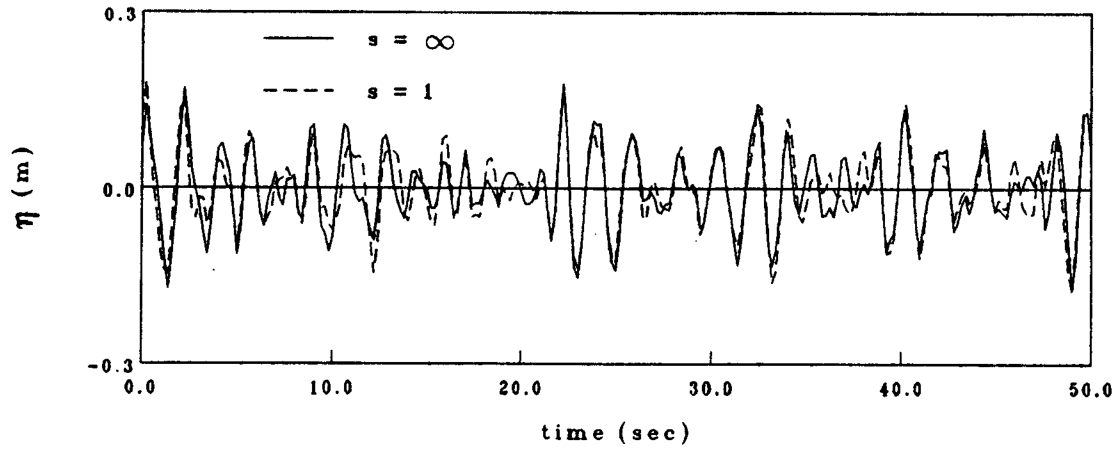

Figure 6.2: Comparison of long-crested and short-crested ($s = 1$) water surface elevation time series

of the standard deviation of the inline velocity σ_u for this particular degree of spreading.

The directional wave analysis methods require an estimate of the cross-spectral density matrix. The matrix is obtained from an FFT analysis of the synthesized elevation and velocity time series. The FFT spectral estimates were smoothed over frequency bands of width 0.02Hz, in order to match the bandwidth used in the synthesis. For 8192 data points, this corresponds to 128 chi-squared degrees of freedom.

The cross-spectral density matrix of the simulated multi-directional sea states was used in the Fourier series method to estimate directional spreading functions at each frequency band. Figures 6.5 and 6.6 show a comparison of the target and truncated Fourier series estimated spreading functions at the peak frequency for $s = 1$ and $s = 20$ respectively. No smoothing function was applied to ensure a positive directional distribution, so the Fourier method yields spurious second peaks with negative values. The use of a smoothing function results in further loss of directional resolution since it acts as a fixed window, unable to adapt to different data. The Fourier method is also unable to adequately resolve the sharp peaked distribution ($s = 20$). Even though only five Fourier coefficients can be estimated from measurements of η, u, and v, use

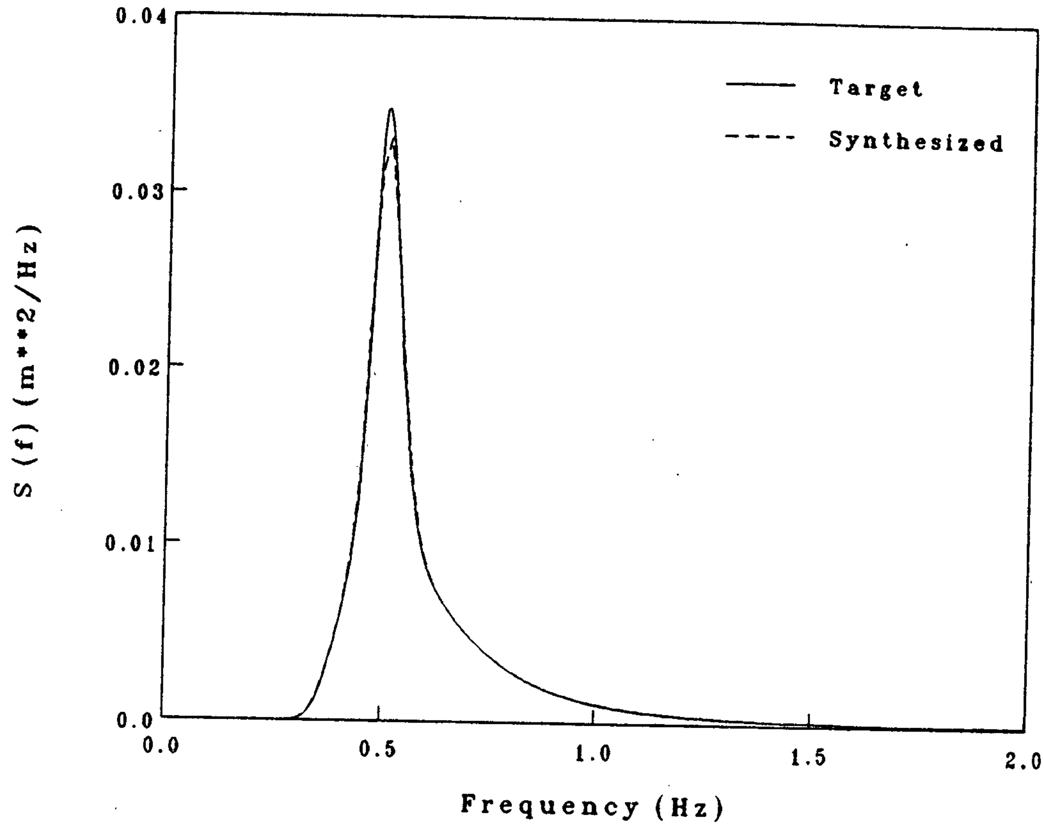

Figure 6.3: Comparison of target and synthesized water surface elevation spectra (f_p = 0.5Hz, H_{m0} = 0.3m)

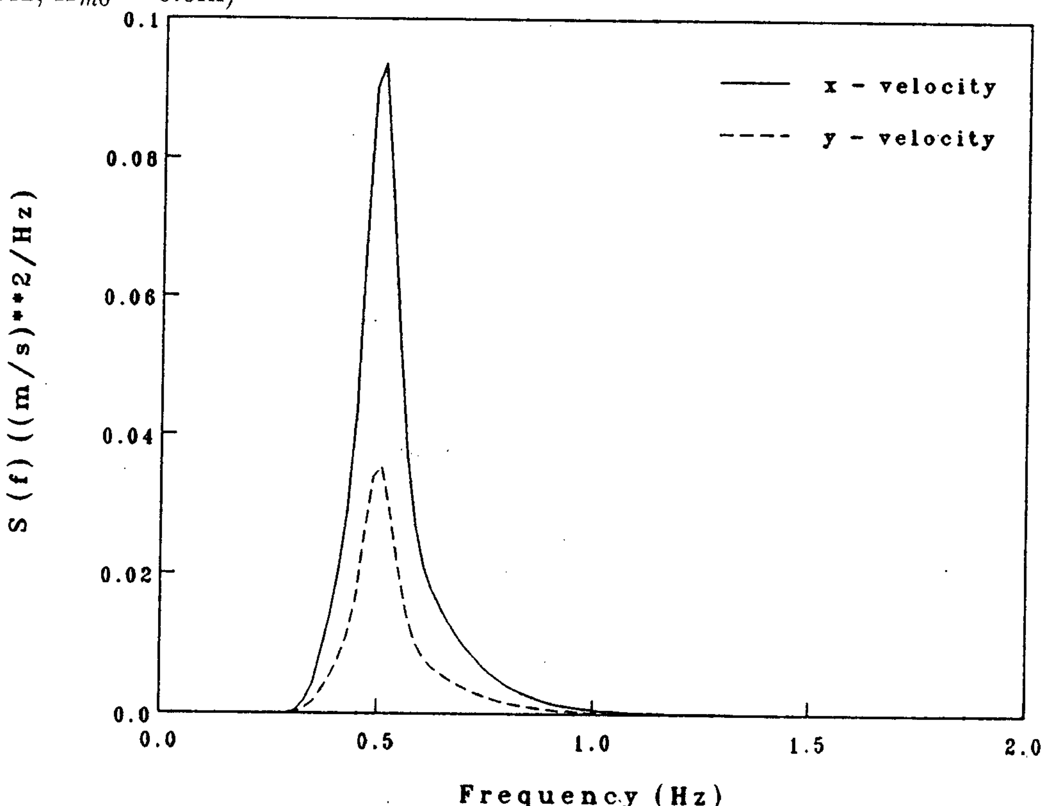

Figure 6.4: Inline and transverse velocity spectra in short-crested seas (s = 1)

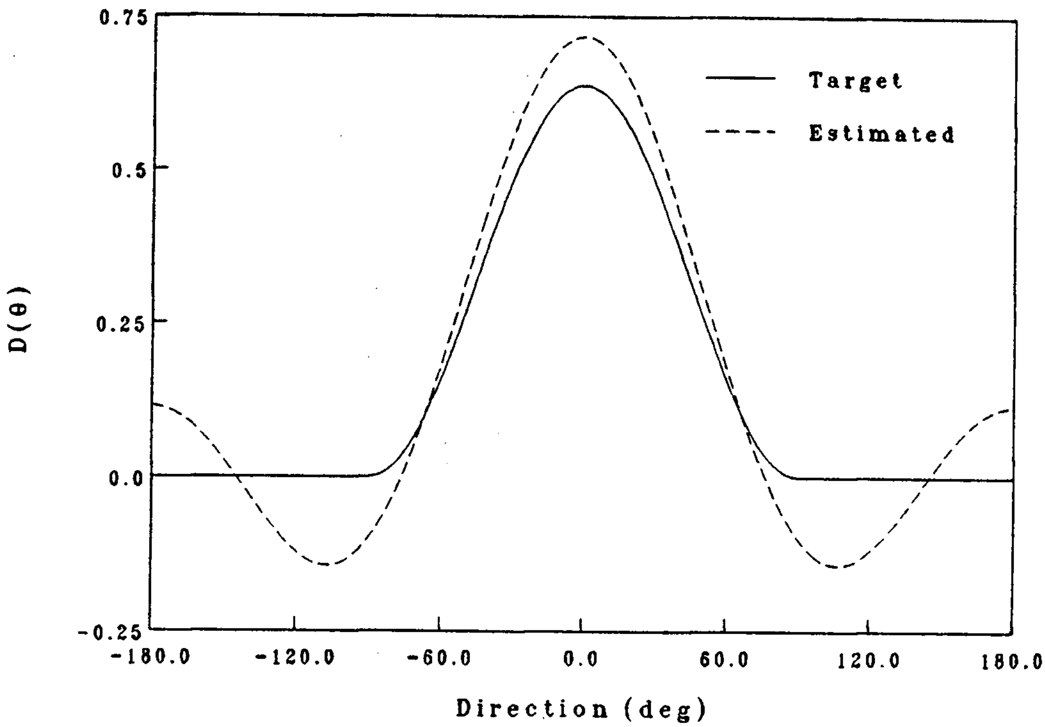

Figure 6.5: Comparison of target and Fourier estimated directional spreading functions (f = f_p, $s = 1$)

of additional measurement quantities improves the resolution marginally. The Fourier method can thus be seen as inadequate for most directional wave analysis needs.

The MLM and MEM provide better directional resolution using the limited amount of information available from the measured quantities. While the MLM has found widespread use, the application of the MEM to directional wave analysis is relatively new. The MEM however offers the best directional resolution from all the presently available tools. The MEM estimated distribution maximizes the entropy associated with the distribution, subject to constraints imposed by the relationship between the cross-spectral density matrix and the directional spreading function (equation (2.25)). The constraints are similar to circular moments of a distribution.

Figure 6.7 to 6.9 show the target, MEM, and MLM estimated directional spreading functions at the peak frequency for s = 1, 5, and 20 respectively. The corresponding MEM estimated directional wave spectra for $s = 1$ and $s = 20$ are shown in figures 6.10

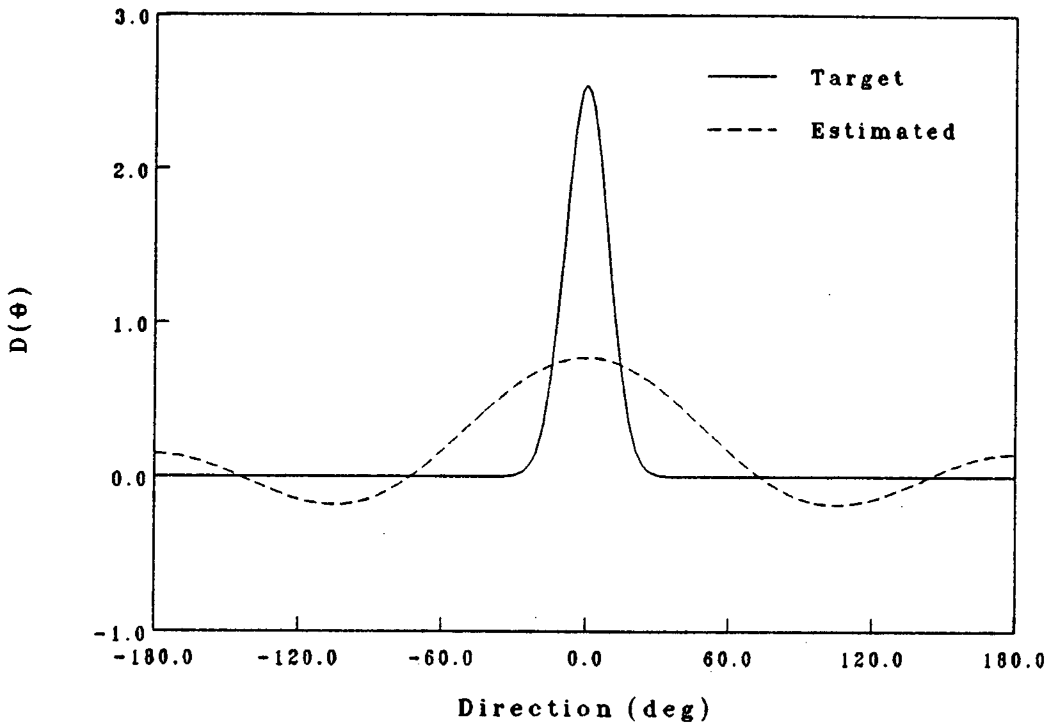

Figure 6.6: Comparison of target and Fourier estimated directional spreading functions (f = f_p, $s = 20$)

and 6.11. It can be seen from figures 6.7 to 6.9 that the MEM estimate matches the target distribution most closely.

The MLM always estimates wider distributions because it does not have to satisfy the constraints imposed by the relationship between the directional spreading function and the cross-spectral density matrix. The MEM estimate is however forced to satisfy that relationship. The slight differences between the MEM estimate and the target distribution are due to errors introduced in the estimation of the cross-spectral density matrix components from the finite record length time series. If a direct integration of equation (2.25) is used to obtain the cross-spectral density matrix, the MEM and target distributions become virtually indistinguishable for $s \geq 3$.

The mean direction of wave propagation $\overline{\theta}$, and standard deviation of the directional distribution σ_θ can be used to compare the target and estimated spreading functions at other frequency bands without actually plotting the distributions. The quantities $\overline{\theta}$ and

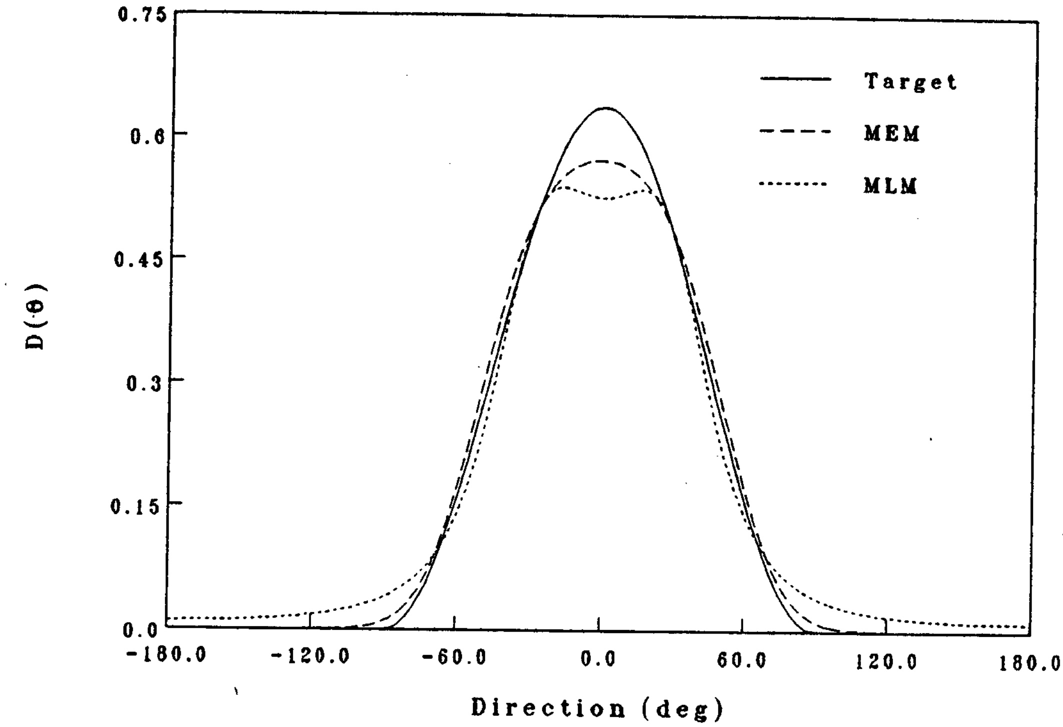

Figure 6.7: Comparison of target, MLM, MEM estimated directional spreading functions (f = f_p, $s = 1$)

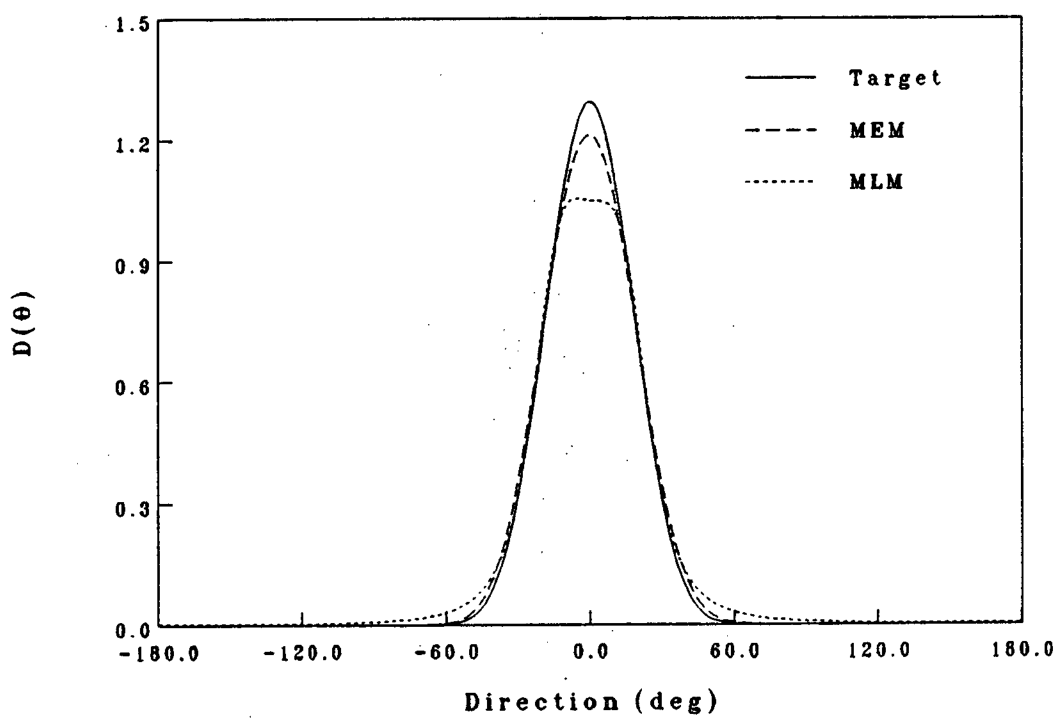

Figure 6.8: Comparison of target, MLM, MEM estimated directional spreading functions (f = f_p, $s = 5$)

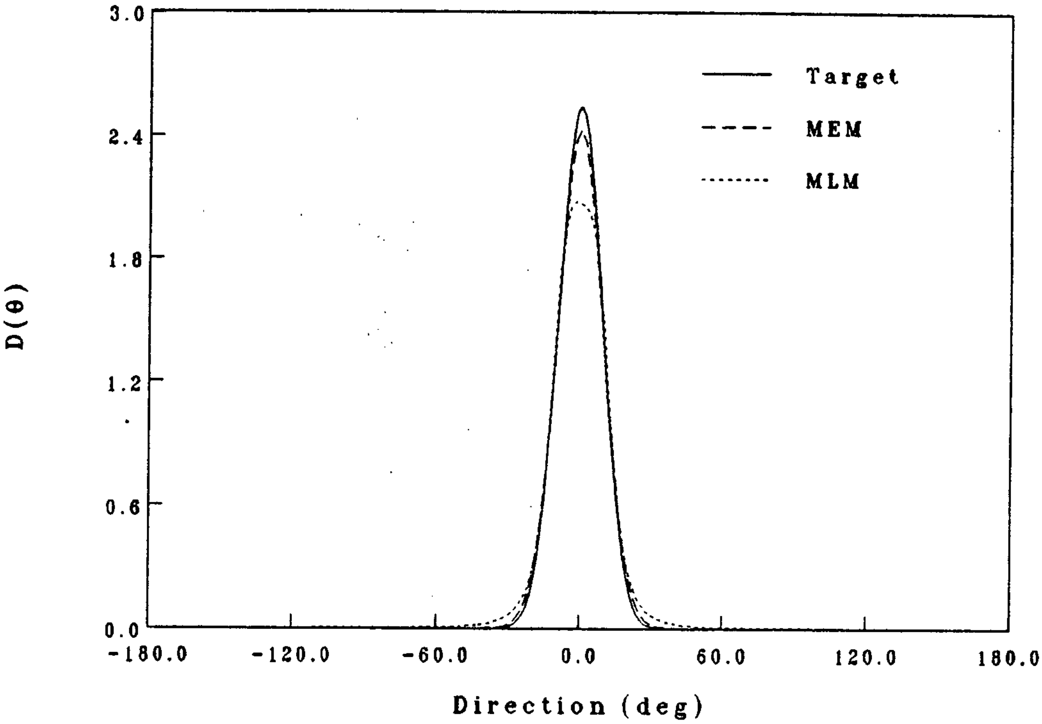

Figure 6.9: Comparison of target, MLM, MEM estimated directional spreading functions (f = f_p, s = 20)

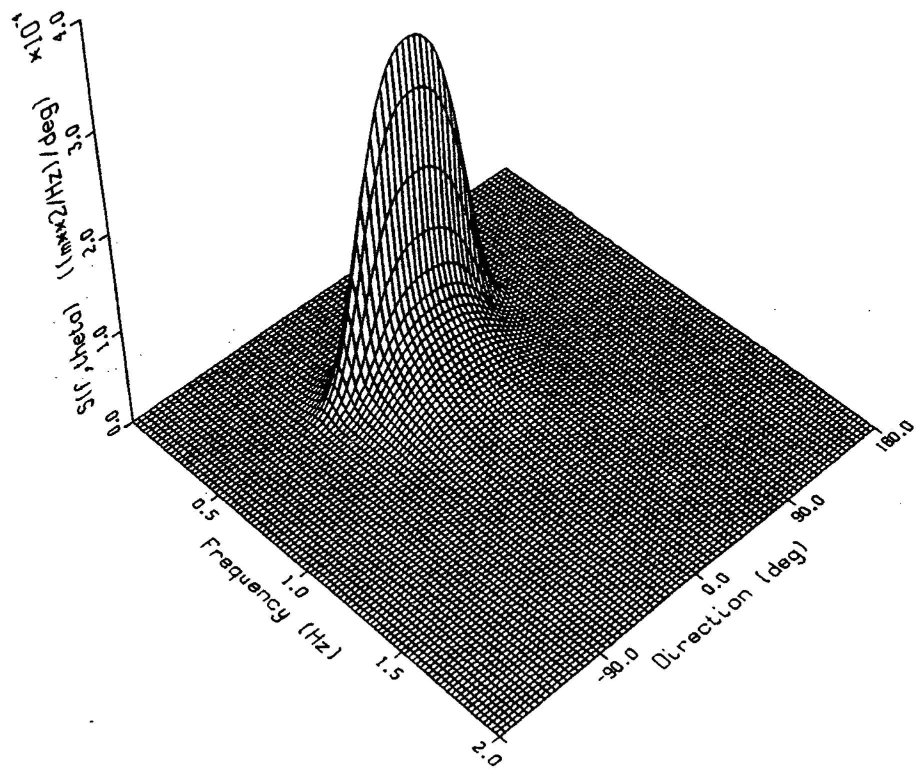

Figure 6.10: MEM estimated directional wave spectrum (s = 1)

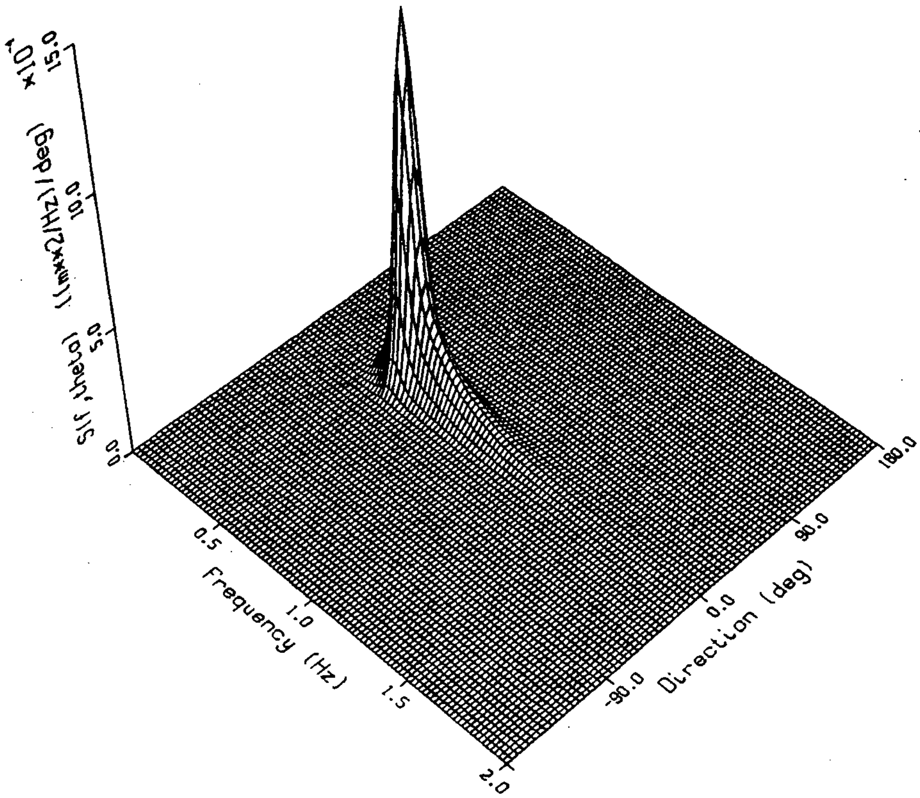

Figure 6.11: MEM estimated directional wave spectrum ($s = 20$)

σ_θ are defined as

$$\overline{\theta}(\omega) = \int_{-\pi}^{\pi} D(\omega,\theta)\,\theta\,d\theta \tag{6.1}$$

$$\sigma_\theta^2(\omega) = \int_{\overline{\theta}-\pi/2}^{\overline{\theta}+\pi/2} D(\omega,\theta)(\theta-\overline{\theta})^2\,d\theta \tag{6.2}$$

The standard deviation of the directional distribution provides an indication of the degree of directional spreading, and is inversely related to the spreading index s, as shown in Figure 6.12. As the value of σ_θ increases, the distributions become broader.

Figure 6.13 shows the mean direction of the MLM, and MEM estimated distributions as a function of frequency for the case $s = 5$. Both methods estimate the mean direction accurately with deviations from the expected value of less than 0.1°. The standard deviation of the estimated distributions are plotted against frequency in figure 6.14. The standard deviation of a $\cos^{10}\theta$ distribution is 17.25°. The MEM and MLM estimated distributions have standard deviations of 18.4° and 21.4° at the peak frequency respec-

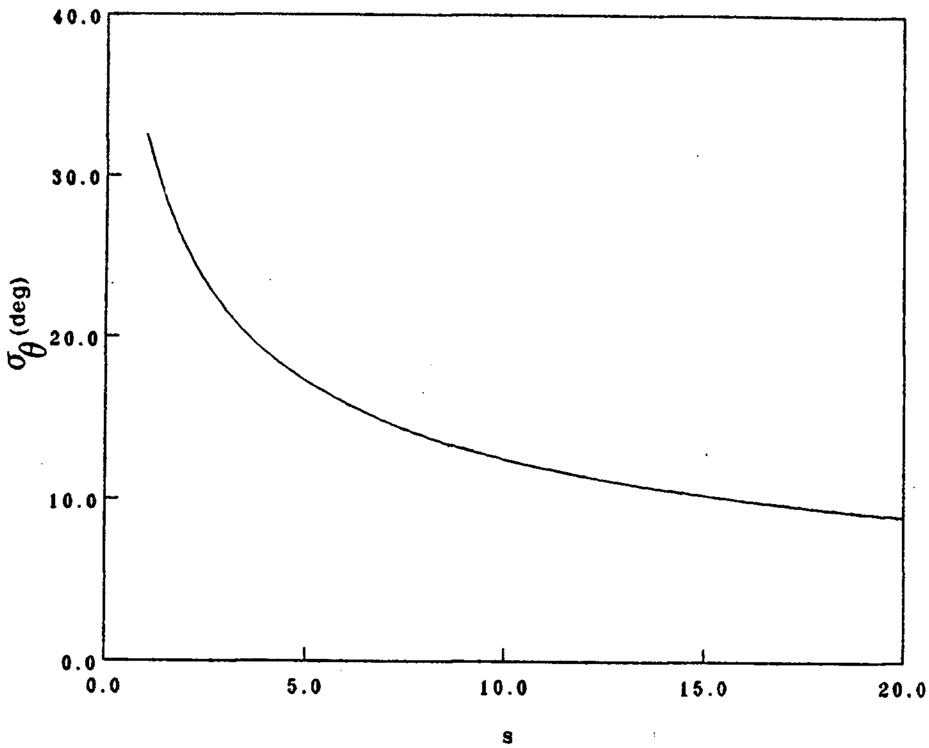

Figure 6.12: Relationship between spreading index, s, and standard deviation σ_θ

tively. The higher standard deviation of the MLM distribution confirms the broadness of the distribution, relative to the target.

The MEM yielded the best directional estimate over the entire frequency range for all the sea states tested. The only drawback of the MEM is that it is an iterative procedure and does not converge for very narrow spreading functions. The MEM procedure as presently implemented was able to converge for s values as high as 50, which is essentially long-crested for most practical purposes.

Most current meters used in laboratory wave basins have a relatively high level of noise present in the signals. The effect of noise on the directional resolution of the MEM was investigated by adding bandwidth limited white noise with constant spectral density from zero to the Nyquist frequency to the synthesized time series. The Nyquist frequency, f_N, is defined as

$$f_N = \frac{1}{2\Delta t} \tag{6.3}$$

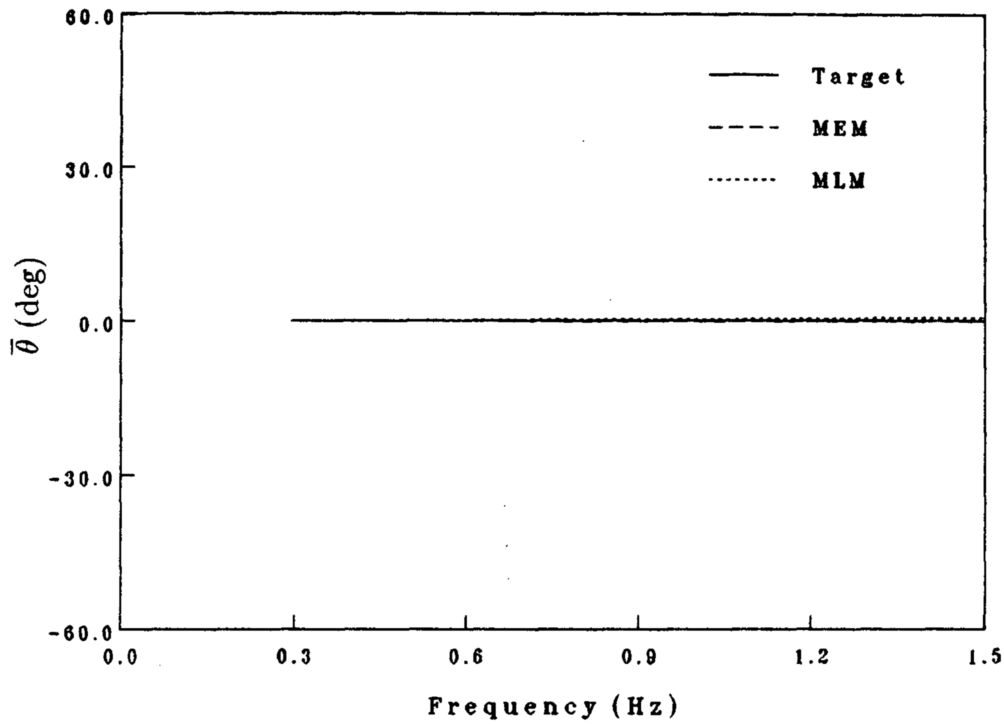

Figure 6.13: Comparison of target, MLM, and MEM estimated mean directions of wave propagation ($s = 5$)

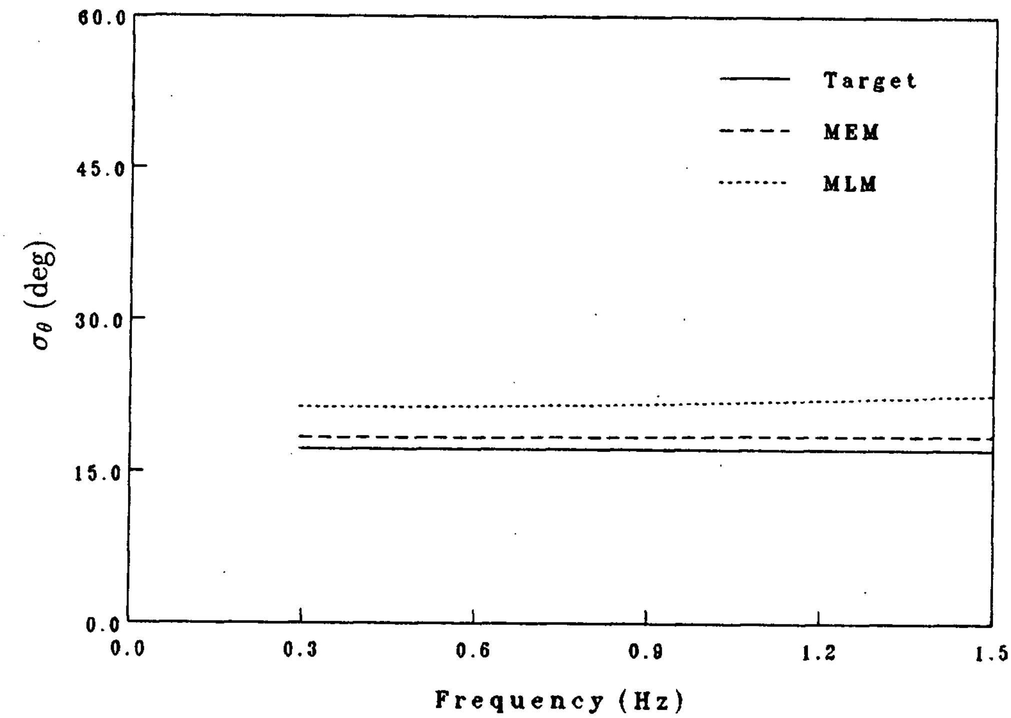

Figure 6.14: Comparison of standard deviations of target, MLM, and MEM directional distributions ($s = 5$)

where Δt is the time interval of the time series. The root mean square (rms) noise amplitude is set equal to a specified percentage of the rms amplitude of the elevation or velocity data. The time series of the noise component is then generated by an inverse FFT of the noise spectrum using the random phase method. Different random seeds were used for the water surface elevation and velocity data in order to make the different signals uncorrelated.

Figure 6.15 shows the mean direction obtained by the MEM for the case $s = 5$ with 0%, 10%, and 20% noise. It can be seen that at the low and high frequency ends of the spectrum, the estimated mean direction starts to deviate significantly from the expected value. This is because the noise to signal ratio is higher at the ends of the spectrum where there is little wave energy. This affects the cross-spectral density matrix estimate at those frequencies and degrades the resolution of the MEM. It can be seen from the velocity spectra (figure 6.4) that there is very little wave energy for $f > 2f_p$ (1.0Hz) and the method cannot be expected to give reasonable results for those frequencies.

The standard deviation of the directional distribution is similarly affected by noise at the low and high frequency ends of the spectrum as shown in figure 6.16. The standard deviation tends to decrease at the higher frequencies, indicating a narrower distribution. The MEM however starts detecting a spurious second peak at 180° for the higher frequencies ($f \geq 2f_p$) . This can be seen in a comparison of the target and estimated distributions at twice the peak frequency (figure 6.17).

There are other multi-directional sea states where the spreading functions have more than one peak. These include wave fields with significant reflection and refraction effects, and sea states with the simultaneous presence of a long distance swell and a local wind generated sea. The analysis methods as presently formulated cannot handle spatially non-homogeneous wave fields such as reflected wave fields. This is because the wave components in such wave fields are correlated, making the relationship between the

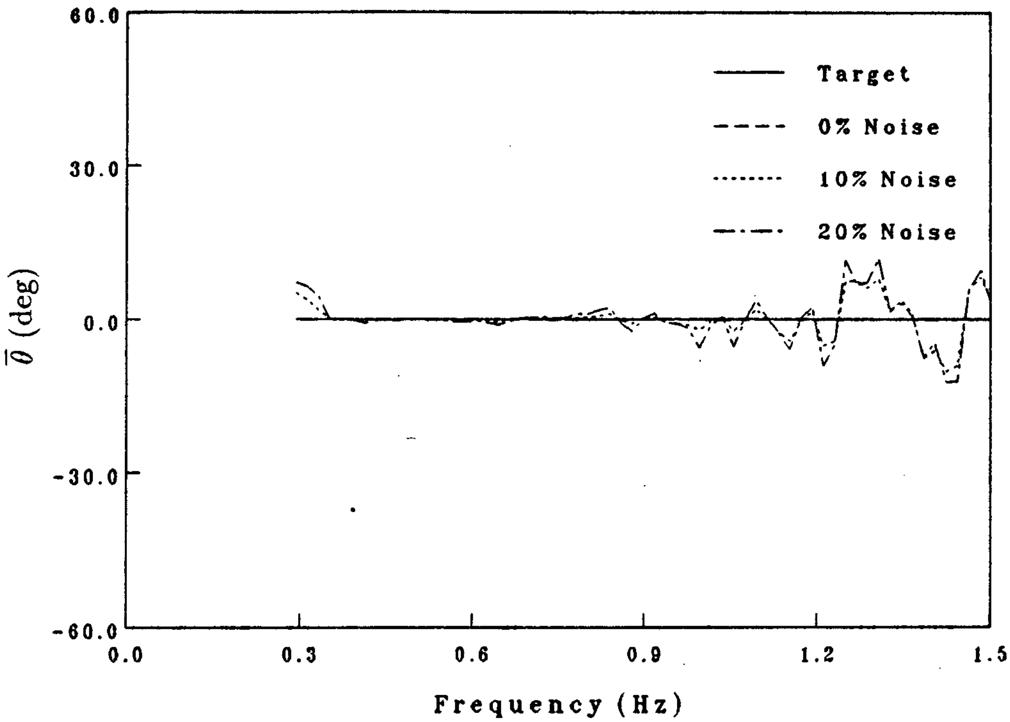

Figure 6.15: Comparison of target and MEM estimated mean directions of wave propagation with noise ($s = 5$)

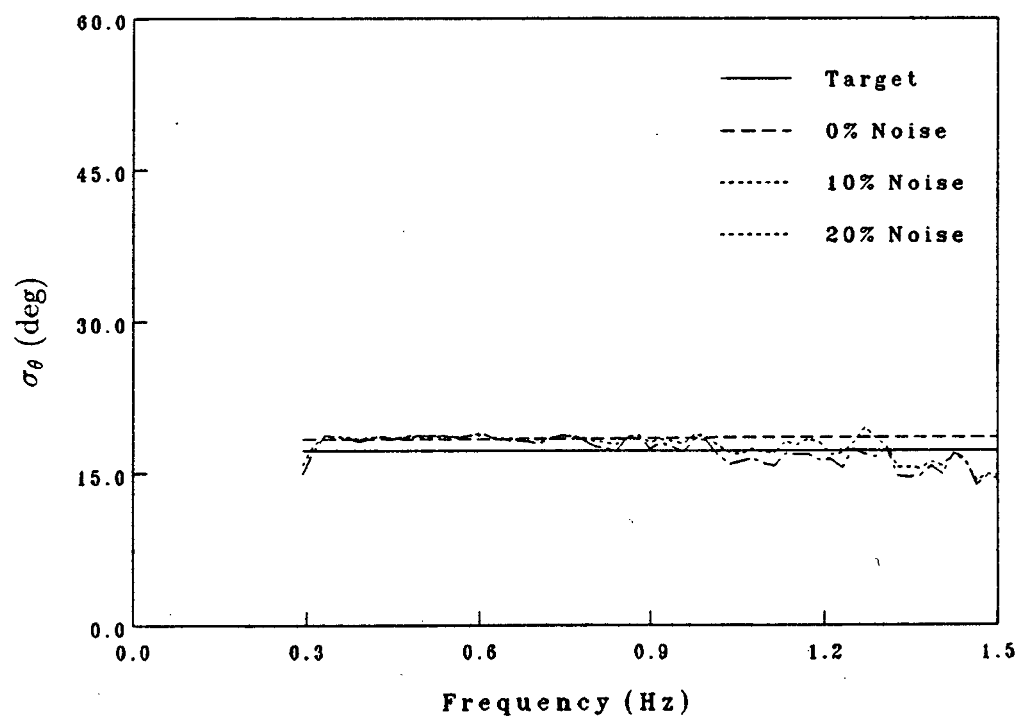

Figure 6.16: Comparison of standard deviations of target and MEM directional distributions with noise ($s = 5$)

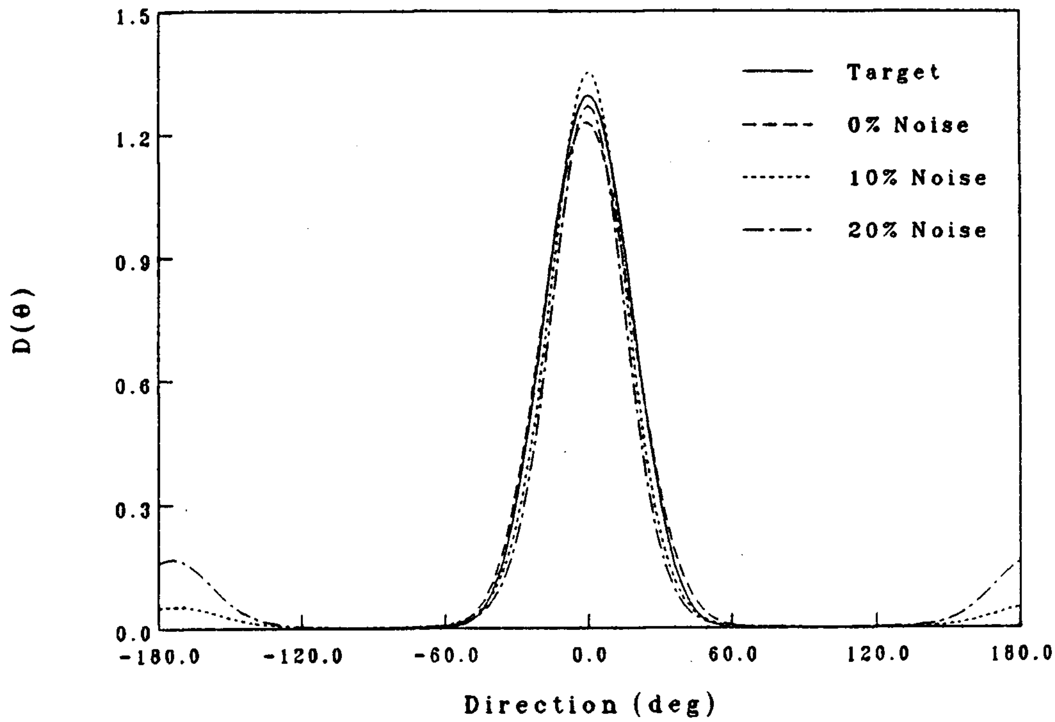

Figure 6.17: Comparison of target and MEM estimated directional spreading functions with noise (f = $2f_p$, $s = 5$)

function and cross-spectral density matrix (equation (2.25)) invalid. Equation (2.25) can however be modified to account for a reflecting boundary (see Isobe and Kondo, 1984), but this case is not dealt with in this thesis.

The resolution of MLM and MEM of bidirectional sea states with totally random phases between all the wave components will now be investigated. Consider a sea-state with the same JONSWAP frequency spectrum as the previous examples where one wave train has $\theta_0 = 90°$ and $s = 5$, while the other one has $\theta_0 = -90°$ and $s = 5$. The frequencies of the two wave trains were interlaced in the synthesis so as to produce a wave field with no correlation between the wave components. Frequency bands of width 0.02Hz were used in the synthesis with 16 wave directions used to approximate the spreading function of each wave train, in each frequency band. Figure 6.18 shows a comparison of the target, MEM, and MLM spreading functions. It can be seen that the MEM distribution is very close to the target while MLM distribution is too broad.

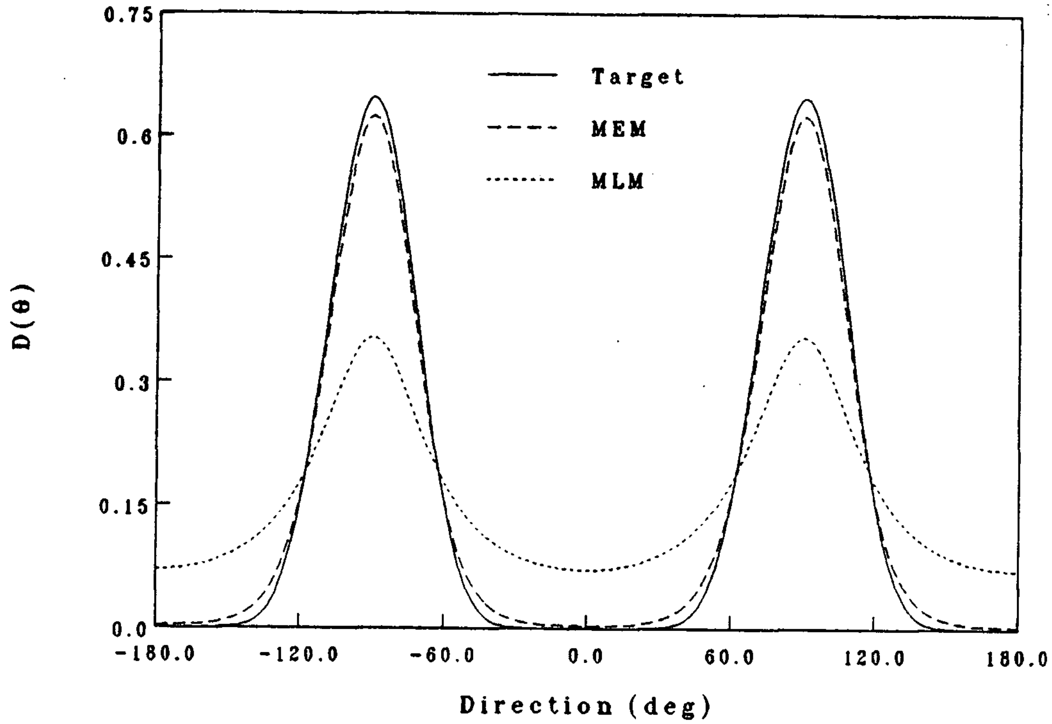

Figure 6.18: Comparison of target, MLM and MEM estimated directional spreading functions for a bidirectional sea state (f = f_p)

The next example considered is a sea state where the principal directions of the two wave trains are no longer as far apart. One wave train has $\theta_0 = 60°$ and $s = 5$, while the other has $\theta_0 = -60°$ and $s = 1$. Figure 6.19 shows a comparison of the target, MEM, and MLM estimated distributions. While the difference between the target and estimated distributions is more pronounced in this case, the MEM is still able to resolve the directionality of the sea state much better than the MLM.

Another bidirectional sea state of interest is one with local sea and swell components. Figure 6.20 shows the directional wave spectrum of a test case with the significant wave height, peak period, spreading index and principal direction of the components given in Table 6.1. Frequency bands of width 0.01Hz were used in the synthesis with 16 angles used to model the spreading function of each wave train in each frequency band. This resulted in time series with record lengths of 3276.8s, at a time interval of 0.4s. Figure 6.21 shows a comparison of the target and synthesized water surface elevation spectra.

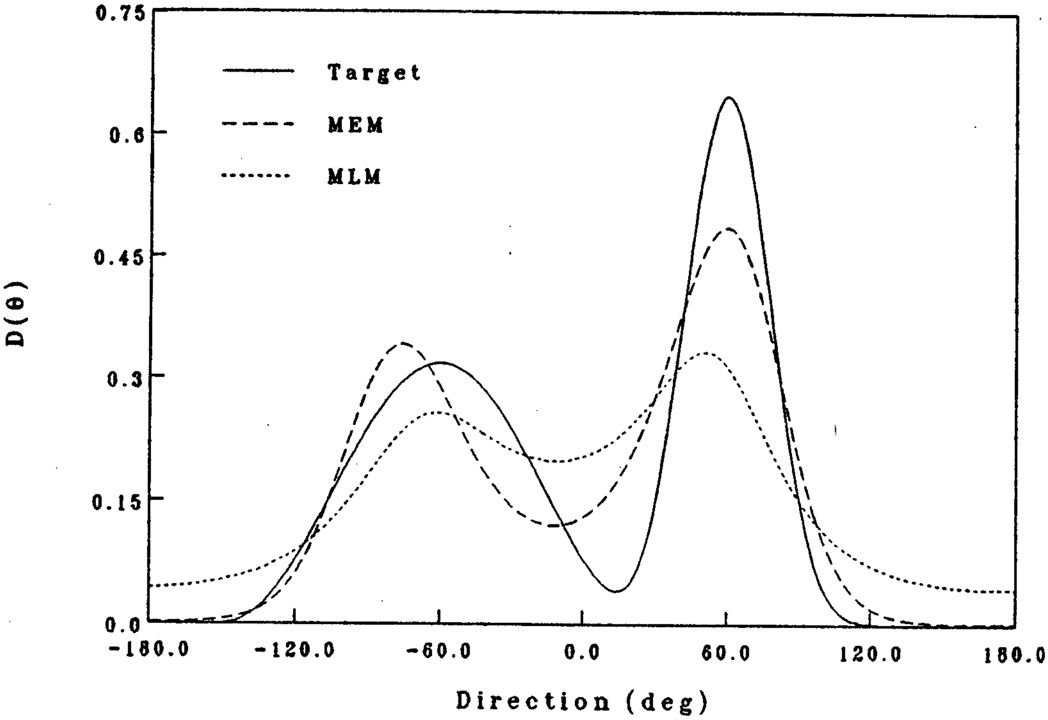

Figure 6.19: Comparison of target, MLM and MEM estimated directional spreading functions for a bidirectional sea state (f = f_p)

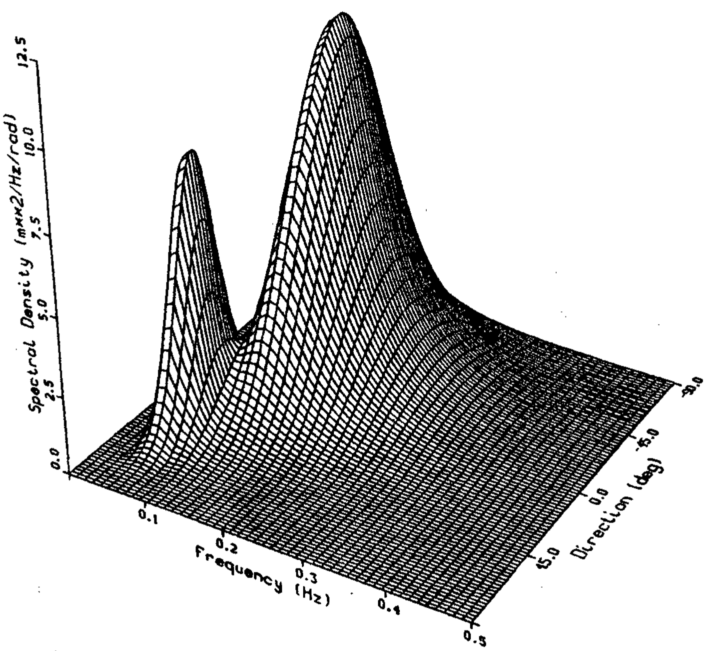

Figure 6.20: Directional wave spectrum of bidirectional sea state

Table 6.1: Characterisitics of simulated bidirectional sea state

	Swell	Local Sea
H_{m0} (m)	2	5
T_p (s)	16	7
s	10	2
θ_0 (deg)	-30	30

The single summation, random phase method of synthesis is seen to reproduce the target bimodal frequency spectrum quite well.

The target, MEM, and MLM estimated directional distributions close to the peak frequencies of the local sea (0.147Hz) and swell (0.068Hz) are shown in figures 6.22 and 6.23 respectively. As expected, the MEM estimate matches target functions better than the MLM at both peak frequencies. Figure 6.24 shows the MEM and MLM estimated spreading functions at an intermediate frequency (0.098Hz). The contributions from local sea and swell are well pronounced at that frequency and the distribution has two peaks.

Finally, the mean and standard deviation of the directional distributions are plotted against frequency in figure 6.25 and 6.26. Both the MLM and MEM estimate the change in the mean direction from $-30°$ at the lower frequencies corresponding to the swell to $30°$ at the higher frequencies of the local sea. The change in the standard deviation of the directional distribution from $12.5°(s = 10)$ to $25.5°(s = 2)$ is also reasonably predicted.

6.1.2 Wave Probe Array

Wave probes used in laboratory basins have a relatively lower noise to signal ratio than current meters. They are also less expensive and easier to calibrate, making them more convenient for use in laboratories for estimating directional wave spectra. The

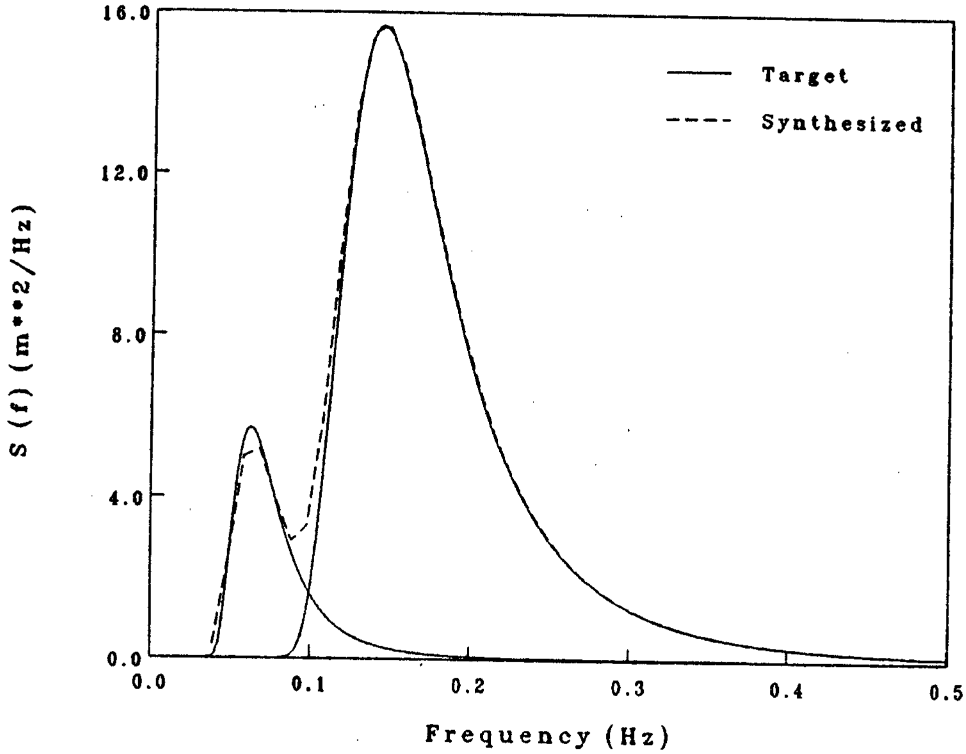

Figure 6.21: Comparison of target and synthesized water surface elevation spectra for bimodal sea state

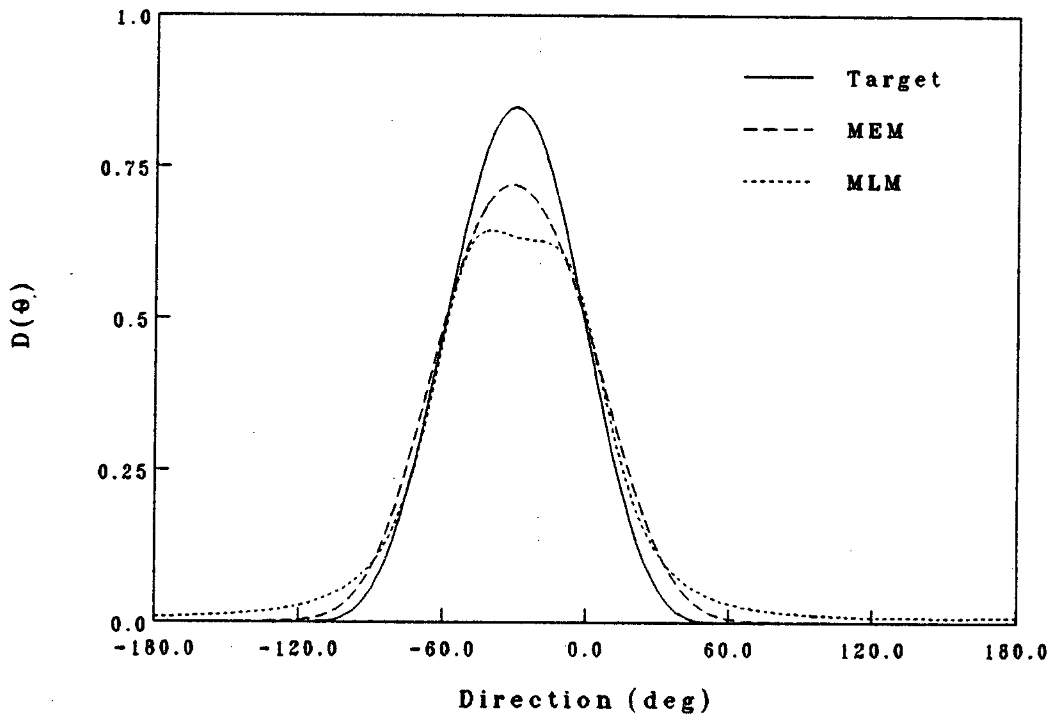

Figure 6.22: Comparison of target, MLM, and MEM estimated directional spreading functions (f = f_p(local sea))

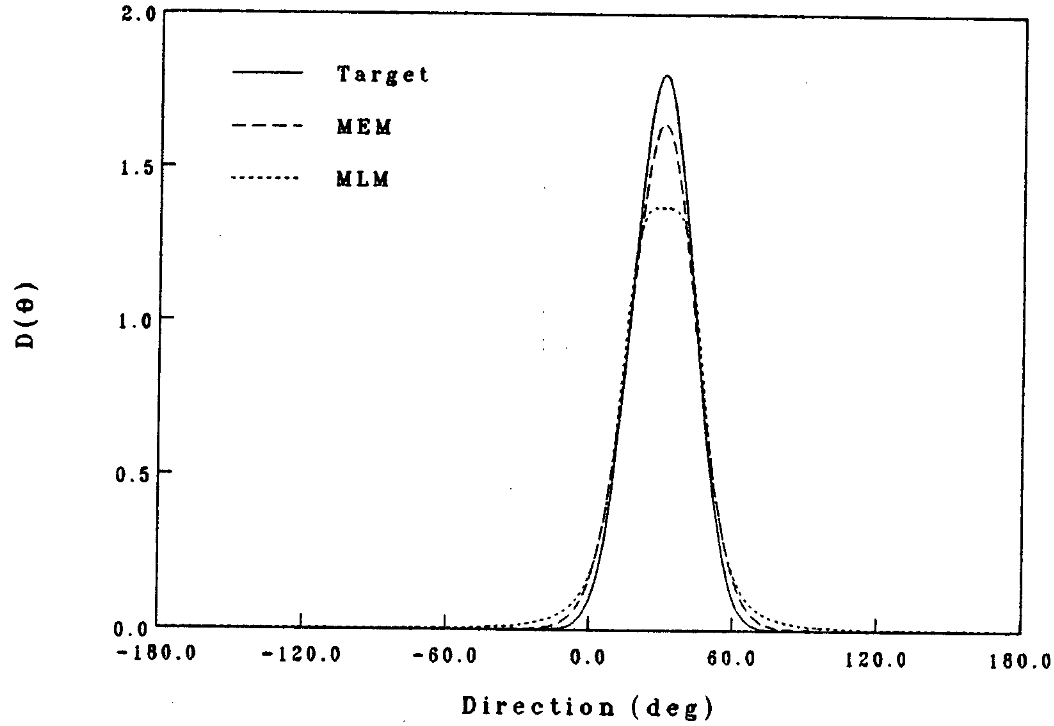

Figure 6.23: Comparison of target, MLM, and MEM estimated directional spreading functions (f = f_p(swell))

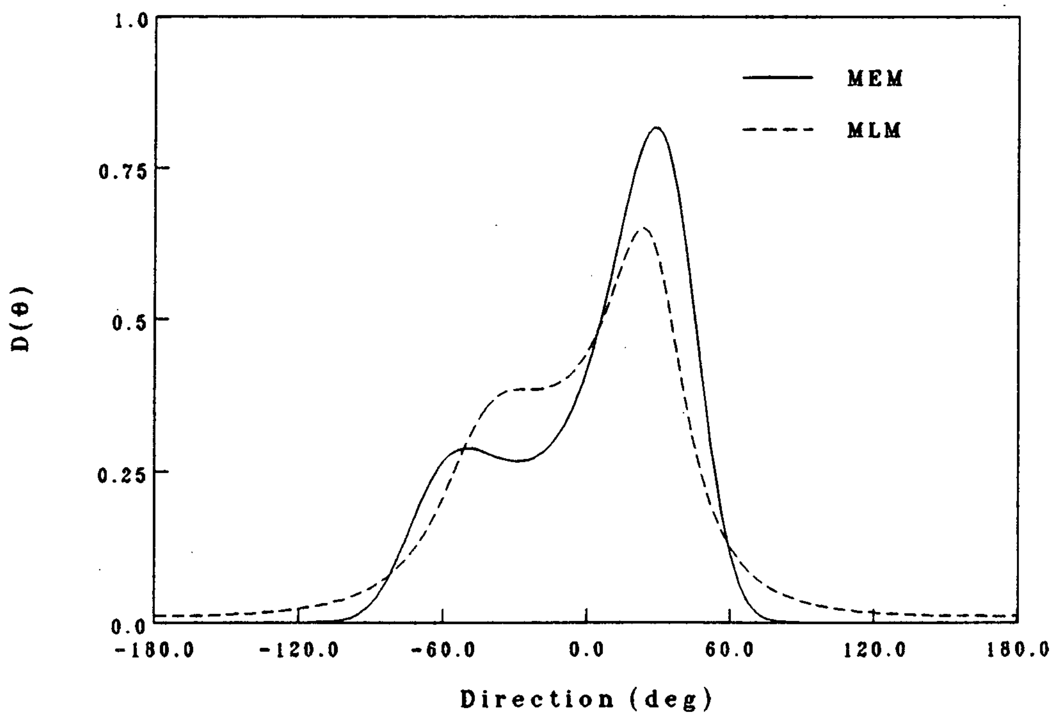

Figure 6.24: Comparison of MLM and MEM estimated directional spreading functions (f = 0.1Hz)

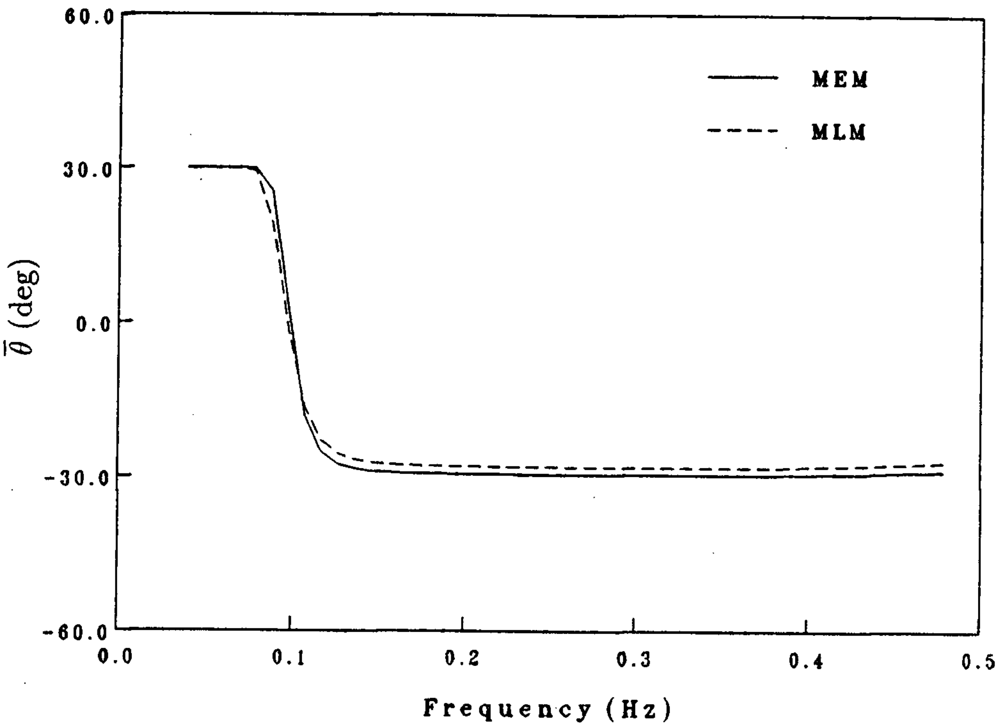

Figure 6.25: Comparison of MLM and MEM estimated mean direction of wave propagation

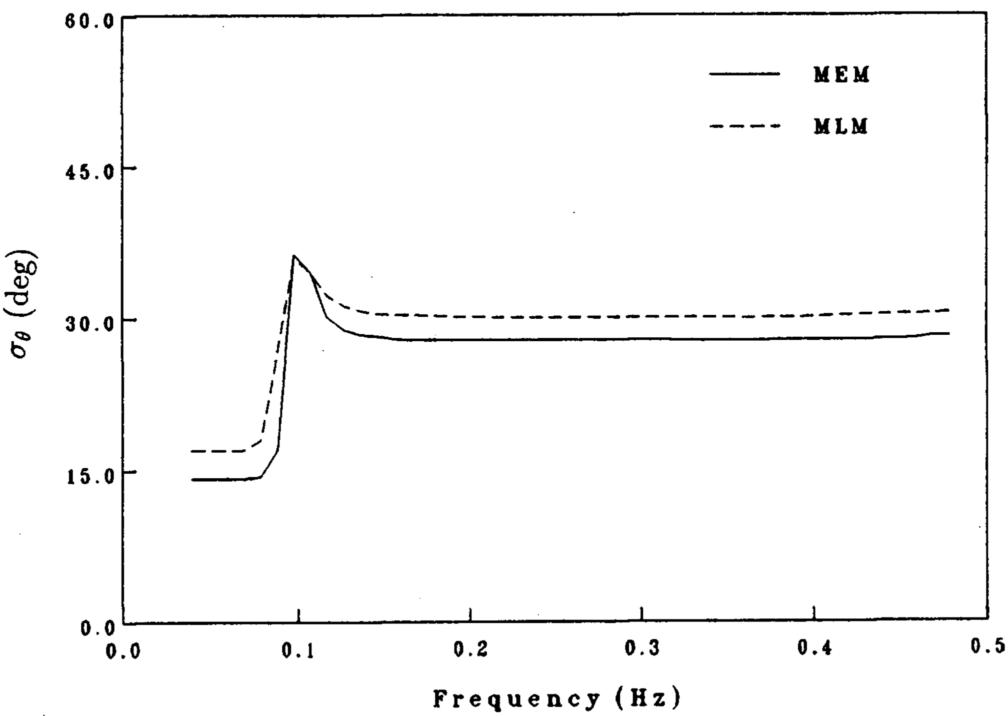

Figure 6.26: Comparison of standard deviations of MLM and MEM directional spreading functions

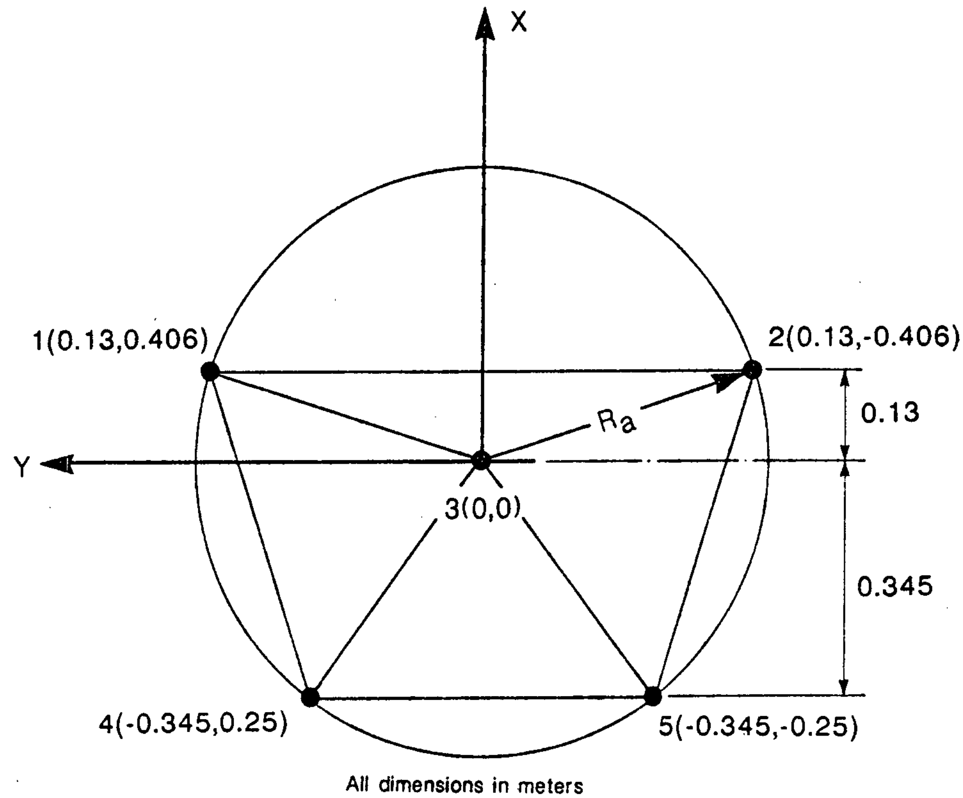

Figure 6.27: Arrangement of five probe array

performance of the MEM and MLM for a wave probe array will now be evaluated using numerically synthesized data.

The random phase method was used to synthesize the water surface elevation time series at five wave probe locations for different multi-directional sea states. The dimensions of the five probe array are given in figure 6.27 and correspond to the inner five probes of the nine probe array used in the laboratory experiments. The test cases used for the wave probe-current meter array were also used for the wave probe array for comparative purposes.

The simulated sea states were described by a JONSWAP spectrum with $f_p = 0.5$Hz, $H_{m0} = 0.3$m, and $\gamma = 3.3$. Figure 6.28 to 6.30 shows a comparison of the target, MEM, and MLM estimated spreading functions at the peak frequency for $s = 1$, 5, and 20 respectively. The estimated distributions from the wave probe array follow the same trend as the wave probe-current meter array with the MLM estimating wider distributions, and

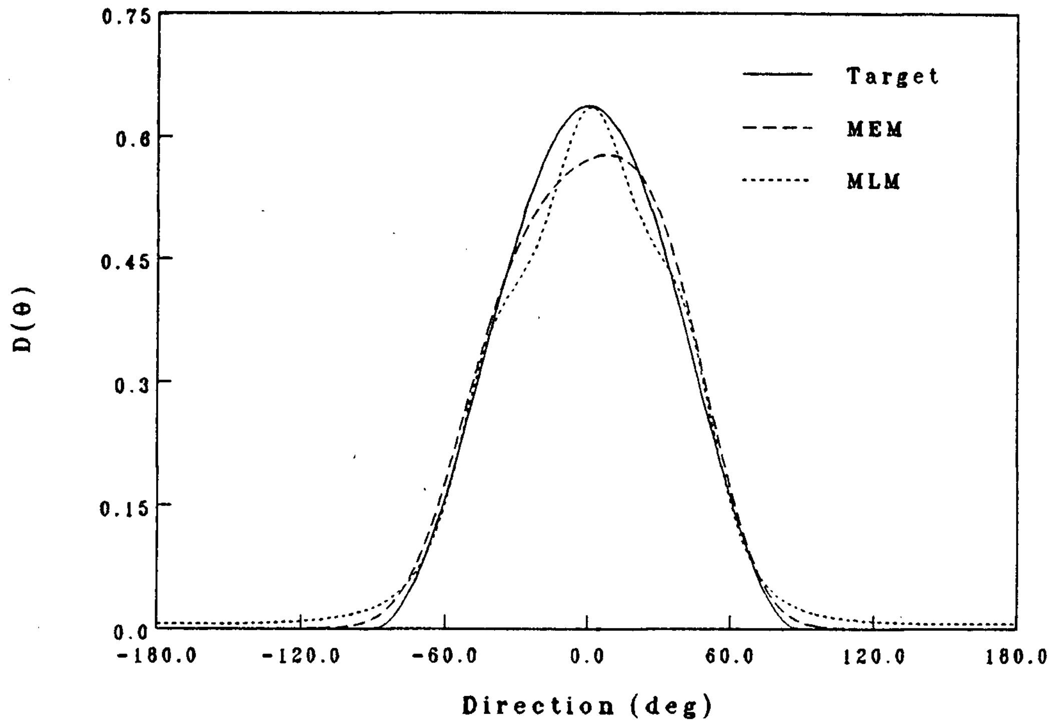

Figure 6.28: Comparison of target, MLM, MEM estimated directional spreading functions (f = f_p, $s = 1$)

the MEM matching the target distributions more closely. In the absence of noise, there is very little difference between the distributions estimated from a wave probe array and a wave probe-current meter array. The differences would however be more pronounced for laboratory data.

The MEM procedure for the wave probe array is more complicated than that for a wave probe-current meter array because of the non-orthogonality of the measurement variables. An eigenvalue analysis is first performed to transform the problem into one with orthogonal variables. Variables with zero eigenvalues are dropped, and questions arise as to the relative importance of the eigenvalues close to zero. If all the non-zero eigenvalues are retained, the procedure becomes unstable for most test cases. A criterion was used to select the number of 'important' eigenvalues based on the ratio of each eigenvalue to the maximum eigenvalue. This however led to some convergence problems. Overall, the MEM procedure for a wave probe array worked quite well for most test cases,

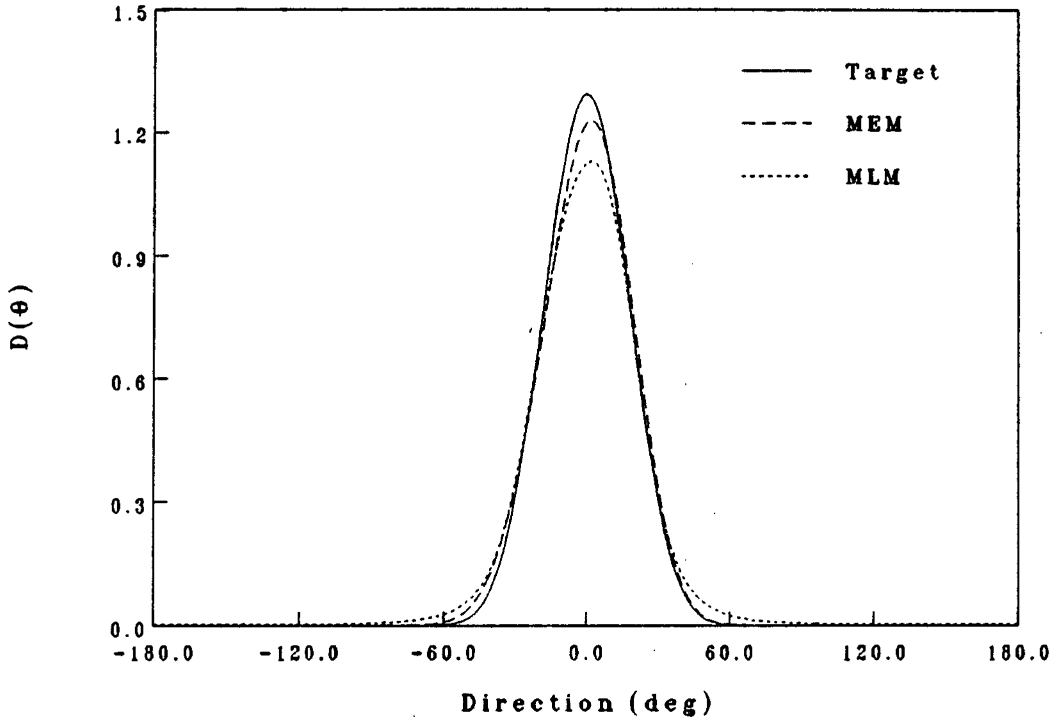

Figure 6.29: Comparison of target, MLM, MEM estimated directional spreading functions (f = f_p, $s = 5$)

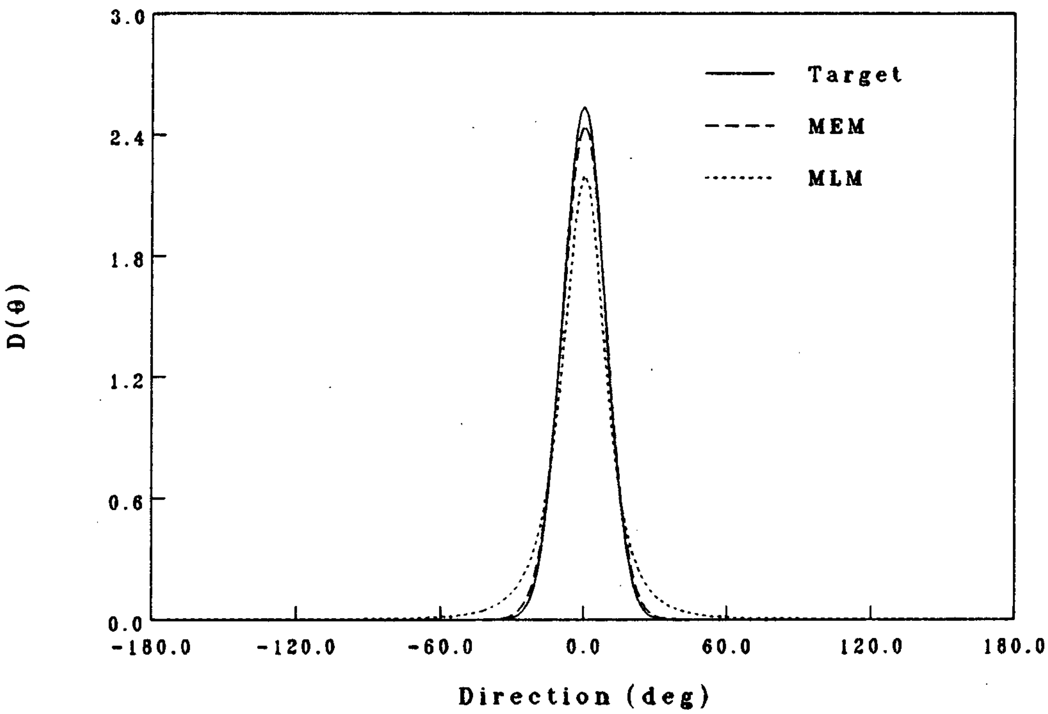

Figure 6.30: Comparison of target, MLM, MEM estimated directional spreading functions (f = f_p, $s = 20$)

but had more convergence problems than the MEM procedure for a wave probe-current meter array.

The effect of changing the array spacing and configuration on the resolution of the MLM and MEM was not investigated in great detail because of the data adaptive nature of the procedures. Both methods optimize the information available from the data in a nonlinear manner and as such are not as sensitive to array spacing and configuration as say the Fourier method would be. In general, it was observed that the CERC five probe array configuration was adequate for the resolution of all the directional sea states tested by the MEM. It is however useful to determine for what range of wavelengths a given array would provide reasonable resolution. On the basis of several test cases, it was determined that the array provided reasonable results when the ratio of the array radius R_a to wavelength was in the range of 0.05 to 0.5 with optimum resolution at a ratio of about 0.15.

6.1.3 Application to Laboratory Data

The maximum entropy method was used to analyze data obtained during the calibration of the waves for the floating barge experiments. The nine probe array with a biaxial current meter under one of the wave probes was use to provide information on the water surface elevation and water particle velocities in the basin.

Attention is now focussed on the sea state described by a JONSWAP spectrum with $H_{m0} = 0.22$m, $f_p = 0.5$Hz, and $\gamma = 3.3$. Multi-directional sea states with target cosine power spreading indices of 1, 3, and 6, and a mean direction $\theta_0 = 0°$ were generated in the basin. Data was sampled at a rate of 10Hz for a duration of 819.2s. The FFT cross-spectral density estimates were smoothed over frequency bands of width 0.02Hz.

Figure 6.31 shows a comparison of the target and measured frequency spectrum at the central probe for the sea state with $s = 1$. The target and measured directional distributions at the peak frequency are plotted in figures 6.32 to 6.34 for $s = 1$, 3, and 6

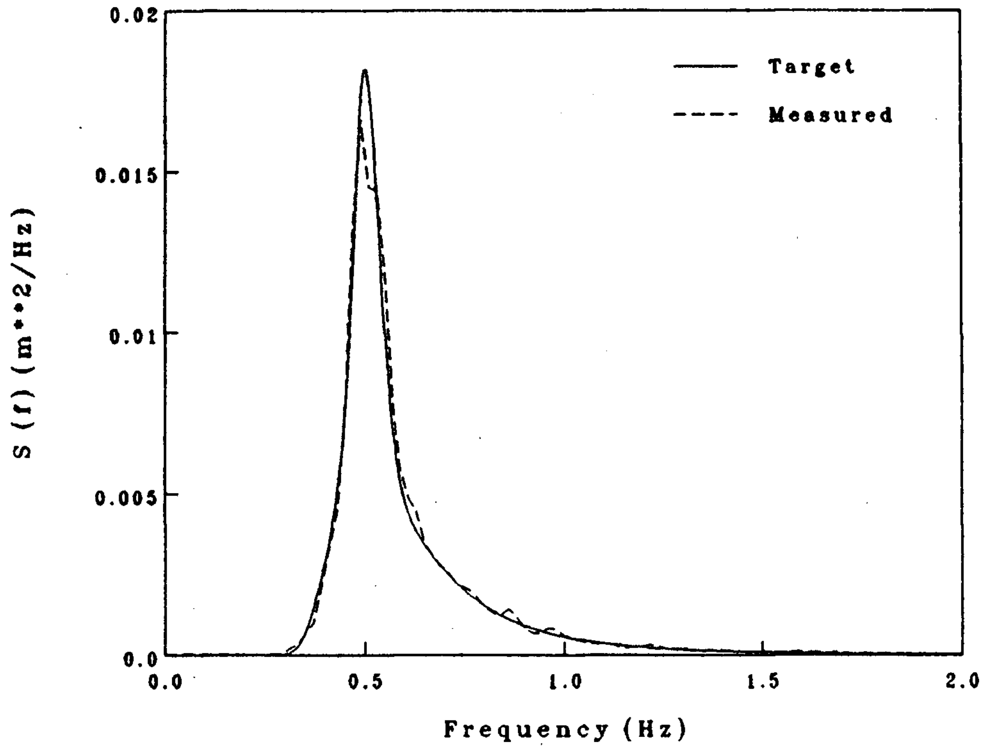

Figure 6.31: Comparison of target and measured water surface elevation spectra (f_p = 0.5Hz, H_{m0} = 0.22m)

respectively. The measured distributions were estimated using data from both the outer four and central probe, and the current meter array. The figures clearly show that the measured directional distributions in the basin were close to the target distributions. The slight shift in the mean directions is probably due to the fact that no careful attempt was made to align either the wave probe array or the current meters with respect to the x axis of the basin. The figures also indicate that there is very little difference between the distributions estimated from the wave probe array and the wave probe - current meter array when the noise level is not significant.

The mean and standard deviation of the directional distribution is plotted against frequency in figures 6.35 and 6.36 for the sea state with $s = 3$. It can be seen that at the higher frequencies, the current meter results start deviating more significantly from the target due to the higher noise to signal ratio at those frequencies.

Finally, a comparison is made of the measured directional distributions at the peak

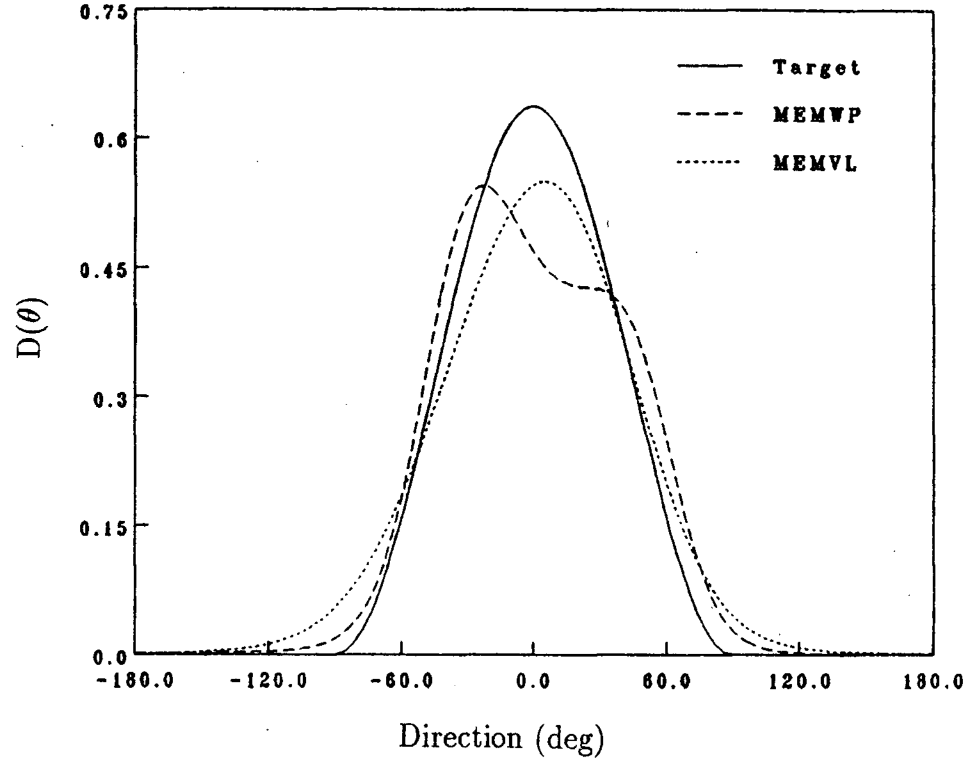

Figure 6.32: Comparison of target and measured directional spreading functions (f = f_p, $s = 1$)

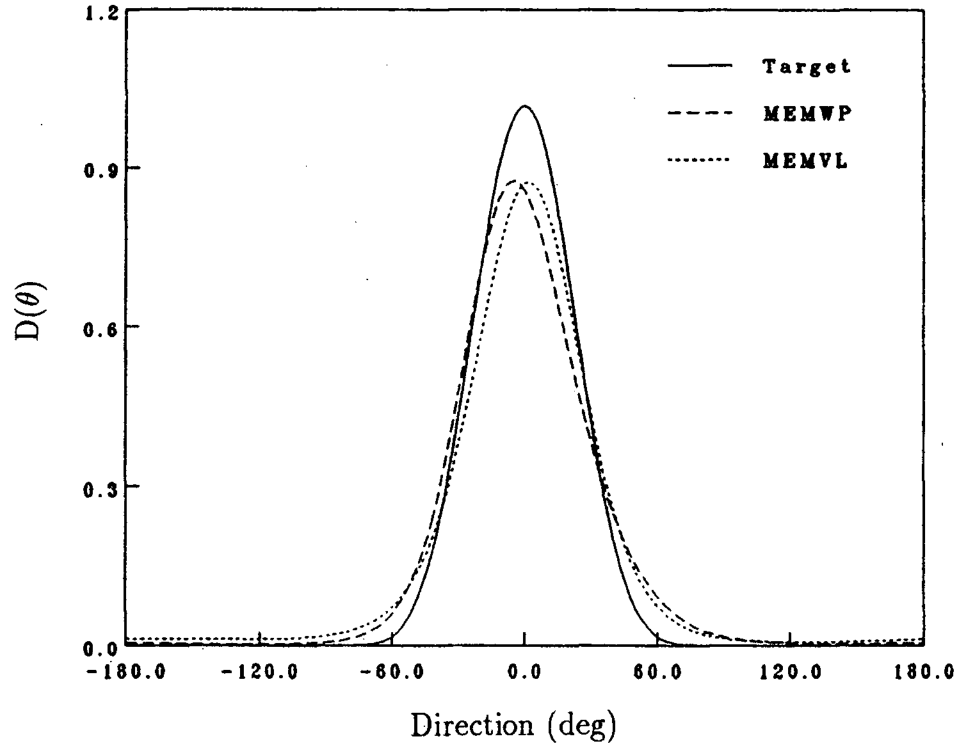

Figure 6.33: Comparison of target and measured directional spreading functions (f = f_p, $s = 3$)

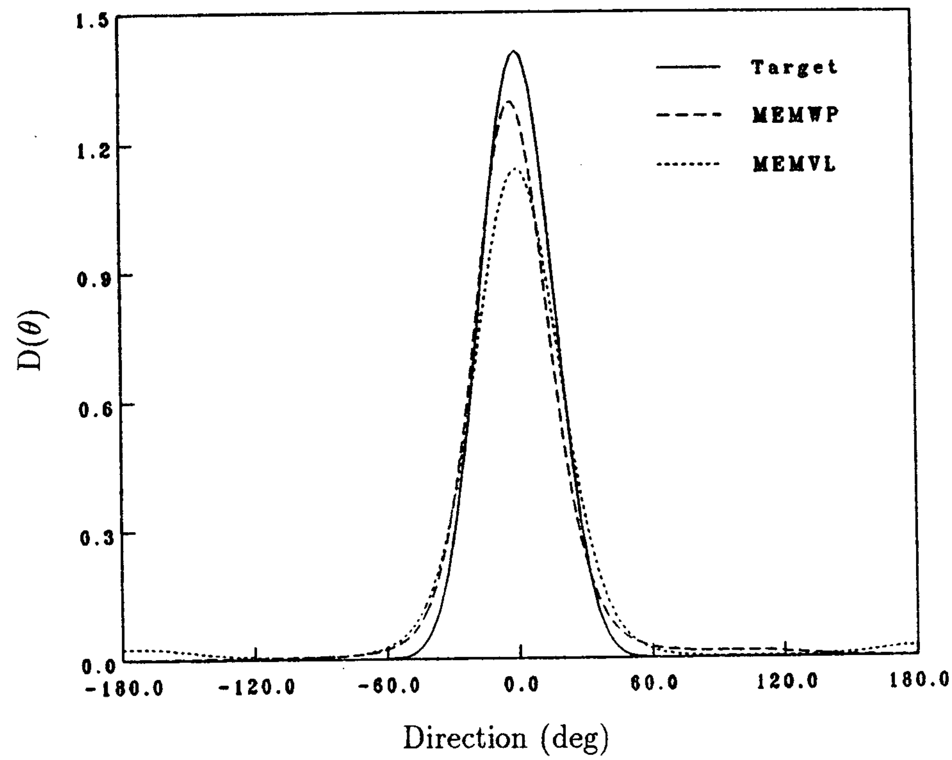

Figure 6.34: Comparison of target and measured directional spreading functions (f = f_p, s = 6)

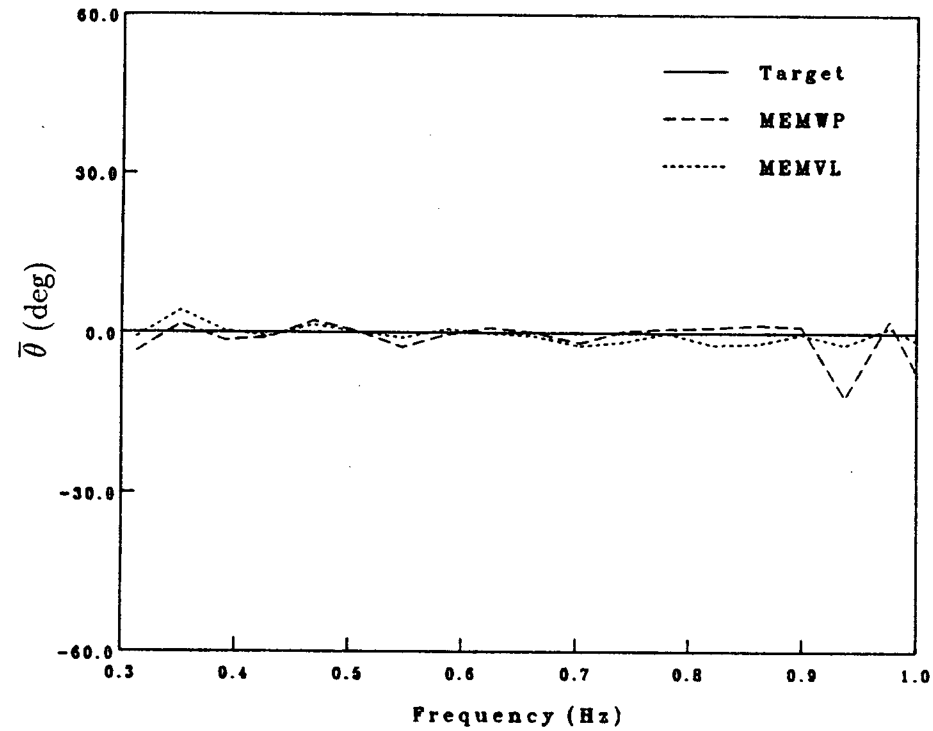

Figure 6.35: Comparison of target and measured mean direction of wave propagation (s = 3)

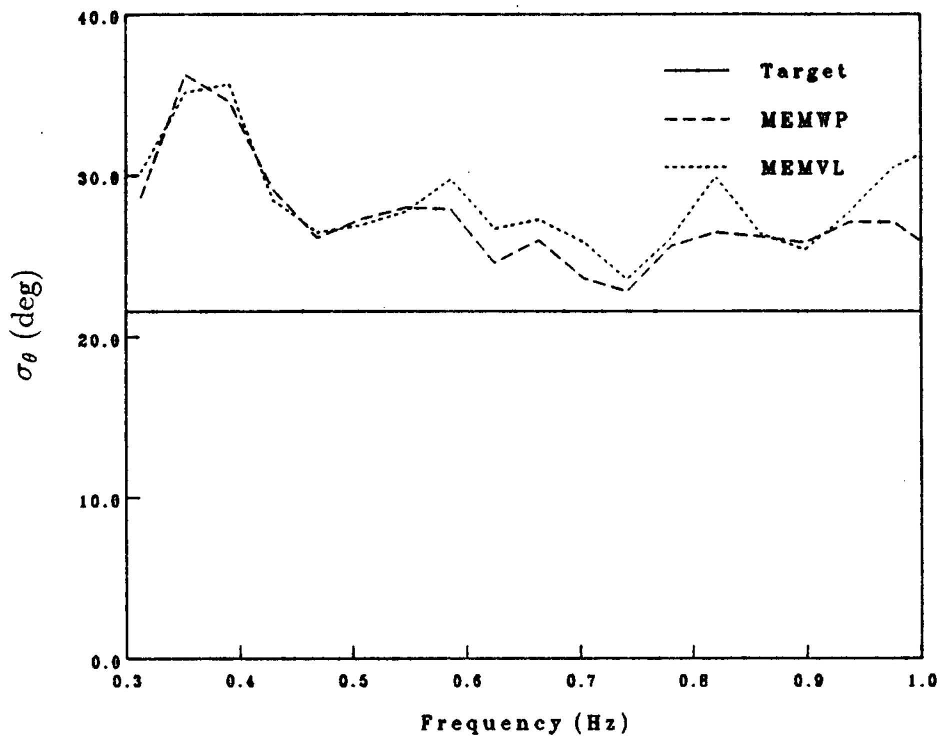

Figure 6.36: Comparison of target and measured spreading function standard deviations ($s = 3$)

frequency using data from five and nine probes respectively. The distributions are shown in figures 6.37 and 6.38 for $s = 3$ and 6. It can be seen that the use of information provided by the additional four probes does not improve the directional resolution of the method. The use of five probes seemed adequate for directional spectra resolution by the maximum entropy method, provided that the ratio of the array radius to wavelength was within the limits previously stated.

6.2 Forces on a Cylinder

The segmented cylinder was tested in random waves described by a Bretschneider spectrum with peak frequencies f_p of 0.33, 0.4, and 0.5Hz. The corresponding significant wave heights were approximately 0.45, 0.40, and 0.32m respectively. One unidirectional and three multi-directional sea states were generated for each spectrum. The water surface elevation, water particle velocities, and wave forces on all 9 segments were sampled

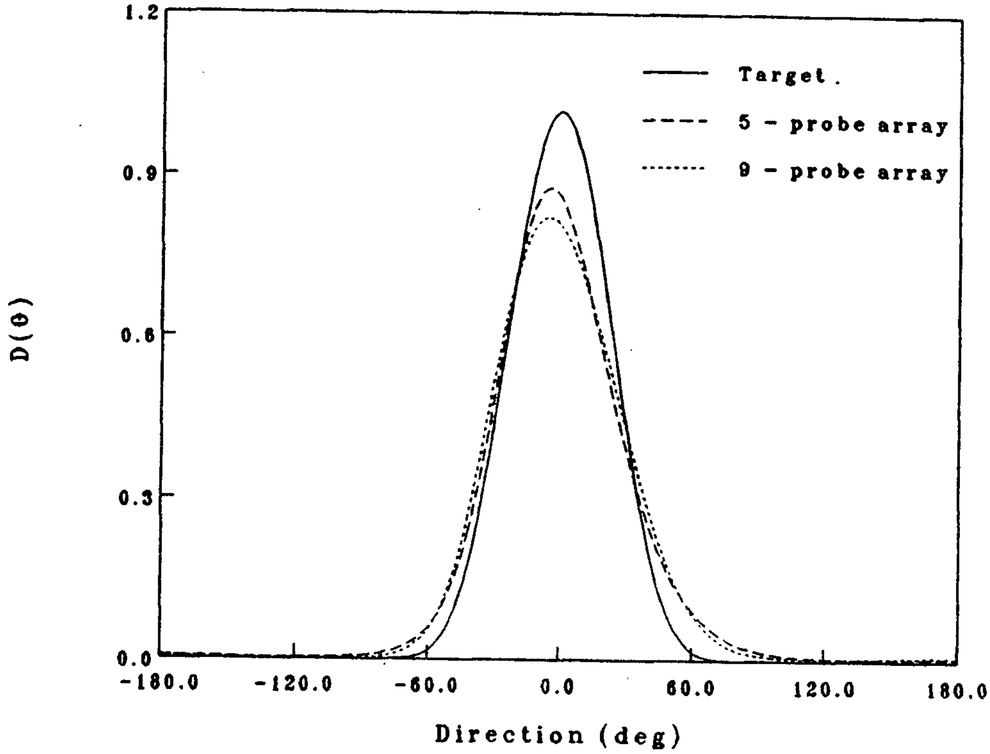

Figure 6.37: Comparison of target and measured directional spreading functions for a five and nine probe array (f = f_p, s = 3)

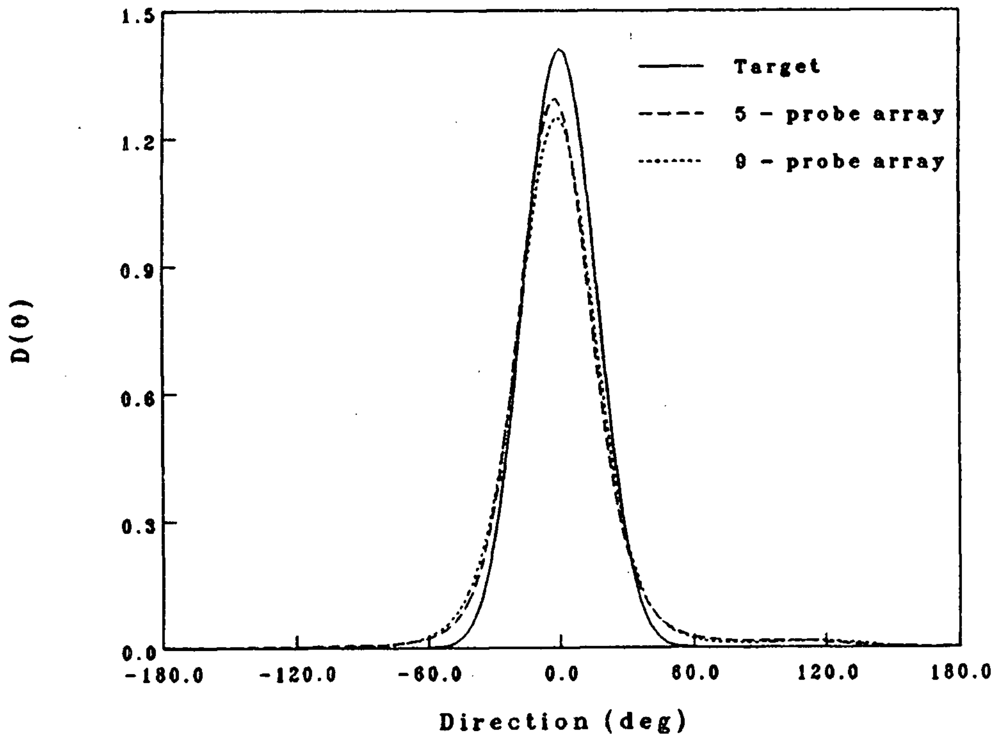

Figure 6.38: Comparison of target and measured directional spreading functions for a five and nine probe array (f = f_p, s = 6)

for a duration of 204.8s. In addition, a second set of data was collected with the span of the wave generator reduced by 30%.

6.2.1 Presentation of Raw Data

Typical measured signals for the sea state with $f_p = 0.33$Hz are shown in figures 6.39 to 6.41 for the long-crested case, and figures 6.42 to 6.44 for the $\cos^2\theta$ short-crested case. It can be seen from figures 6.39 and 6.42 that the current meter at an elevation of 1.68m had a high level of noise present in the signal, particularly in the transverse direction. The noise was due to the presence of a wave probe near the current meters, interfering with the magnetic field produced by the current meter. An attempt to suppress the level of noise by wrapping the metallic part of the wave probe with electrical tape reduced the noise level but did not eliminate it.

It can also be seen from figures 6.41 and 6.44 that transverse load cells for segments 2, 4, and 5 did not produce any output signals. This was because those load cells failed during the tests. The transverse load cell for segment 1 also failed during the tests even though it later produced an output signal. The figures also show clearly the nature of the loading on the segments above the still water level. The higher segments experience impulsive type loads with durations of less than half a second. This can be seen more clearly in figure 6.45 which shows the force on segment 9 over a 10s interval.

The forces in the transverse direction for the long-crested wave, shown in figure 6.40 are due to vortex shedding. It can be seen from the figure that the lift forces in random waves are highly grouped, with high values of the force corresponding to the occurence of bigger waves. It can also be seen that both segments above and below the still water level experience lift forces.

The vertical distribution of the standard deviation of the force per unit length are shown in figure 6.46 for all three long-crested sea states. The corresponding profiles of the maximum force experienced by the segments are also shown in figure 6.46. The figures

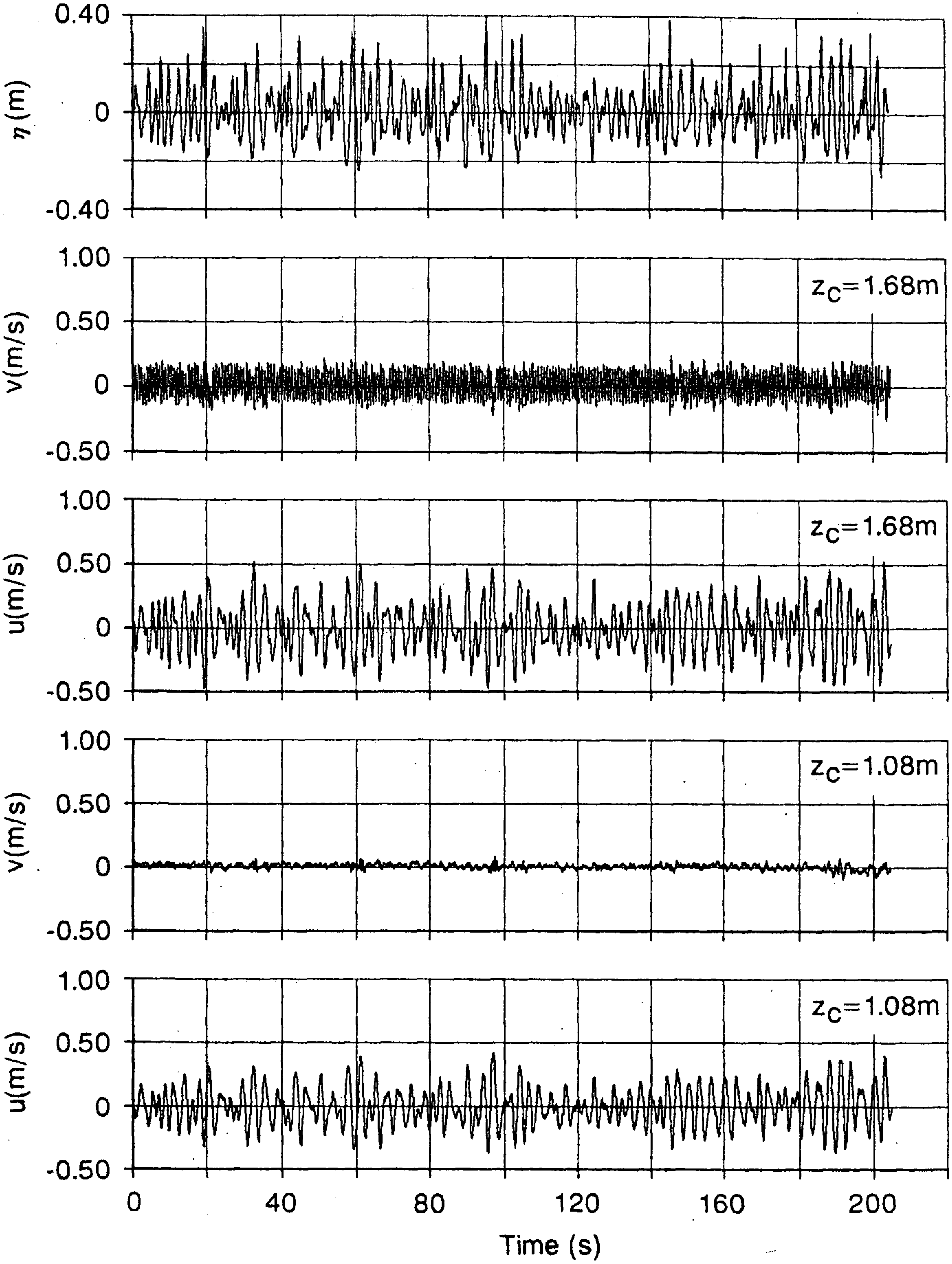

Figure 6.39: Measured water surface elevation and velocity time series for a long-crested sea state (f_p = 0.33Hz)

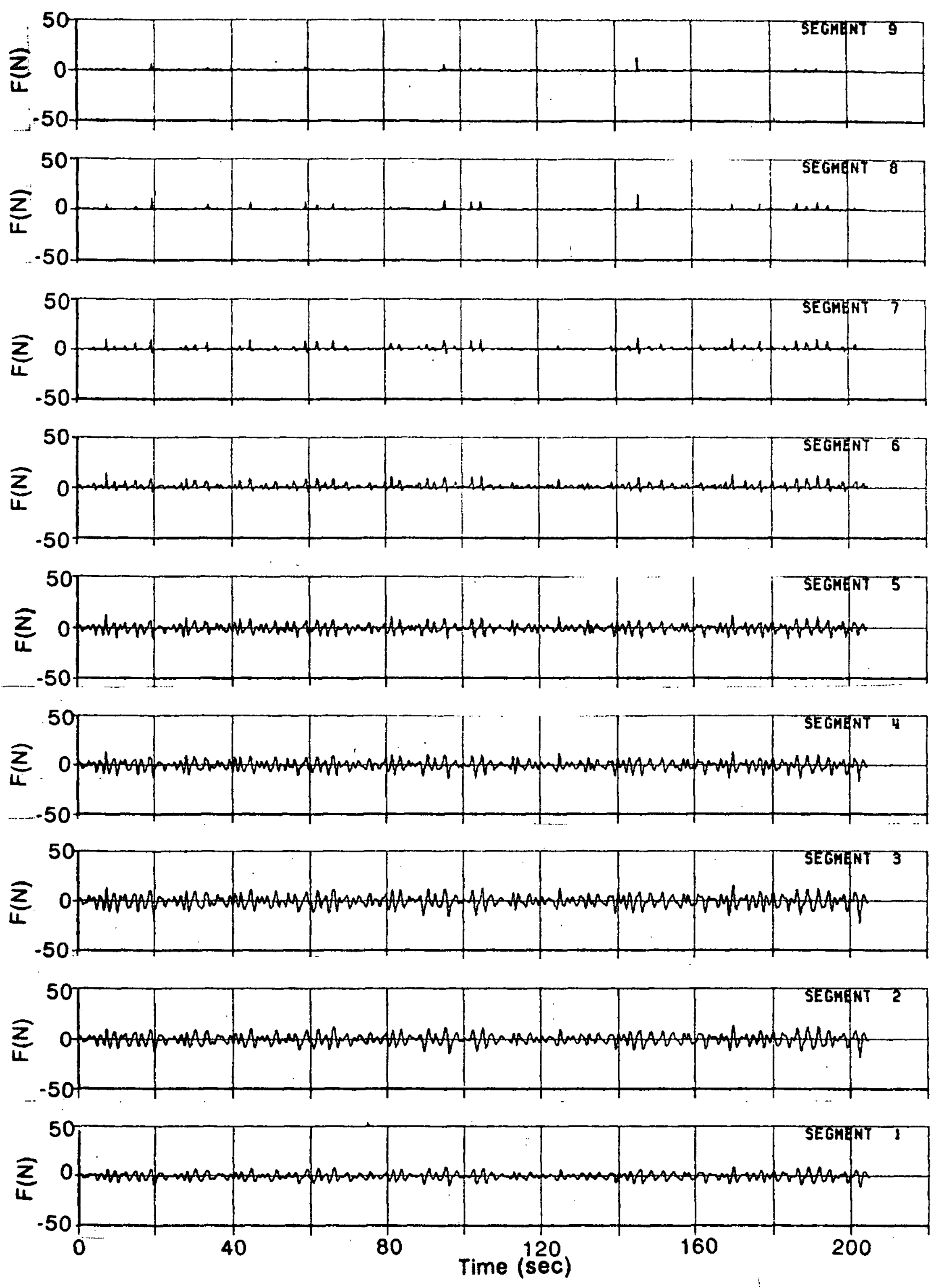

Figure 6.40: Measured inline force time series for a long-crested sea state (f_p = 0.33Hz)

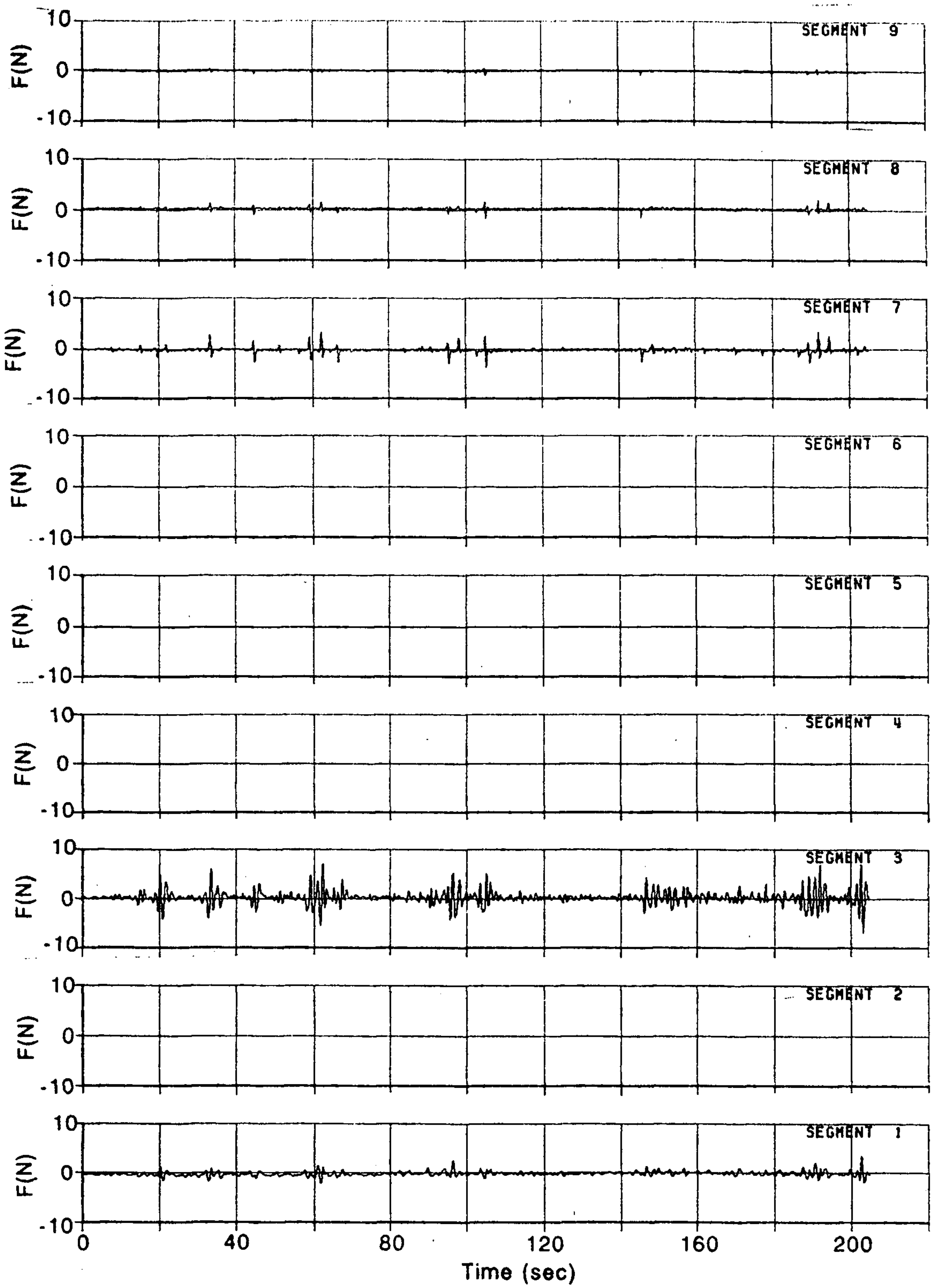

Figure 6.41: Measured transverse force time series for a long-crested sea state (f_p = 0.33Hz)

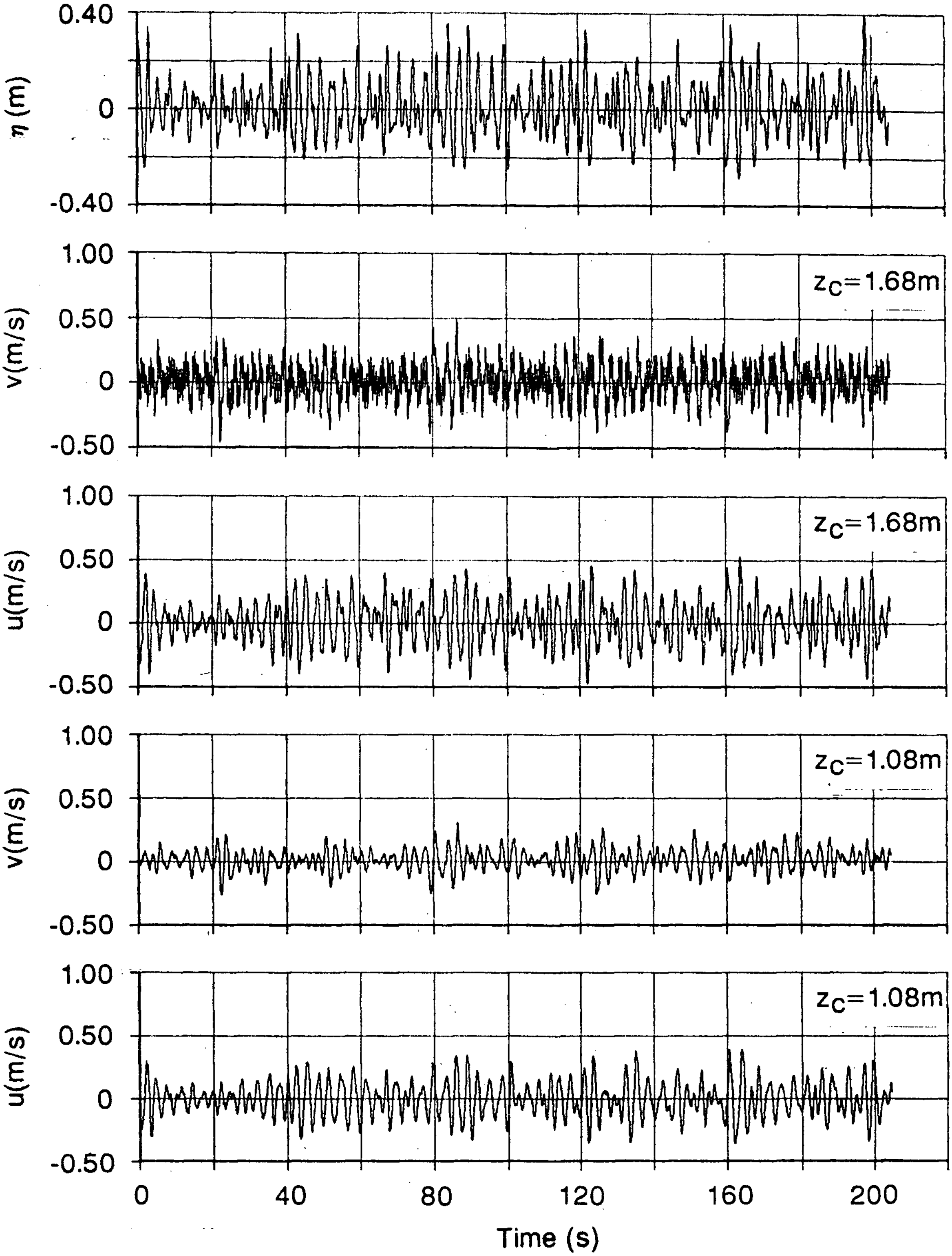

Figure 6.42: Measured water surface elevation and velocity time series for a short-crested sea state ($f_p = 0.33$Hz, $s = 1$)

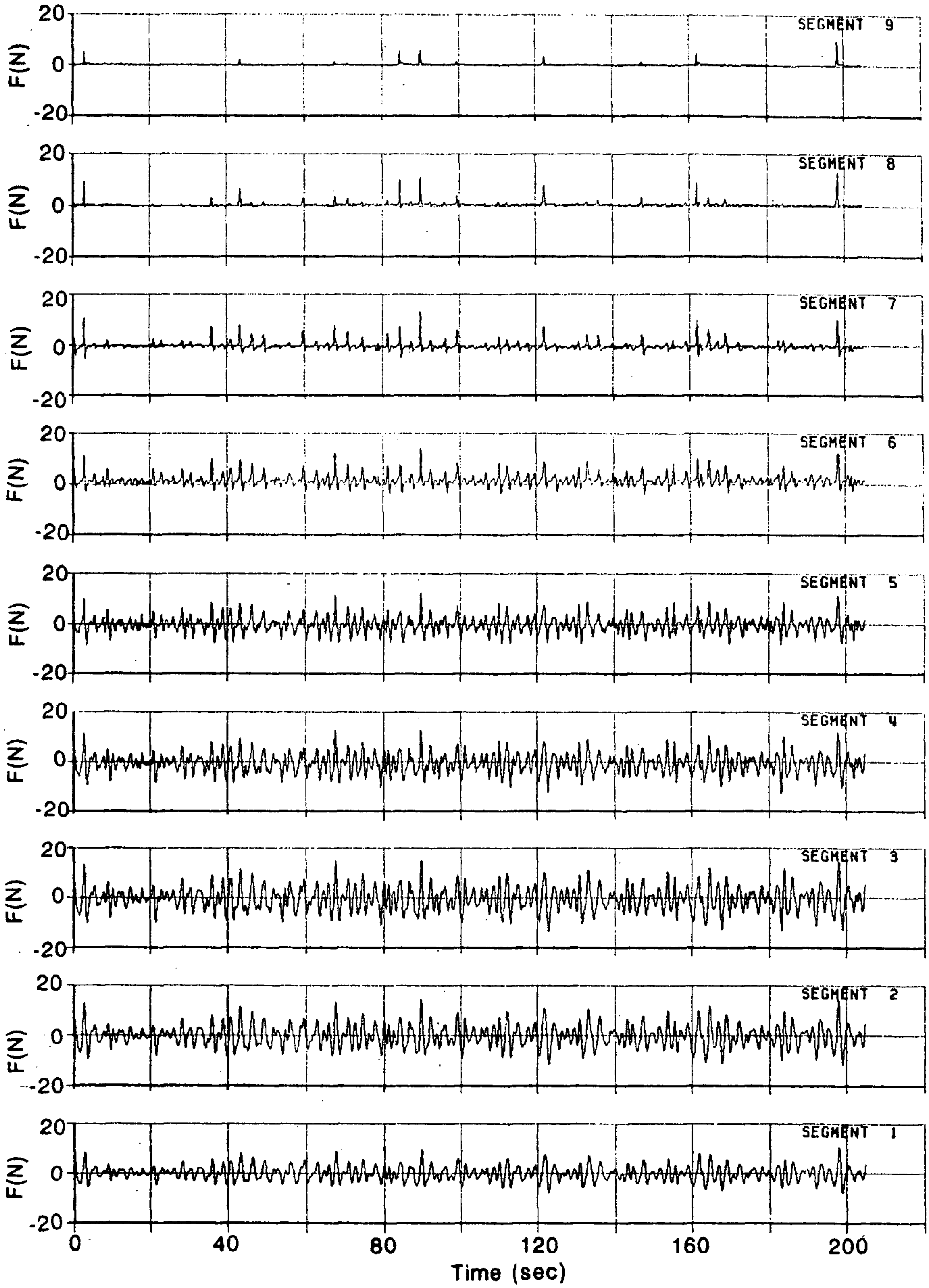

Figure 6.43: Measured inline force time series for a short-crested sea state ($f_p = 0.33$Hz, $s = 1$)

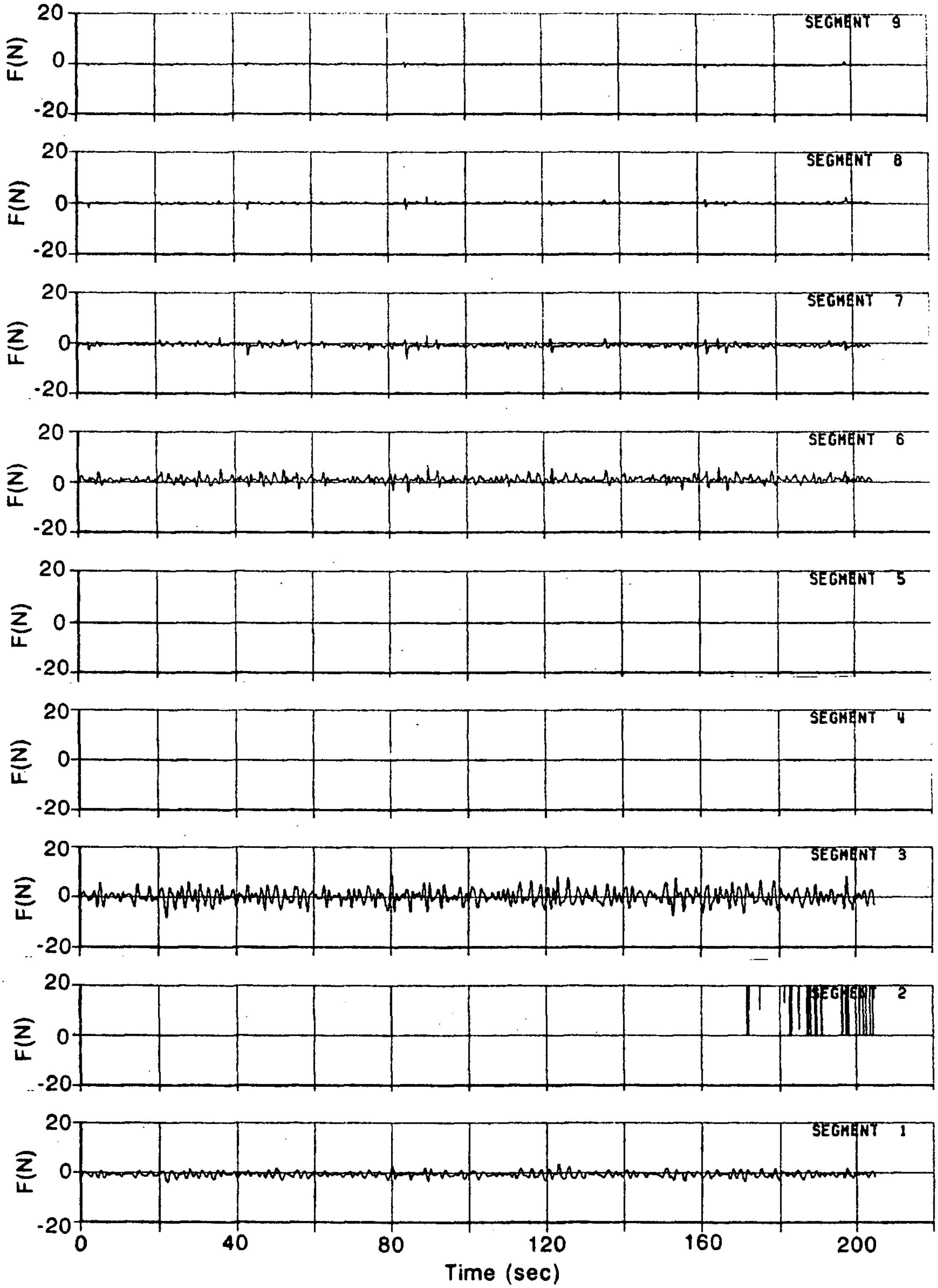

Figure 6.44: Measured transverse force time series for a short-crested sea state (f_p = 0.33Hz, s = 1)

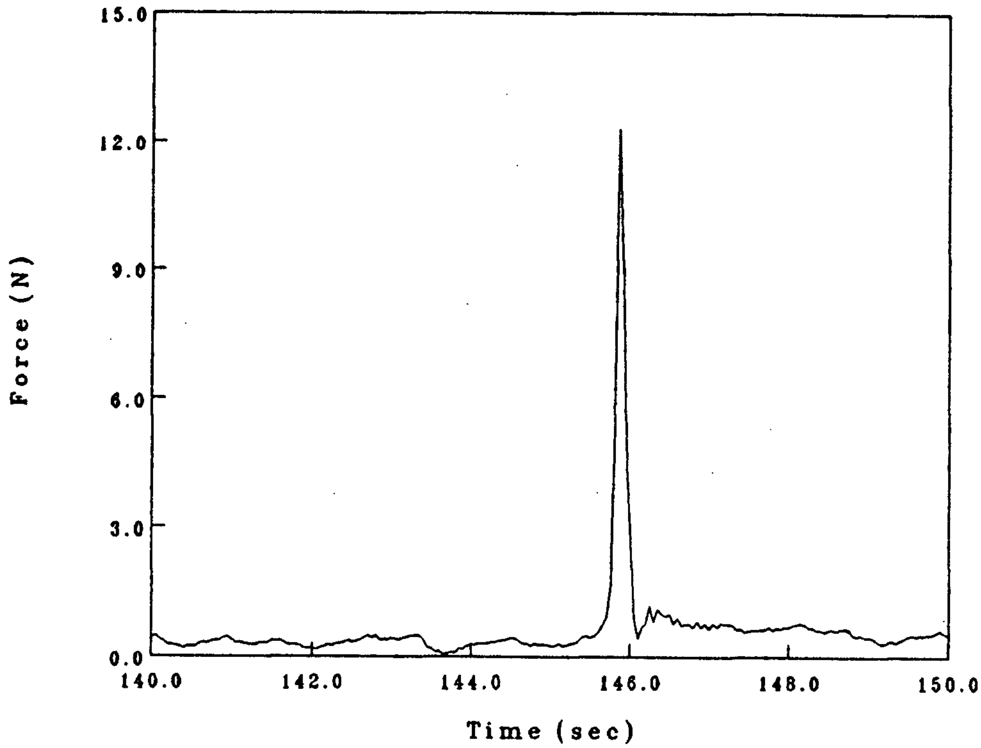

Figure 6.45: Measured inline force on segment 9 over a 10s interval

show that even though the standard deviation of the force decreases for the segments above the still water level, the maximum forces experienced by those segments are still quite high.

6.2.2 Water Surface Elevation and Velocity Spectra

The measured water surface elevation and velocity time series were Fourier transformed to obtain the spectral densities. The FFT analysis was carried out at a frequency resolution of 0.04Hz, corresponding to 32 chi-squared degrees of freedom.

Figures 6.47 to 6.49 show a comparison of the measured and target water surface elevation spectra for the three long-crested waves with f_p = 0.33, 0.4, and 0.5Hz respectively. While the agreement between the measured and target wave spectra is generally fair, much better reproduction of target wave spectra can now be obtained in the basin. This is because the tests were carried out in the basin before full implementation of the wave generator control software. The lack of a good fit of the target spectra does not

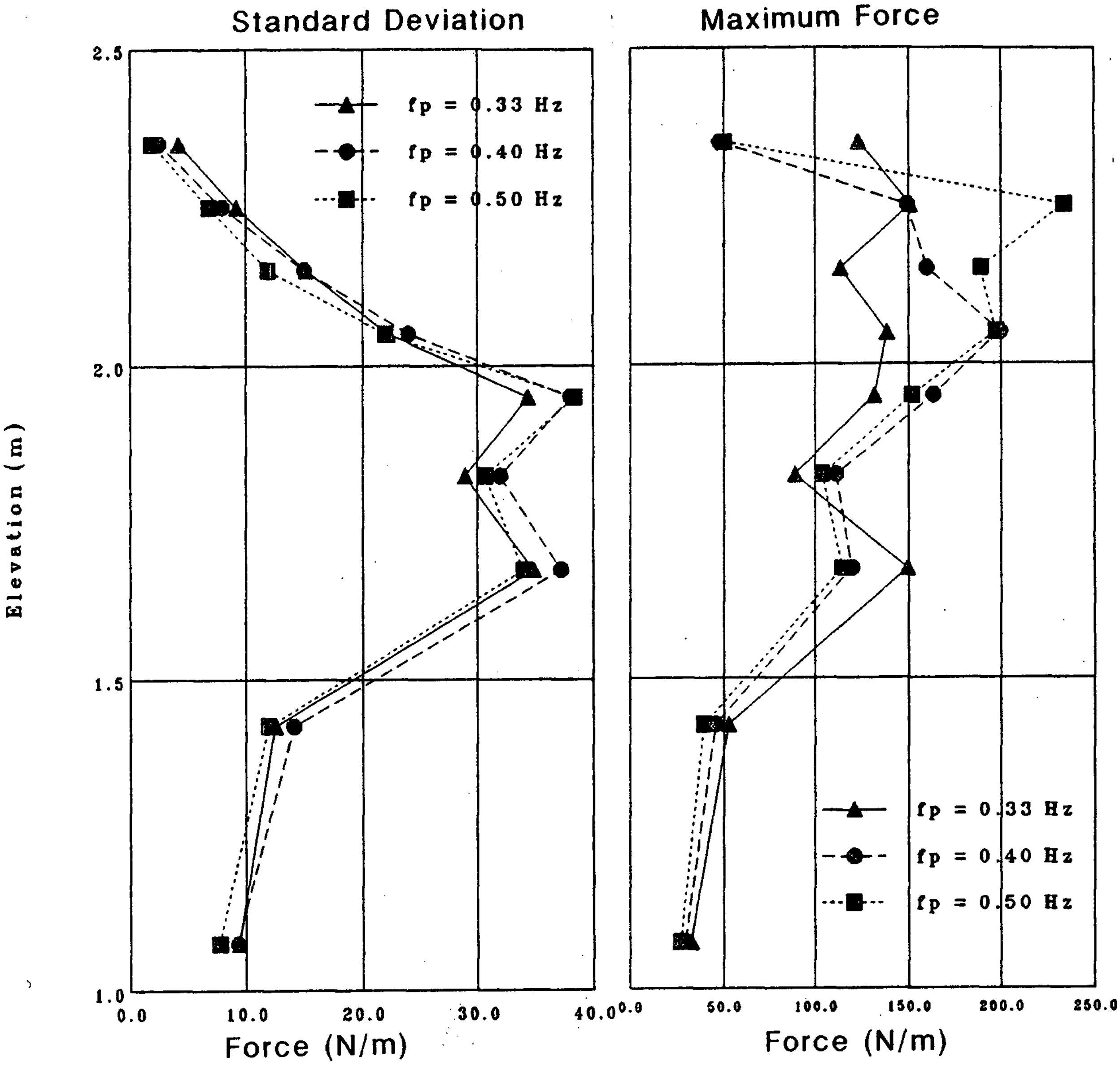

Figure 6.46: Vertical distribution of the standard deviation and maximum values of the force

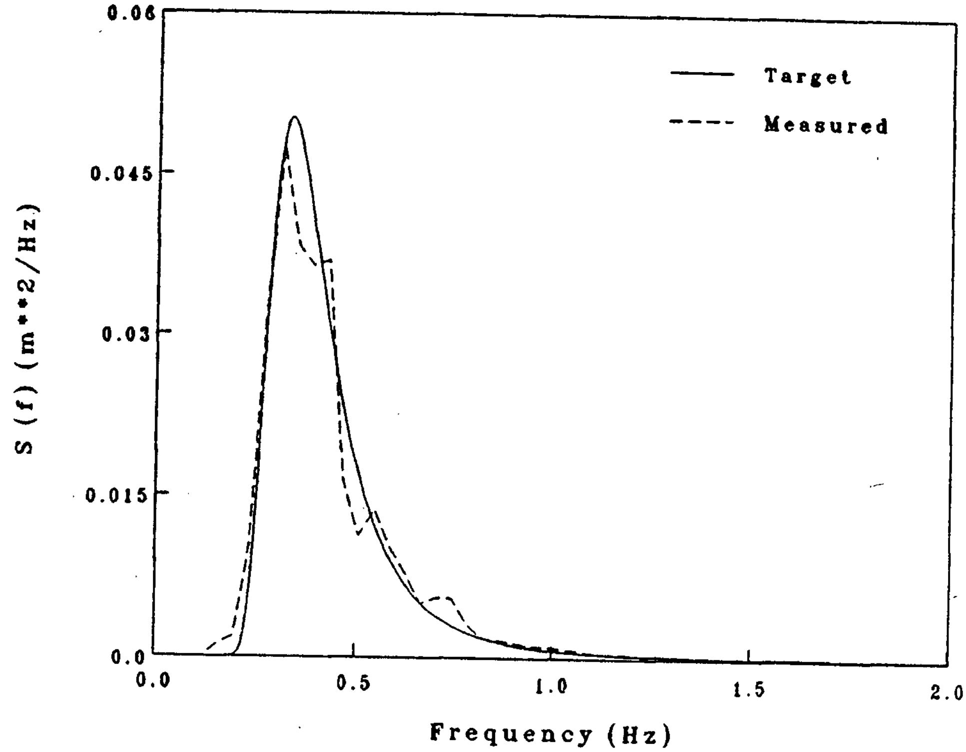

Figure 6.47: Comparison of target and measured water surface elevation spectra (f_p = 0.33Hz, H_{m0} = 0.45m)

however affect any subsequent force data analysis since the measured spectra are used for all analysis.

The spectral densities of the measured water particle velocities for the 0.33Hz sea state at elevations z_c of 1.08m and 1.68m are compared with predictions determined from the measured water surface elevation spectra using linear wave theory in figures 6.50 and 6.51. It can be seen from the figures that the velocity spectrum of the lower current meter is well predicted by linear wave theory, while spectrum of the upper current meter was not as well predicted.

6.2.3 Force Spectral Densities and Coefficients

Constant force coefficients were determined for the long-crested random waves by a least squares fit of the measured to the predicted force sprectra. The procedure is described in Section 3.3.2. The predicted force spectrum was calculated from the spectrum

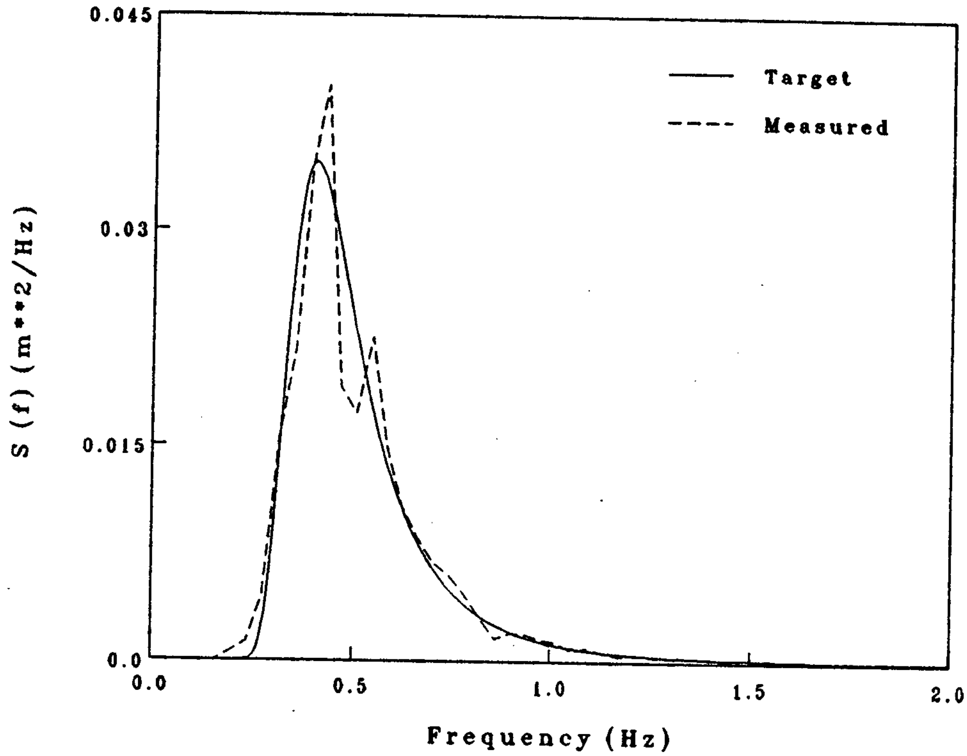

Figure 6.48: Comparison of target and measured water surface elevation spectra (f_p = 0.4Hz, H_{m0} = 0.4m)

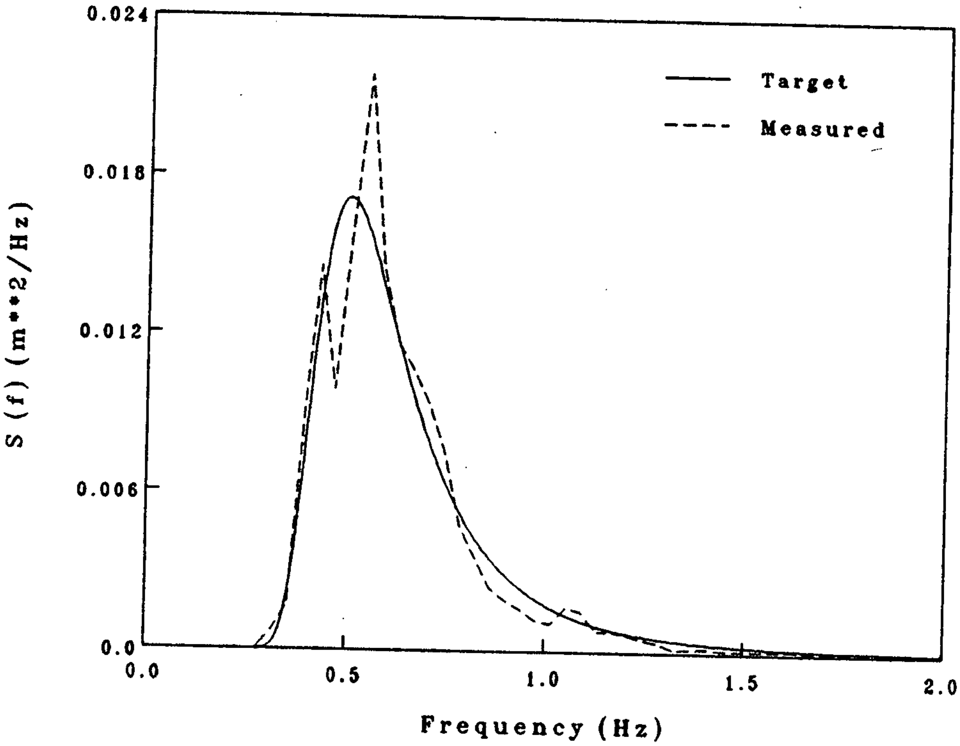

Figure 6.49: Comparison of target and measured water surface elevation spectra (f_p = 0.5Hz, H_{m0} = 0.32m)

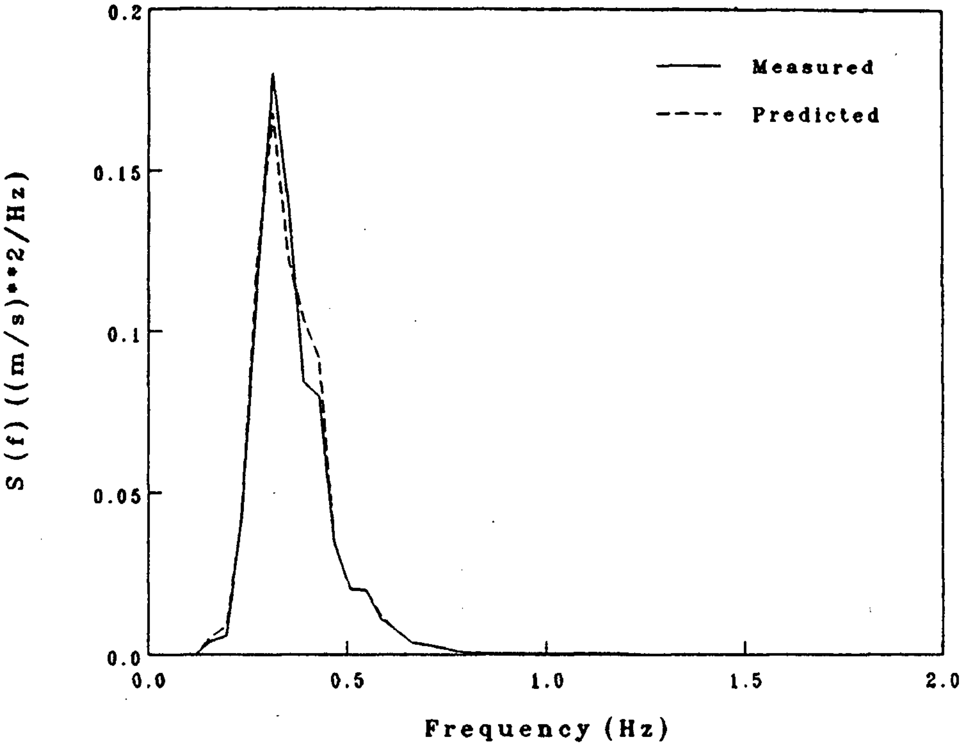

Figure 6.50: Comparison of target and measured inline velocity spectra (f_p = 0.33Hz, z_c = 1.08m)

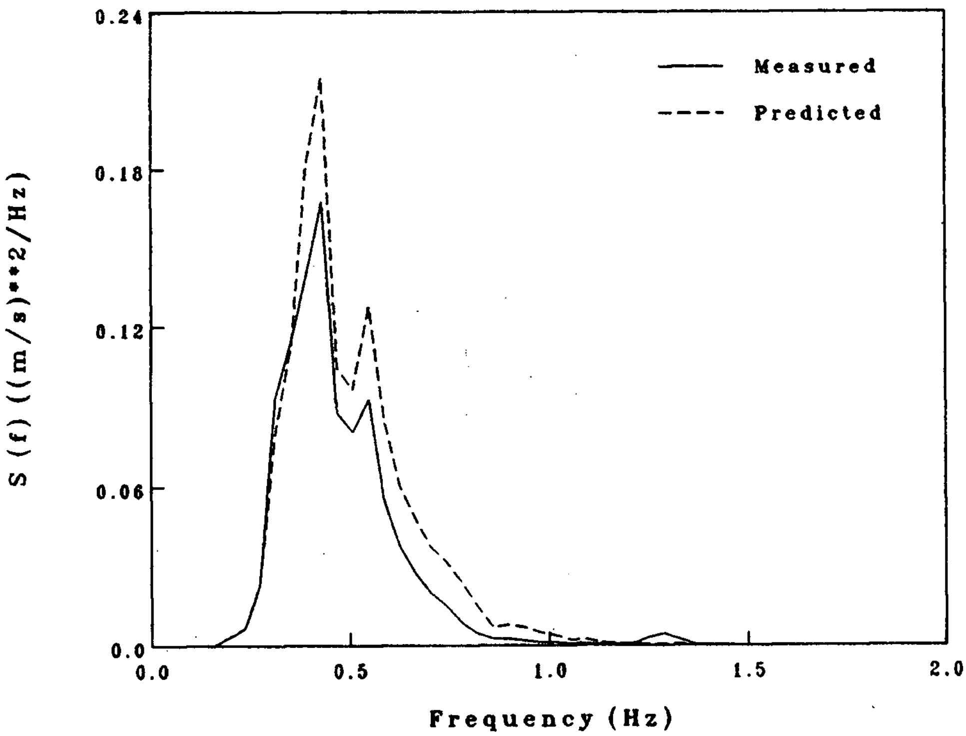

Figure 6.51: Comparison of target and measured inline velocity spectra (f_p = 0.33Hz, z_c = 1.68m)

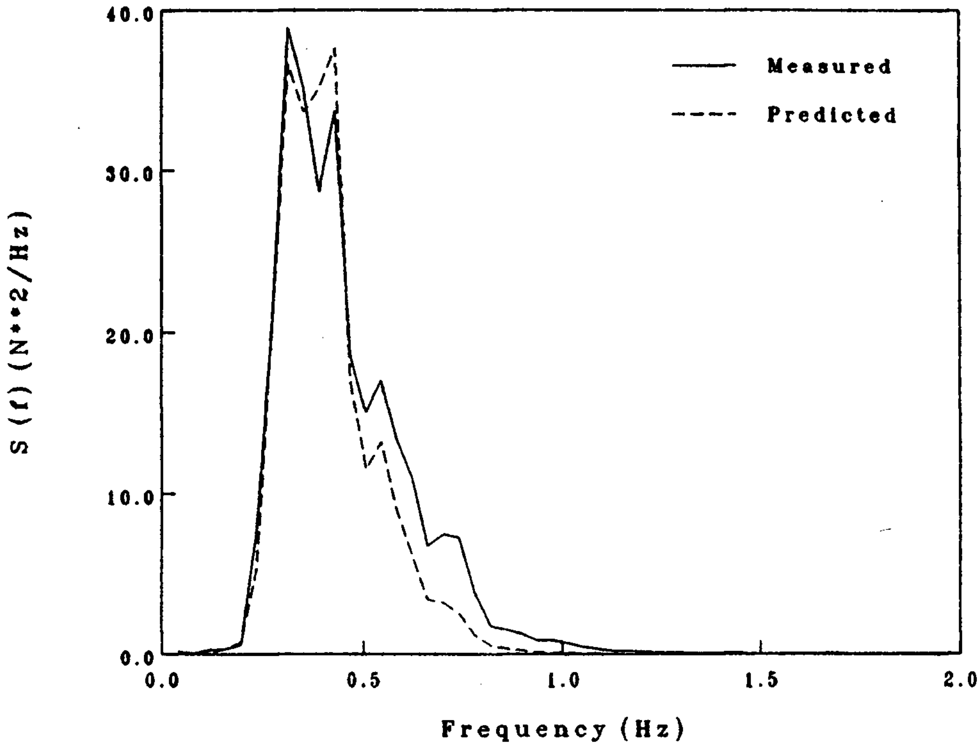

Figure 6.52: Comparison of measured and predicted inline force spectra for long-crested waves (segment 1, $C_M = 0.95$, $C_D = 0.0$, $f_p = 0.33$Hz)

of the measured water surface elevation time series using linear wave theory for the kinematics. The calculations were carried out for segments 1, 2, and 3 which remain fully submerged at all times.

Figures 6.52 to 6.60 show a comparison of the measured and predicted force spectral densities for segments 1 to 3 for all three long-crested sea states. The best fit coefficients are also indicated on the figures. It can be seen from the figures that the constant coefficient, linearized Morison formulation predicts the measured force spectrum reasonably well for segments 2 and 3. The measured force spectral density for segment 1 was however consistently underpredicted at the higher frequencies. This might be partly due to the weakness of the assumption of constant force coefficients over the entire frequency range.

The estimated inertia force coefficients are plotted against the Keulegan-Carpenter number in figure 6.61. The best fit inertia coefficients for segments 1 and 2 were consis-

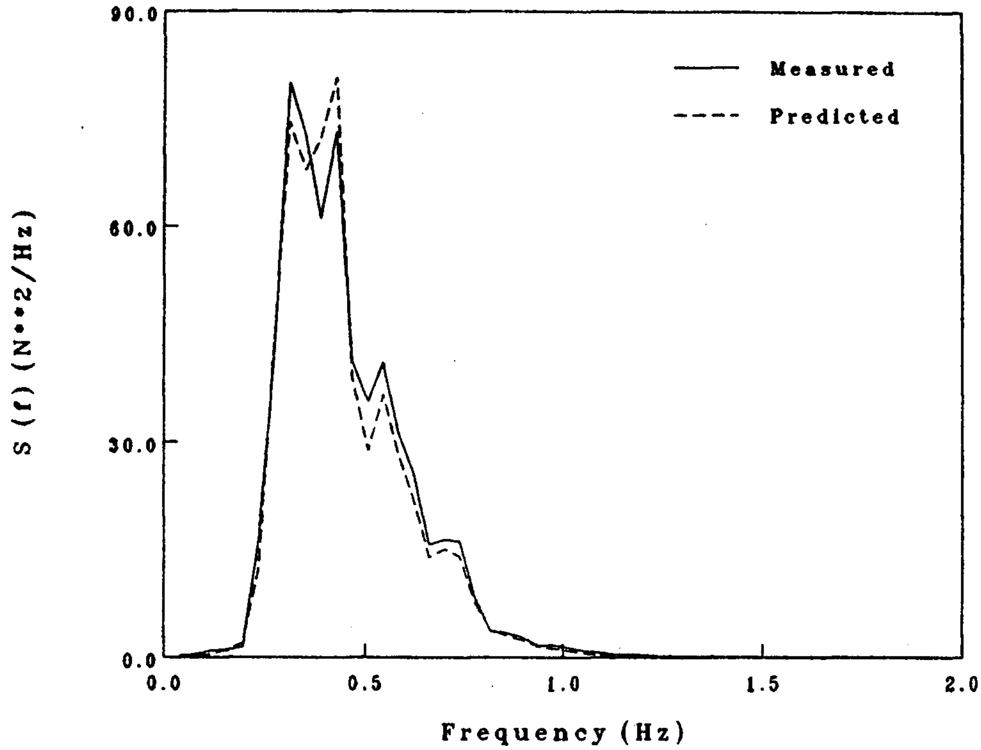

Figure 6.53: Comparison of measured and predicted inline force spectra for long-crested waves (segment 2, $C_M = 0.99$, $C_D = 0.4$, $f_p = 0.33$Hz)

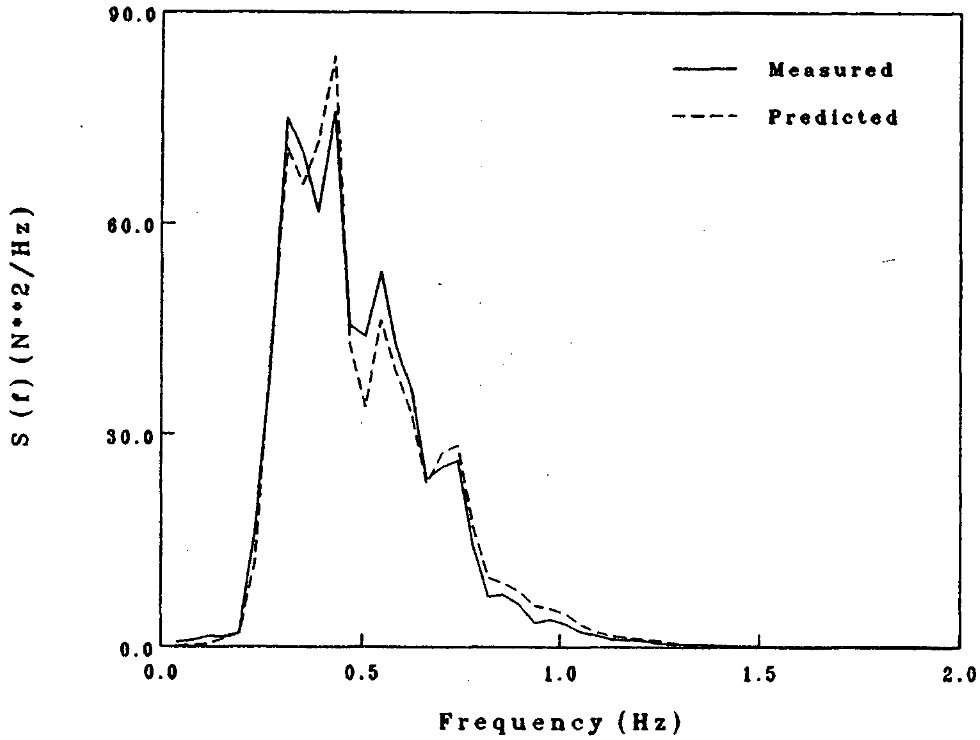

Figure 6.54: Comparison of measured and predicted inline force spectra for long-crested waves (segment 3, $C_M = 1.84$, $C_D = 0.9$, $f_p = 0.33$Hz)

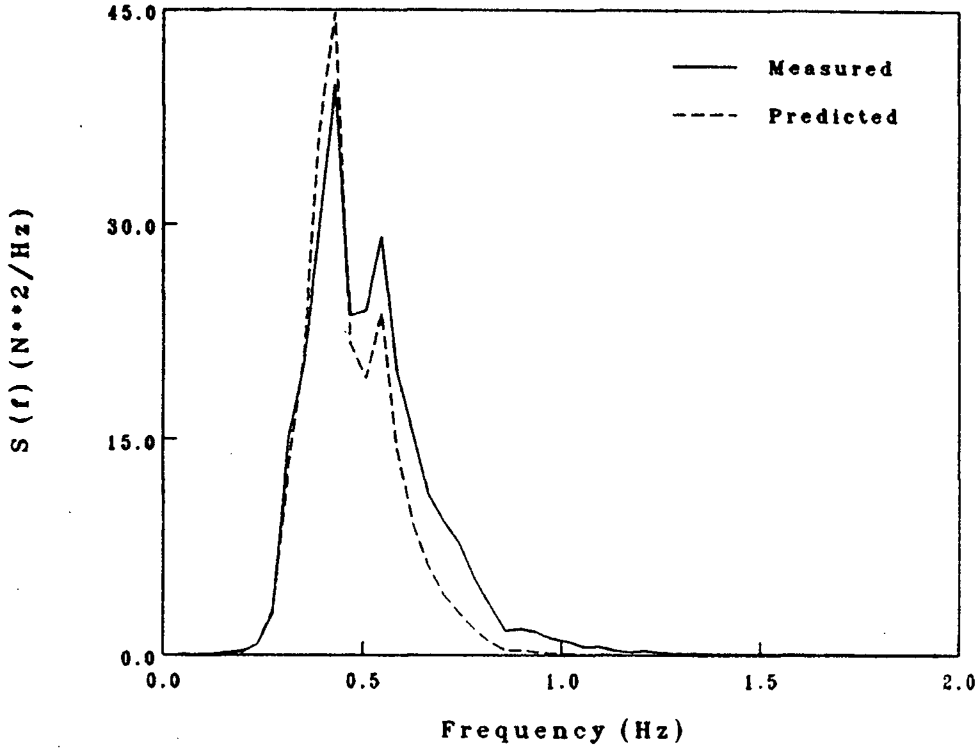

Figure 6.55: Comparison of measured and predicted inline force spectra for long-crested waves (segment 1, $C_M = 0.99$, $C_D = 0.0$, $f_p = 0.4$Hz)

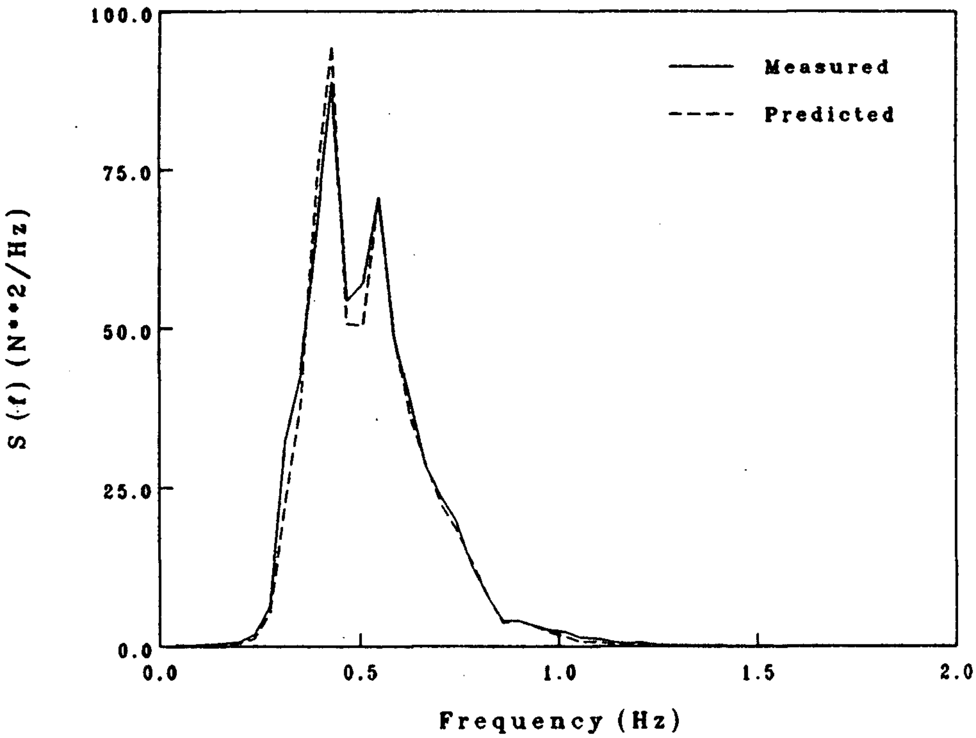

Figure 6.56: Comparison of measured and predicted inline force spectra for long-crested waves (segment 2, $C_M = 1.15$, $C_D = 0.1$, $f_p = 0.4$Hz)

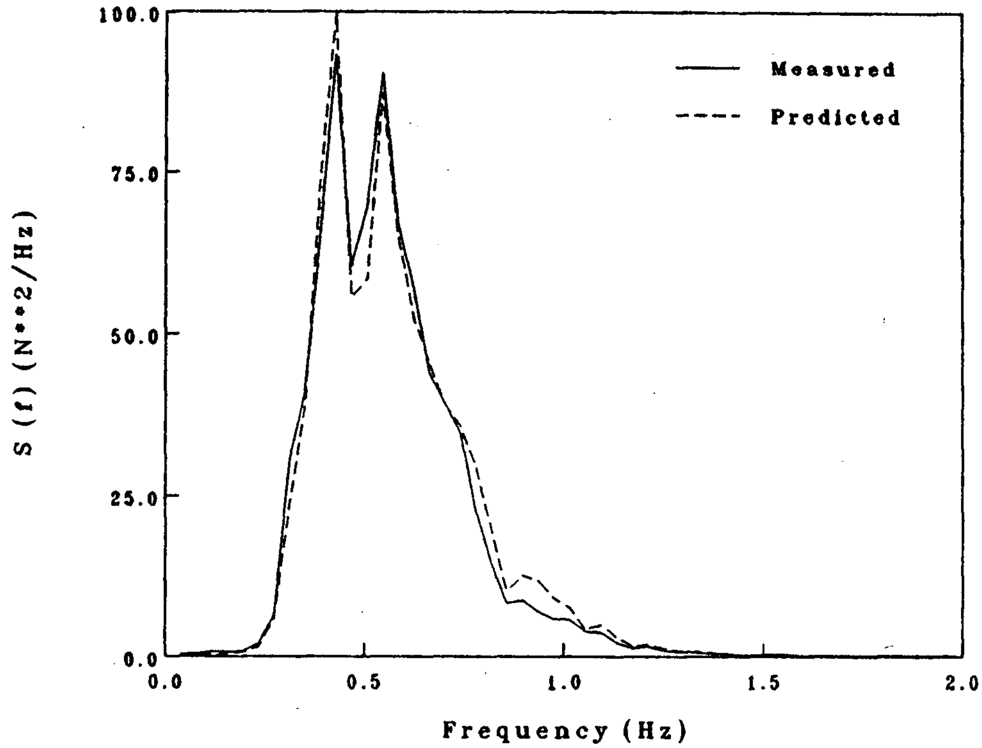

Figure 6.57: Comparison of measured and predicted inline force spectra for long-crested waves (segment 3, $C_M = 2.07$, $C_D = 0.8$, $f_p = 0.4$Hz)

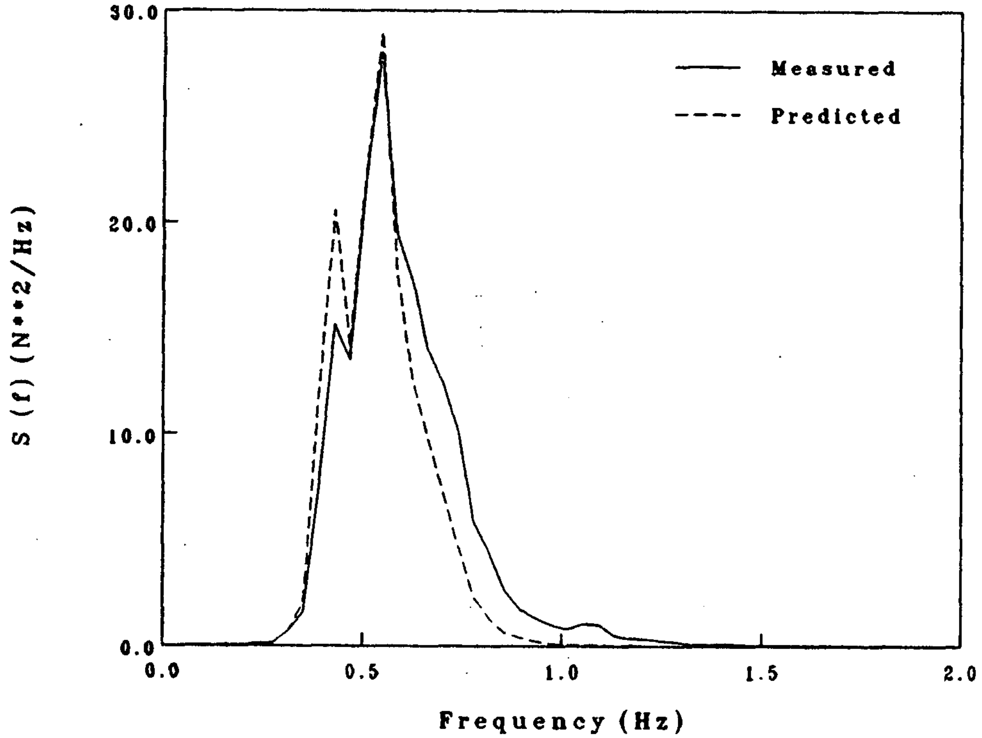

Figure 6.58: Comparison of measured and predicted inline force spectra for long-crested waves (segment 1, $C_M = 1.11$, $C_D = 0.0$, $f_p = 0.5$Hz)

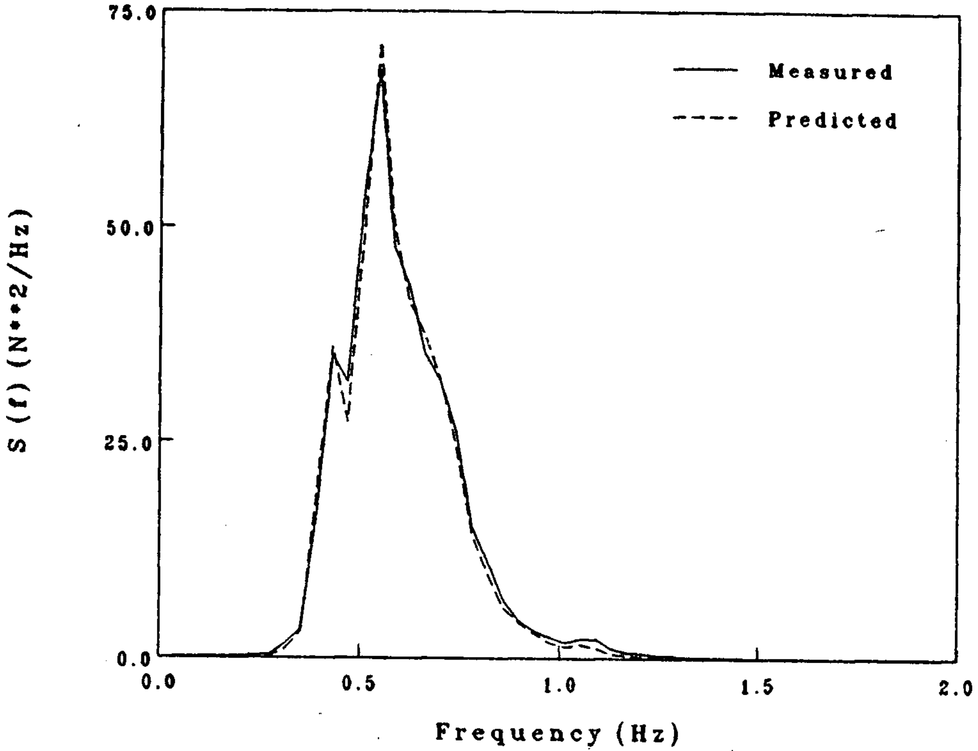

Figure 6.59: Comparison of measured and predicted inline force spectra for long-crested waves (segment 2, $C_M = 1.18$, $C_D = 0.1$, $f_p = 0.5$Hz)

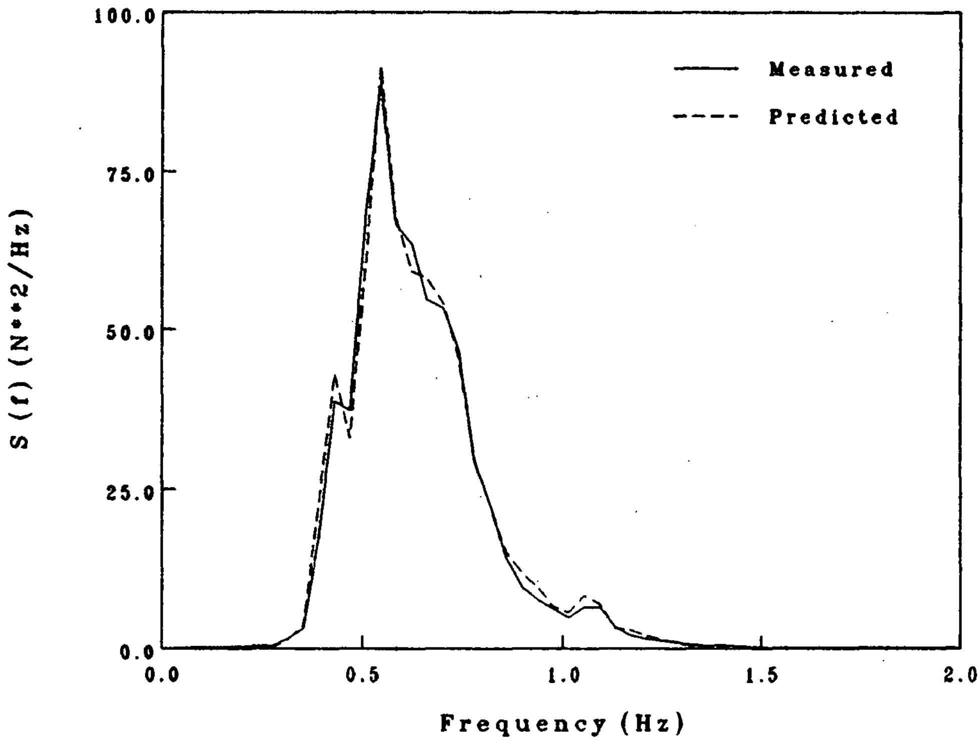

Figure 6.60: Comparison of measured and predicted inline force spectra for long-crested waves (segment 3, $C_M = 1.93$, $C_D = 1.2$, $f_p = 0.5$Hz)

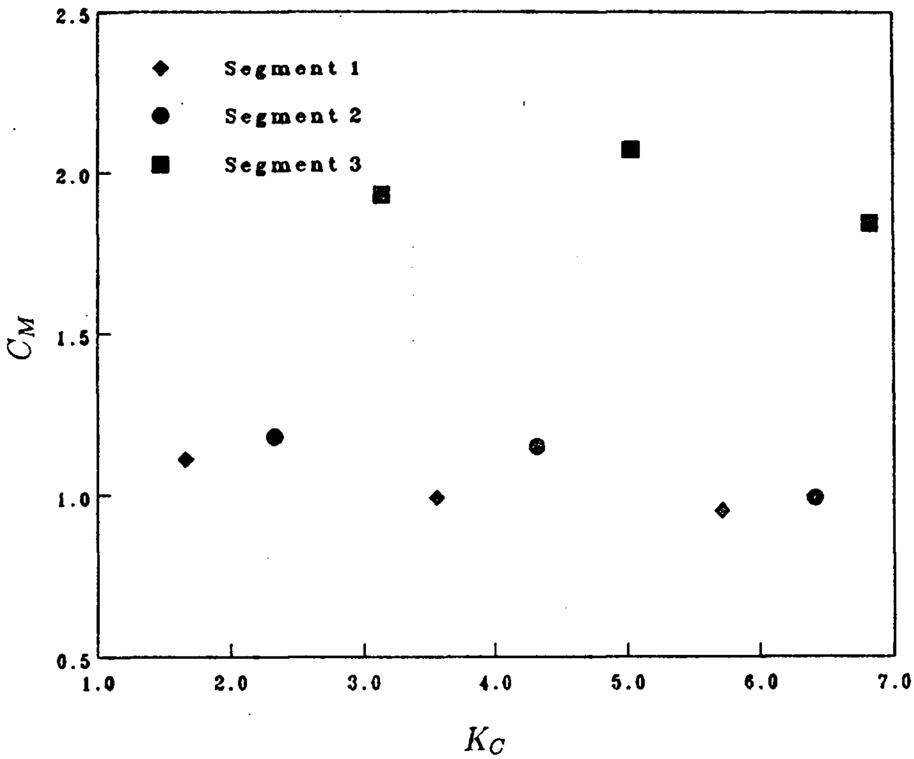

Figure 6.61: Measured inertia force coefficients versus K_C

tently around 1.0, while the coefficients for segment 3 were around 1.9. The coefficients appear to depend more on the segment elevation rather than the Keulegan-Carpenter number. Similar force coefficients were obtained for the sea states with the significant wave heights reduced by 30%. The reason for the big difference between the inertia force coefficients of segments 1 and 3 is not quite clear. The drag coefficients are not plotted because the test conditions were ill-suited for determination of drag coefficients. The drag component of the total force was usually less than 15%, and a variation of the drag coefficient from 0 to 1 had very little effect on the predicted force spectrum.

Lift forces were most significant for the $f_p = 0.33$Hz sea state with a Keulegan-Carpenter number of 6.5 at the midpoint of the third segment. Figure 6.62 shows the spectral density of the lift force for segment 3. It can be seen that most of the lift force energy is concentrated at about twice the peak frequency of the inline force. The standard deviation of the lift force is 25% of the standard deviation of the inline force

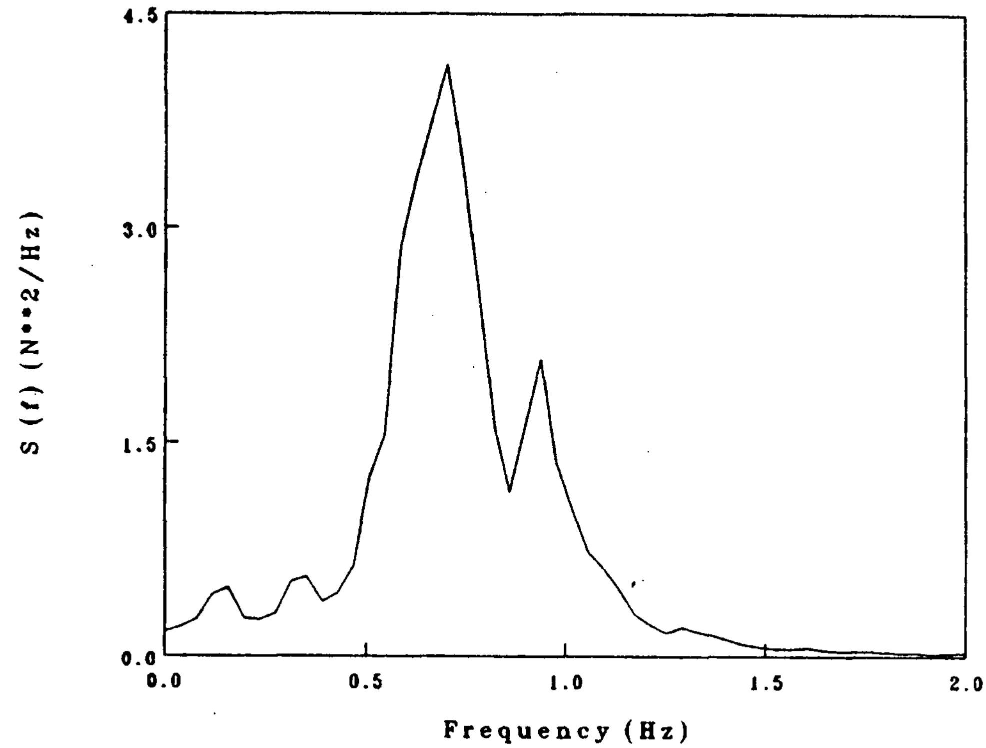

Figure 6.62: Measured transverse force spectrum for long-crested waves (segment 3, f_p = 0.33Hz)

for this case. The maximum lift force value is however about 50% of the maximum inline force value and could give a relatively large resultant force.

6.2.4 Short-Crested Force Spectral Densities

The force coefficients obtained from long-crested waves were used to compute the inline and transverse force spectral densities in short-crested waves. The inline and transverse velocity spectra were obtained from the measured water surface elevation spectrum using linear wave theory and the estimated directional spreading function. The measured and predicted inline and transverse force spectral densities for segment 3 for three multi-directional sea states with f_p = 0.33, 0.4, and 0.5Hz, and $s \approx 1$ are compared in figures 6.63 to 6.68. It can be seen that both the inline and transverse force spectral densities are reasonably well predicted by the Morison equation with the same constant coefficients used for both the inline and transverse direction.

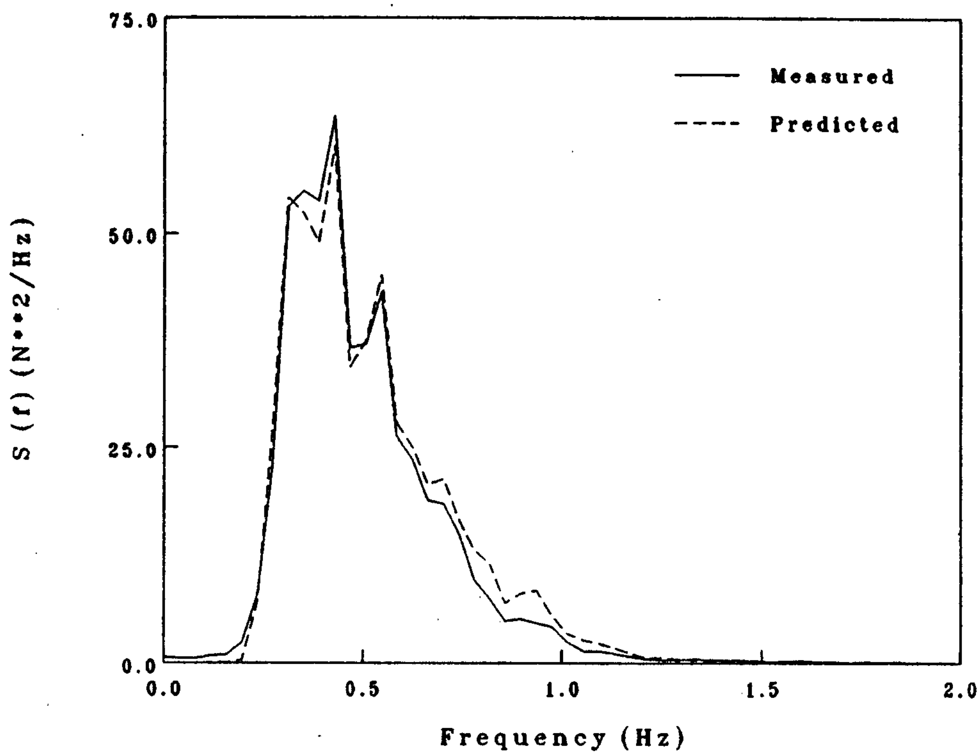

Figure 6.63: Comparison of measured and predicted inline force spectra for short-crested waves (segment 3, $f_p = 0.33$Hz, $s \approx 1$)

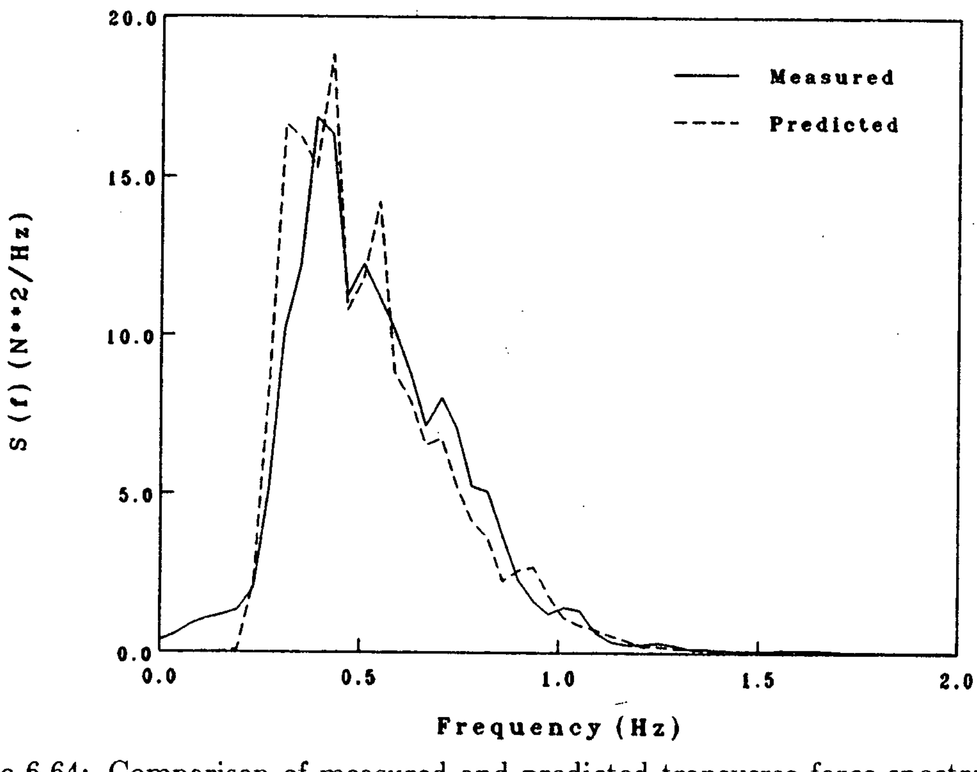

Figure 6.64: Comparison of measured and predicted transverse force spectra for short-crested waves (segment 3, $f_p = 0.33$Hz, $s \approx 1$)

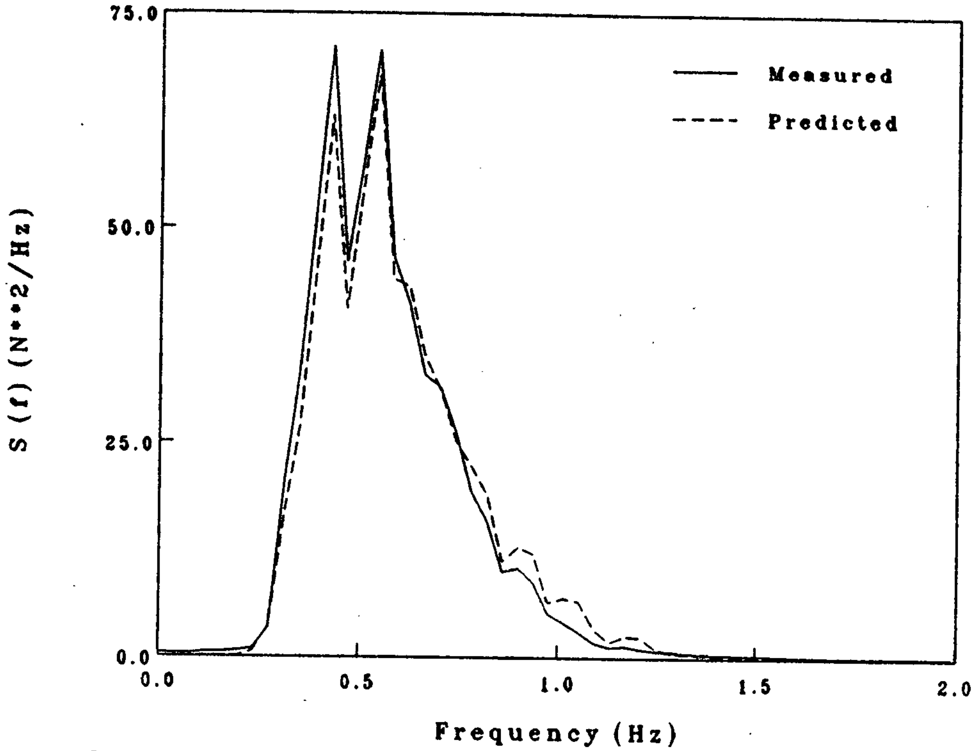

Figure 6.65: Comparison of measured and predicted inline force spectra for short-crested waves (segment 3, $f_p = 0.4$Hz, $s \approx 1$)

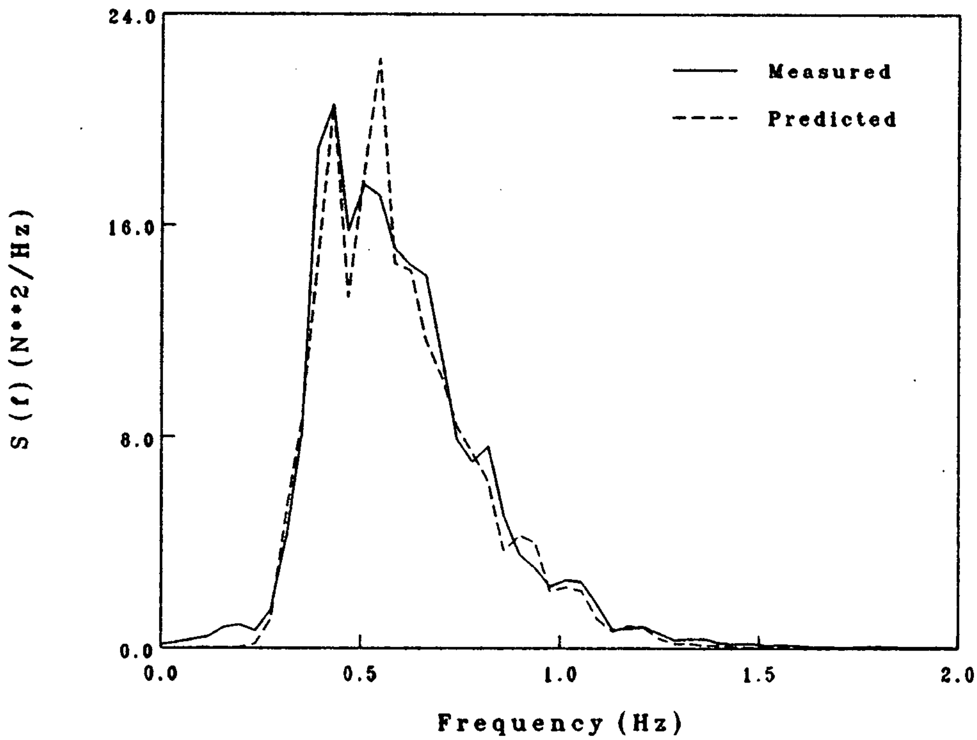

Figure 6.66: Comparison of measured and predicted transverse force spectra for short-crested waves (segment 3, $f_p = 0.4$Hz, $s \approx 1$)

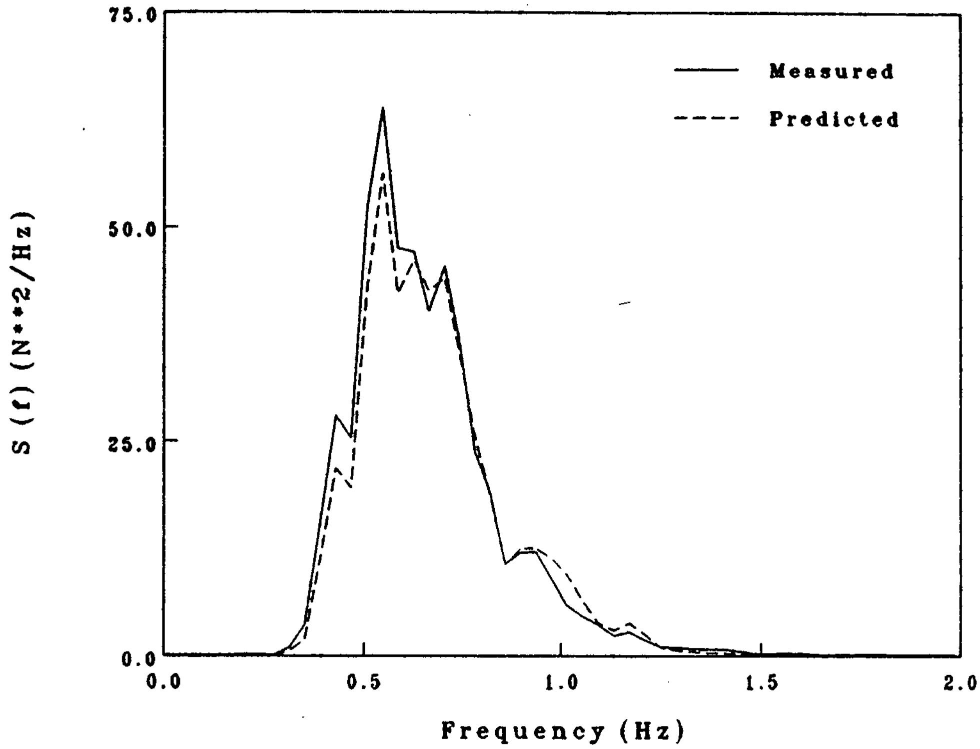

Figure 6.67: Comparison of measured and predicted inline force spectra for short-crested waves (segment 3, $f_p = 0.5$Hz, $s \approx 1$)

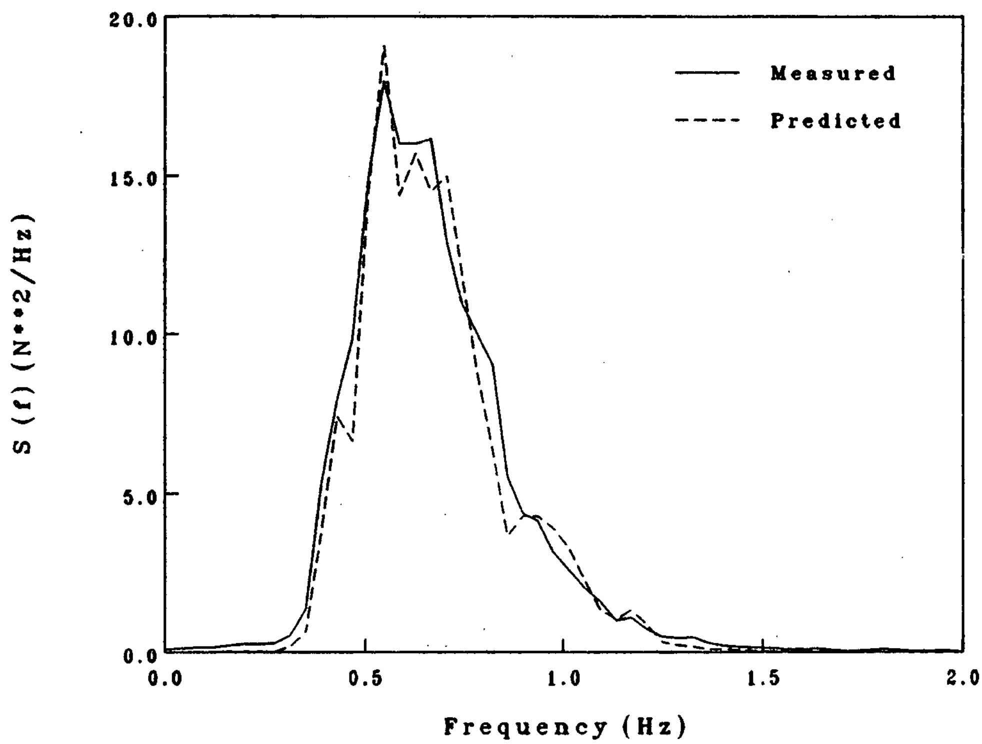

Figure 6.68: Comparison of measured and predicted transverse force spectra for short-crested waves (segment 3, $f_p = 0.5$Hz, $s \approx 1$)

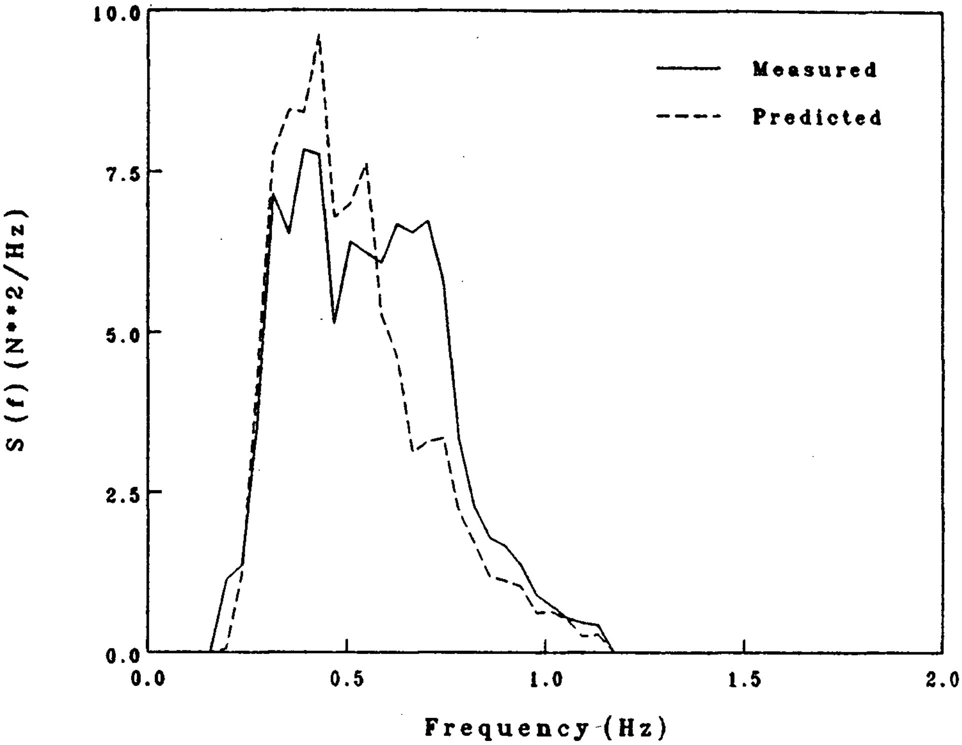

Figure 6.69: Comparison of measured and predicted transverse force spectra for short-crested waves (segment 3, f_p = 0.33Hz, $s \approx 3$)

The lift force component at twice the peak frequency of the incident waves which was significant for the 0.33Hz long-crested sea state is not observed for the multi-directional sea state with $s \approx 1$. This might be anticipated since the sea state is more confused for that degree of spreading, and the shedding of vortices would not be as highly correlated as in a unidirectional flow. The corresponding transverse force spectrum for the f_p = 0.33Hz multi-directional sea states with $s \approx 3$ and $s \approx 6$ are shown in figures 6.69 and 6.70. It can be seen that for $s \approx 3$, a component at twice the frequency of the waves becomes noticeable, while for $s \approx 6$, the component at twice the frequency dominates the transverse loading on that segment.

6.2.5 Force Reduction Factors

In unidirectional and multi-directional sea states with the same wave spectrum, the effect of the directional spreading of wave energy is to reduce the inline force and increase

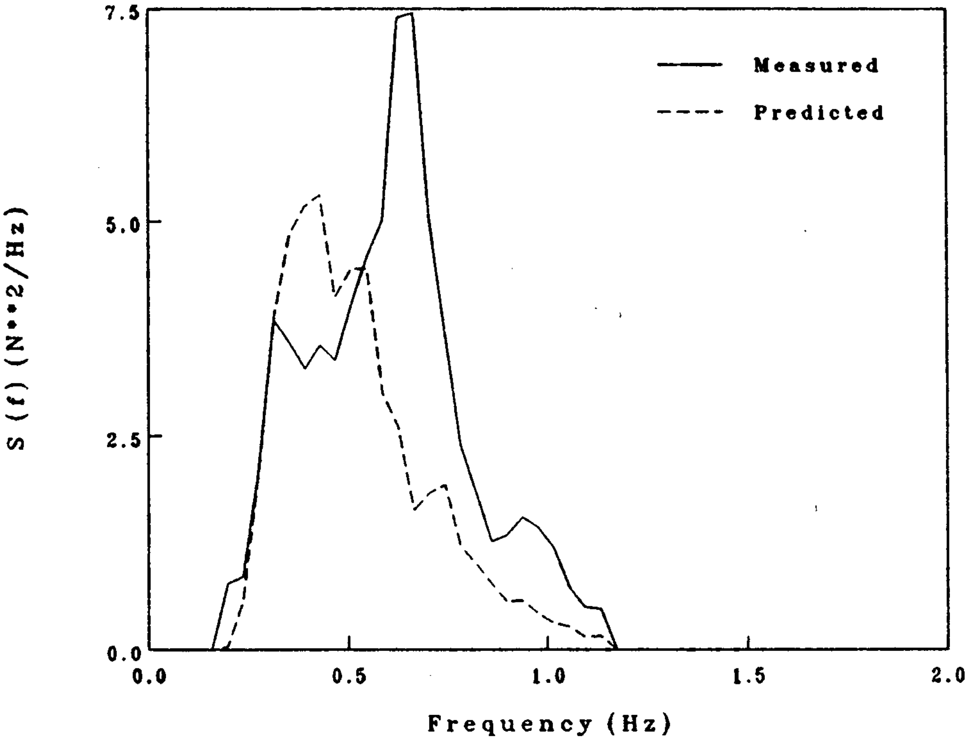

Figure 6.70: Comparison of measured and predicted transverse force spectra for short-crested waves (segment 3, $f_p = 0.33$Hz, $s \approx 6$)

the transverse force. It is thus useful to define a reduction factor which relates the standard deviations of the inline and transverse forces in short-crested waves to the standard deviation of the inline force in long-crested waves. For the inline force, this factor is defined as

$$R_{F_X} = \frac{\sigma_{F_X}}{\sigma_F} = \left[\frac{\int_0^\infty S_{F_X}(\omega)\, d\omega}{\int_0^\infty S_F(\omega)\, d\omega} \right]^{\frac{1}{2}} \tag{6.4}$$

A similar factor can be defined for the transverse direction. The spectral densities of the inertia component of the long-crested and short-crested forces are given by equations (3.10), (3.84), and (3.85) as

$$S_F(\omega) = K_M^2 S_a(\omega) \tag{6.5}$$

$$S_{F_X}(\omega) = K_M^2 S_a(\omega) q_u^2 \tag{6.6}$$

$$S_{F_Y}(\omega) = K_M^2 S_a(\omega) q_v^2 \tag{6.7}$$

where q_u and q_v are the ratios of the standard deviations of the inline and transverse velocities (or accelerations) in short-crested seas to the standard deviation of the inline velocity (or acceleration) in long-crested seas, given by equations (3.73) and (3.74) as

$$q_u^2 = \int_{-\pi}^{\pi} D(\theta) \cos^2 \theta \, d\theta \tag{6.8}$$

$$q_v^2 = \int_{-\pi}^{\pi} D(\theta) \sin^2 \theta \, d\theta \tag{6.9}$$

The reduction factors for inertia forces can be obtained by substituting equations (6.5) to (6.7) into equation (6.4), resulting in

$$R_{F_X} = q_u \tag{6.10}$$

$$R_{F_Y} = q_v \tag{6.11}$$

The above equations indicate that the inline and transverse inertia forces in short-crested seas are reduced in a similar manner as the velocities and accelerations. For a $\cos^2 \theta$ directional distribution of wave energy, the standard deviation of the inline force is reduced by 14%, while the standard deviation of the transverse force becomes 50% of the standard deviation of the inline force in long-crested waves.

In a totally drag regime, the standard deviations of the forces in long-crested and short-crested seas are given by equations (3.34), (3.101), and (3.102) as

$$\sigma_F^2 = 3K_D^2 \sigma_u^4 \tag{6.12}$$

$$\sigma_{F_X}^2 = 3K_D^2 \sigma_u^4 + K_D^2 \sigma_u^2 \sigma_v^2 \tag{6.13}$$

$$\sigma_{F_Y}^2 = 3K_D^2 \sigma_v^4 + K_D^2 \sigma_u^2 \sigma_v^2 \tag{6.14}$$

The above equations for the standard deviations of the forces were derived from the force probability distributions and have involved no linearization. Since q_u and q_v represent the ratios of the standard deviations of the inline and transverse velocities in short-crested seas to long-crested seas, the reduction factors for drag dominated forces can be expressed as

$$R_{F_X} = \sqrt{q_u^4 + q_u^2 q_v^2/3} \tag{6.15}$$

$$R_{F_Y} = \sqrt{q_v^4 + q_u^2 q_v^2/3} \tag{6.16}$$

For a $\cos^2\theta$ directional distribution, the inline force is reduced by 21% while the transverse force is increased by 35%. The 21% reduction of the inline force for the drag dominated regime is much higher than the 14% reduction obtained for the inertia dominated regime. It is also worth noting that because of the nonlinearity of the drag force, the summation of the variance of the inline and transverse components of the drag force in short-crested seas is no longer equal to the variance of the drag force in long-crested seas, that is

$$\sigma_{F_X}^2 + \sigma_{F_Y}^2 \neq \sigma_F^2 \tag{6.17}$$

It can actually be shown that the left hand side of the above equation is always less than or equal to the right hand side, implying a more significant reduction of the resultant force in drag dominated regimes.

The reduction factors obtained from the experimental data for segment 3 are presented in Table 6.2. The measured reduction factors compare reasonably well with theoretical values $R_{F_X} = 0.866$, 0.935, and 0.964, and $R_{F_Y} = 0.5$, 0.353, and 0.267 for $s = 1$, 3, and 6 respectively, for inertia dominated forces.

6.2.6 Probability Distribution of the Peak Forces

The probablity distribution of the maximum resultant forces are of ultimate interest in the design of offshore structures. In Chapter 3, the probability distribution of the peaks of the resultant force in short-crested seas was derived. The derivation retains the full nonlinearity of the Morison equation and only makes an assumption of a narrow-band incident wave spectrum. The effect of wave directionality on the maximum resultant force will now be investigated, and distributions obtained from both numerical and experimental data will be compared with the theoretical distribution.

Table 6.2: Force standard deviation reduction factors

f_p (Hz)	H_{m0} (m)	$s \approx 1$		$s \approx 3$		$s \approx 6$	
		R_{F_X}	R_{F_Y}	R_{F_X}	R_{F_Y}	R_{F_X}	R_{F_Y}
0.33	0.45	0.872	0.489	0.944	0.366	0.966	0.316
	0.31	0.884	0.467	0.948	0.318	0.969	0.246
0.40	0.40	0.865	0.500	0.938	0.348	0.962	0.278
	0.29	0.875	0.484	0.947	0.320	0.971	0.237
0.50	0.32	0.863	0.504	0.941	0.337	0.965	0.260
	0.23	0.868	0.496	0.945	0.327	0.968	0.253

Numerical Data

Consider a sea state described by a JONSWAP wave spectrum with f_p = 0.5Hz, H_{m0} = 0.3m, and γ = 3.3. The waves are incident on a 0.1m high section of an offshore structure located an elevation of 1.5m above the seabed in water of depth 2m. Typical force coefficient values $C_D = 1$ and $C_M = 2$ are assumed. Cylinder diameters D of 0.17m and 0.03m are used to model inertia and drag dominated regimes respectively. The ratio of the standard deviation of the drag to inertia forces are 0.13 and 0.73 for D = 0.17m and D = 0.03m respectively.

The theoretical probability density of the peaks of the resultant force are plotted in figures 6.71 and 6.72 for inertia and drag regimes respectively. The distributions are plotted for a long-crested and three short-crested cases (s = 1, 3, and 6). For the long-crested case, the distribution is essentially Rayleigh for the inertia case and exponential at the high force levels for the drag case.

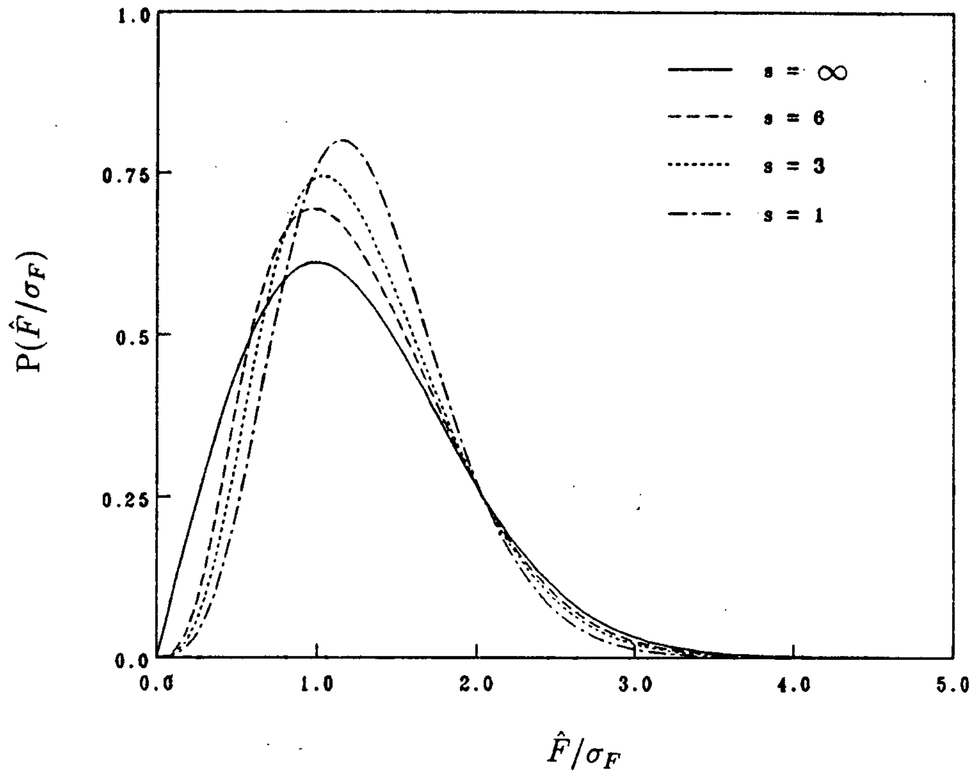

Figure 6.71: Probability distribution of the peaks of the resultant force in long-crested and short-crested seas (D = 0.17m)

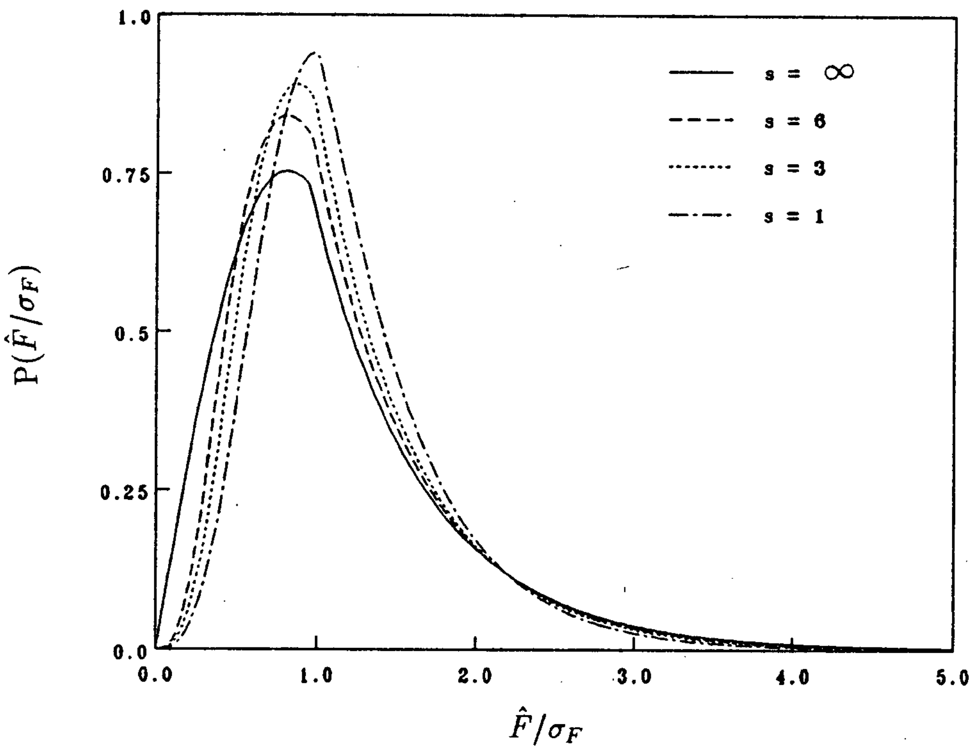

Figure 6.72: Probability distribution of the peaks of the resultant force in long-crested and short-crested seas (D = 0.03m)

Table 6.3: Nondimensional resultant force values F_R/σ_{F_R} for different probabilities of exceedance

$1 - P(\frac{F_R}{\sigma_{F_R}})$	$D = 0.17$m		$D = 0.03$m	
	$s = 1$	$s = \infty$	$s = 1$	$s = \infty$
$1/10^2$	2.69	3.01	3.15	3.62
$1/10^3$	3.25	3.68	4.35	5.20
$1/10^4$	3.72	4.25	5.53	6.75
$1/10^5$	4.13	4.74	6.54	8.14

It is useful to observe the differences between the long-crested and resultant short-crested wave forces at the tails of the distribution. It can be seen that for a given high force value (e.g. $3\sigma_F$), the probability of exceeding that level is much higher for long-crested than for short-crested waves. Alternately stated, design force values based on a certain level of exceedance will be much higher in long-crested than in short-crested waves. This can be seen more clearly in Table 6.3 where design force values based on low levels of exceedance are presented for the long-crested and $\cos^2\theta$ multi-directional sea states. It can be seen from Table 6.3 that for any given probability of exceedance, the design values of the resultant force maxima in the $\cos^2\theta$ multi-directional sea state are reduced. For a probability of exceedance of $1/10^5$, the design force value is reduced by 13% for the inertia case, and by 20% for the drag case.

The importance of retaining the nonlinearity of the drag force in extreme value predictions becomes apparent when the design force values of the inertia and drag dominated forces are compared. For the long-crested drag dominant case, the design force value with a $1/10^5$ chance of being exceeded is $8.14\sigma_F$. Linearization would result in a Rayleigh distribution of force peaks, which predicts a design force value of $4.74\sigma_F$. Linearization thus results in an underestimation of the design force value by 42% for this particular example. For force distributions with a higher ratio of drag to inertia forces, the underestimation of the extreme force values would be even more severe.

The distribution of the force peaks can be used to obtain the probability distribution of the maximum force value in a sea state with N peaks which in turn is used to determine the expected value and standard deviation of the single largest peak force in a storm of a given duration. Figures 6.73 to 6.76 show the probability distributions of the single largest resultant force in inertia and drag dominated long-crested and short-crested sea states respectively, for $N = 1900$. The maximum force distributions are plotted together with the peak force distributions. The figures show a wider maximum force distribution for the drag dominated regimes, implying a broader range of possible maximum force values. As N increases, the extreme force distribution shifts to the right and becomes narrower.

The expected value of the maximum resultant force in a sea state with N peaks is plotted against N for different multi-directional sea states in figures 6.77 and 6.78. The expected values are shown for inertia and drag dominated forces respectively. The figures clearly show that the expected value of the maximum resultant force is reduced in multi-directional waves. As an example, consider a sea state with 10000 peaks. The expected value of the maximum resultant force is reduced by 12.8%, 6.5%, and 3.8% for $s = 1$, 3, and 6 respectively for the inertia case, and by 18.4%, 8.9%, and 5.0% respectively for the drag case.

Numerically synthesized water particle velocities and accelerations were used to compute the force time series in long-crested and short-crested seas. The wave kinematics were synthesized by the single summation, random phase method for a long-crested and three multi-directional sea states ($s = 1$, 3, and 6). Frequency bandwidths of 0.02Hz

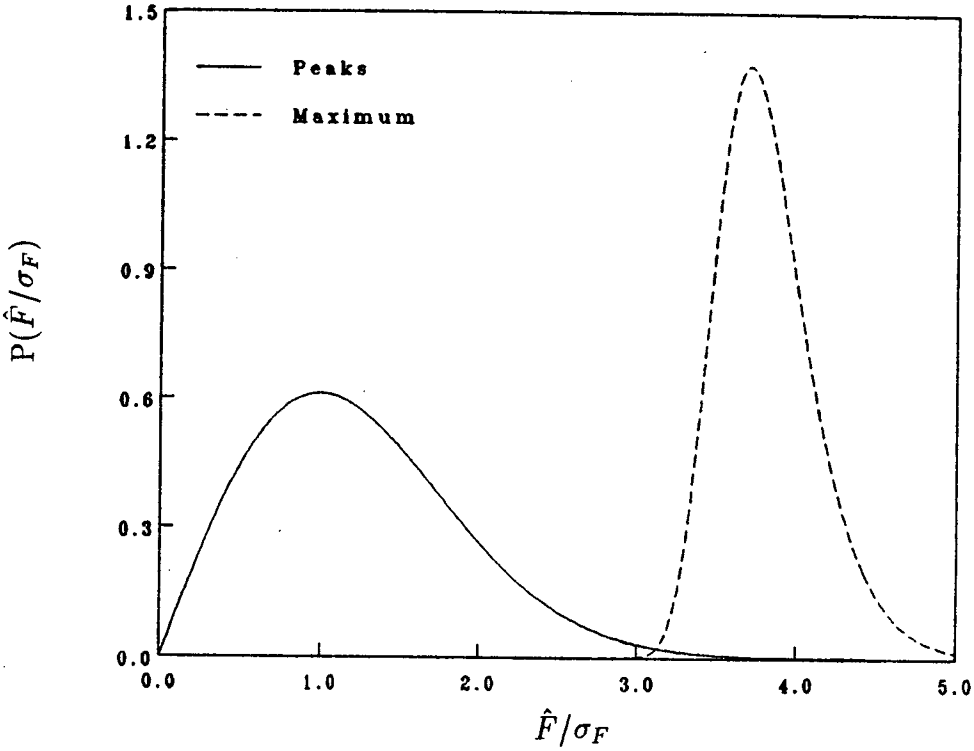

Figure 6.73: Peak and extreme force distributions for long-crested waves (D = 0.17m)

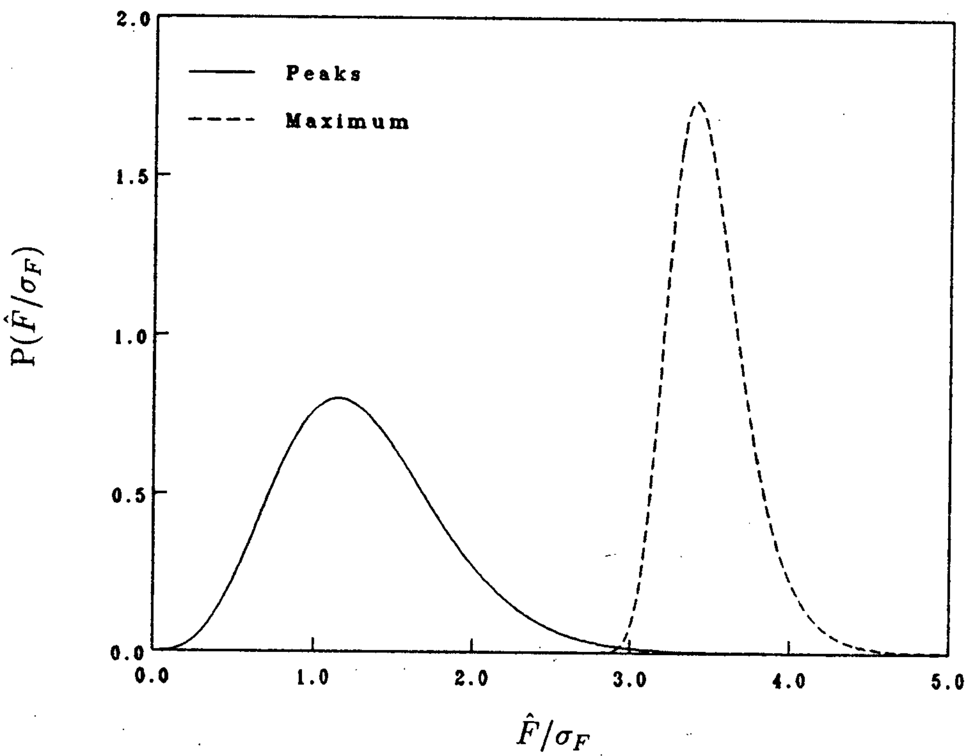

Figure 6.74: Peak and extreme force distributions for short-crested waves (D = 0.17m, s = 1)

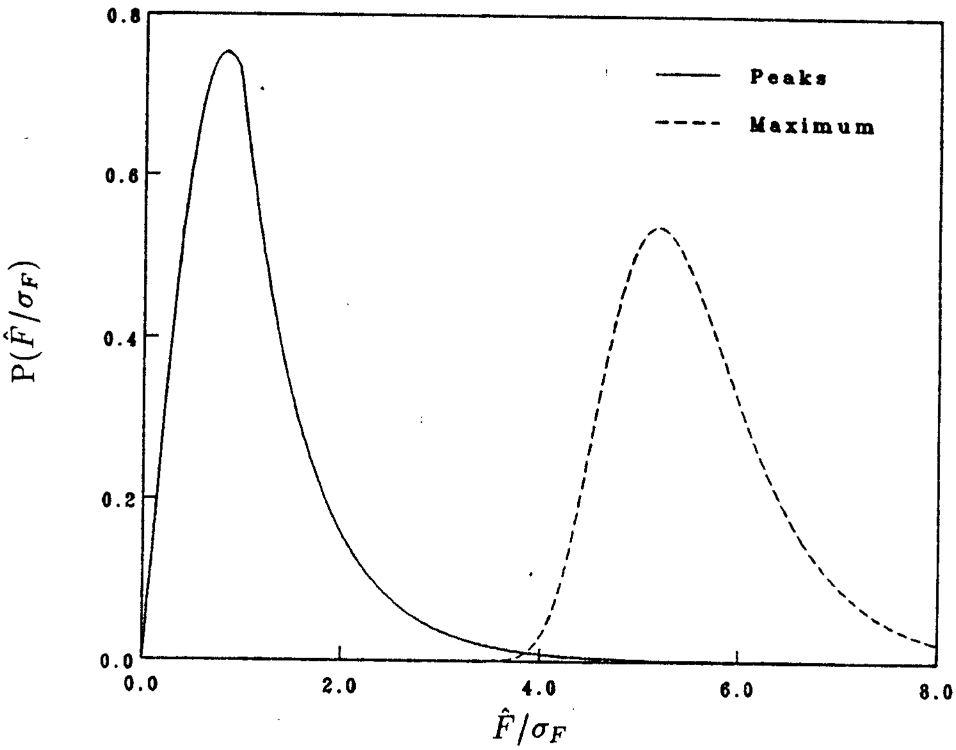

Figure 6.75: Peak and extreme force distributions for long-crested waves (D = 0.03m)

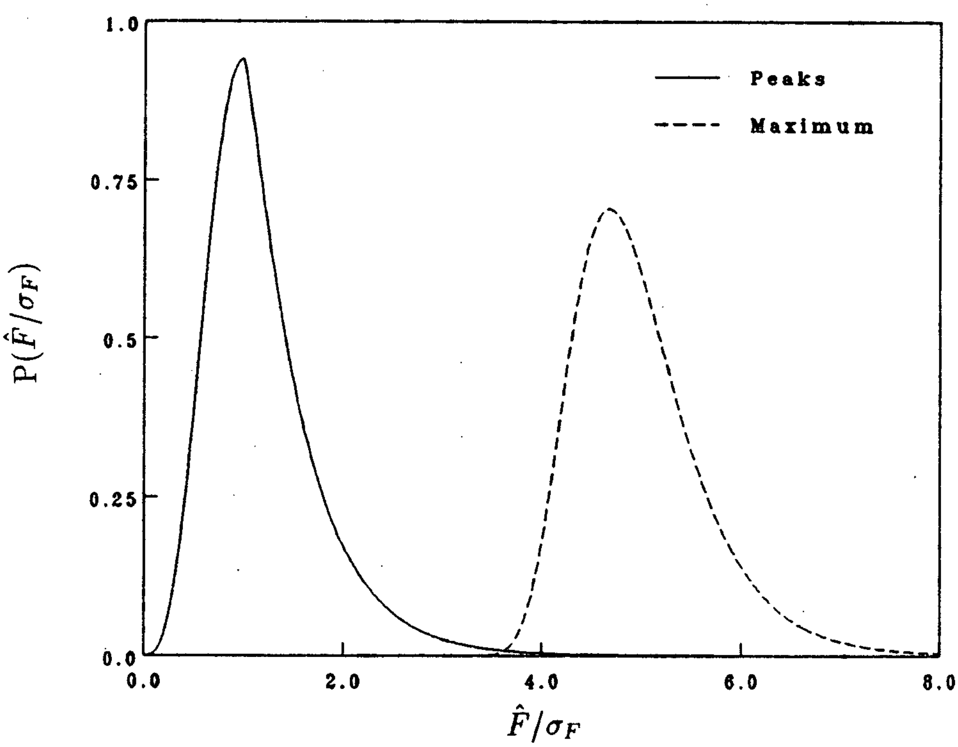

Figure 6.76: Peak and extreme force distributions for short-crested waves (D = 0.03m, s = 1)

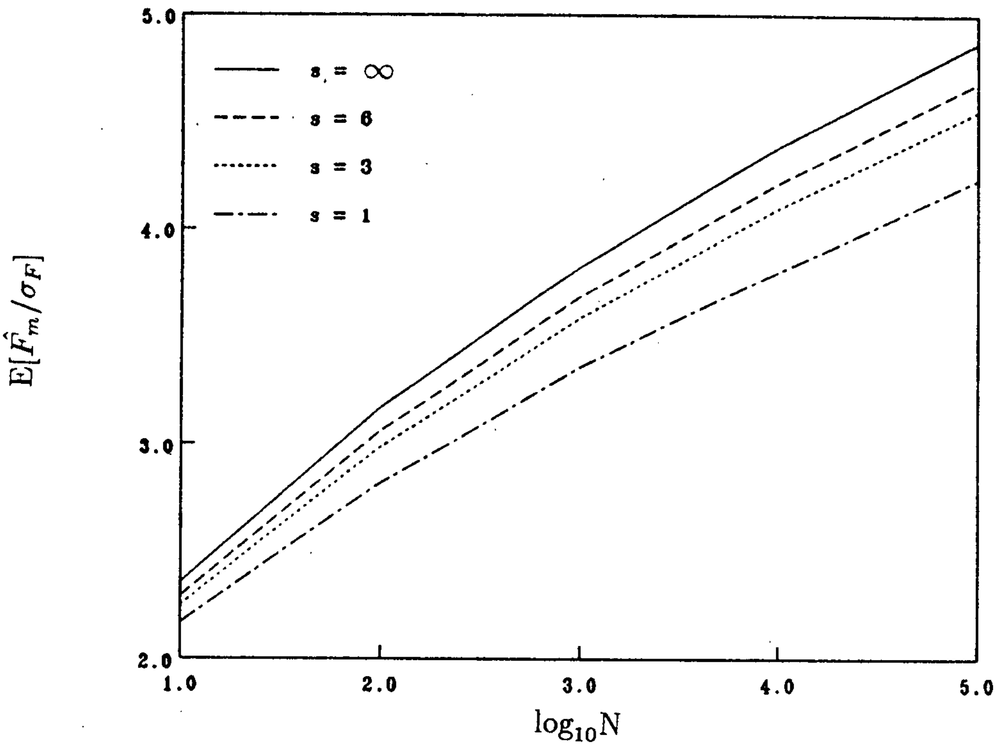

Figure 6.77: Expected values of the maximum force in long-crested and short-crested waves (D = 0.17m)

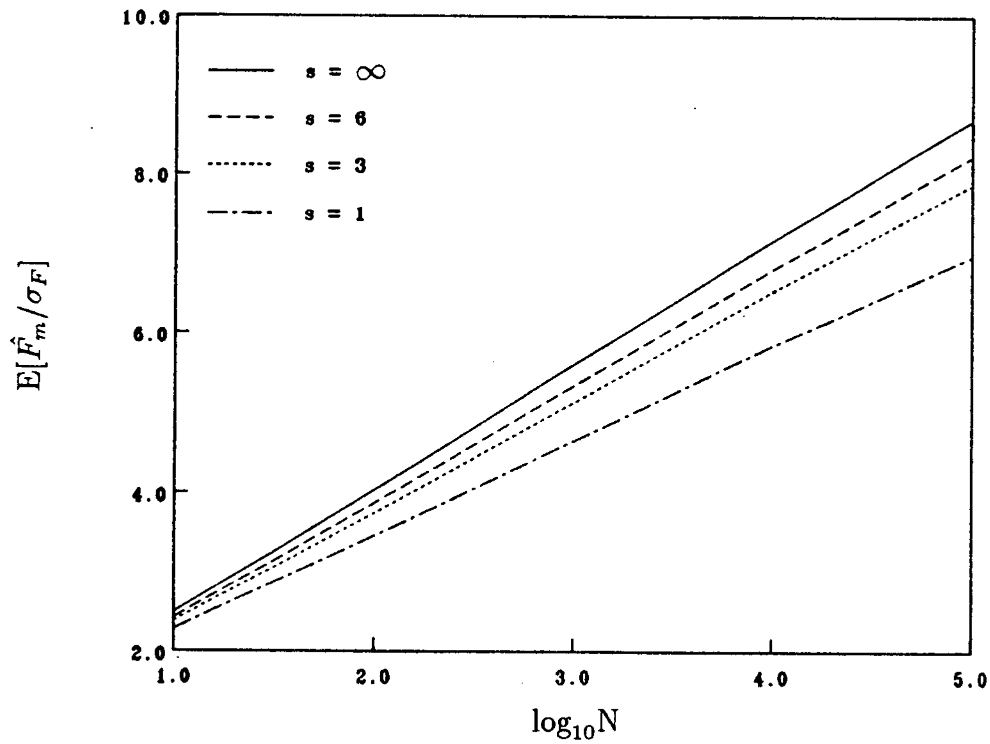

Figure 6.78: Expected values of the maximum force in long-crested and short-crested waves (D = 0.03m)

Table 6.4: Standard deviation and maximum values of the resultant force in multi-directional waves (numerical data)

	$D = 0.17$m		$D = 0.03$m	
	σ_{F_R} (N)	F_{Rmax} (N)	σ_{F_R} (N)	F_{Rmax} (N)
$s = 1$	2.155	7.32	0.079	0.40
$s = 3$	2.158	7.44	0.081	0.43
$s = 6$	2.159	7.61	0.082	0.43
$s = \infty$	2.159	8.28	0.082	0.41

were used in the synthesis with 32 directions per frequency band. This resulted in time series with record lengths of 1638.4s at a time interval of 0.2s.

The standard deviation and maximum values of the resultant force obtained from the synthesized data are presented in Table 6.4 for cylinder diameters of 0.17m and 0.03m. It should be noted that the maximum values presented in Table 6.4 correspond to only one simulation. The use of a different set of random number seeds would produce a different set of maximum force values, even though the standard deviation would stay approximately the same.

For the inertia dominated force ($D = 0.17$m), the standard deviation of the resultant force in short-crested and long-crested waves are approximately the same, while the maximum value of the force decreased by as much as 11%. For the drag dominated force ($D = 0.03$m), the standard deviation of the resultant force decreased in short-crested waves. This confirms the earlier observation that the nonlinearity of the drag force results in a reduction of the standard deviation of the resultant force in short-crested seas.

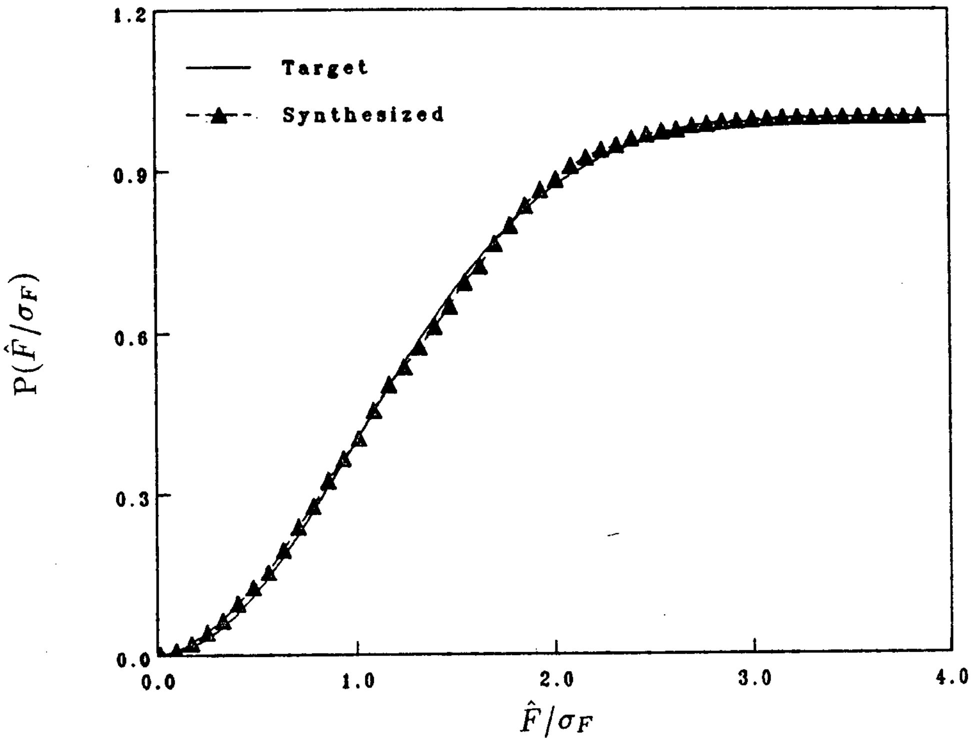

Figure 6.79: Simulated and predicted probability distribution of the force peaks in long-crested waves (D = 0.17m)

The maximum force values for the drag dominant case were not as much reduced in multi-directional waves. This might be anticipated since the extreme force distribution for drag dominated regimes are quite broad, implying a possible large variation of the maximum force value from one simulation to the next. The values presented correspond to only one simulation. If a large number of simulations were carried out and an ensemble average of the maximum force was taken, one would expect to see a reduction of the maximum resultant drag force in multi-directional waves.

The distribution of the peaks of the simulated forces are compared with the theoretical distribution in figures 6.79 to 6.82. The comparisons are shown for both long-crested and short-crested ($s = 1$) waves. The theoretical distributions fit the simulated data distributions rather well, particularly at the tail of the distribution.

The maximum force values obtained from the numerically synthesized data are compared with predictions from the theoretical distribution in Table 6.5. All the synthesized

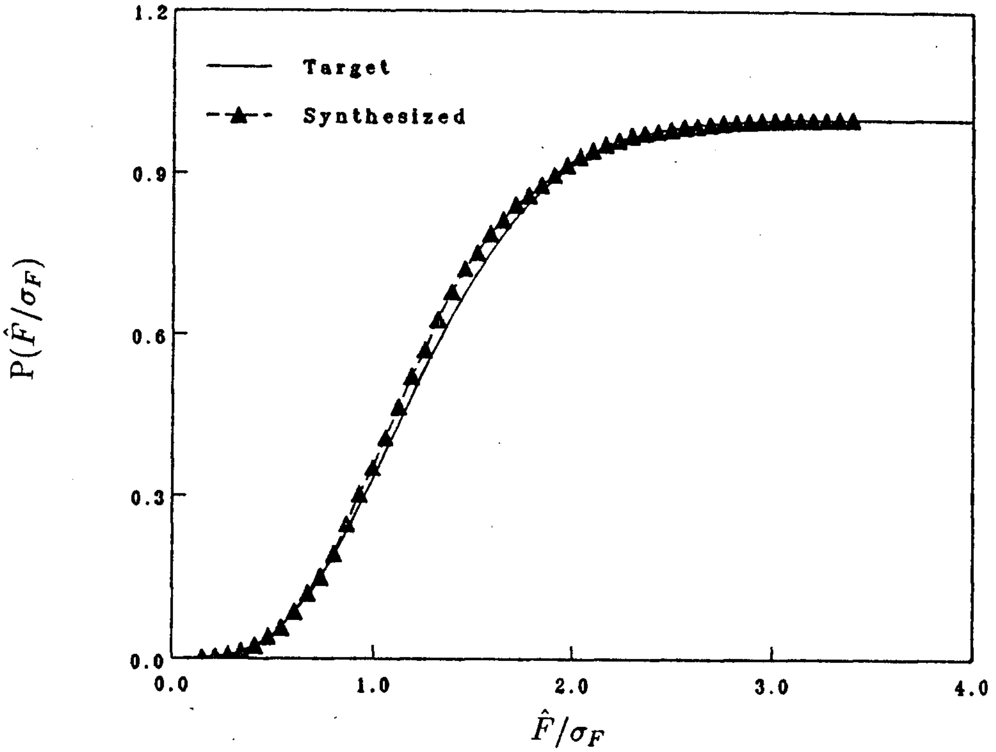

Figure 6.80: Simulated and predicted probability distribution of the resultant force peaks in short-crested waves (D = 0.17m, s = 1)

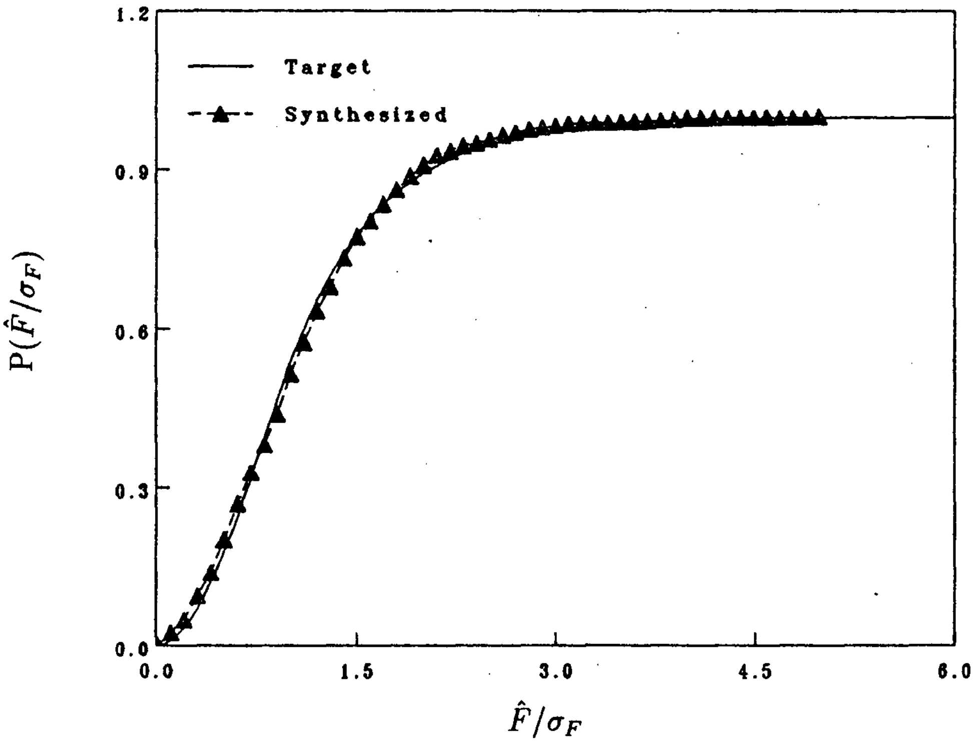

Figure 6.81: Simulated and predicted probability distribution of the force peaks in long-crested waves (D = 0.03m)

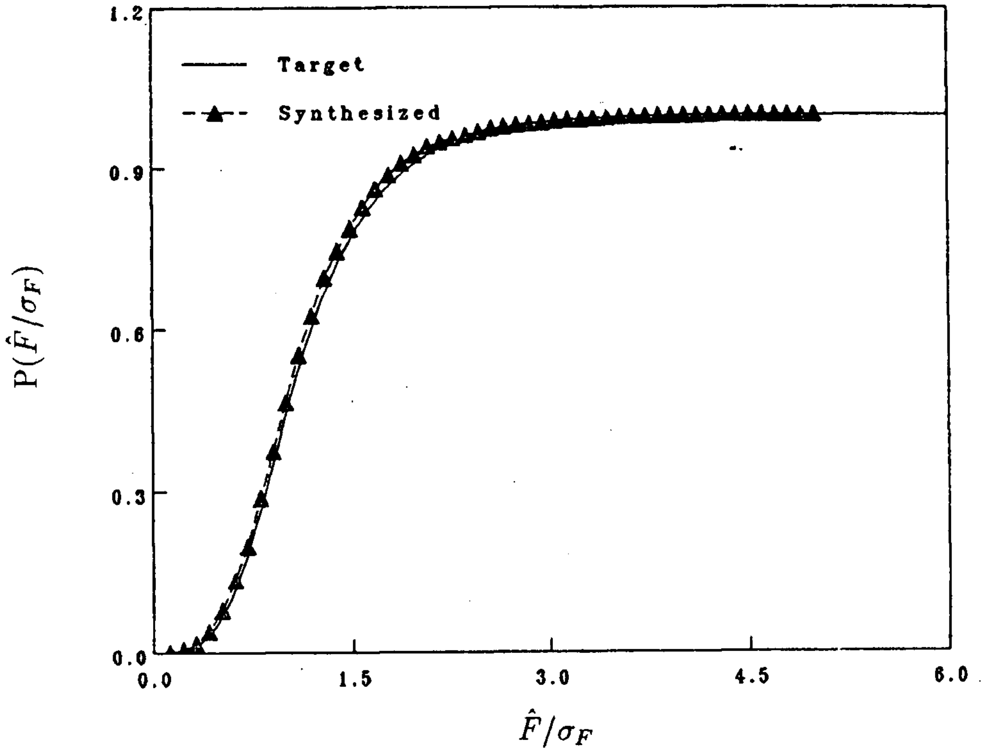

Figure 6.82: Simulated and predicted probability distribution of the resultant force peaks in short-crested waves (D = 0.03m, s = 1)

Table 6.5: Simulated and predicted maximum values of the resultant force

		N	simulated	predicted	
			F_{Rmax}/σ_{F_R}	$E[F_{Rmax}]/\sigma_{F_R}$	$\sigma_{F_{Rmax}}/\sigma_{F_R}$
$D = 0.17$m	$s = \infty$	956	3.85	3.82	0.32
	$s = 1$	1915	3.40	3.50	0.25
$D = 0.03$m	$s = \infty$	950	4.99	5.46	0.88
	$s = 1$	1906	4.99	4.98	0.67

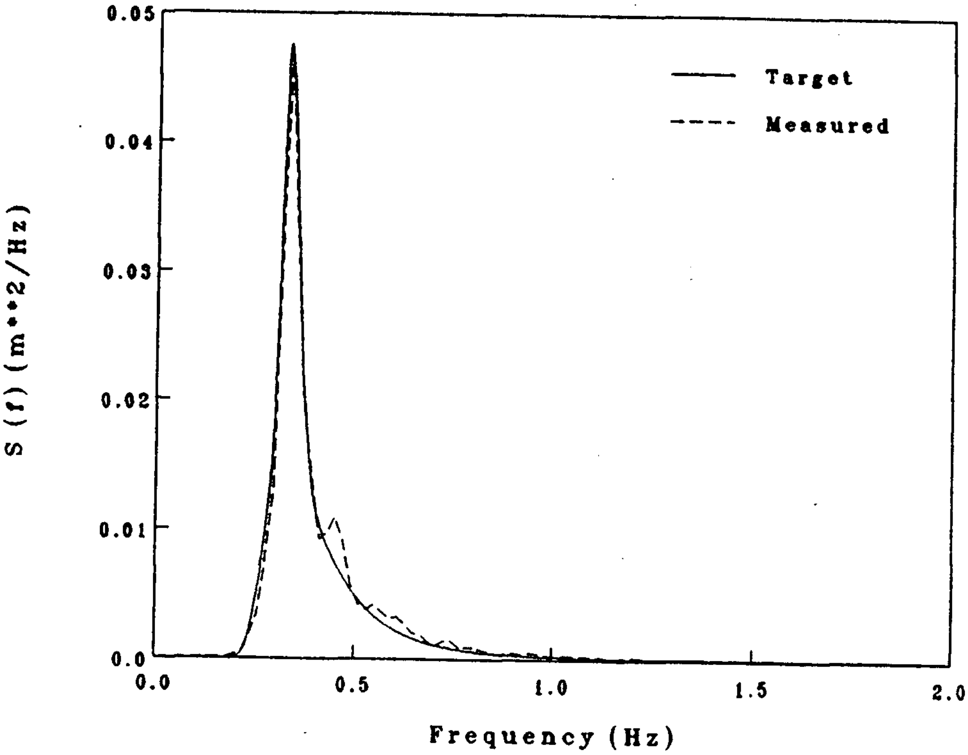

Figure 6.83: Comparison of measured and target water surface elevation spectra (f_p = 0.33Hz, H_{m0} = 0.29m)

maximum force values are seen to lie within one standard deviation of the theoretical expected maximum force values.

Experimental Data

Force data obtained in the second phase of the experiments with the segmented cylinder were used to obtain probability distributions which are compared with the theoretical distributions. Attention is now focussed on the unidirectional and multi-directional sea states described by a JONSWAP spectrum with f_p = 0.33Hz, H_{m0} = 0.29m, and γ = 3.3. Data was sampled at a rate of 10Hz for 819.2s. Figure 6.83 shows a comparison of the measured and target water surface elevation spectrum for the long-crested case. The measured spectrum is seen to match the target wave spectrum reasonably well.

Force coefficients were obtained from a least squares fit of the measured to the predicted force spectra. The best fit force coefficients of the bottom seven segments which

Table 6.6: Drag and Inertia force coefficients for long-crested waves ($f_p = 0.33$Hz, $H_{m0} = 0.29$m, $\gamma = 3.3$)

Segment	C_M	C_D
1	0.94	0.00
2	1.50	0.00
3	2.00	0.00
4	2.01	0.00
5	2.68	0.00
6	1.83	0.00
7	2.14	0.16

remained fully submerged at all times are presented in Table 6.6. The inertia coefficient is seen to vary from 1 to 2.7 over the height of the column. The variation of the inertia force coefficient over the height of the column did not show any apparent dependence on the Keulegan-Carpenter or Reynolds numbers. The significant variation of the force coefficient might be due to either a significant deviation of the measured kinematics from linear wave theory predictions, or coupling of the loading on some segments. An overall inertia force coefficient for the whole column was determined by weighting each segment coefficient with the standard deviation of the segment force. This yielded an overall C_M value of 2.04 which is in keeping with previously published experimental values.

The estimated drag force coefficients are mostly zero because the data was ill-suited for the determination of the drag force coefficient. The predicted force spectrum is not noticeably affected by a change of the drag force coefficient from 0 to 1, and the least squares approach cannot be expected to yield reasonable values of the drag force

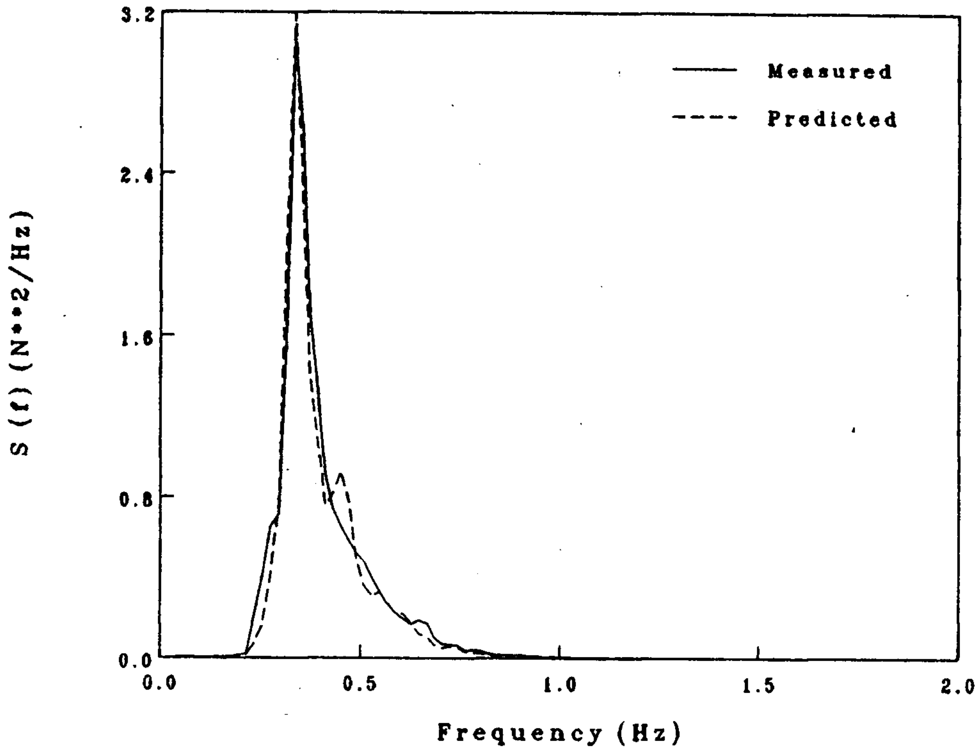

Figure 6.84: Comparison of measured and predicted inline force spectra for long-crested waves (segment 1)

coefficient in such situations.

The measured and predicted force spectral densities of segments 1 and 7 are compared in figures 6.84 and 6.85 respectively. The linearized Morison formulation is seen to predict the measured force spectra quite well. The force spectrum for segment 7 is seen to have more high frequency components. This is because of the relative magnification of the linear theory transfer function for the water particle acceleration as the segment elevation approaches the still water level.

The measured water surface crest elevations of the long-crested and short-crested ($s \approx 1$) sea states are compared with the Rayleigh distribution in figures 6.86 and 6.87 respectively. The Rayleigh distribution is seen to fit the measured crest elevations quite well. The corresponding measured and predicted probability distributions of the long-crested and short-crested resultant forces of segments 1 and 7 are shown in figures 6.88 to 6.91. The theoretical distribution is based on a narrow-band assumption and is seen

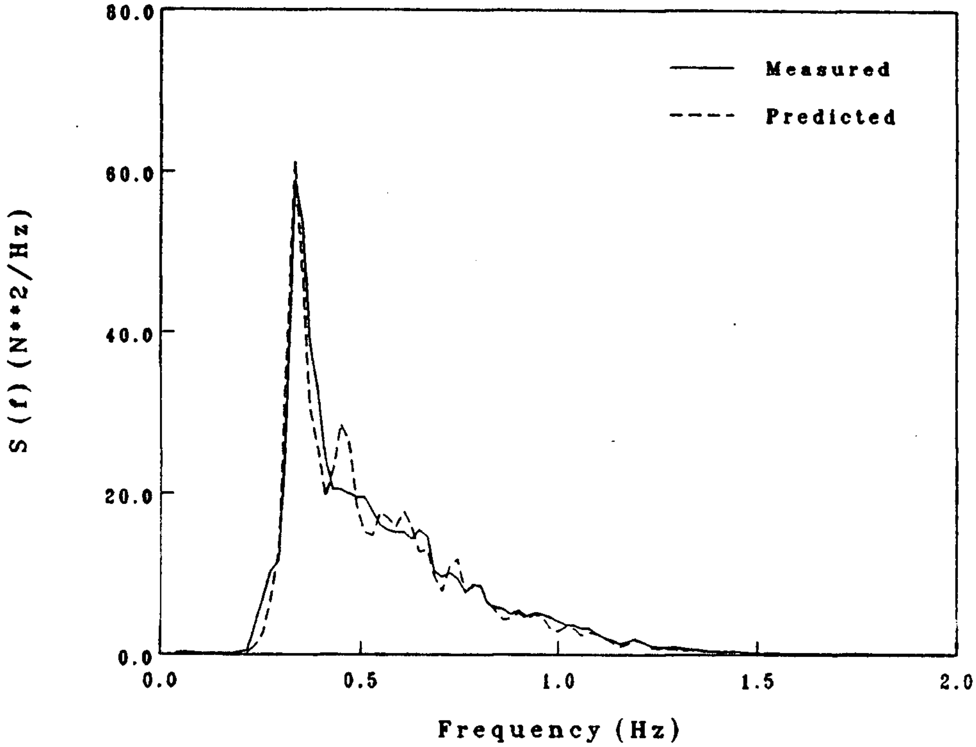

Figure 6.85: Comparison of measured and predicted inline force spectra for long-crested waves (segment 7)

to fit the measured distributions better at the tails of the distributions.

The measured maximum values of the force on all seven submerged segments for all the tests are presented in Table 6.7. The measured maximum resultant force values did not decrease in multi-directional waves as is predicted by theory, but did increase for most of the segments. Since the time histories of the long-crested and short-crested waves were not identical, one does expect some statistical variability in the measured maximum force values. The Rayleigh distribution predicts an expected maximum force value of $3.76\sigma_F$ to $3.86\sigma_F$ with a standard deviation of about $0.3\sigma_F$ for the number of peaks N (positive and negative) ranging from 650 to 950. Most of the long-crested maximum force values fall within that range while the short-crested ($s = 1$ & 3) maximum force values, particularly for segment 7, are much higher.

In order to understand why the measured maximum force in short-crested waves was higher than that in long-crested waves, time histories of the measured water surface

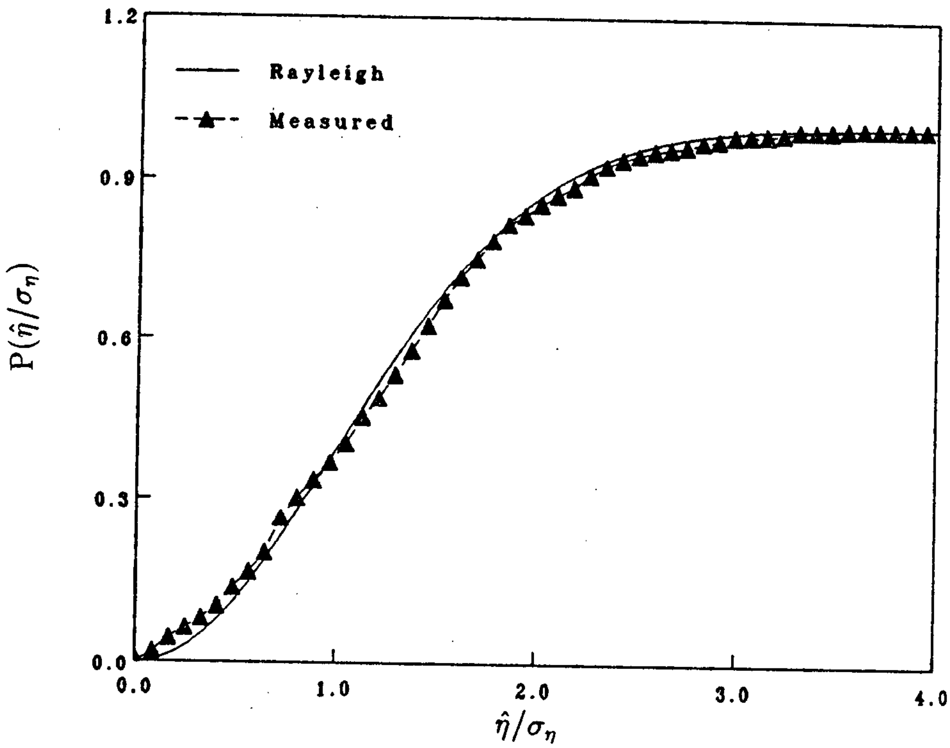

Figure 6.86: Comparison of measured crest elevation distribution with Rayleigh distribution (long-crested waves)

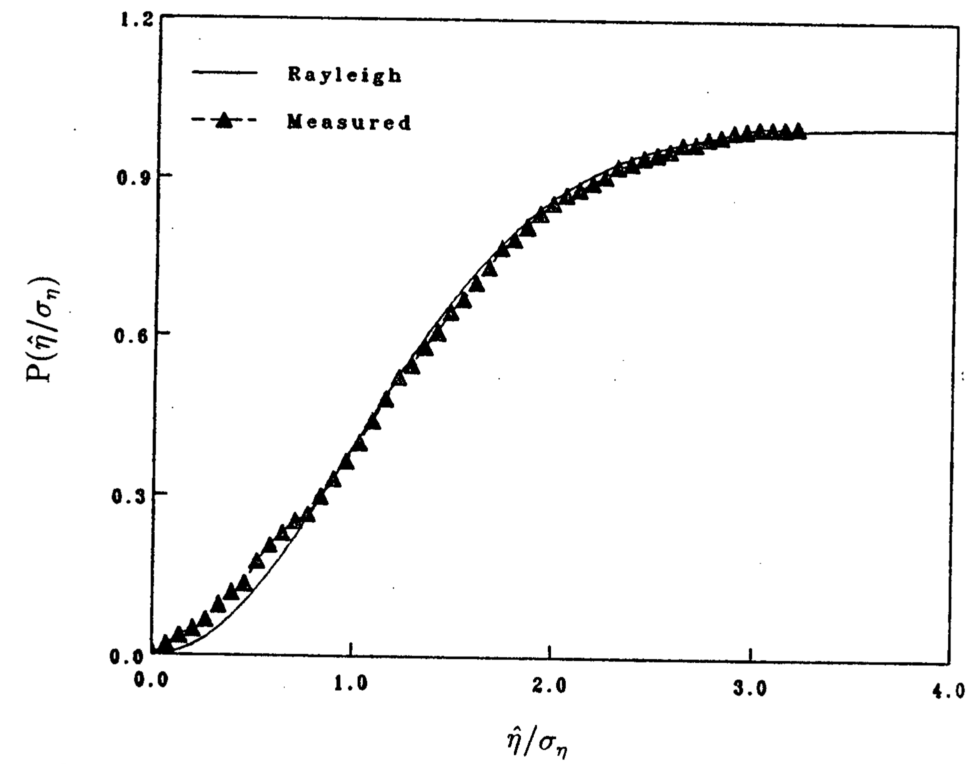

Figure 6.87: Comparison of measured crest elevation distribution with Rayleigh distribution ($s = 1$)

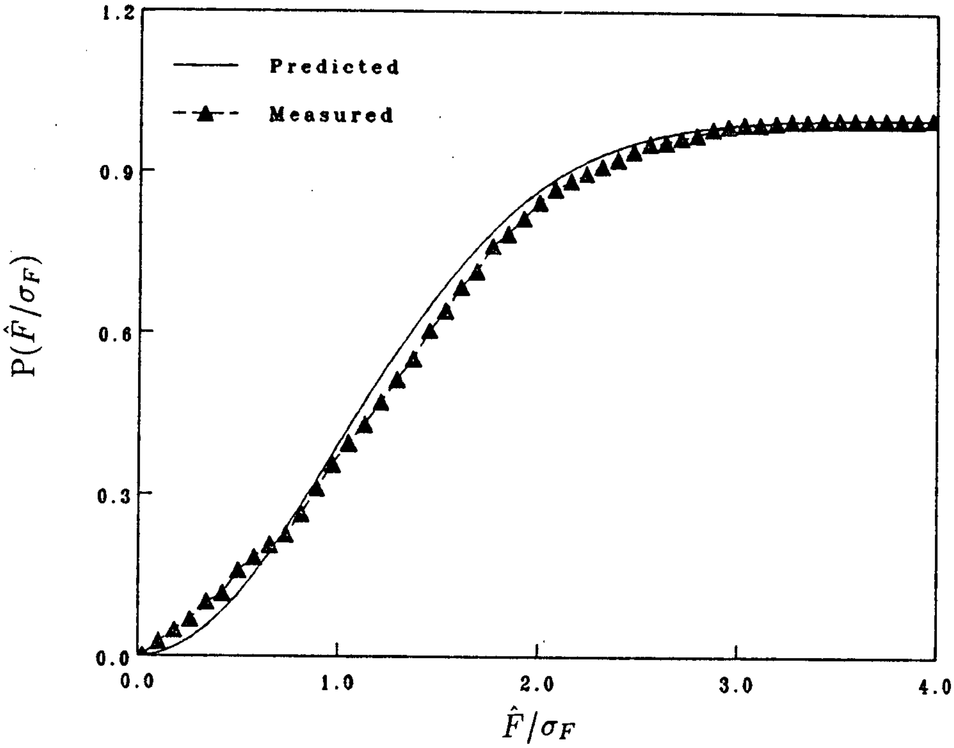

Figure 6.88: Measured and predicted probability distributions of the force peaks in long-crested waves (segment 1)

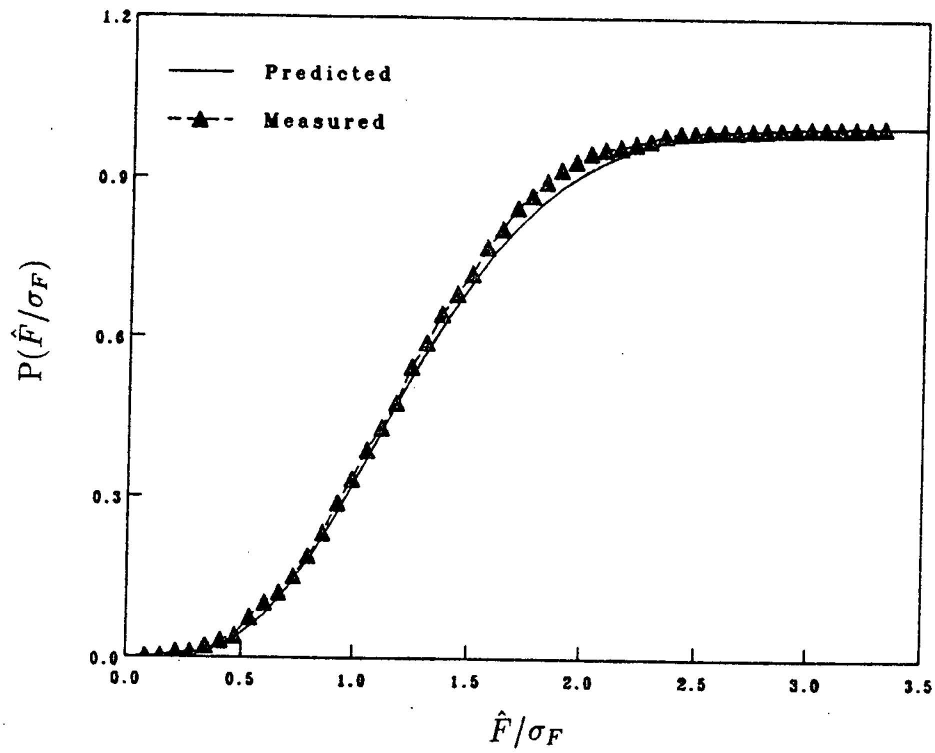

Figure 6.89: Measured and predicted probability distributions of the resultant force peaks in short-crested waves (segment 1, $s = 1$)

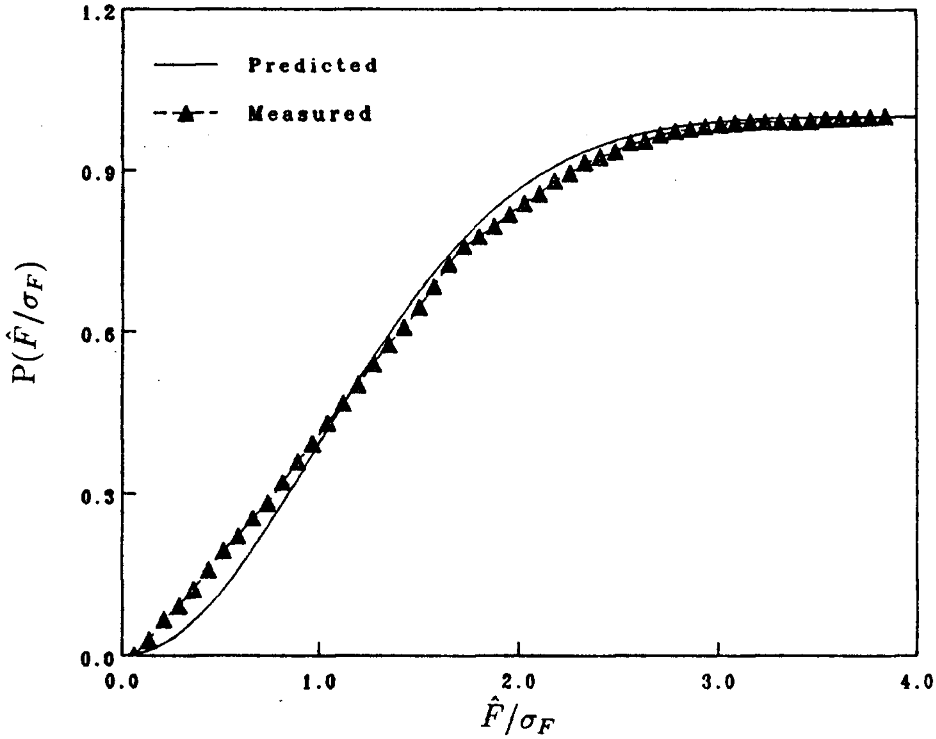

Figure 6.90: Measured and predicted probability distributions of the force peaks in long-crested waves (segment 7)

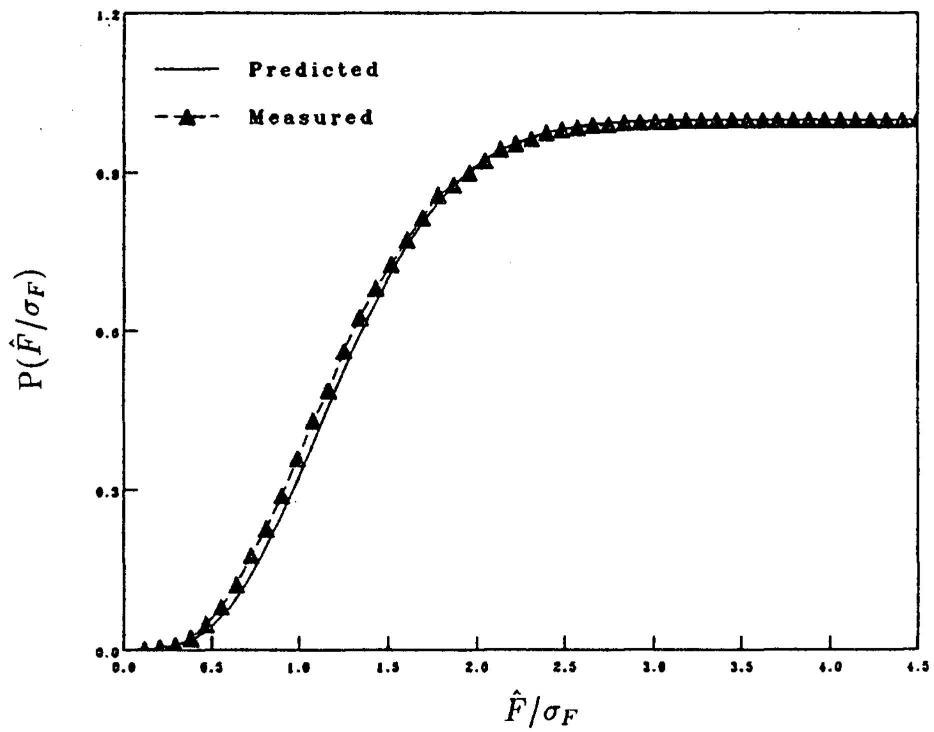

Figure 6.91: Measured and predicted probability distributions of the resultant force peaks in short-crested waves (segment 7, $s = 1$)

Table 6.7: Measured nondimensional maximum force values (F_{Rmax}/σ_{F_R}) - phase II

Segment	$s \approx 1$	$s \approx 3$	$s \approx 6$	$s \to \infty$
1	3.31	3.51	3.41	3.98
2	3.01	3.12	3.22	3.38
3	3.53	3.54	3.47	3.30
4	3.23	3.38	3.28	3.27
5	3.79	3.76	3.69	3.41
6	3.99	4.05	3.81	3.53
7	4.50	4.40	3.82	3.87

elevation, inline velocity, and inline forces on segments 1 and 7 are plotted over a small duration where the maximum segment forces occur. Figures 6.92 and 6.93 show the time histories for the long-crested and short-crested ($s \approx 1$) waves respectively. The figures clearly show that although the crests of the water surface elevation and inline water particle velocity were smaller for the short-crested wave, the corresponding maximum inline force on segment 7 is larger for the short-crested wave. The maximum force on segment 1 at the same instant of time is however smaller for the short-crested wave. A more careful look at the time histories of the water surface elevation and inline velocity of the short-crested wave shows a flat crest and a sharp decrease of the velocity at the crest, indicating that the maximum force might be due to wave breaking.

The maximum values of the resultant force on segment 3, obtained in first phase of the experiments, are presented in Table 6.8. Both the maximum positive and negative values of the long-crested wave force are presented in order to highlight the differences

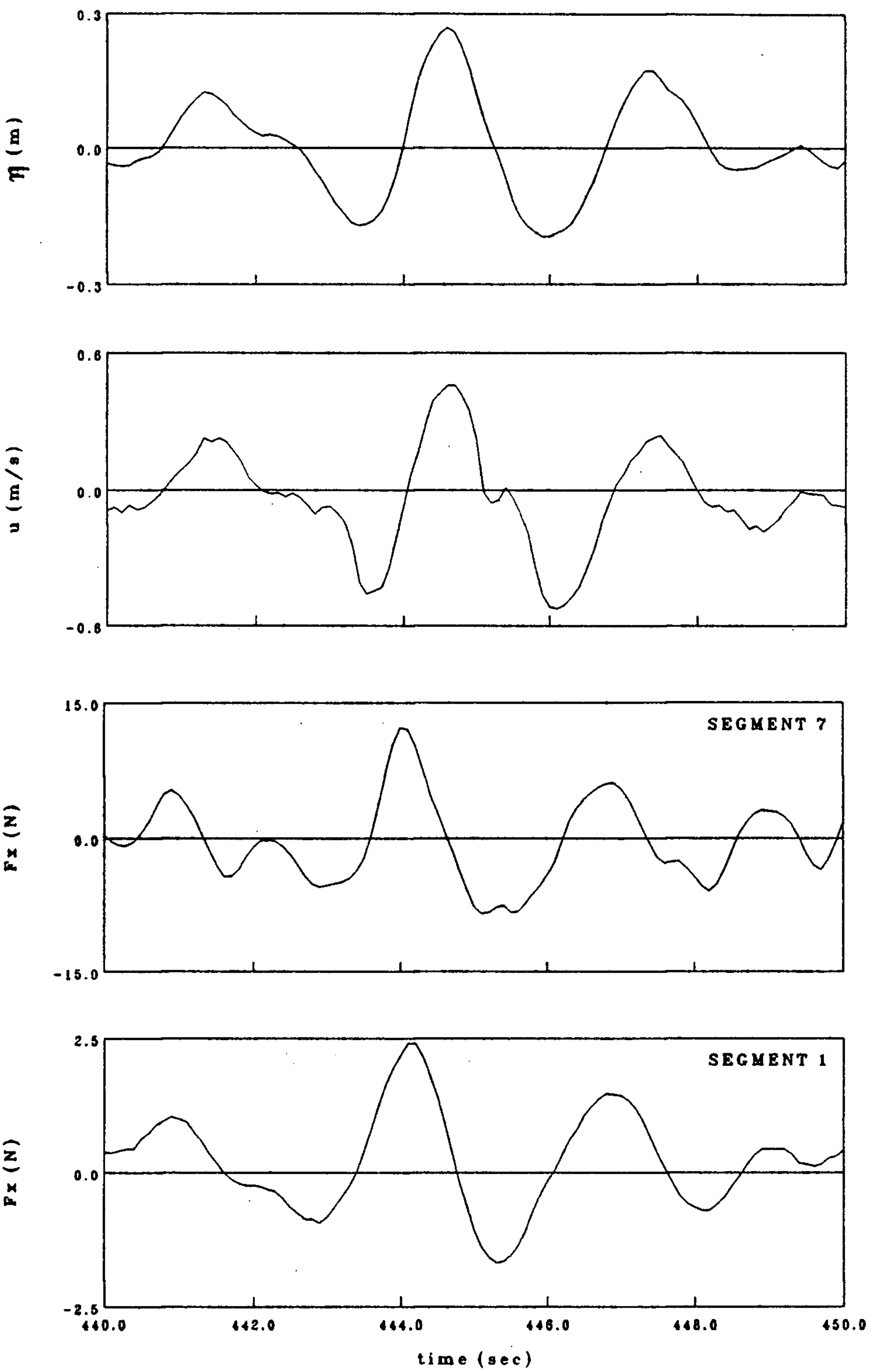

Figure 6.92: Time histories of water surface elevation, inline velocity, and maximum force for a long-crested wave

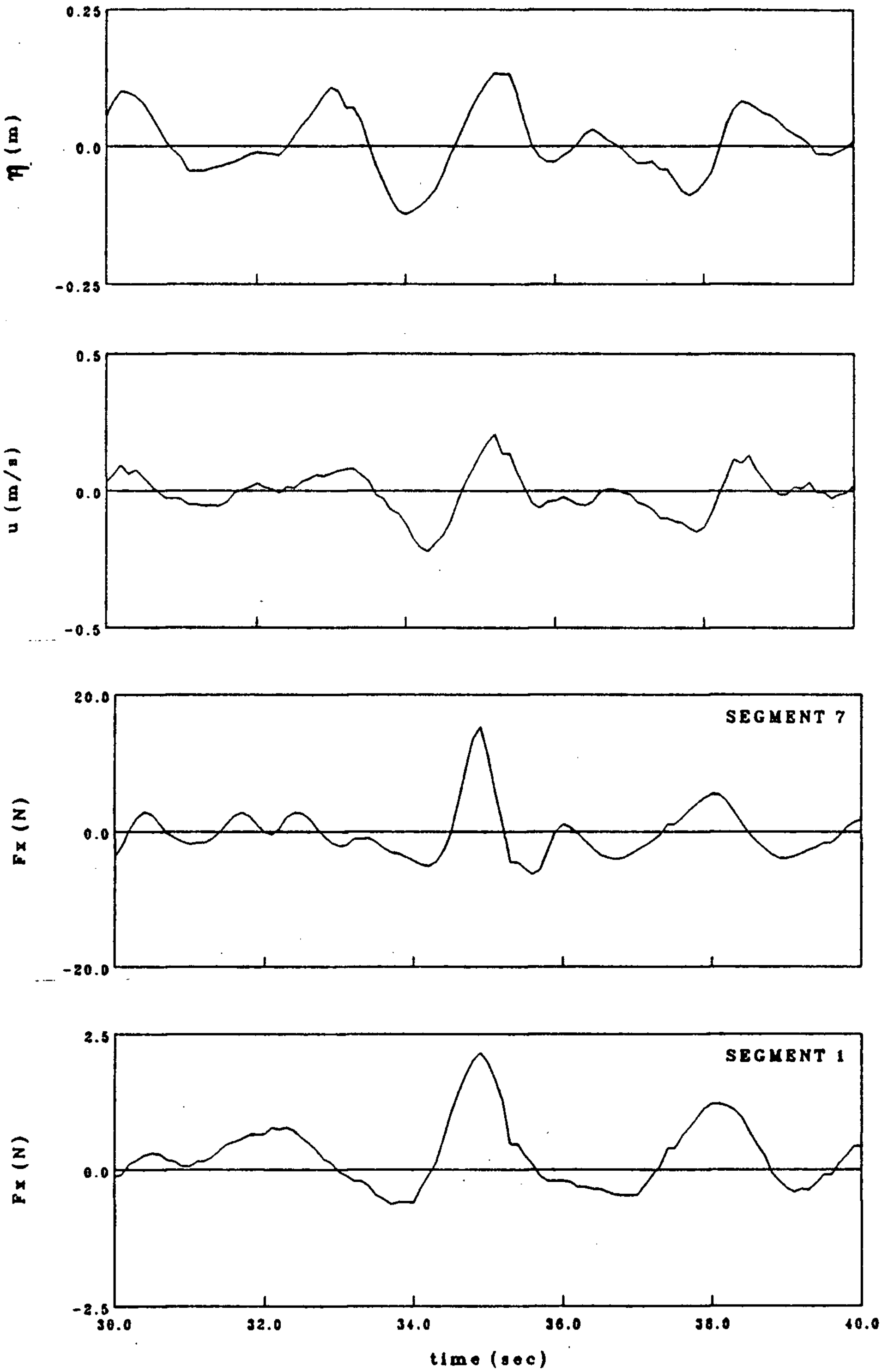

Figure 6.93: Time histories of water surface elevation, inline velocity, and maximum force for short-crested wave ($s = 1$)

Table 6.8: Measured nondimensional maximum force values (F_{Rmax}/σ_{F_R}) - phase I

f_p (Hz)	H_{m0} (m)	$s \approx 1$	$s \approx 3$	$s \approx 6$	$s \to \infty$
0.33	0.45	2.89	3.06	3.01	2.95(-4.29)
	0.31	2.86	3.22	3.33	2.65(-3.47)
0.40	0.40	2.88	3.27	3.60	3.17(-3.22)
	0.29	2.86	3.31	3.60	2.95(-3.83)
0.50	0.32	2.91	2.77	2.97	2.97(-3.38)
	0.23	3.11	3.01	3.37	3.03(-3.69)

between the positive and negative maximum peak forces. The maximum resultant forces are seen to be generally reduced in multi-directional waves for this set of tests.

The theoretical expected value of the maximum force varies from $3.41\sigma_F$ to $3.50\sigma_F$ for the long-crested waves, and from $3.06\sigma_{F_R}$ to $3.13\sigma_{F_R}$ for the short-crested waves ($s = 1$), for N varying from 210 to 280. The corresponding standard deviation of the maximum force is $0.35\sigma_F$ and $0.30\sigma_{F_R}$ for the long-crested and short-crested waves respectively. Most of the measured maximum force values are seen to lie within one standard deviation of the theoretical expected maximum force values.

6.3 Motions of a Floating Barge

The floating barge was tested in regular and random, unidirectional and multi-directional waves. A computer program based on linear diffraction theory (see Isaacson, 1985a) was used to compute the first order motions and steady drift force in regular waves. The measured response amplitude operators and mean drift force coefficients are compared with the computed results. The effect of wave directionality on the mooring line forces and motions of the barge in random seas is investigated by comparing results obtained for unidirectional and multi-directional sea states with the same frequency spectrum. The measured low frequency surge response spectra are compared with theoretical predictions based on the quadratic transfer function approach. Finally, the probability distributions of the first and second order motions are compared with the normal distribution.

6.3.1 Regular Waves

The regular wave test conditions consisted of six regular long-crested waves with periods ranging from 1.2s to 3.0s and wave heights ranging from 0.12m to 0.34m, and six crossing waves ($\alpha = 15°, 30°, 45°$) with periods of 1.5s and 2.0s.

General Observations

Typical time histories of the measured surge, heave, and pitch motions of the barge for the 1.5s, and 3.0s long-crested waves are shown in figures 6.94 and 6.95. Also shown on the figures are the forces on the most heavily loaded mooring line. The surge motion for the 1.5s wave is seen to have a large mean component and a relatively small first order oscillation component. The first order surge motions are however more dominant for the longer period waves with the surge motion for the 3.0s wave being almost entirely first order.

The diffraction pattern around the barge was observed to be more pronounced for the 1.2s and 1.5s waves, with substantial runup at the front of the barge. At a wave period of 1.5s which is close to the natural period for the heave and pitch motions, the barge motions were quite large with a large amount of water getting on the deck. The displacement of the wave generator had to be reduced during the experiments in order to minimize the motions of the barge.

Another important observation during the experiments was the restriction of the first

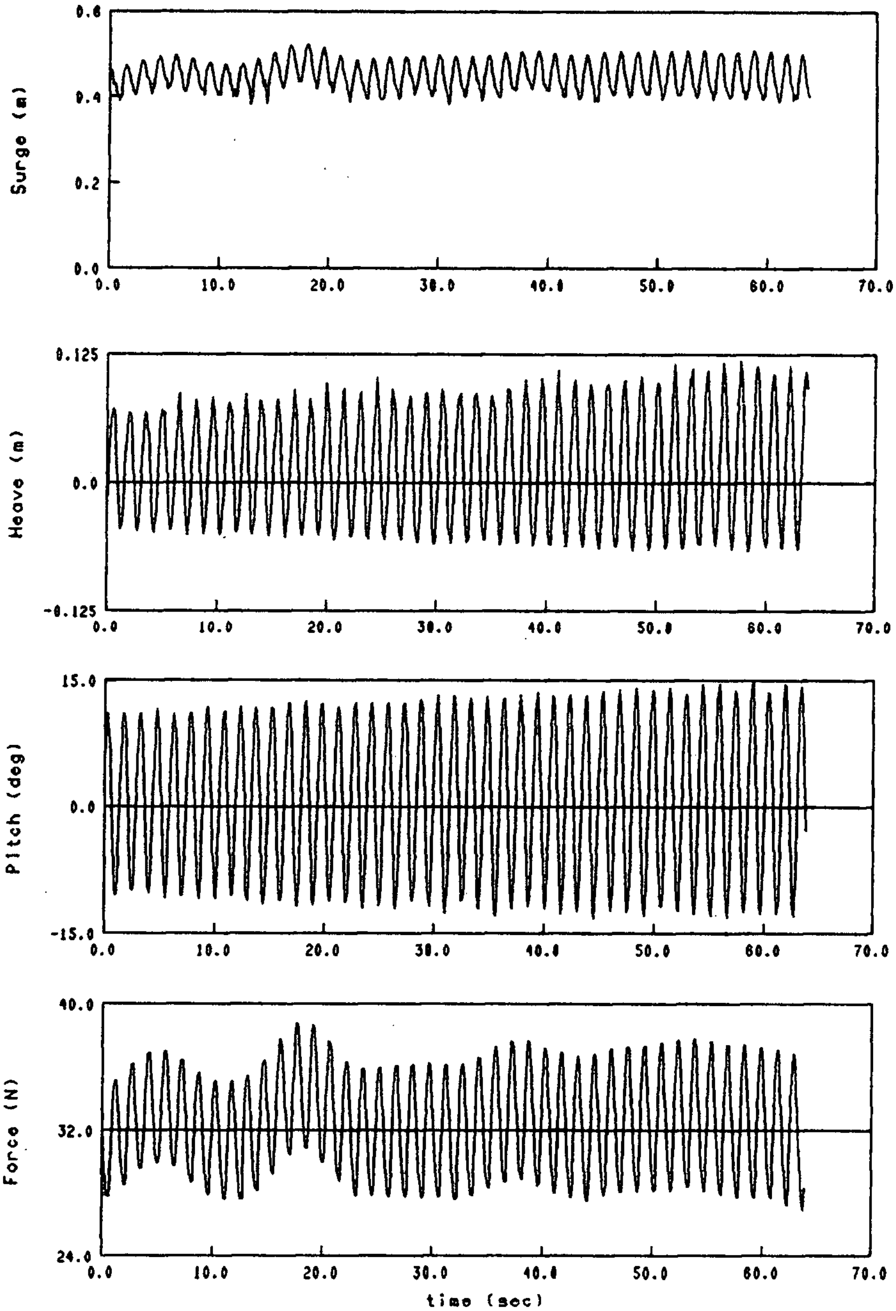

Figure 6.94: Time histories of the barge motions and mooring line force in regular waves (T = 1.5s)

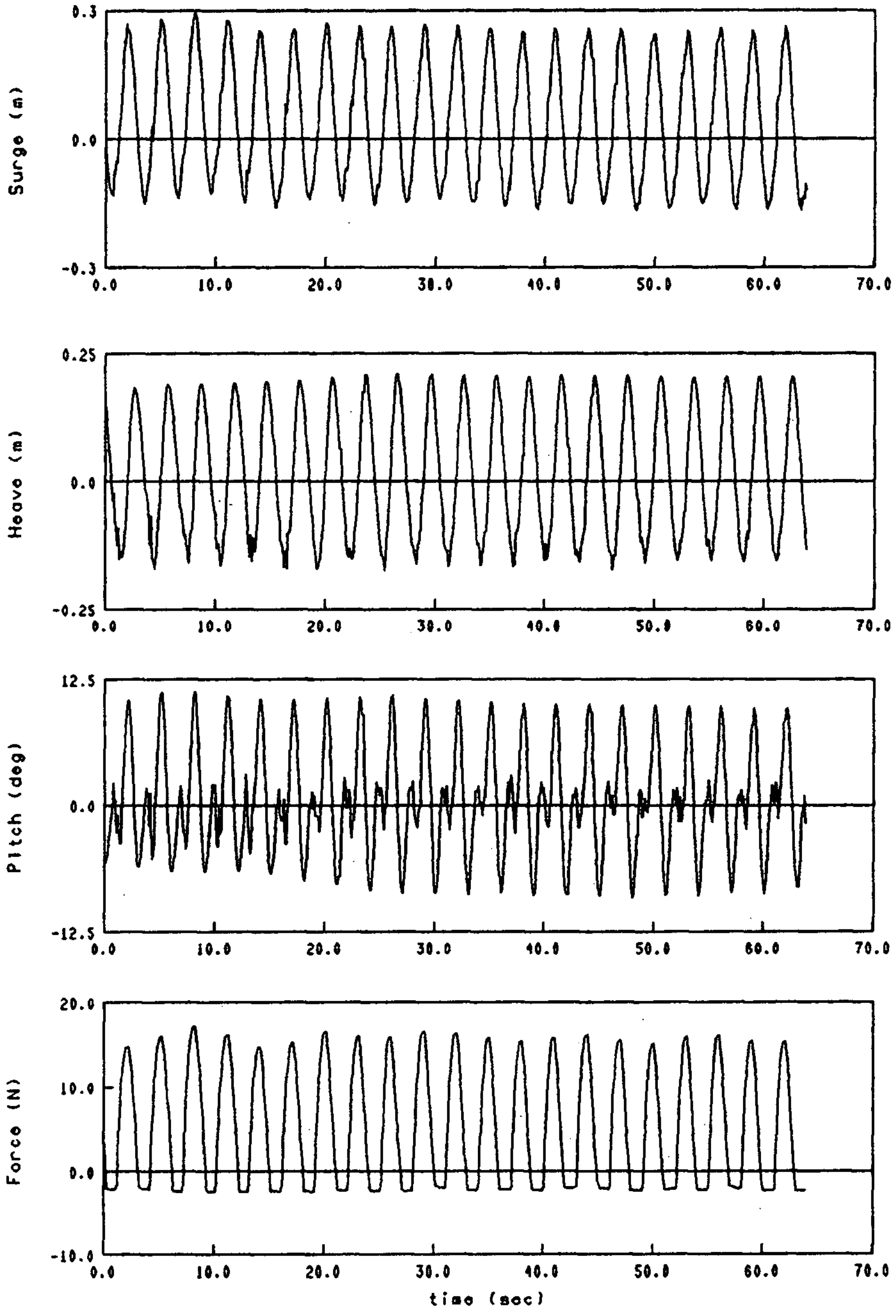

Figure 6.95: Time histories of the barge motions and mooring line force in regular waves (T = 3.0s)

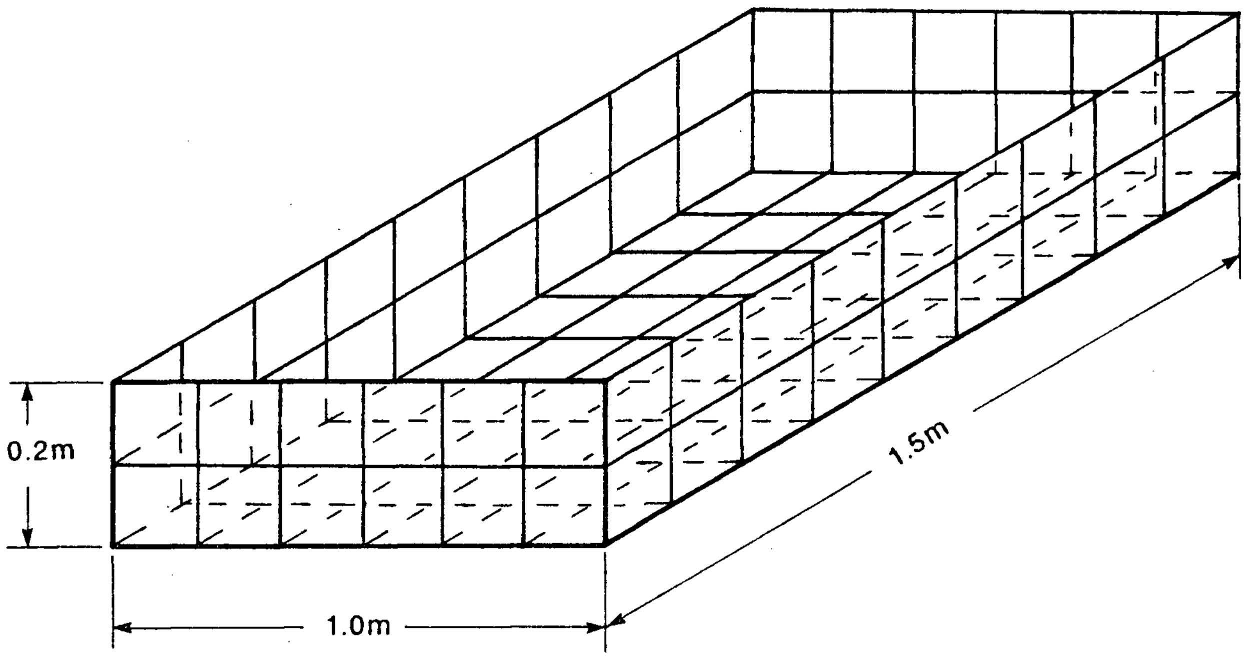

Figure 6.96: Discretized surface of rectangular barge

order surge motions of the barge by the mooring lines for the longer period 2.5 and 3.0s waves. This affected the amplitude of the pitch motions for those waves as can be seen in figure 6.95.

Comparison with Linear Diffraction Theory

Theoretical predictions of the first order motions of the barge were obtained using linear diffraction theory. The wetted surface of the box was modelled with 9 facets along its length, 6 facets along its width, and 2 facets along its depth, as shown in figure 6.96. This resulted in a total of 114 facets.

The measured and computed response amplitude operators for the first order surge, heave, and pitch motions of the barge are plotted in figures 6.97 to 6.99. The measured average peak to trough motion amplitudes have been nondimensionalized with respect to the wave height for the surge and heave motions, and with respect to the half-beam

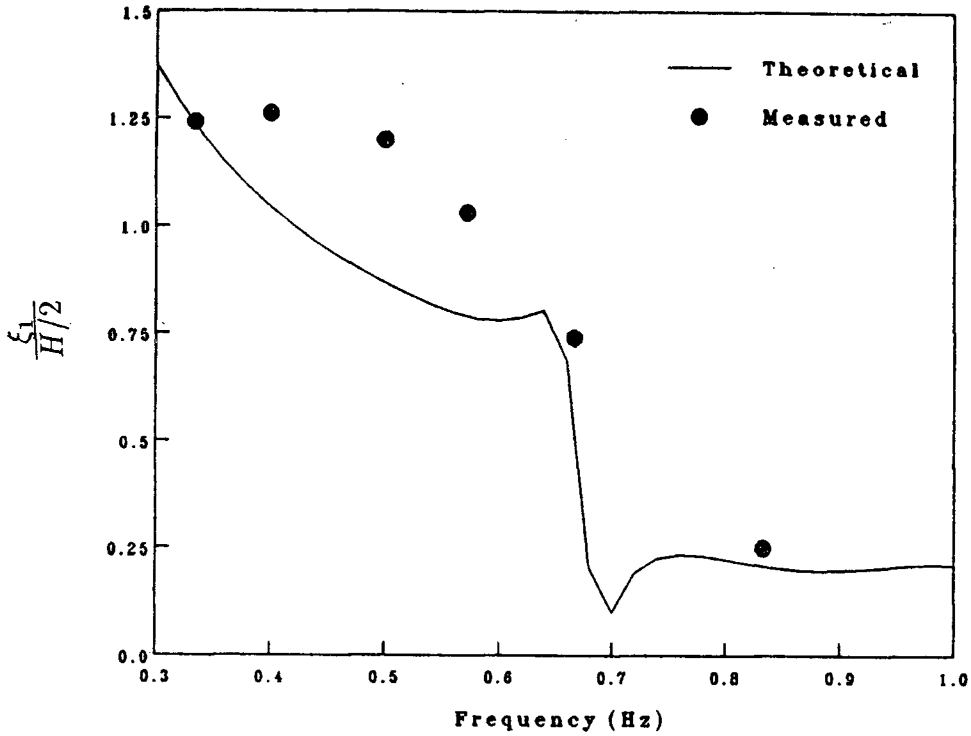

Figure 6.97: Measured and computed surge response amplitude operator in regular waves

(0.5m) and wave height for the pitch motion. In the computation of the pitch response amplitude operator, a constant viscous damping ratio of 4% was assumed. The measured response amplitude operators all compare reasonably well with linear diffraction theory predictions. The computed surge response amplitude operator has a sudden drop near the pitch natural frequency because of coupling between the surge and pitch motions.

The measured steady drift force coefficients obtained from the mean surge displacement are compared with theoretical predictions in figure 6.100. Agreement between the measured and predicted results is poor. The far field approach seems to generally under-predict the measured drift forces. Differences between the measured and predicted mean drift forces were as high as 50%. The differences between the predicted and measured drift forces might also be due to other factors not accounted for in the theory such as the presence of long waves in the basin and reflection effects.

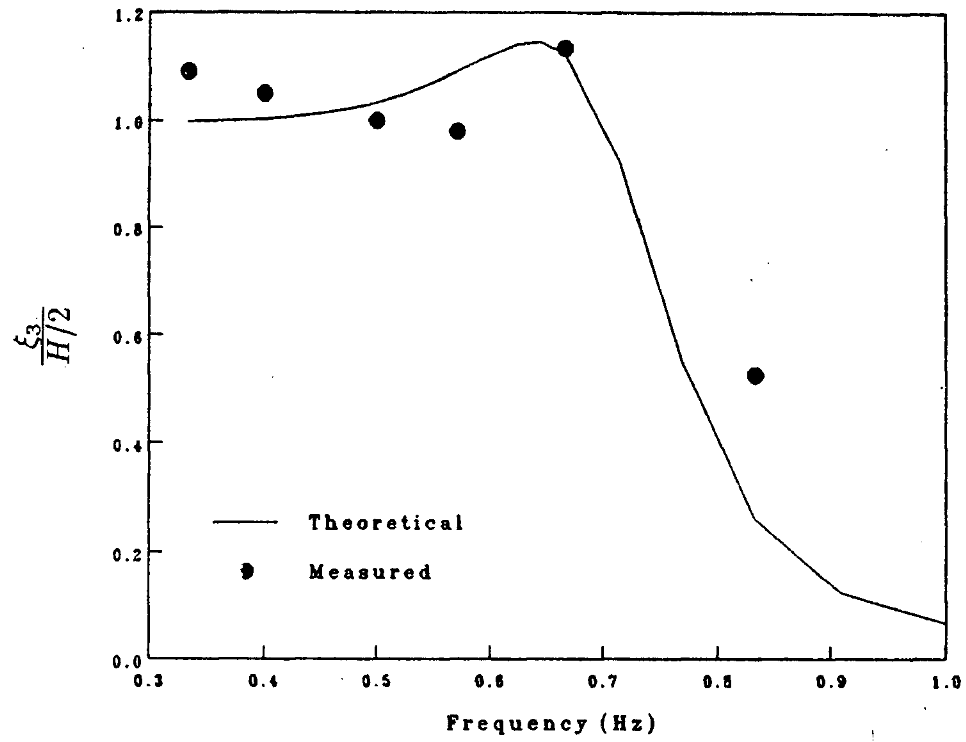

Figure 6.98: Measured and computed heave response amplitude operator in regular waves

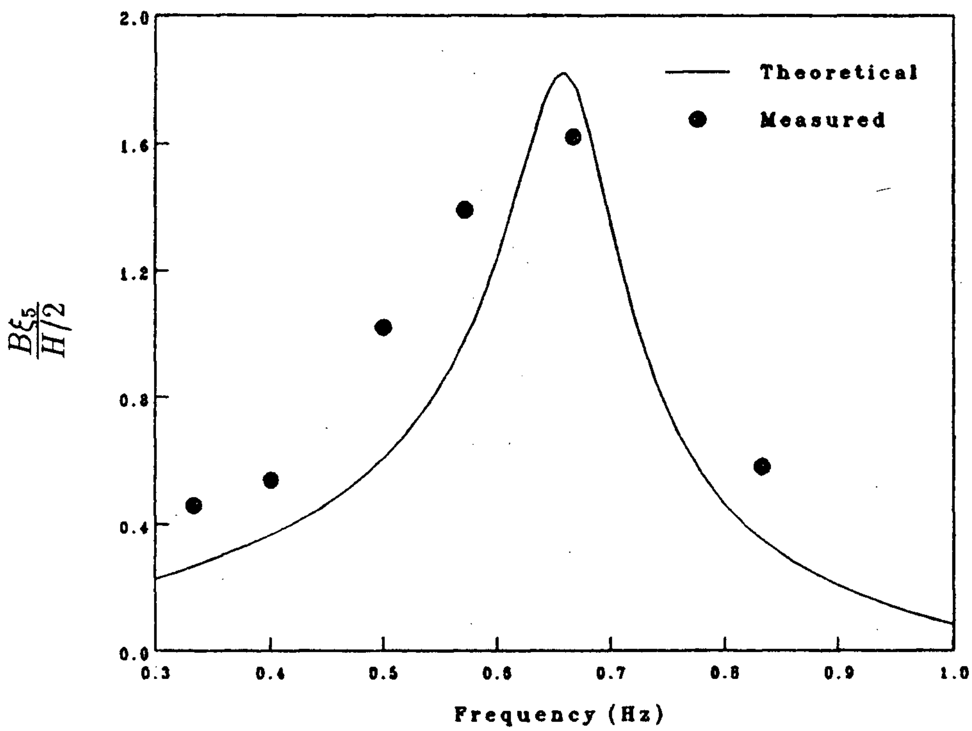

Figure 6.99: Measured and computed pitch response amplitude operator in regular waves

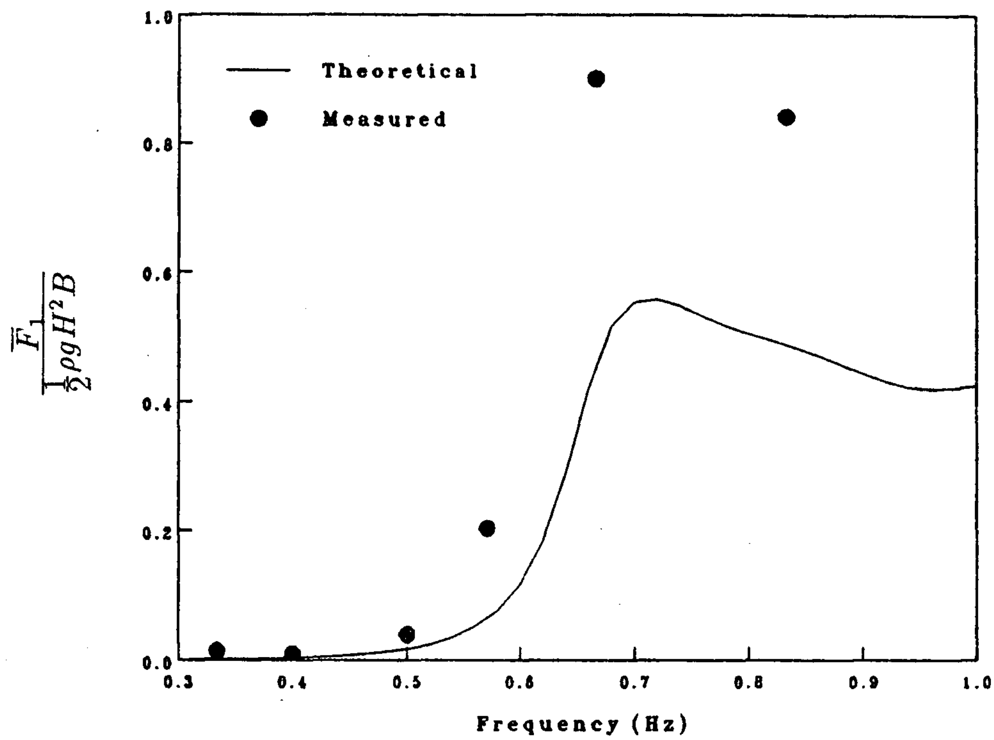

Figure 6.100: Measured and computed steady drift force coefficient in regular waves

Effect of Crossing Wave Angle

The effect of crossing wave angle on the mean and first order motions is now investigated by comparing the measured surge, heave, and pitch motions in regular short-crested waves with different crossing angles. The experimental results are presented in Table 6.9. The crossing waves were synthesized to have the same wave height but different crossing angles so that one could examine the effect of only the crossing wave angle on the motions. The span of the wave generator was however reduced during the tests in order to reduce the motions of the barge. This affected the different crossing waves differently, resulting in the observed variation of wave height for the different crossing waves. The experimental results are thus only used to provide a qualitative indication about the effect of crossing wave angle on the barge motions because of the uncertainty about the actual wave heights in the basin during the tests, and the poor quality of some of the crossing waves generated in the basin.

Table 6.9: Measured barge motion amplitudes in crossing waves

T(s)	H(m)	α (deg)	Surge (m) (mean)	Surge (m) (ampl)	Heave (m)	Pitch (deg)
1.5	0.186	15	0.74	0.07	0.13	15.0
	0.205	30	0.45	0.05	0.10	12.5
	0.165	45	0.15	0.04	0.10	9.6
2.0	0.195	15	0.09	0.15	0.16	14.2
	0.242	30	0.07	0.14	0.22	12.9
	0.153	45	0.0	0.05	0.08	4.4

It can be seen from Table 6.9 that the mean surge motions are significantly reduced in crossing waves, particularly for $\alpha = 45°$. The first order surge motions were not however as significantly reduced. The pitch motions are also reduced in crossing waves. Unfortunately, useful conclusions cannot be drawn about the validity of linear superposition, or the relative contribution of the interaction term to the mean surge motions from these tests.

In order to theoretically evaluate the effect of crossing wave angle on the barge motions, response amplitude operators for the heave, pitch, and surge motions for different angles of wave incidence were computed using the linear diffraction theory program. Drift force coefficients for different wave propagation angles were also computed. Figure 6.101 to 6.104 show the surge, heave, and pitch response amplitude operators, and the drift force coefficients for 1.2s, 1.5s and 2.0s waves.

Figure 6.102 shows that the heave response amplitude operator increases with increasing angle of incidence, with the maximum heave motions occuring in beam seas. The rate of increase is however dependent on the wave period, or equivalently ka. For a

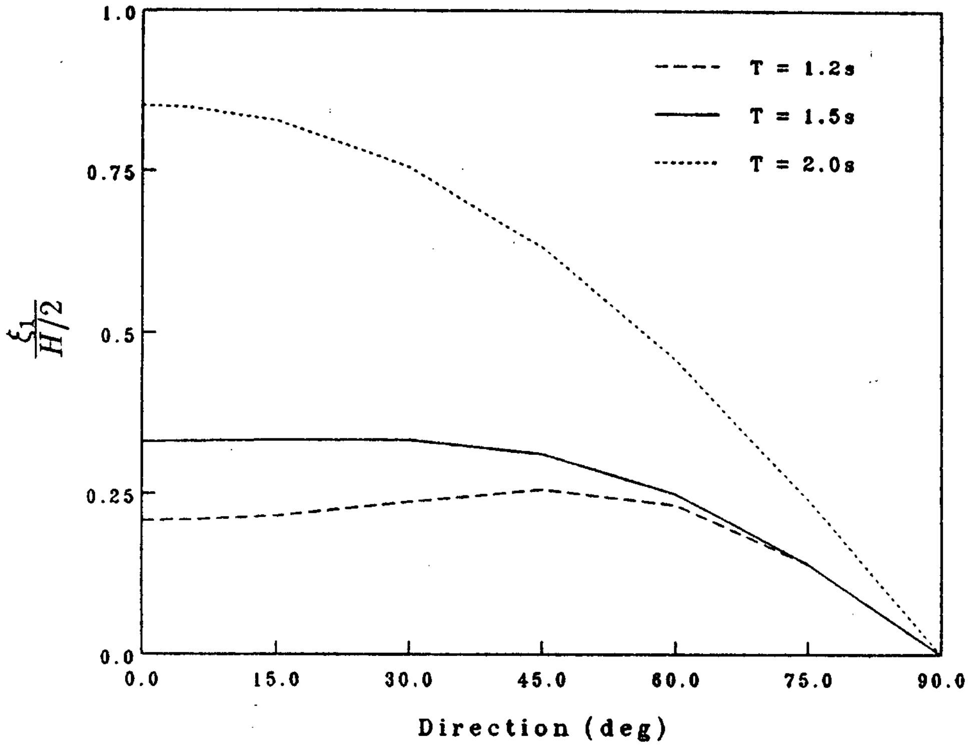

Figure 6.101: Surge response amplitude operator in oblique waves

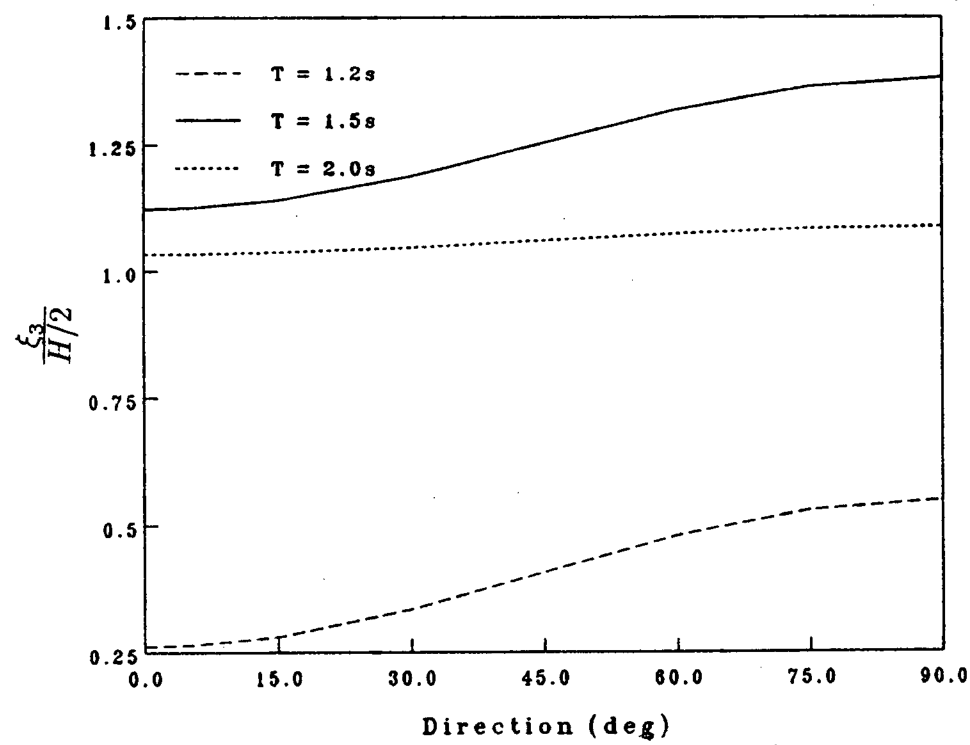

Figure 6.102: Heave response amplitude operator in oblique waves

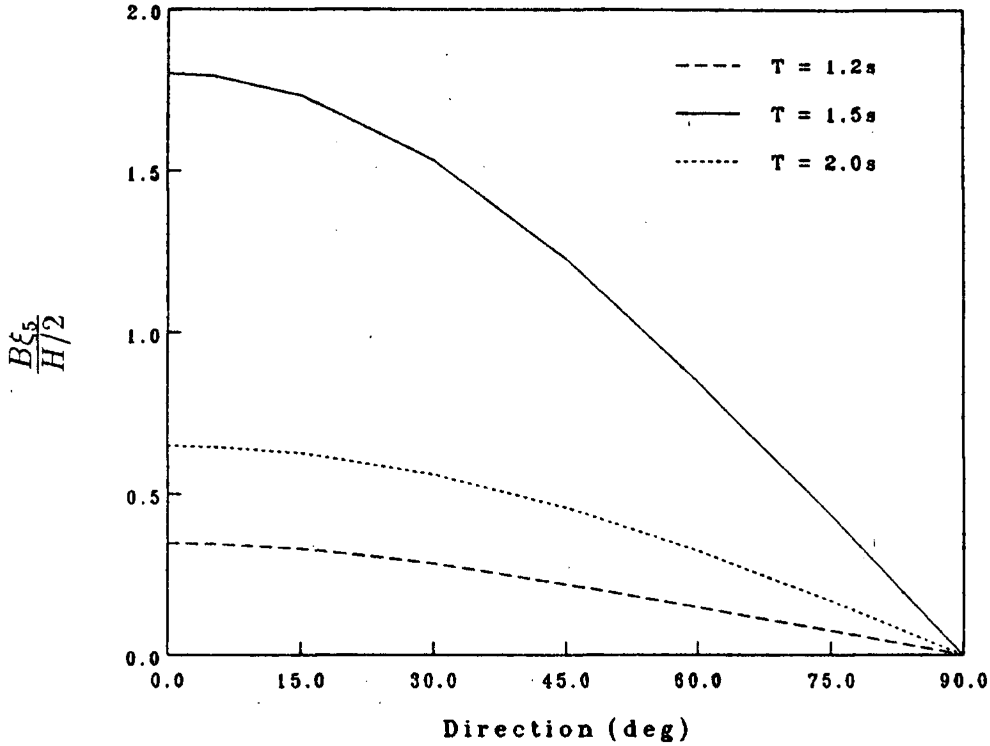

Figure 6.103: Pitch response amplitude operator in oblique waves

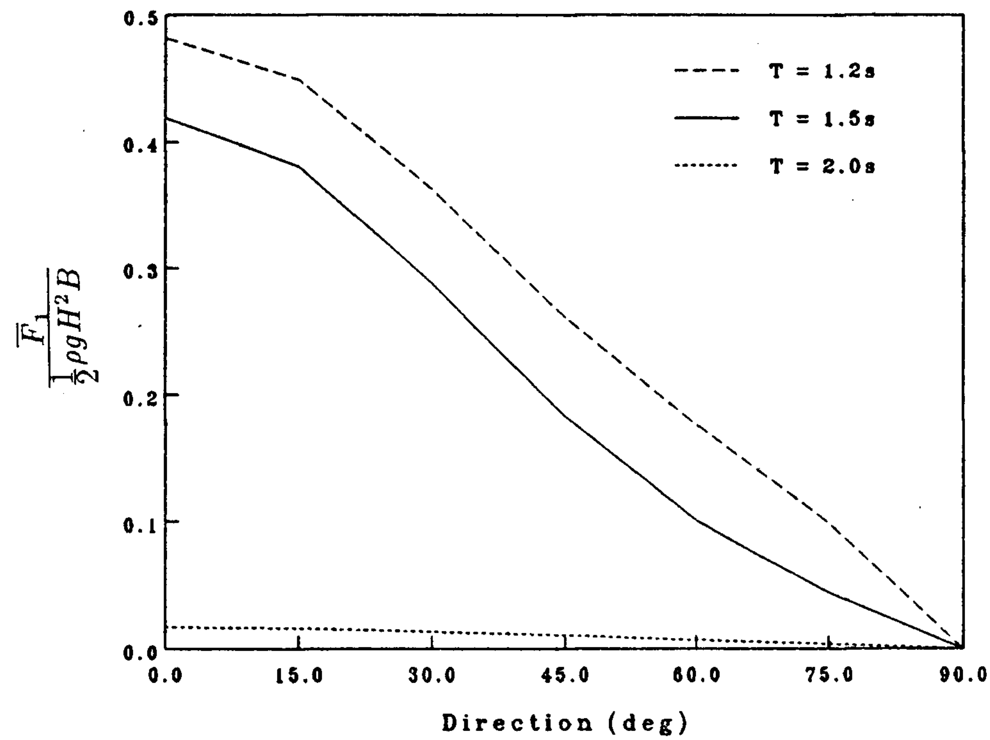

Figure 6.104: Steady drift force coefficient in oblique waves

wave period of 1.2s ($ka = 1.4$), the amplitude of the heave motions in beam seas is almost twice that in head seas, while for $T = 2.0$s ($ka = 0.5$), the heave amplitude is almost independent of the angle of incidence. The variation of the surge motion amplitude with angle of incidence is also dependent on the period of the incident wave, with the motion for the longer period waves decreasing more sharply with angle of incidence.

The pitch response amplitude operator consistently decreased with increasing angle of incidence for the different wave periods. The variation of the pitch amplitude with angle of incidence was close to a $\cos\theta$ variation. The surge drift force coefficient decreased the most sharply with angle of incidence. At an angle of incidence of 45°, the mean drift force values are reduced by 46%, 56%, and 40% for the 1.2, 1.5, and 2.0s waves respectively. This is much higher than reductions of 37%, 32%, and 30% obtained for the pitch motions, and -25%, 13%, and 26% obtained for the surge motions.

6.3.2 Long-Crested Bichromatic Waves

The tests in long-crested bichromatic waves were carried out to show how the second order surge motions respond to the envelope of the wave train rather the actual water surface elevation process. Figure 6.105 and 6.106 show the time series and spectral density of a typical bichromatic wave train ($f_1 = 0.67$Hz, $f_2 = 0.58$Hz). The amplitude of the wave train is seen to be slowly modulated at the difference frequency of the component waves.

The measured surge, heave, and pitch motions are shown in figure 6.107. It can be seen that while the heave and pitch motions occur at frequencies close to the frequencies of the individual waves, the surge response occurs at a much lower frequency close to the difference frequency of the component waves. The low frequency surge response is due to second order effects and is thus related to the envelope of the wave train rather than the actual water surface elevation.

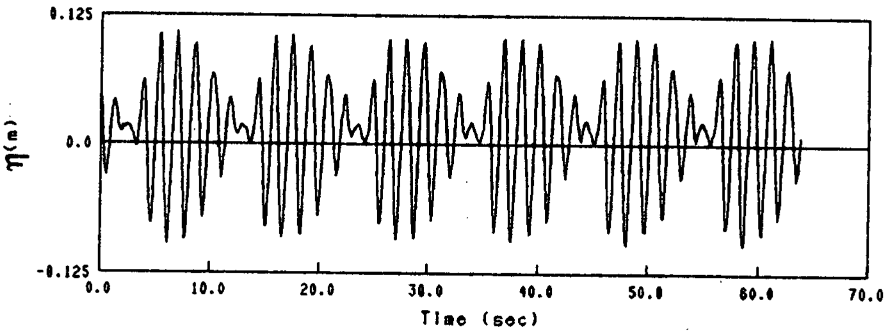

Figure 6.105: Water surface elevation time history for bichromatic wave train

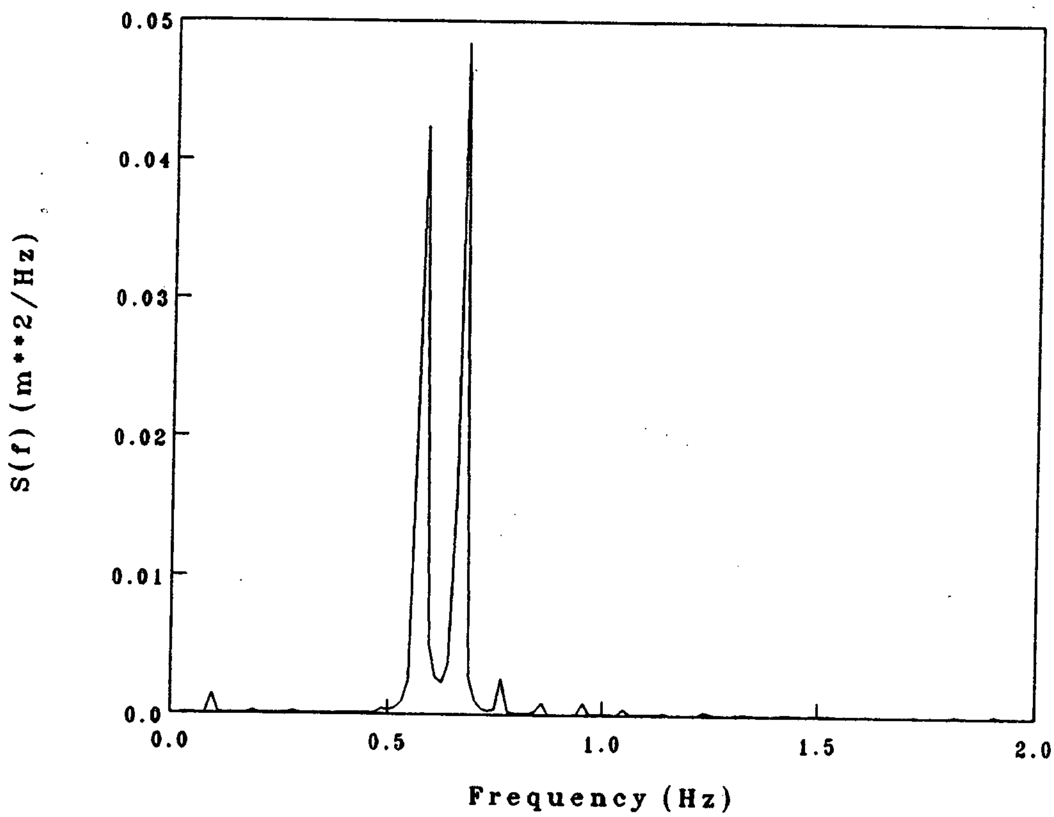

Figure 6.106: Water surface elevation spectrum for bichromatic wave train

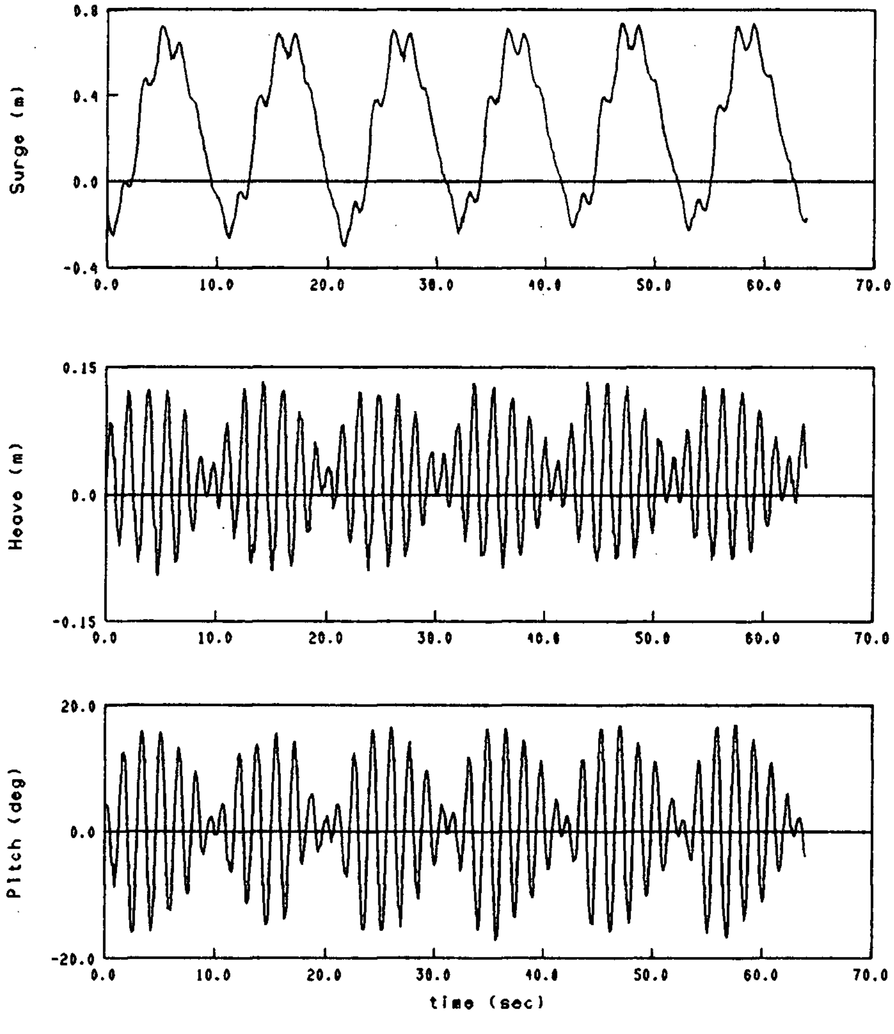

Figure 6.107: Time histories of barge motions for bichromatic wave train

6.3.3 Random Waves

The barge was also tested in random waves described by a JONSWAP spectrum. Two JONSWAP spectra with peak frequencies f_p of 0.5 and 0.67Hz, significant wave heights H_{m0} of 0.191m and 0.174m respectively, and peak enhancement factor $\gamma = 3.3$ were used. For each spectrum, one unidirectional and three multi-directional sea states were generated. The multi-directional sea states had target cosine power spreading indices s of 1, 3, and 6 with principal direction $\theta_0 = 0°$.

The target and measured water surface elevation spectral densities for a multi-directional sea state ($f_p = 0.67$Hz, $s \approx 1$) are compared in figure 6.108. The measured water surface elevation spectrum matches the target spectrum reasonably well. The corresponding time series and spectral densities of the six degree of freedom barge motions are shown in figures 6.109 and 6.110. The surge, sway, and yaw motions are seen to occur at frequencies much lower than the incident wave frequencies while the heave, roll, and pitch motions occur at frequencies close to the wave frequencies.

6.3.4 Response Amplitude Operators

The response amplitude operators for the first order motions were obtained by dividing the spectral densities of the barge motions by the water surface elevation spectrum. The surge, heave, and pitch response amplitude operators obtained from the two long-crested sea states are compared with linear diffraction theory predictions in figures 6.111 to 6.113. The results obtained from the regular wave tests are also shown on the figures. The response amplitude operators obtained from the two irregular sea states compare reasonably well with each other, with the regular wave test results, and the theoretical predictions.

The surge, sway, heave, roll and pitch response amplitude operators for the multi-directional as well as unidirectional sea states are shown in figures 6.114 to 6.118. The

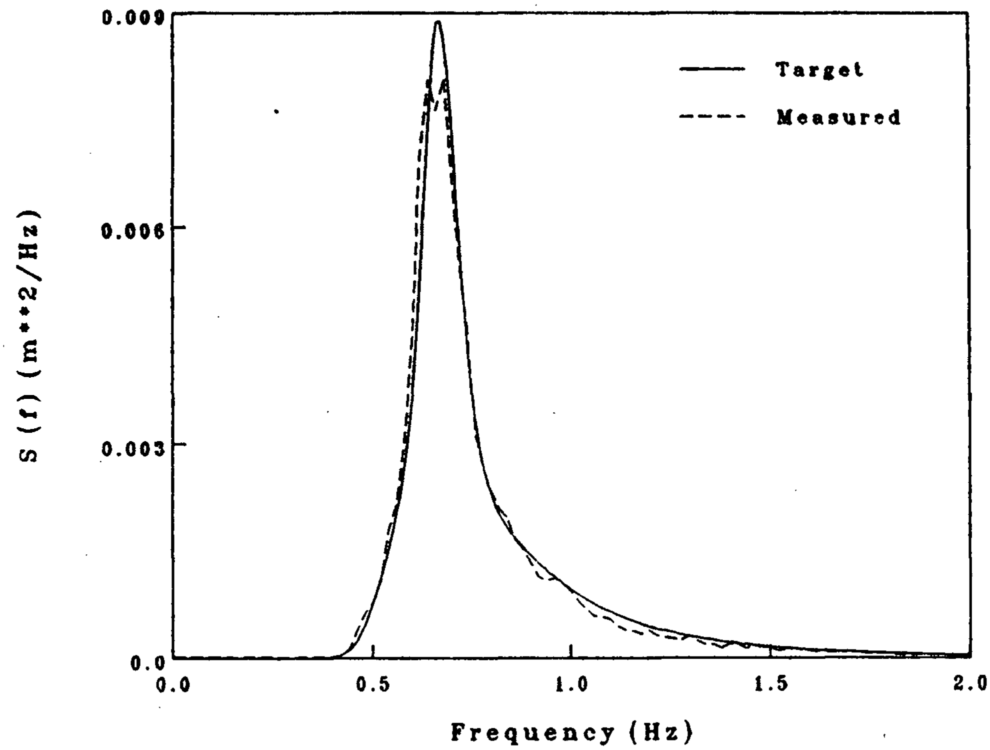

Figure 6.108: Comparison of target and measured water surface elevation spectra (f_p = 0.67Hz, H_{m0} = 0.175m)

response amplitude operators for the multi-directional sea states represent directionally averaged transfer functions since they depend only on frequency. The response amplitude operators show clearly the effect of wave directionality in the frequency domain. The first order surge response amplitude operator is seen to be reduced in multi-directional waves, with the amount of reduction dependent on the frequency. At frequencies greater than the pitch natural frequency, the reduction of the surge response is seen to be marginal. The effect of wave directionality on the sway response is also seen to be frequency dependent with the increase of the sway motion relatively smaller at the higher frequencies.

The pitch response amplitude operator is consistently reduced in multi-directional waves over the entire frequency range, while the roll response amplitude operator increased. The pitch and roll response amplitude operator for a $\cos^2\theta$ sea state are about 83% and 56% of the long-crested pitch response amplitude operator. The heave response amplitude operator was not significantly affected by wave directionality for the range

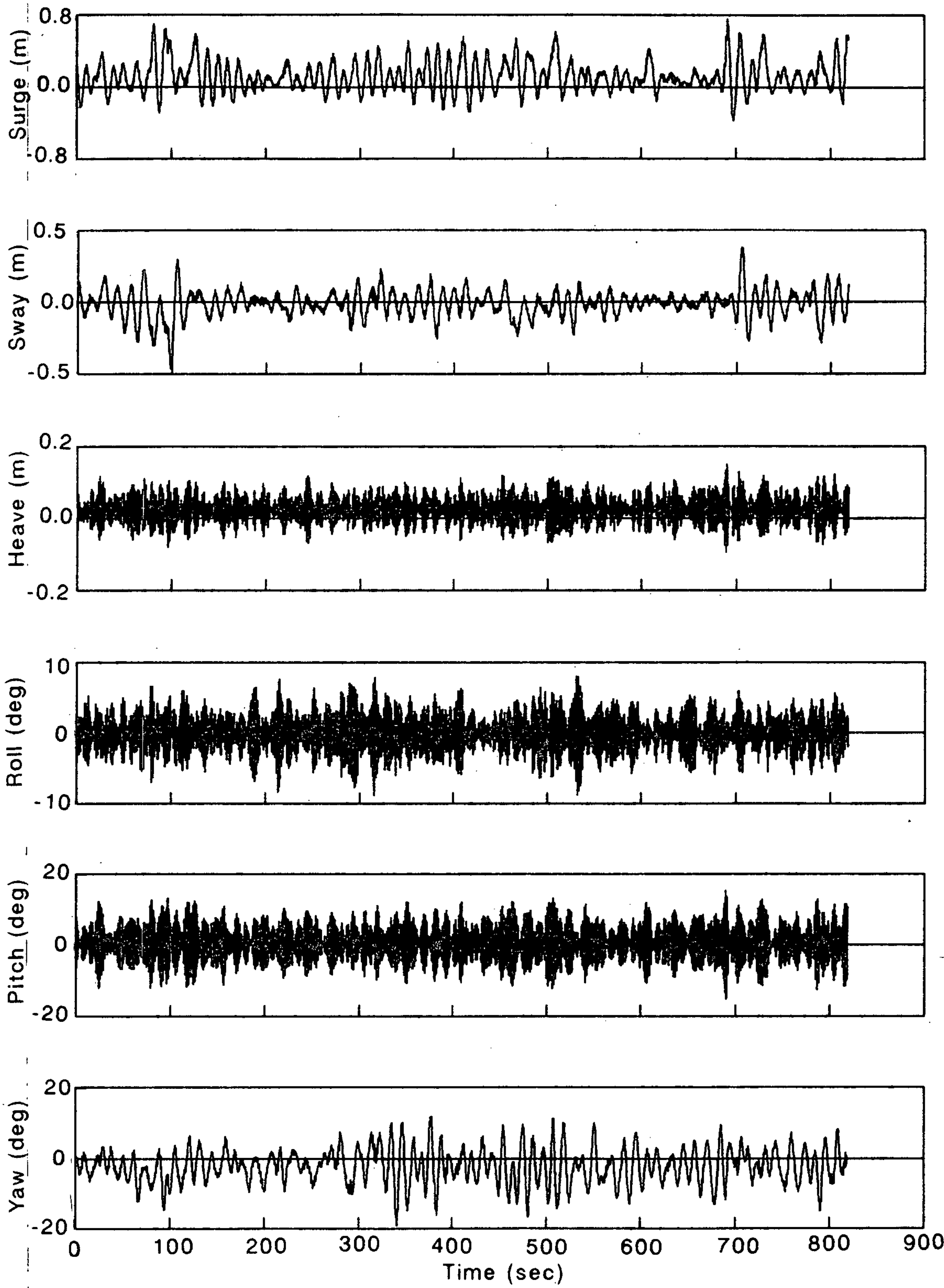

Figure 6.109: Time histories of six degree of freedom barge motions in multi-directional seas (s =1, f_p = 0.67Hz)

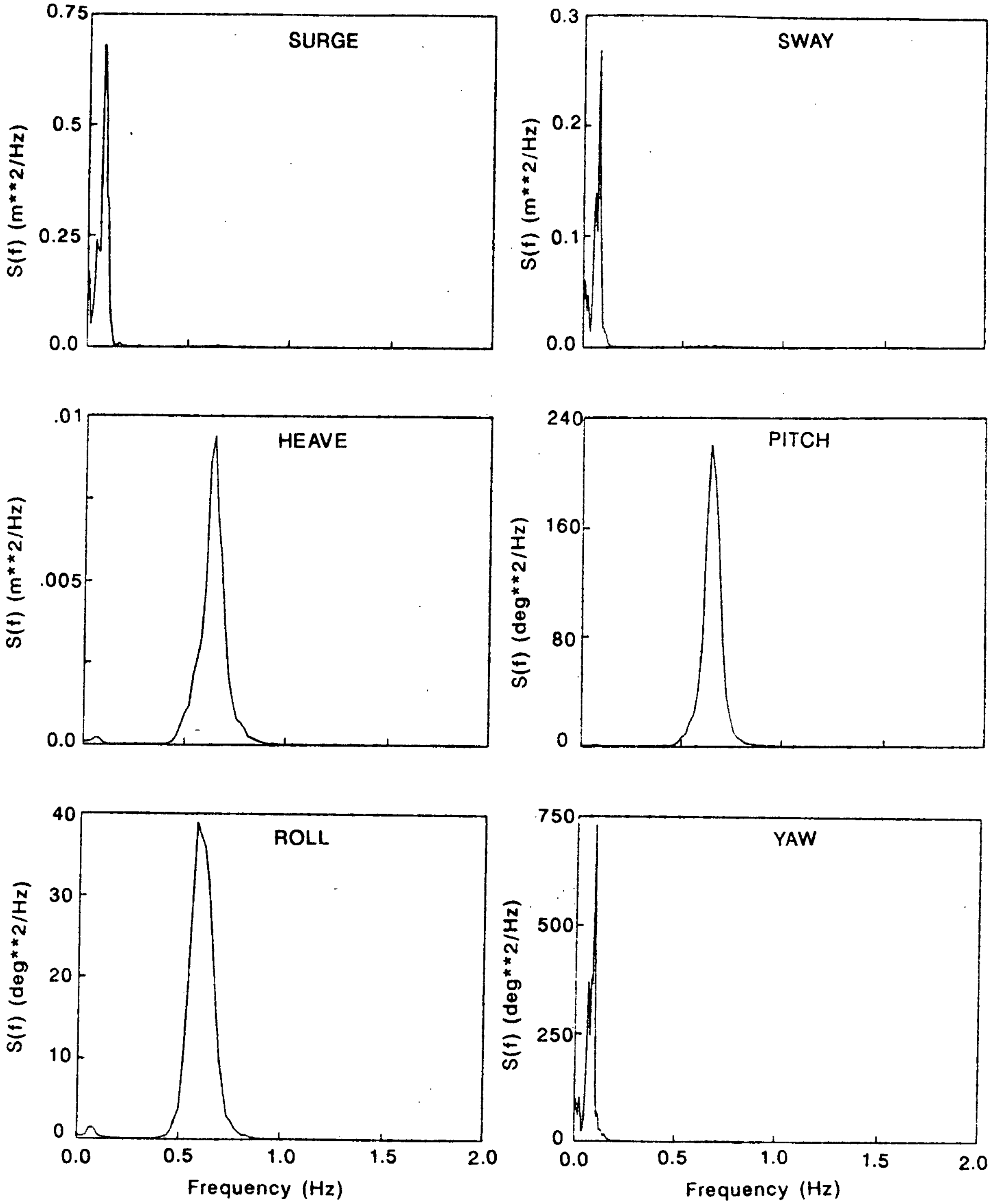

Figure 6.110: Spectral densities of six degree of freedom barge motions in multi-directional seas (s =1, f_p = 0.67Hz)

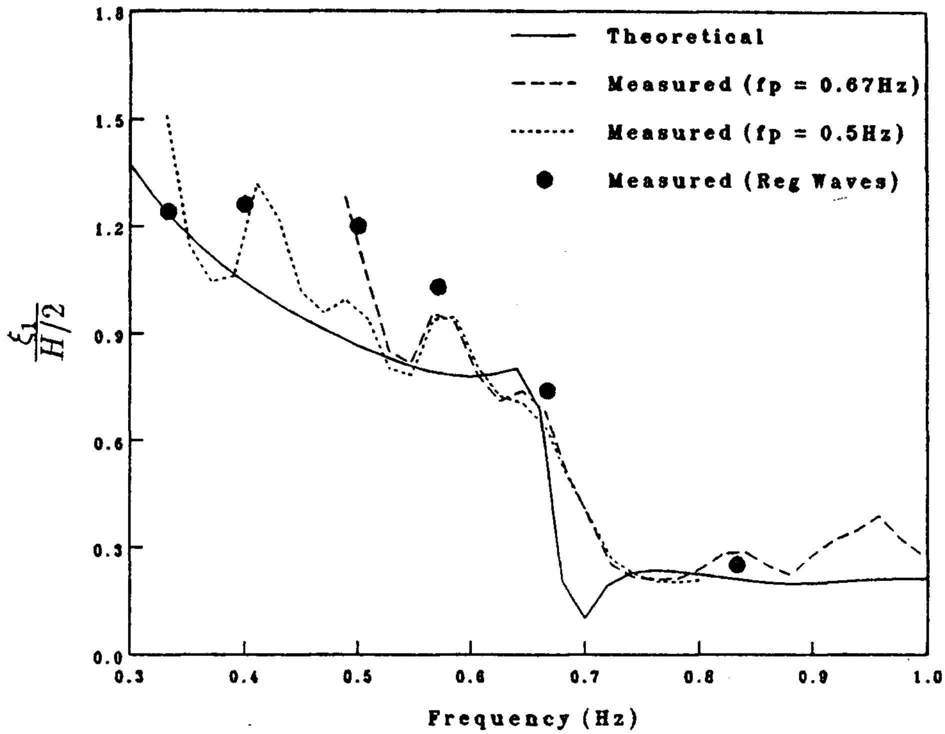

Figure 6.111: Measured and computed surge response amplitude operator in random waves

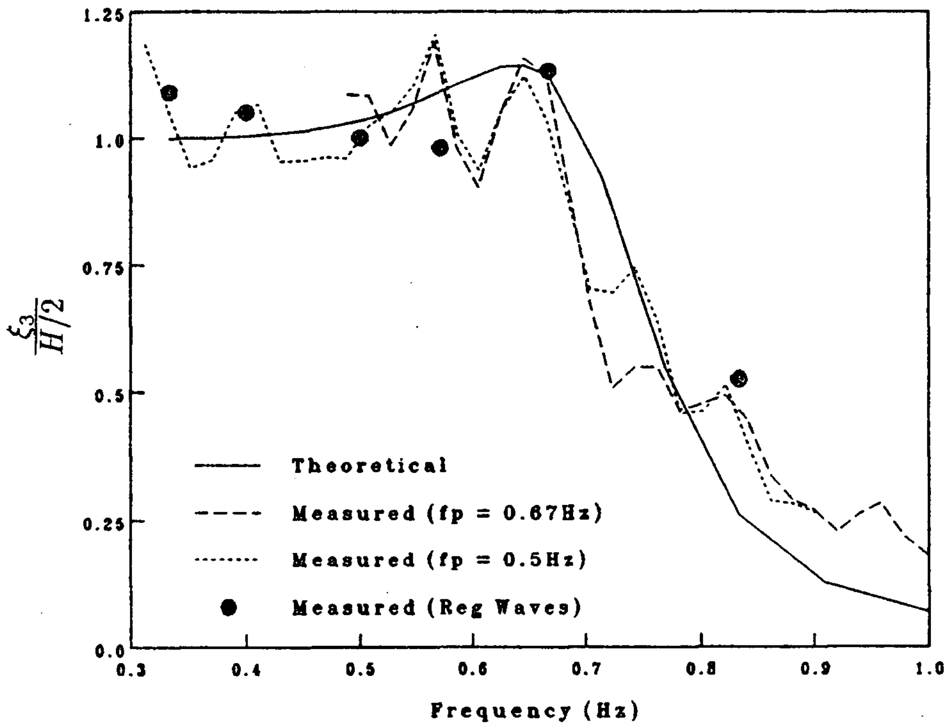

Figure 6.112: Measured and computed heave response amplitude operator in random waves

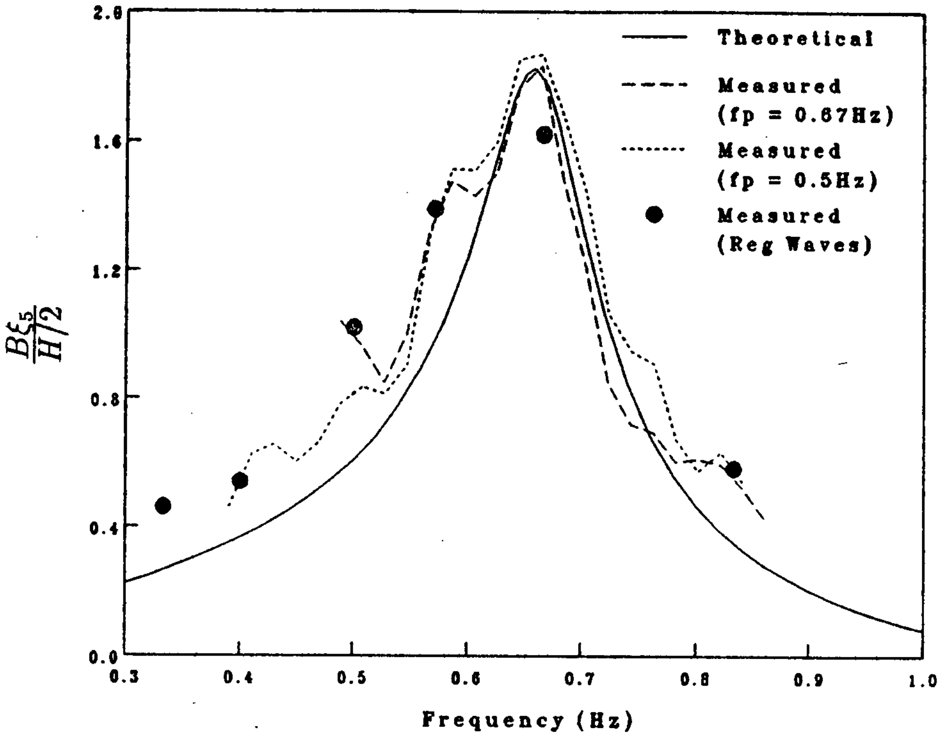

Figure 6.113: Measured and computed pitch response amplitude operator in random waves

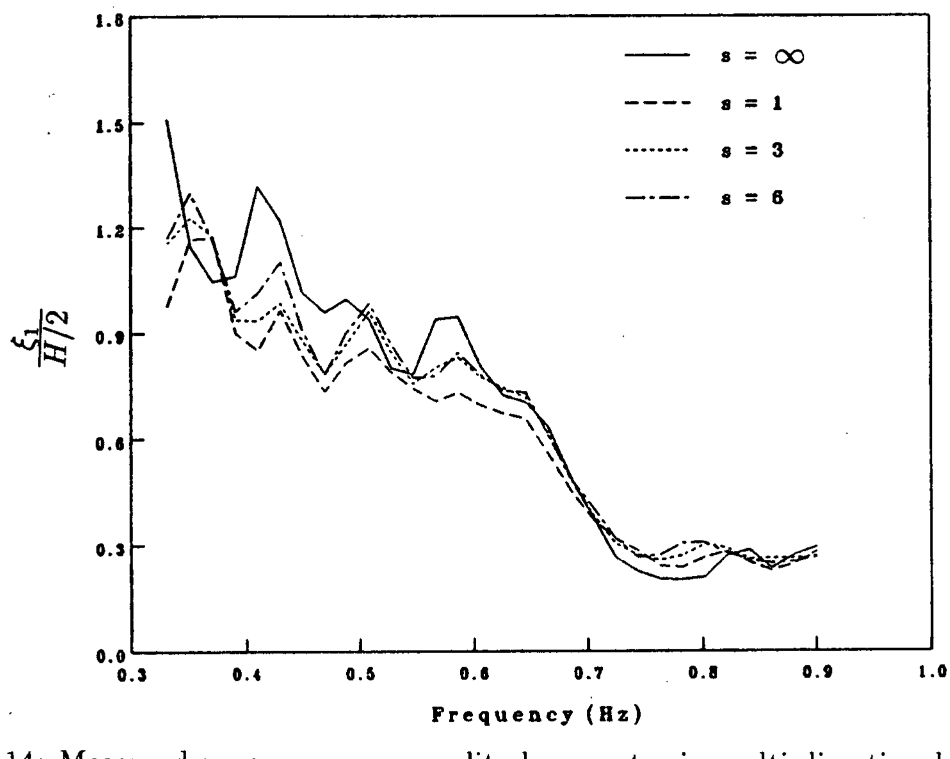

Figure 6.114: Measured surge response amplitude operator in multi-directional waves

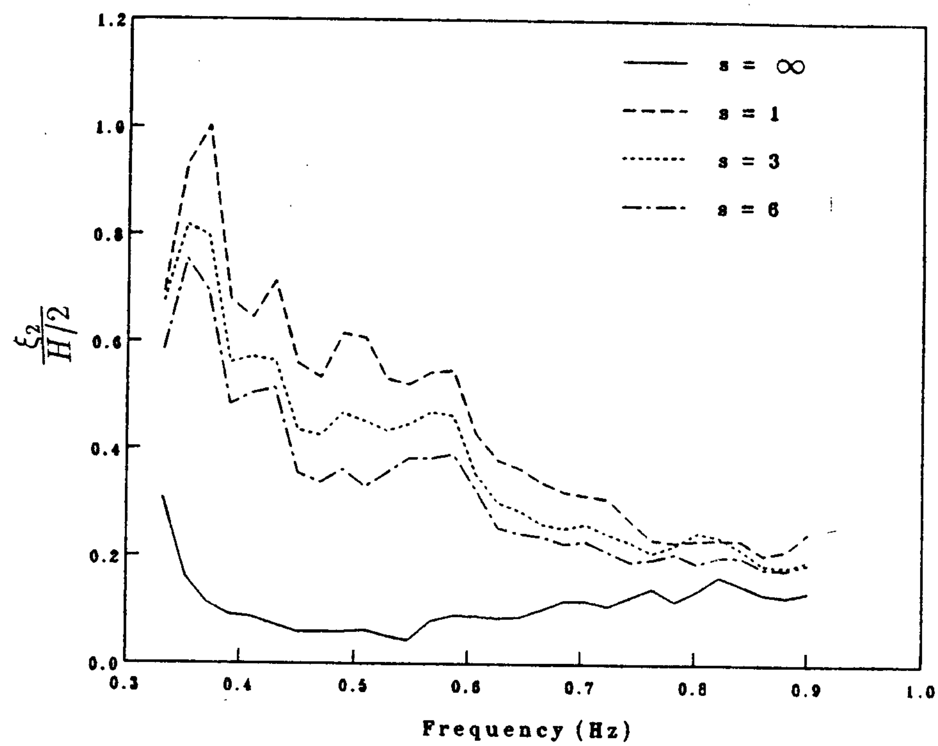

Figure 6.115: Measured sway response amplitude operator in multi-directional waves

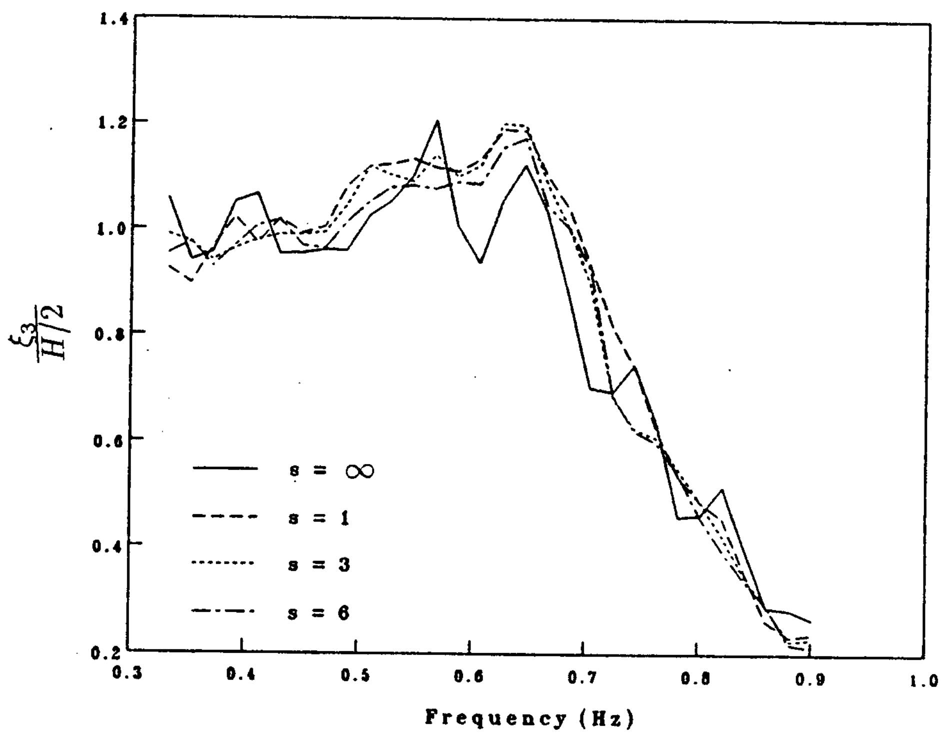

Figure 6.116: Measured heave response amplitude operator in multi-directional waves

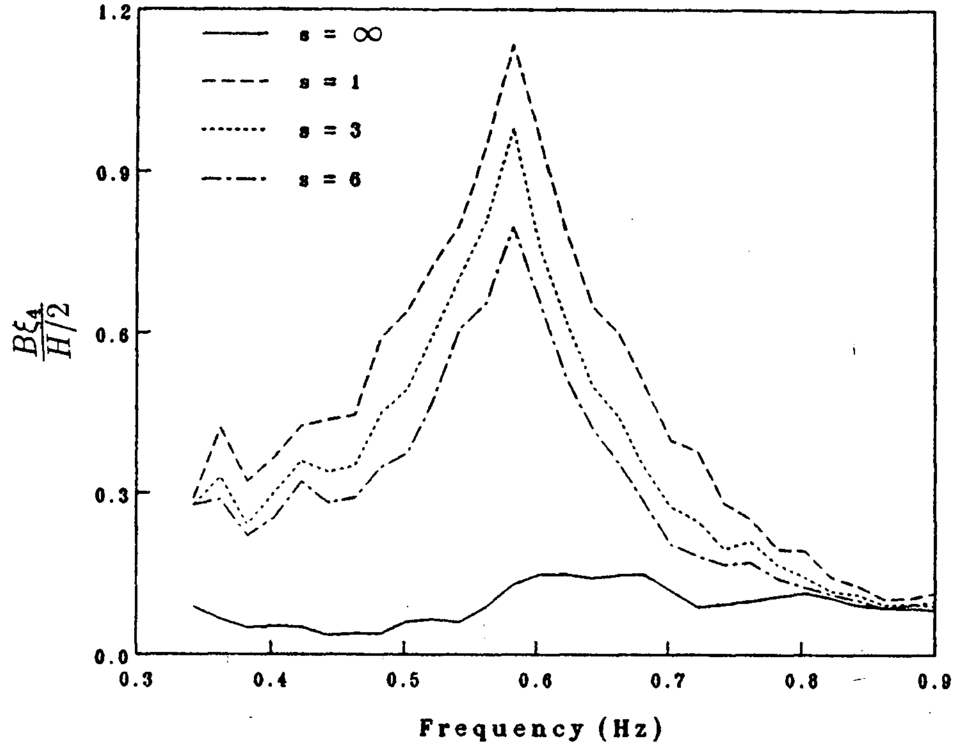

Figure 6.117: Measured roll response amplitude operator in multi-directional waves

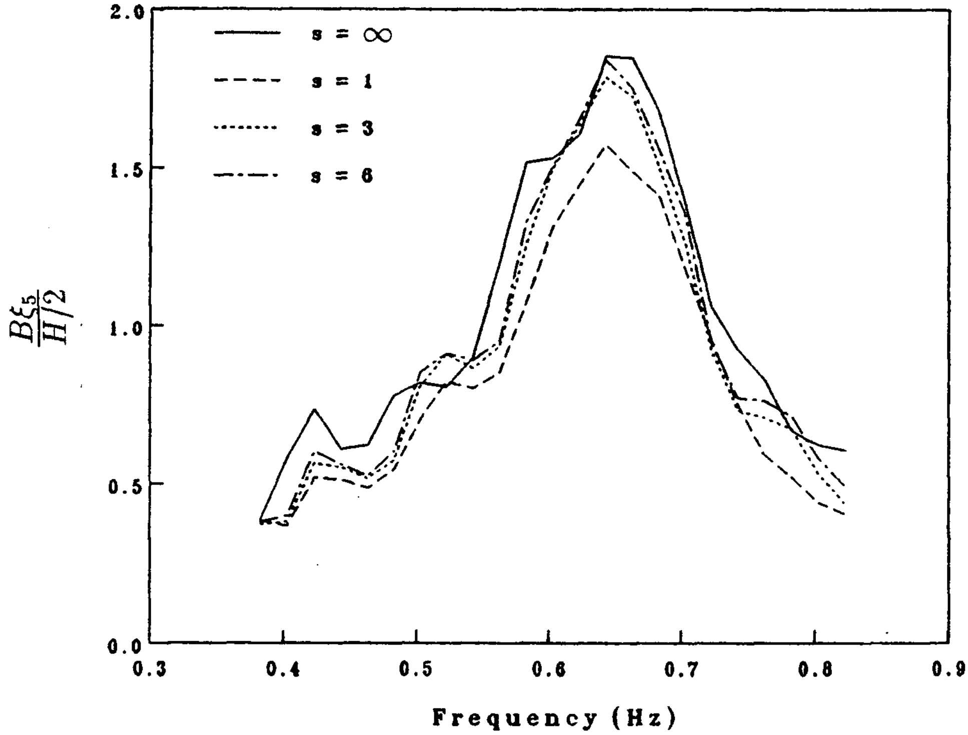

Figure 6.118: Measured pitch response amplitude operator in multi-directional waves

Table 6.10: Standard deviations of measured barge motions (f_p = 0.5Hz)

	s $\approx$ 1	s $\approx$ 3	s $\approx$ 6	s $\rightarrow \infty$
mean surge (m)	0.069	0.084	0.094	0.118
surge$^{(2)}$ (m)	0.110	0.130	0.139	0.160
surge$^{(1)}$ (m)	0.0344	0.0362	0.0364	0.0401
sway$^{(2)}$ (m)	0.059	0.052	0.050	0.031
sway$^{(1)}$ (m)	0.0247	0.0197	0.0158	0.0040
heave (m)	0.048	0.046	0.044	0.045
roll (deg)	3.5	2.77	2.25	0.52
pitch (deg)	4.44	4.79	4.93	5.33
yaw (deg)	4.38	4.15	3.74	2.22

of frequencies shown. Linear diffraction theory however predicts an increase or decrease (depending on the principal direction of wave propagation) of the heave motions in multi-directional seas for large relative structure lengths (ka). The theory predicts an increase of the heave motion in head seas ($\theta_0 = 0°$), and a reduction in beam seas ($\theta_0 = 90°$).

Motion Reduction Factors

The directionality of the waves results in a reduction of the surge and pitch motions, and an increase of the sway, roll, and yaw motions. Reduction factors relating the standard deviations of the motions in multi-directional seas to corresponding values for long-crested waves can thus be used to express the overall effect of wave directionality. The standard deviations of the barge motions for all 8 tests are presented in Tables 6.10 and 6.11. The superscripts (1) and (2) are used to denote the first and second order components of the response respectively.

Table 6.11: Standard deviations of measured barge motions (f_p = 0.67Hz)

	s $\approx$ 1	s $\approx$ 3	s $\approx$ 6	s $\to\infty$
mean surge (m)	0.124	0.155	0.172	0.230
surge$^{(2)}$ (m)	0.175	0.205	0.219	0.246
surge$^{(1)}$ (m)	0.0204	0.0221	0.0229	0.0253
sway$^{(2)}$ (m)	0.094	0.079	0.066	0.038
sway$^{(1)}$ (m)	0.0137	0.0112	0.0096	0.0044
heave (m)	0.034	0.034	0.034	0.035
roll (deg)	2.4	1.85	1.53	0.6
pitch (deg)	4.68	5.17	5.41	5.85
yaw (deg)	4.98	4.07	3.48	1.99

The tables clearly show that the directionality of the waves had very little effect on the heave motions for the two frequency spectra used. The first order surge, sway, pitch, and roll motions were however affected by wave directionality. For the f_p = 0.5Hz sea state with $s \approx 1$, the first order surge and pitch motions are reduced by 14% and 17% respectively, while the first order sway and roll response are about 62% and 66% of the long-crested surge and pitch response respectively. For the f_p = 0.67Hz multi-directional sea state ($s \approx 1$), the first order surge and pitch motions are reduced by 19% and 20% respectively, while the first order sway and roll response are about 54% and 41% of the long-crested surge and pitch response respectively. The differences between the relative reduction of the pitch motions for the two sea states might be due to the resonant pitch behaviour occuring in the 0.67Hz sea state.

The low frequency motions were more affected by wave directionality. The mean values of the surge motion were reduced by as much as 46% for the $\cos^2\theta$ sea state, while

Table 6.12: Mean, standard deviations, and maximum values of the mooring line forces

f_p(Hz)		$s \approx 1$	$s \approx 3$	$s \approx 6$	$s \to \infty$
0.50	Mean (N)	6.5	7.7	8.4	10.0
	Std. Dev. (N)	8.1	8.8	9.1	10.6
	Maximum (N)	43.3	41.1	46.2	54.9
0.67	Mean (N)	10.7	12.6	13.8	17.0
	Std. Dev. (N)	12.3	13.6	14.4	16.3
	Maximum (N)	66.2	64.0	72.1	77.9

the standard deviations were about 70% of corresponding values in long-crested waves. The low frequency sway motions were about 38% of the long-crested surge motions. Even if the resultant of the surge and sway motions are compared with the long-crested surge motions, the ratio increases only to about 80%. The reduction of low frequency motions is thus quite significant in multi-directional waves.

The mean, standard deviation, and maximum values of the force in the heaviest loaded mooring line are presented in Table 6.12. The results indicate that the mooring line forces are also significantly reduced in multi-directional waves. For the $\cos^2\theta$ sea state, the mean and standard deviation of the mooring line forces are about 65% and 75% of the corresponding values for long-crested waves. The maximum values of the mooring line force were reduced by as much 21%.

Comparison of Measured and Predicted Surge Motion Spectral Densities

The spectral densities of the surge motion were computed for the two long-crested sea states using the steady drift force coefficients predicted by linear diffraction theory and Newman's approximation for the quadratic transfer function. The surge drift force

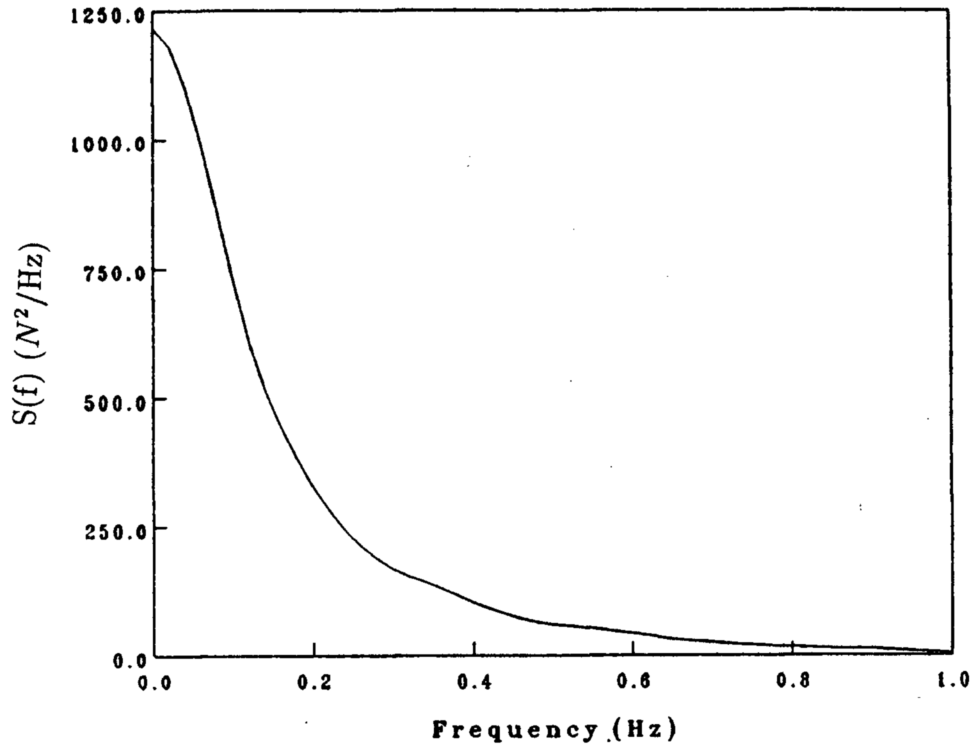

Figure 6.119: Surge drift force spectrum for long-crested waves (f_p = 0.67Hz)

spectrum for the f_p = 0.67Hz sea state is shown in figure 6.119. The measured and computed surge motion spectral densities for the 0.5Hz and 0.67Hz sea states are compared in figures 6.120 and 6.121 respectively. The measured surge motion spectrum for the 0.5Hz sea state is significantly underpredicted with the mean and standard deviation of the predicted surge response 49% and 44% less than measured.

Agreement between the measured and predicted surge motion spectra is better for the 0.67Hz sea state with the mean and standard deviation of the motion underpredicted by 39% and 10% respectively. The measured surge motion spectrum is severely underpredicted primarily because linear diffraction theory severely underpredicted the measured drift force coefficients in regular waves. Other reasons for the differences between the measured and predicted response spectra include the narrow-band approximation of the quadratic transfer function, linearization of the viscous damping term, and neglect of wave drift damping term.

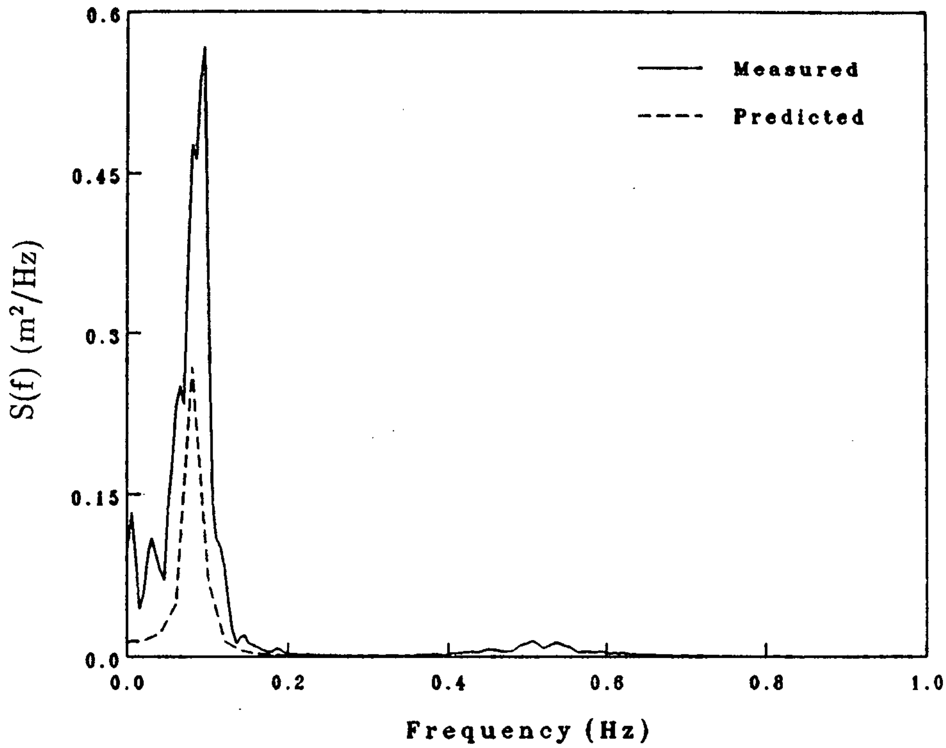

Figure 6.120: Measured and predicted surge motion spetra for long-crested waves (f_p = 0.5Hz)

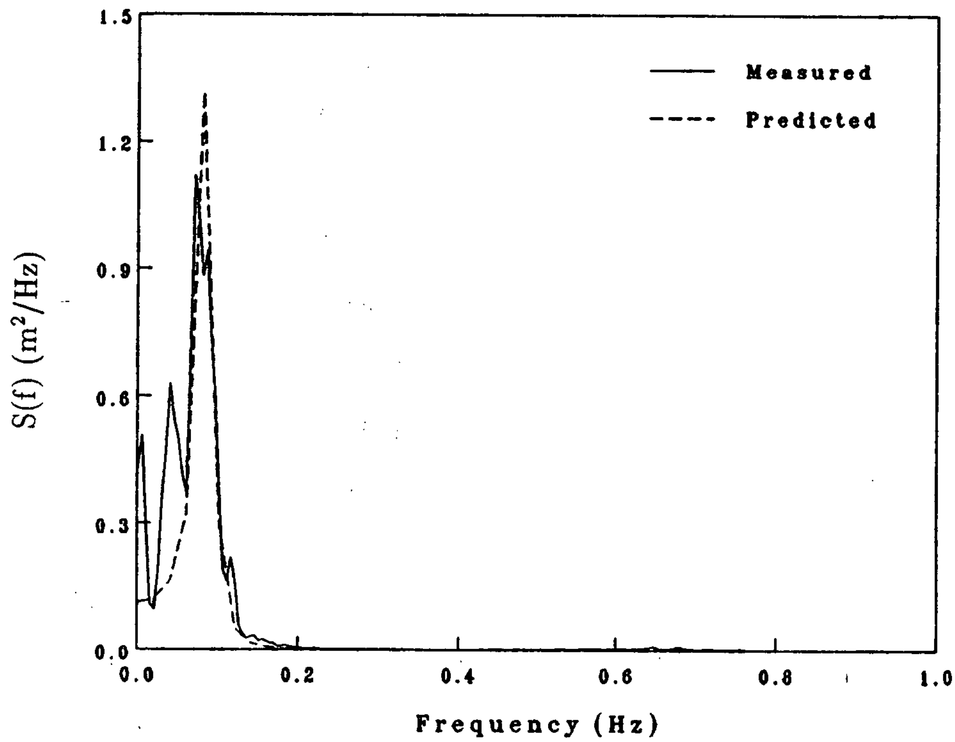

Figure 6.121: Measured and predicted surge motion spetra for long-crested waves (f_p = 0.67Hz)

Table 6.13: Standard deviations of barge motions in differently grouped sea states

f_p (Hz)	H_{m0} (m)	G_F	Surge (m)		Heave (m)	Pitch (deg)
			mean	std. dev.		
0.66	0.144	0.48	0.160	0.117	0.030	5.1
	0.144	0.67	0.159	0.165	0.029	5.1
	0.143	0.89	0.139	0.203	0.026	5.0
0.52	0.242	0.44	0.166	0.162	0.052	6.2
	0.240	0.64	0.159	0.162	0.051	6.0
	0.240	0.81	0.13	0.209	0.050	5.7

Effect of Wave Grouping

The barge was also tested in sea states with approximately the same frequency spectrum but different grouping characterisitics. Two JONSWAP frequency spectra were used with three degrees of groupiness per spectrum. The groupiness factors were calculated by a procedure described by Funke and Mansard (1979), based on the concept of the Smoothed Instantaneous Wave Energy History (SIWEH). The standard deviations of the surge, heave and pitch motions of the barge in the differently grouped sea states are presented in Table 6.13. The standard deviations of the heave and pitch motions and the mean of the surge motions are not noticeably affected by wave grouping. The standard deviations of the surge motions are however significantly affected by wave grouping with the more highly grouped waves inducing larger oscillations.

Probability Distribution of the Motions

The first order motions should be normally distributed since the motions are linearly related to the water surface elevation which has been assumed to be a random Gaussian

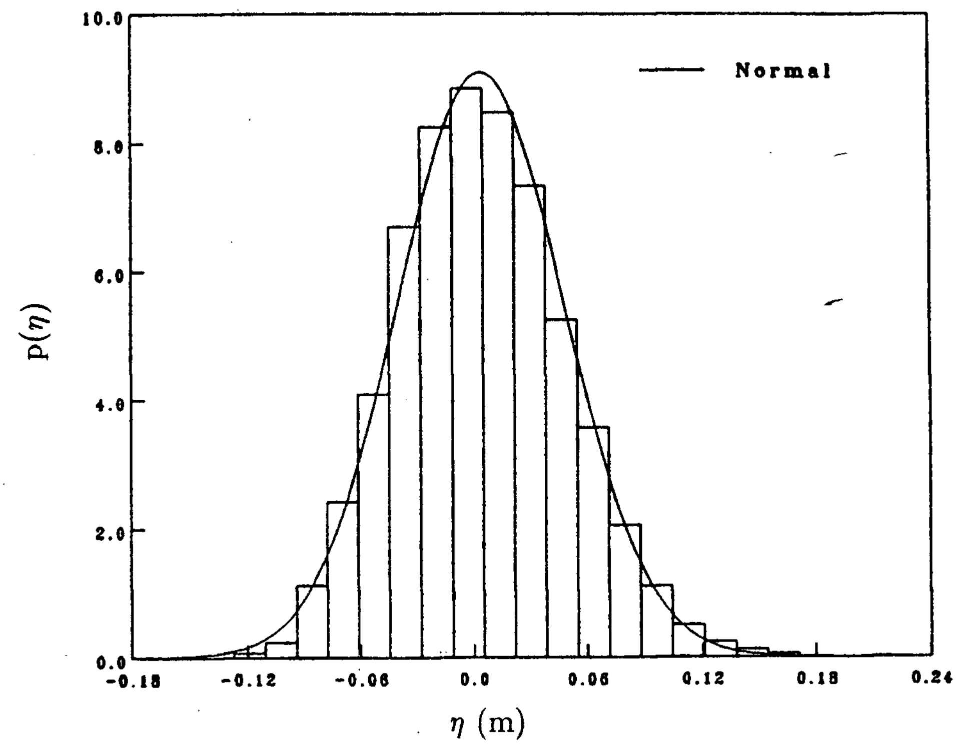

Figure 6.122: Probability distribution of measured water surface elevation (f_p = 0.67Hz, $s \approx 1$)

process. The validity of the Gaussian assumption for the laboratory generated waves and corresponding barge motions is now investigated by comparing the measured probability distributions with the normal distribution. Figure 6.122 shows a comparison of the probability distribution of the measured water surface elevation for the multi-directional sea state (f_p = 0.67Hz, $s \approx 1$) with the normal distribution. The normal distribution is seen to fit distribution of the water surface elevation reasonably well.

The probability distributions of the first order heave, pitch, and roll motions for the f_p = 0.67Hz ($s \approx 1$) sea state are compared with the normal distribution in figures 6.123 to 6.125. The heave and roll motions are well represented by the normal distribution while the pitch motion is not. The pitch motion is not well represented by a normal distribution for this particular sea state because the peak frequency of the sea state corresponds to the pitch natural frequency. The barge thus experiences resonant pitch motions making the effect of nonlinear viscous damping more important. The probability distribution of

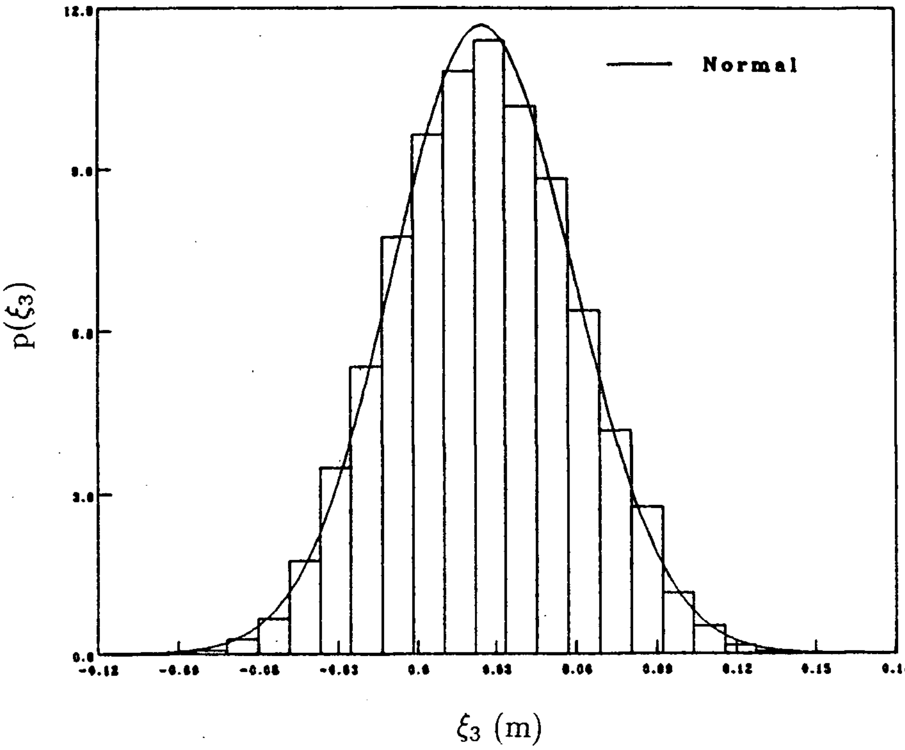

Figure 6.123: Probability distribution of heave motions in multi-directional waves ($f_p =$ 0.67Hz, $s \approx 1$)

the pitch motions for two other sea states ($f_p = 0.5$Hz, $s = 1$ and ∞) are shown in figures 6.126 and 6.127. The normal distribution is seen to match the measured distributions much better.

The probability distribution of the second order drift forces is non-Gaussian since the drift forces are nonlinearly related to the water surface elevation. It has however been postulated (see Roberts (1981), and Vinje (1983)) that the distribution of the motions of a linear system subjected to non-Gaussian excitation should approach a Gaussian distribution as the damping approaches zero. The drift motions are thus often assumed to be normally distributed since they are usually lightly damped (5 to 15% of critical).

The probability distributions of the measured low frequency surge, sway, and yaw motions for the $f_p = 0.67$Hz ($s \approx 1$) sea state are compared with the normal distribution in figures 6.128 to 6.130. The surge and sway distributions are not well fitted by a normal distribution while the yaw distribution is better fitted. The skewness and kurtosis of the

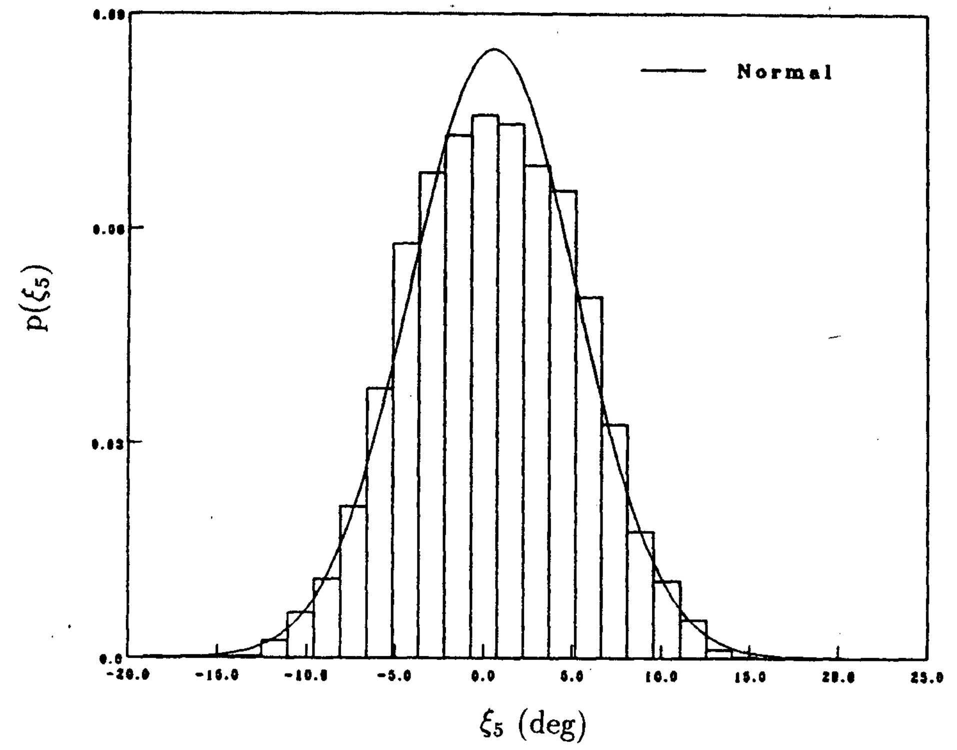

Figure 6.124: Probability distribution of pitch motions in multi-directional waves ($f_p =$ 0.67Hz, $s \approx 1$)

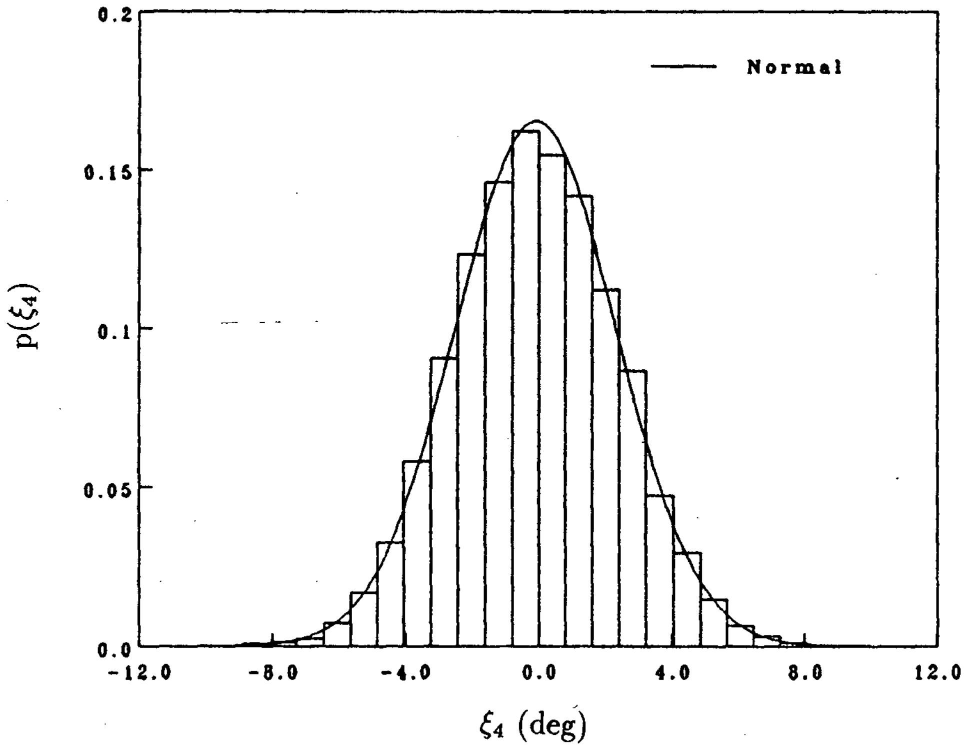

Figure 6.125: Probability distribution of roll motions in multi-directional waves ($f_p =$ 0.67Hz, $s \approx 1$)

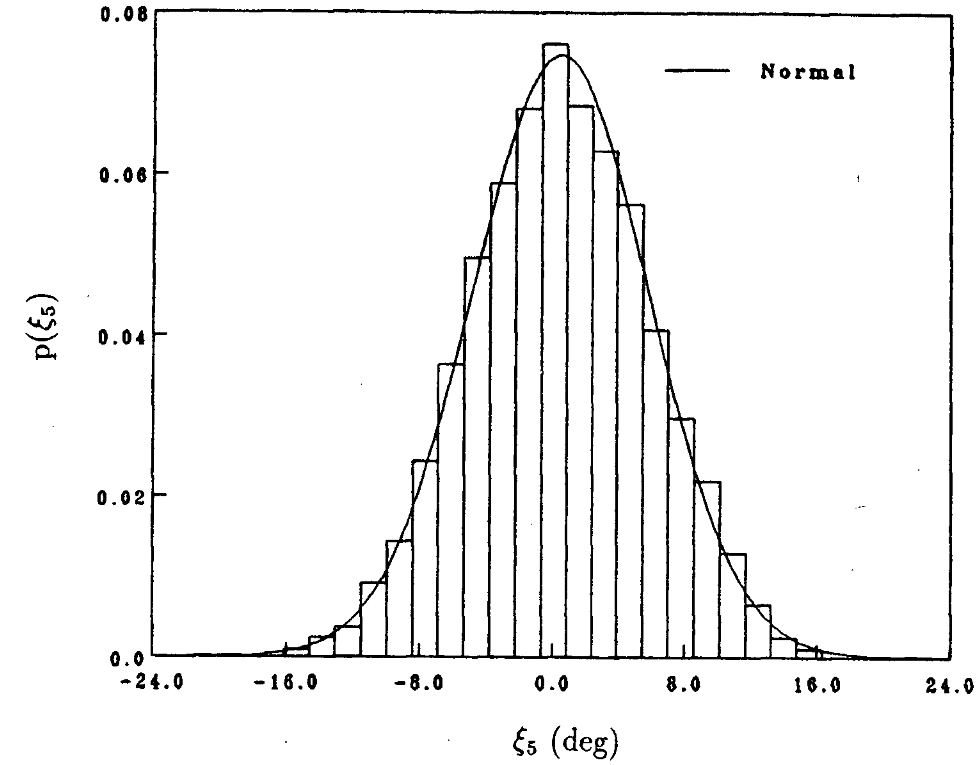

Figure 6.126: Probability distribution of pitch motions in long-crested waves ($f_p = 0.5$Hz, $s \approx 1$)

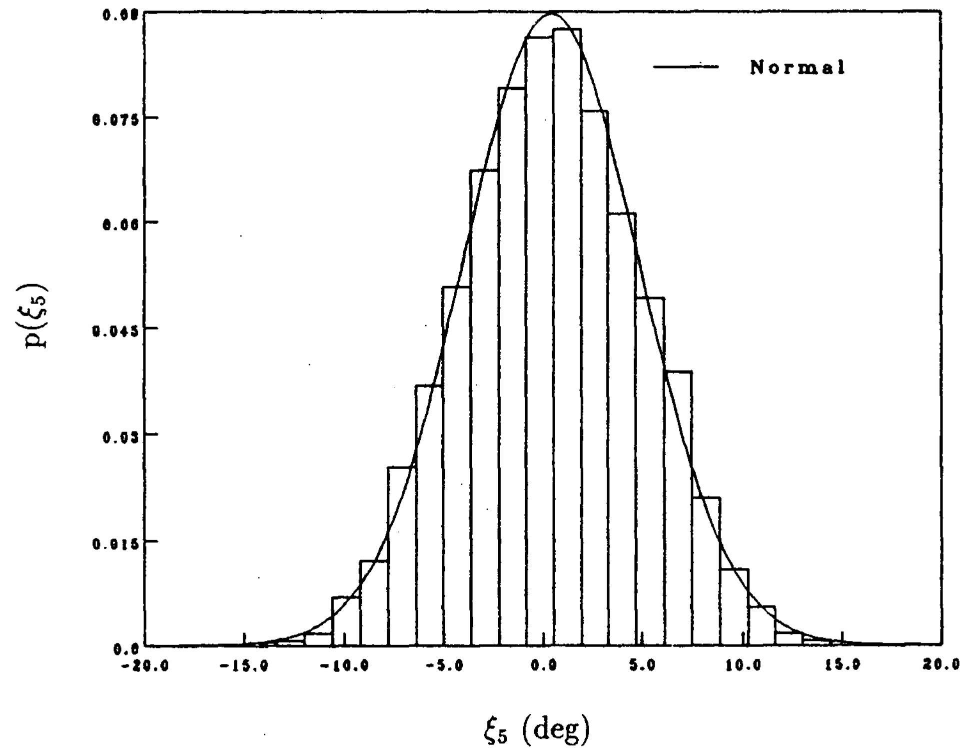

Figure 6.127: Probability distribution of pitch motions in multi-directional waves ($f_p =$ 0.5Hz, $s \approx 1$)

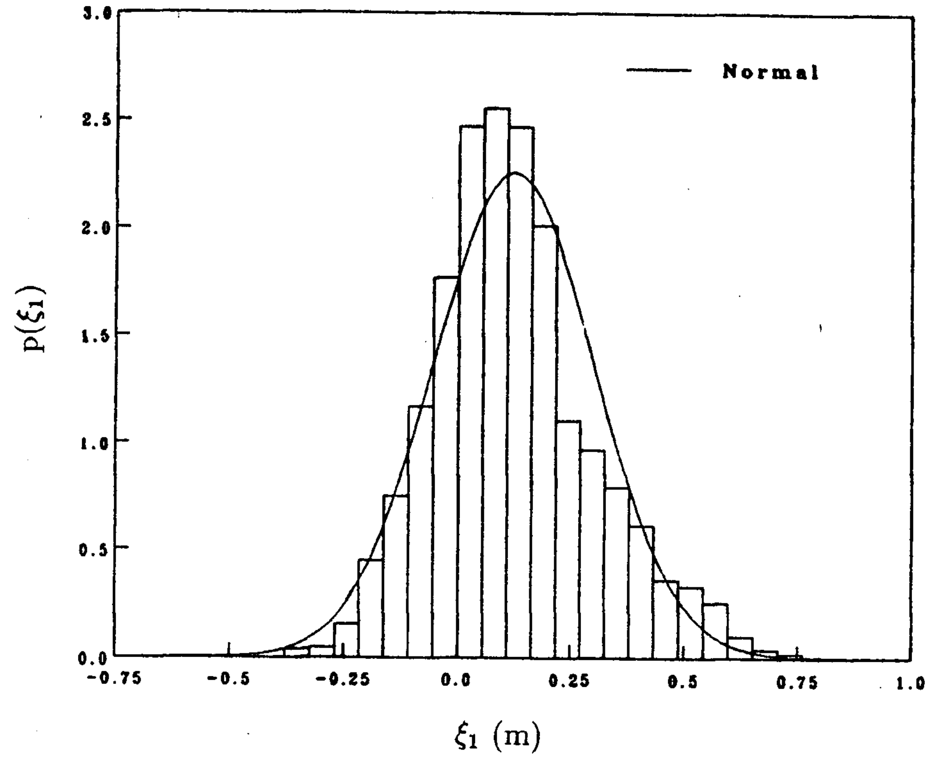

Figure 6.128: Probability distribution of surge motions in multi-directional waves (f_p = 0.67Hz, $s \approx 1$)

low frequency distributions are clearly non-zero. The probability distributions of the surge motion for three additional sea states (f_p = 0.67Hz, $s = \infty$; f_p = 0.5Hz, $s = 1$ and ∞) are also compared with the normal distribution in figures 6.131 to 6.133. The probability distributions of the low frequency motions for the different sea states were all non-Gaussian. The viscous damping ratio for the surge and sway motions were around 10%. For more lightly damped systems, the distribution of the low frequency motions might be closer to a Gaussian distribution.

The maximum motions experienced by a structure in a given sea state are also of interest in the design of structures such as ships and floating production systems. If the motions are assumed to be normally distributed, the maximum motions of the structure can be calculated using equation (4.39). The measured and predicted expected values of the maximum barge motions for the 0.5Hz and 0.67Hz sea states are compared in Tables 6.14 and 6.15 respectively. The maximum values of the heave and roll motions are

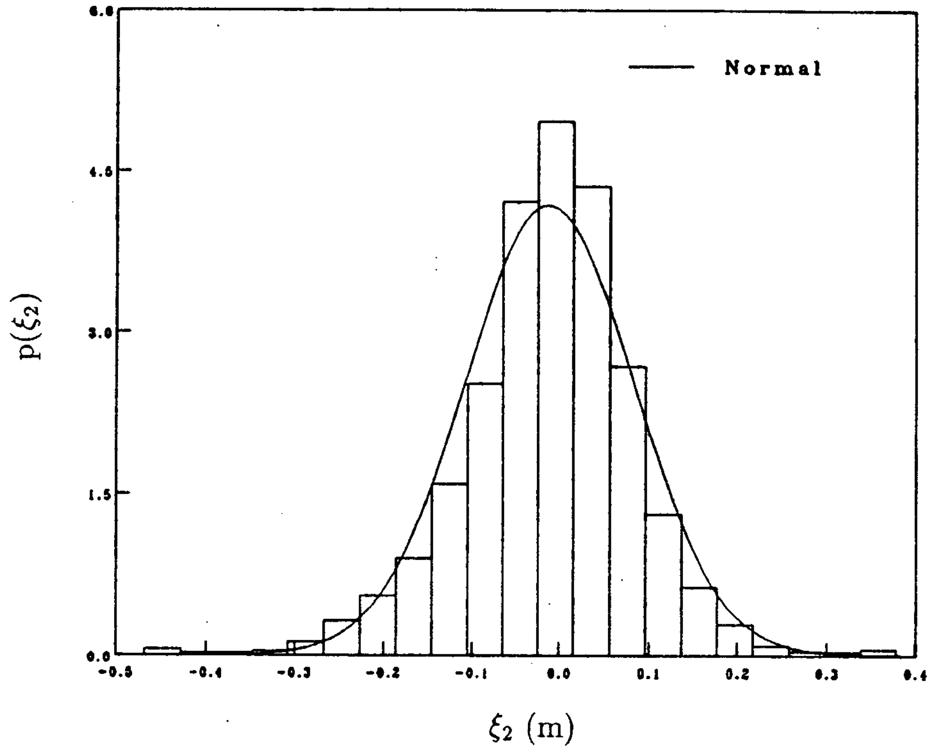

Figure 6.129: Probability distribution of sway motions in multi-directional waves (f_p = 0.67Hz, $s \approx 1$)

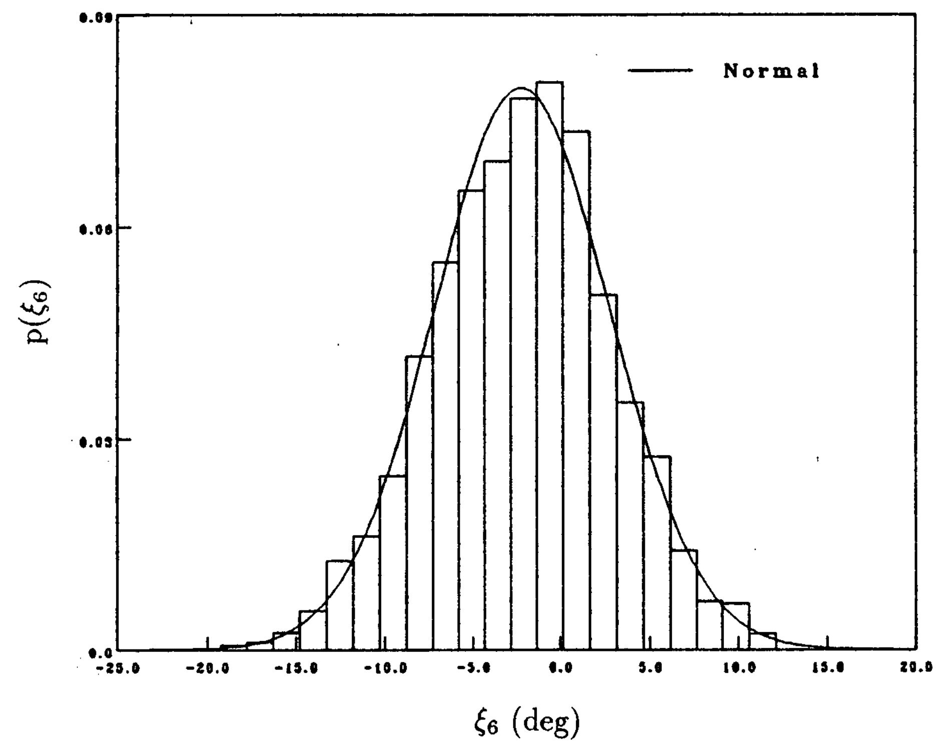

Figure 6.130: Probability distribution of yaw motions in multi-directional waves (f_p = 0.67Hz, $s \approx 1$)

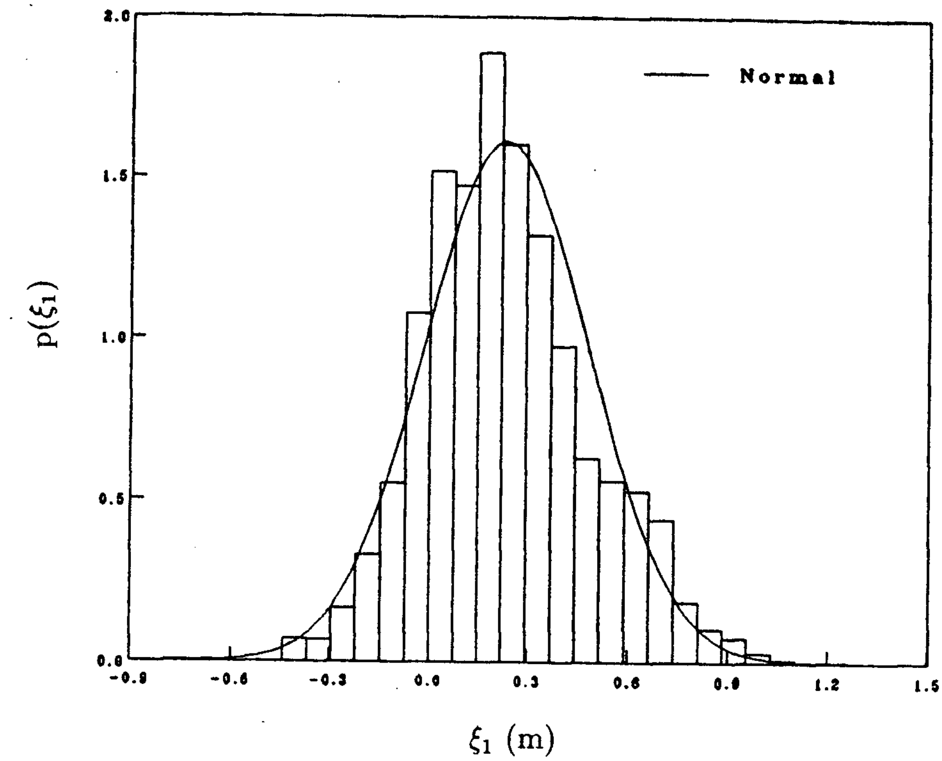

Figure 6.131: Probability distribution of surge motions in long-crested waves (f_p = 0.67Hz)

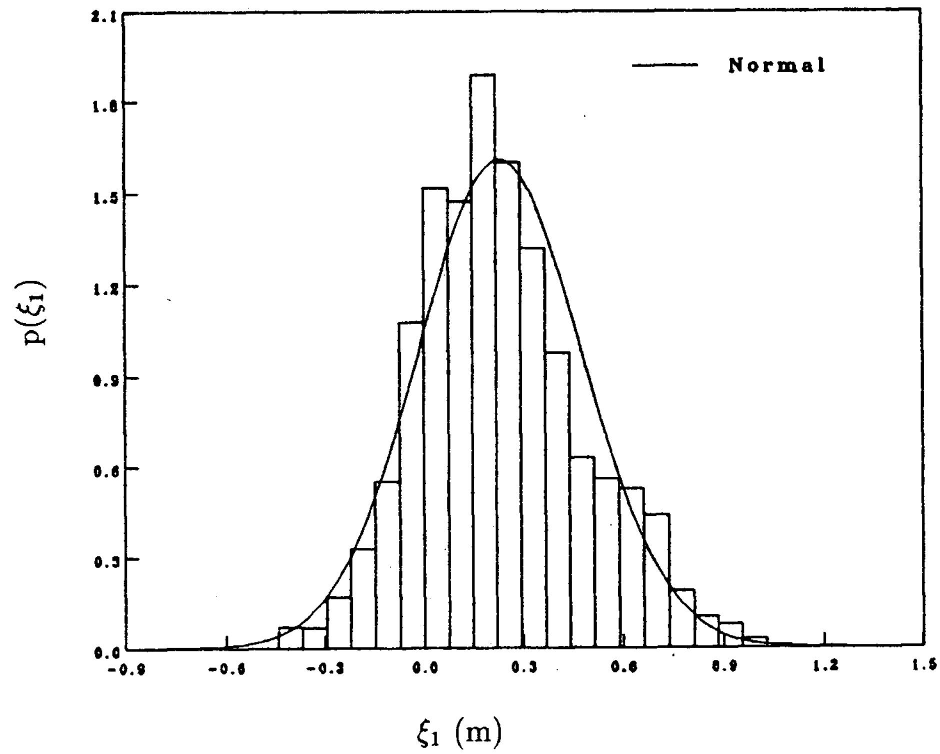

Figure 6.132: Probability distribution of surge motions in long-crested waves ($f_p = 0.5$Hz)

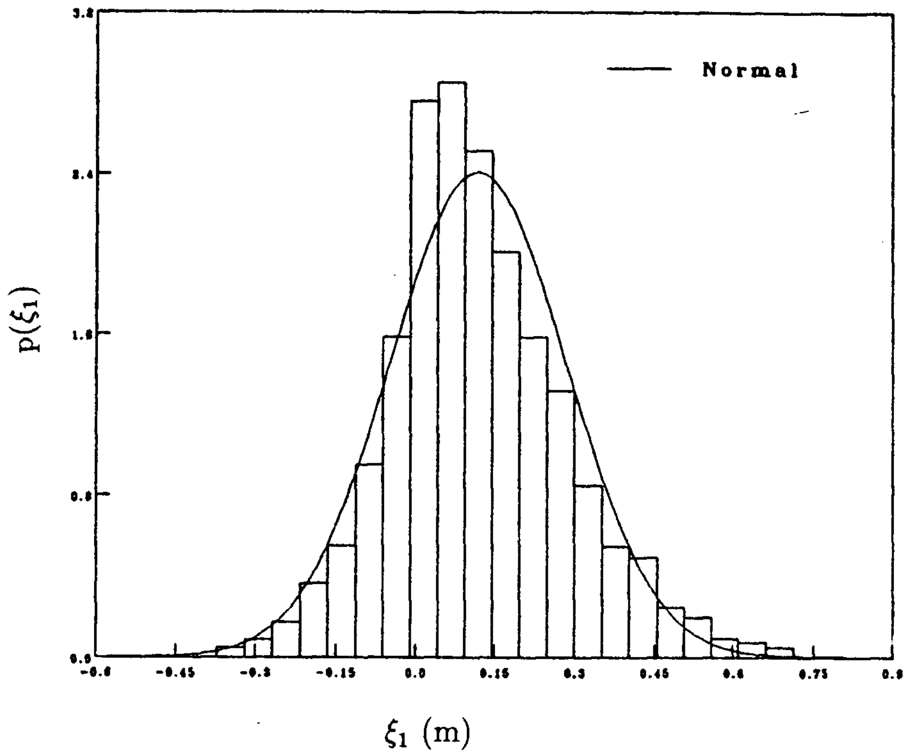

Figure 6.133: Probability distribution of surge motions in multi-directional waves(f_p = 0.5Hz, $s \approx 1$)

well predicted by the theoretical expression while maximum pitch motions were slightly overpredicted. The maximum values of the low frequency surge, sway, and yaw motions were however consistently underpredicted by the theoretical expression.

Table 6.14: Measured and predicted nondimensional maximum values (ξ_{max}/σ_ξ) of the barge motions (f_p = 0.5Hz)

	$s \approx 1$		$s \to \infty$	
	measured	predicted	measured	predicted
surge	4.61	3.94	4.30	3.96
sway	4.38	3.43	—	—
heave	3.31	3.65	3.32	3.66
roll	3.79	3.66	—	—
pitch	3.32	3.68	3.06	3.68
yaw	3.79	3.18	—	—

Table 6.15: Measured and predicted nondimensional maximum values (ξ_{max}/σ_ξ) of the barge motions (f_p = 0.67Hz)

	$s \approx 1$		$s \to \infty$	
	measured	predicted	measured	predicted
surge	4.31	3.88	4.41	4.08
sway	4.76	3.25	—	—
heave	3.69	3.70	3.31	3.71
roll	3.65	3.69	—	—
pitch	3.29	3.71	3.32	3.68
yaw	3.41	3.20	—	—

Chapter 7

CONCLUSIONS

This thesis has primarily dealt with the influence of the directional spreading of wave energy on the forces and motions of fixed and floating offshore structures. Different methods of estimating directional wave spectra have been investigated and analytical and numerical models have been developed to predict the behaviour of fixed and floating structures in random multi-directional sea states. Experiments have also been carried out with a fixed vertical cylinder and a floating box in a multi-directional wave basin, and comparisons have been made between the theoretical predictions and the experimental results. The conclusions of the present investigation are now presented in three separate sections, each representing a different aspect of the study.

7.1 Directional Wave Analysis

The Fourier, maximum likelihood, and maximum entropy methods of estimating the directional distribution of wave energy have been presented. The maximum entropy method has been further developed to utilize data from a wave probe array. The methods have been used to analyze numerically synthesized and experimental data from both a wave probe array, and a wave probe-current meter array.

The maximum entropy method was consistently found to resolve directional seas better than the Fourier and maximum likelihood methods for all the sea states tested.

The MEM reproduced the input spreading functions quite well for both single peaked and double peaked spreading functions. It was also found that the presence of noise in the simulated or measured signals degraded the resolution of the MEM, particularly at the high and low frequency tails of the spectrum where the noise to signal ratio is relatively high.

The directional spreading functions estimated using data from a wave probe array and a wave probe-current meter array were found to be quite similar at low noise levels. The maximum entropy procedure for a wave probe-current meter array is however numerically more stable than that for a wave probe array. It is also worth noting that the methods as presently formulated cannot be used to analyze wave fields with a significant amount of reflection and would have to be modified to take into account the spatial non-homogeneity of such wave fields.

7.2 Forces on a Fixed Cylinder

Expressions have been developed to compute the spectral density of the inline and transverse components of the force in multi-directional seas, based on a linearization of the Morison equation. An analytical expression has also been developed to predict the probability distribution of the peaks of the resultant force in short-crested seas. The latter expression is based on the assumption of narrow-band sea state but retains the full nonlinearity of the Morison equation.

Experiments were also carried out to measure the wave forces on a segmented vertical pile in random unidirectional and multi-directional waves. Force coefficients were estimated from a least squares fit of the measured to predicted force spectra. The best fit force coefficients showed a high degree of variability over the height of the column.

The spectral densities of the measured forces have been compared with theoretical predictions based on the best fit coefficients. The agreement between the measured and predicted force spectra was quite reasonable. The Morison equation is thus seen as applicable to random wave conditions. The transverse force spectrum for some short-crested waves with a relatively small degree of angular spreading exhibited a significant content at twice the peak frequency of the waves. This component is associated with vortex shedding, and was found to diminish as the sea state became more confused, or the degree of angular spreading increased.

Probability distributions obtained from measured as well as numerically synthesized data have been compared with the theoretical distributions. The theoretical probability distribution is based on a narrow-band assumption and fits the data much better at the tail of the distribution. Prediction of extreme events is however based on the distribution of large values of the force, and the theoretical expression should prove useful in such situations.

The linearization of the drag force and the corresponding Gaussian distribution of the wave force was found to severely underpredict extreme values of the force in drag dominated cases. The retention of the nonlinearity of the Morison equation in deriving the force probability distribution is thus quite important.

The overall effect of wave directionality is to reduce the inline force and increase the transverse force. Reduction factors were used to relate the standard deviations of the force components in short-crested seas to the inline component of the force in long-crested seas. The measured force reduction factors were seen to compare reasonably well with the predicted values. The inline forces in $\cos^2 \theta$ short-crested sea states were reduced by as much as 14%.

The theoretical resultant force probability distribution predicts a reduction of the maxima of the resultant force in short-crested seas. This is because the maxima of the inline and transverse forces do not generally occur at the same time. The resultant force maxima is normally close in magnitude to the inline force maxima, which is reduced in short-crested seas. The numerically simulated resultant force maxima in short-crested seas were found to be reduced. The experimentally measured resultant force maxima however showed some variability with some resultant force maxima in short-crested seas being greater than those in long-crested seas.

7.3 Motions of a Floating Structure

Experiments were also carried out with a moored floating box in multi-directional waves. The tests showed an increase of the roll, sway, and yaw motions of the box in multi-directional waves and a slight reduction of the pitch motions. The heave motions were essentially unaffected by wave directionality. The low frequency surge motions were significantly reduced in short-crested seas. The mean values were reduced by as much as 50% for a $\cos^2\theta$ sea state while the standard deviations were reduced by up to 30%.

The mooring line forces were affected in a similar manner as the low frequency surge motions. The mean, standard deviation, and maxima of the mooring line forces were reduced by as much as 37%, 25%, and 21% respectively. These reductions are quite significant and show the need to incorporate wave directionality into the design process.

Linear diffraction theory was used to compute the response amplitude operators for the heave, pitch, and high frequency surge motions of the box. These were compared with the measured response amplitude operators and agreement was reasonable. The measured mean surge motions in regular waves were however not as well predicted.

A procedure to compute the spectral density of the second order forces in random multi-directional waves was presented. The approach is based on an extension of the quadratic transfer function to directional wave fields. A practical approximation for the quadratic transfer function in narrow-band directional seas was presented. The procedure was used to compute the spectra of the low frequency surge motions of the floating box in directional seas and a comparison of the measured and predicted spectral densities showed poor to satisfactory agreement.

The effect of wave grouping on the low frequency surge motions was investigated by comparing the motions of the box in sea states with the same frequency spectrum but different degrees of wave grouping. As expected, the more highly grouped waves induced larger low frequency surge motions. The rationale behind choosing fixed phase angles for different wave components in order to produce differently grouped wave trains is however still an issue of debate.

7.4 Recommendations for Further Study

There are several areas in which the work carried out in this thesis could be futher extended. In the area of directional wave analysis, the numerical convergence of the maximum entropy procedure for a wave probe array could be improved. There is also the need to modify the present methods so as to analyze wave fields with a significant amount of reflection.

The analysis of the forces on a fixed cylinder carried out in this thesis dealt mainly with the segments which remained continuously submerged. The segments above the still water level however experience maximum forces of the same order of magnitude as the submerged segments. There is thus a need to develop improved methods of predicting the water particle kinematics above still water level in random waves. The probability distribution of the forces above the still water level also needs to be addressed.

A comparison of the measured mean drift forces in regular waves and second order forces and motions in random seas with theoretical predictions based on linear diffraction theory showed poor to satisfactory agreement. There is a need to develop more accurate methods of estimating the mean drift force in regular waves and the quadratic transfer function for random waves. The probability distribution of the low frequency surge motions were not Gaussian and further work could be carried out to develop expressions for the probability distribution of the second order forces in multi-directional waves.

References

1. Abramowitz, M., and Stegun, I.A. 1965. *Handbook of Mathematical Functions*, Dover Publications, New York.

2. Barber, N.F. 1963. Directional Resolving Power of an Array of Wave Detectors. In *Ocean Wave Spectra*, Prentice-Hall, New Jersey, pp. 137-150.

3. Barnard, T.E. 1969. Analytical Studies of Techniques for the Computation of High Resolution Wavenumber Spectra. Texas Instruments Advanced Array Special Report No. 9.

4. Borgman, L.E. 1967a. Spectral Analysis of Ocean Wave Forces on Piling. *Journal of Waterways and Harbors Div.*, ASCE, Vol. 93, No. WW2, pp. 129-156.

5. Borgman, L.E. 1967b. Random Hydrodynamic Forces on Objects. *Annals of Mathematical Statistics*, Vol. 38, No. 1, pp. 37-51.

6. Borgman, L.E. 1972. Statistical Models for Ocean Waves and Wave Forces. *Advances in Hydroscience*, Vol. 8, pp. 139-181.

7. Borgman, L.E. and Yfantis, E. 1981. Directional Spectral Density of Forces on Fixed Platforms. *Proc. Conf. Directional Wave Spectra Applications*, Wiegel, R.L., ed., Berkeley, California, pp. 315-331.

8. Burg, J.P. 1967. Maximum Entropy Spectral Analysis. *Proc. 37th Annual Int. Soc. Explor. Geophys. Meeting*, Oaklahoma City.

9. Capon, J. 1969. High Resolution Frequency Wavenumber Analysis. *Proc. IEEE*, Vol. 57, No. 8, pp. 1408-1418.

10. Clough, R.W., and Penzien, J. 1975. *Dynamics of Structures*, McGraw-Hill, New York.

11. Cornett, A.M. 1987. Short-Crested Wave Forces on a Rigid Segmented Vertical Cylinder. M.A.Sc Thesis, Dept. of Civil Engineering, University of British Columbia, Vancouver.

12. Cramer, H. 1966. *Mathematical Methods of Statistics.* Princeton Univ. Press, Princeton, New Jersey.

13. Cramer, H., and Leadbetter, M.R. 1967. *Stationary and Related Stochastic Processes.* John Wiley, New York.

14. Dalzell, J.F. 1985. Effect of Short-Crested Seas on Quadratic Response. David Taylor Naval Ship Research and Development Center Report No. 85/102.

15. Davenport, A.G. 1964. Note on the Distribution of the Largest Value of a Random Function with Application to Gust Loading. *Proc. Inst. of Civil Engineers*, London, Vol. 28, pp. 187-196.

16. Dowson, D.C., and Wragg, A. 1973. Maximum Entropy Distribution having Prescribed First and Second Moments. *IEEE Trans. on Information Theory*, Vol. 19, No. 5, pp. 689-693.

17. Draper, N.R., and Tierney, D.E. 1972. Regions of Positive and Unimodal Series Expansion of the Edgeworth and Gram-Charlier Approximations. *Biometrika*, Vol. 59, pp. 463-472.

18. Faltinsen, O.M., and Loken, A.E. 1979. Slow Drift Oscillations of a Ship in Irregular Waves. *Applied Ocean Research*, Vol. 1, No. 1, pp. 21-31.

19. Faltinsen, O.M., and Michelsen, F.C. 1974. Motions of Large Structures in Waves at Zero Froude Number. *Proc. Int. Symp. on Dynamics of Marine Vehicles and Structures in Waves*, London, pp. 91-106.

20. Forristall, G.Z. 1981. Kinematics of Directionally Spread Waves. *Proc. Conf. Directional Wave Spectra Applications*, Wiegel, R.L., ed., Berkeley, California, pp. 129-146.

21. Funke, E.R., and Mansard, E.P.D. 1979. On the Synthesis of Realistic Sea States in a Laboratory Flume. NRC Division of Mechanical Engineering Technical Report LTR-HY-66.

22. Funke, E.R., and Mansard, E.P.D. 1984. The NRCC Random Wave Generation Package. NRC Division of Mechanical Engineering Technical Report TR-HY-002.

23. Garrison, C.J. 1978. Hydrodynamic Loading on Large Offshore Structures: Three-Dimensional Source Distribution Methods. In *Numerical Methods in Offshore Engineering*, eds. O.C. Zienkiewicz, R.W. Lewis, and K.G. Stagg, Wiley, Chichester, England, pp. 97-140.

24. Hackley, M.B. 1979. Wave Force Simulation Studies in Random Directional Seas. *Proc. 2nd Int. Conf. on the Behaviour of Offshore Structures*, BOSS'79, London, Vol I, pp. 371- 382.

25. Hasselmann, K. 1966. On Nonlinear Ship Motions in Irregular Waves. *Journal of Ship Research*, Vol. 10, No. 1, pp. 64-68.

26. Havelock, T.H. 1929. Forced Surface Waves on Water. *Philosopical Magazine*, Vol. 8., pp. 569-576.

27. Hearn, G.E., Tong, K.C., and Lau, S.M. 1987. Sensitivity of Wave Drift Damping Coefficient Predictions to the Hydrodynamic Analysis Models used in the Added Resistance Gradient Method. *Proc. 6th Int. Offshore Mechanics and Arctic Engineering Symposium*, Houston, Vol II, pp. 213-225.

28. Houlie, M., Stansberg, C.T., and Werenskiold, P. 1983. Model Tests with a Single-Point Mooring System in Short-Crested Waves. *Proc. Offshore Technology Conference*, Houston, Paper No. OTC 4644, pp. 545-547

29. Hsu, F.H. and Blenkarn, K.A. 1970. Analysis of Peak Mooring Forces Caused by Slow Vessel Drift Oscillations in Random Seas. *Proc. Offshore Technology Conference*, Houston, Paper No. OTC 1159, pp. 135-146.

30. Huntington, S.W., and Thompson, D.M. 1976. Forces on a Large Vertical Cylinder in Multi-Directional Random Waves. *Proc. Offshore Technology Conference*, Houston, Paper No. OTC 2539, pp. 169-183.

31. Isaacson, M. 1985a. Wave Effects on Large Offshore Structures of Arbitrary Shape. *Coastal/Ocean Engineering Report*, Dept. of Civil Engineering, The University of British Columbia, Vancouver.

32. Isaacson, M. 1985b. Laboratory Measurement and Generation of Directional Surface Waves. *Proc. 21st IAHR Congress*, Melbourne, Australia, pp. 116-121.

33. Isaacson, M., and Sinha, S. 1986. Directional Wave Effects on Large Offshore Structures. *Journal of Waterway, Port, Coastal, and Ocean Engineering*, ASCE, Vol. 112, No. 4, pp. 482-497

34. Isobe, M. and Kondo, K. 1986. Method for Estimating Directional Wave Spectrum in Incident and Reflected Wave Field. *Proc. 19th Int. Coastal Engineering Conference*, Houston, pp. 467-483.

35. Isobe, M., Kondo., K., and Horikawa, K. 1984. Extension of MLM for Estimating Directional Wave Spectrum. *Proc. Symp. on Description and Modelling of Directional Seas*, Copenhagen, Denmark, Paper No. A6.

36. Jamieson, W.W., and Mansard, E.P.D., 1987. An Efficient Upright Wave Absorber. *Proc. ASCE Specialty Conference on Coastal Hydrodynamics*, Newark, Delaware, pp. 124-139.

37. Jaynes, E.T. 1957. Information Theory and Statistical Mechanics. Papers I and II, *Phys. Rev*, Vol. 106, pp. 620-630, and Vol. 108, pp. 171-190.

38. Jeffreys, E.R. 1986. Comparison of Three Methods for Calculation of Directional Spectra. *Proc. 5th Int. Offshore Mechanics and Arctic Engineering Symposium*, Tokyo, Japan, Vol I, pp. 45-50.

39. Jeffreys, E.R. 1987. Directional Seas should be Ergodic. *Journal of Applied Ocean Research*, Vol. 9, No. 4, pp. 186-191.

40. John, F. 1950. On the Motion of Floating Bodies. Parts I and II, *Comm. Pure and Applied Mathematics*, Vol. 2, pp. 13-57, Vol. 3, pp. 45-101.

41. Kac, M., and Siegert, J.F. 1947. On the Theory of Noise in Radio Receivers with Square Law Detectors. *Journal of Applied Physics*, Vol. 18, pp. 383-397.

42. Kellogg, O. D. 1929. *Foundations of Potential Theory*. Springer, Berlin.

43. Kim, C.H., and Dalzell, J.F. 1981. An Analysis of the Quadratic Frequency Response for Lateral Drifting Force and Moment. *Journal of Ship Research*, Vol. 25, No. 2, pp. 117-129.

44. Kobune, K. and Hashimoto, N. 1986. Estimation of Directional Spectra from the Maximum Entropy Principle. *Proc. 5th Int. Offshore Mechanics and Arctic Engineering Symposium*, Tokyo, Japan, Vol I, pp. 80-85.

45. Lamb, H. 1945. *Hydrodynamics*, Dover Publications, New York.

46. Langley, R.S. 1984. The Statistics of Second Order Wave Forces. *Applied Ocean Research*, Vol. 6, No. 4, pp. 182-186.

47. Langley, R.S. 1987. A Statistical Analysis of Low Frequency Second Order Forces and Motions. *Journal of Applied Ocean Research*, Vol. 9, No. 3, pp. 163-170.

48. Lighthill, J. 1979. Wave Forces and Hydrodynamic Loading. *Proc. 2nd Int. Conf. on the Behaviour of Offshore Structures*, BOSS'79, London, Vol I, pp. 1-40.

49. Lin, Y.K. 1976. *Probabilistic Theory of Structural Dynamics*, McGraw-Hill Inc., New York.

50. Longuet-Higgins, M.S. 1952. On the Statistical Distribution of the Heights of Sea Waves. *Journal of Marine Research*, Vol. 11, pp. 245-266.

51. Longuet-Higgins, M.S., Cartwright, D.E., and Smith, N.D. 1963. Observations of the Directional Spectrum of Sea Waves Using the Motions of a Floating Buoy. In *Ocean Wave Spectra*, Prentice-Hall, New Jersey, pp. 111-132.

52. Maeda, H., Morooka, C.K., and Kasahara, A. 1986. Motion of Floating Type Offshore Structures in Directional Waves. *Proc. 5th Int. Offshore Mechanics and Arctic Engineering Conference*, Tokyo, Vol. I, pp. 94-101

53. Mansard, E.P.D., Sand, S., and Klinting, P. 1989. Wave Grouping Measures (to be published as NRC Division of Mechanical Engineering Technical Report).

54. Mansard, E.P.D., and Pratte, B.D., 1982. Moored Ship Response in Irregular Waves. *Proc. 18th Coastal Engineering Conference*, Capetown, South Africa, Vol. 3, pp. 2621-2640.

55. Marshall, P.W. 1976. Dynamic and Fatigue Analysis Using Directional Spectra. *Proc. Offshore Technology Conference*, Houston, Paper No. OTC 2537.

56. Marthinsen, T. 1983a. Calculation of Slowly Varying Drift Forces. *Applied Ocean Research*, Vol. 5, No. 3, pp. 141-144.

57. Marthinsen, T. 1983b. The Effect of Short-Crested Sea on Second Order Forces and Motion. *Int. Workshop on Ship and Platform Motions*, Berkeley, pp. 404-414.

58. Maruo, H. 1960. The Drift of a Body Floating on Waves. *Journal of Ship Research*, Vol. 4, No. 3, pp. 1-10.

59. Matsui, T. 1986. Analysis of Slowly Varying Wave Drift Forces on Compliant Structures. *Proc. 5th Int. Offshore Mechanics and Arctic Engineering Symposium*, Tokyo, Japan, Vol I, pp. 289-296.

60. Mead, L.R., and Papanicolaou, N. 1984. Maximum Entropy in the Problem of Moments. *Journal of Mathematical Physics*, Vol. 25, No. 8, pp. 2404-2417.

61. Moe, G. and Crandall, S.H. 1978. Extremes of Morison-Type Loading on a Single Pile. *J. Mech. Design, Trans. ASME*, Vol. 100, No. 1, pp. 100-104.

62. Miles, M.D., Laurich, P.H., and Funke, E.R. 1986. A Multi Mode Segmented Wave Generator for the NRC Hydraulics Laboratory. *Proc. 21st American Towing Tank Conference*, Washington, D.C.

63. Miles, M.D., and Funke, E.R. 1987. A Comparison of Methods for the Synthesis of Directional Seas. *Proc. 6th Int. Offshore Mechanics and Arctic Engineering Symposium*, Houston, Vol II, pp. 247-255.

64. Mitsuyasu, H., *et al.* 1975. Observations of the Directional Spectrum of Ocean Waves Using a Cloverleaf Buoy. *Journal of Physical Oceanography*, Vol. 5, pp. 750 - 760.

65. Molin, B. and Fauveau, V. 1984. Effect of Wave Directionality on Second Order Loads Induced by the Set-Down. *Applied Ocean Research*, Vol. 6, No. 2, pp. 66-72.

66. Morison, J.R., O'Brien, M.P., Johnson, J.W., and Schaaf, S.A. 1950. The Forces Exerted by Surface Waves on Piles. *Petroleum Trans., AIME*, Vol. 189, pp. 149-157.

67. Naess, A. 1986. The Statistical Distributions of Second Order Slowly Varying Forces and Motions. *Journal of Applied Ocean Research*, Vol. 8, No. 2, pp. 110-118.

68. Nakamura, S., Saito, K., and Takagi, M. 1986. On the Increased Damping of a Moored Body during Low Frequency Motions in Waves. *Proc. 5th Int. Offshore Mechanics and Arctic Engineering Symposium*, Tokyo, Japan, Vol I, pp. 281-288.

69. Neal, E. 1974. Second Order Hydrodynamic Forces due to Stochastic Excitation. *Proc. 10th ONR Symposium*, Cambridge, Mass.

70. Newman, J.N. 1967. The Drift Force and Moment on Ships in Waves. *Journal of Ship Research*, Vol. 11, No. 1, pp. 51-60.

71. Newman, J.N. 1974. Second Order, Slowly Varying Forces on Vessels in Irregular Waves. *Proc. Int. Symp. on Dynamics of Marine Vehicles and Structures in Waves*, London, pp. 182-186.

72. Newman, J.N. 1977. *Marine Hydrodynamics*, MIT press, Cambridge, Massachusetts.

73. Oakley, O.H. and Lozow, J.B. 1977. Directional Spectra Measurement by Small Arrays. *Proc. Offshore Tech. Conf.*, Houston, Paper No. OTC2745, pp. 155-166.

74. Panicker, N.N., and Borgman, L.E. 1970. Directional Spectra from Wave Gauge Arrays. Hydrogr. Eng. Lab. Rep. HEL1-18, University of California, Berkeley.

75. Pierson, W.J. and Holmes, P. 1965. Irregular Waves Forces on a Pile. *J. Waterways and Harbors Div.*, ASCE, Vol. 91, No. WW4, pp. 1-10.

76. Pinkster, J.A. 1976. Low Frequency Second Order Forces on Vessels Moored at Sea. *Proc. 11th Symp. on Naval Hydrodynamics*, London, pp. 603-615.

77. Pinkster, J.A. 1980. Low Frequency Second Order Exciting Forces on Floating Structures. Netherlands Ship Model Basin Report No. 650.

78. Pinkster, J.A. 1984. Numerical Modelling of Directional Seas. *Proc. Symp. on Description and Modelling of Directional Seas*, Copenhagen, Denmark.

79. Pinkster, J.A. 1985. Drift Forces in Directional Seas. *Proc. MARINTEC Conference*, Shanghai, pp. 1-63.

80. Pinkster, J.A., and Wichers, J.E.W., 1987. The Statistical Properties of Low Frequency Motions of Nonlinearly Moored Tankers. *Proc. Offshore Technology Conference*, Houston, Paper No. OTC 5457, pp. 317-331.

81. Roberts, J.B. 1981. Nonlinear Analysis of Slow Drift Oscillations of Moored Vessels in Random Seas. *Journal of Ship Research*, Vol. 25, No. 2, pp. 130-140.

82. Romeling, J.U., Marol, P., and Sand, S.E. 1984. Bi-articulated Mooring Column tested in Directional Waves. *Proc. Symp. on Description and Modelling of Directional Seas*, Copenhagen, Denmark, Paper No. B4.

83. Salvesen, N. 1974. Second Order Steady State Forces on Surface Ships in Oblique Regular Waves. *Proc. Int. Symp. on Dynamics of Marine Vehicles and Structures in Waves*, London, pp. 212-226.

84. Sand, S.E., Romeling, J., and Kirkegaard, J. 1987. Influence of Wave Directionality on Response of a Semisubmersible. *Proc. 6th Int. Offshore Mechanics and Arctic Engineering Symposium*, Houston, Vol II, pp. 239-245.

85. Sarpkaya, T. 1975. Forces on Cylinders and Spheres in an Oscillating Fluid. *Journal of Applied Mechanics*, Trans. ASME, Vol. 42, pp. 32-37.

86. Sarpkaya, T. and Isaacson, M. 1981. *Mechanics of Wave Forces on Offshore Structures.* Van Nostrand Reinhold, New York.

87. Shinozuka, M., Fang, S.L.S., and Nishitani, A. 1979. Time Domain Structural Response Simulation in a Short-Crested Sea. *Journal of Energy Resources Technology*, Trans. ASME, Vol. 101, pp. 270-275.

88. Spangenberg, S., and Jacobsen, B.K. 1980. The Effect of Wave Grouping on Slow Drift Oscillations of an Offshore Structure. *Proc. Int. Symp. on Ocean Engineering Ship Handling*, Gottenburg, Sweden, pp. 8:1-8:14.

89. Standing, R.G., Brendling, W.J., and Wilson, D. 1987. Recent Developments in the Analysis of Wave Drift Forces, Low Frequency Damping, and Response. *Proc. Offshore Technology Conference*, Houston, Paper No. OTC 5456, pp. 307-315.

90. Teigen, P.S. 1983. The Response of a TLP in Short-Crested Waves. *Proc. Offshore Technology Conference*, Houston, Paper No. OTC 4642, pp. 525-528.

91. Tickell, R.G. 1977. Continuous Random Wave Loading on Structural Members. *The Structural Engineer*, Vol. 55, No. 5, pp. 209-222.

92. Tickell, R.G. and Elwany, M.H.S. 1979. A Probabilistic Description of Forces on a Member in a Short-Crested Random Sea. In*Mechanics of Wave Induced Forces on Cylinders*, Shaw, T.L., ed., Pitman, London, pp. 561-576.

93. Vinje, T. 1983. On the Statistical Distribution of Second Order Forces and Motions. *International Shipbuilding Progress*, Vol. 30, pp. 58-68.

94. Volterra, V. 1930. *Theory of Functionals*, Dover Publications, New York.

95. Wichers, J.E.W., and van Sluijs, M.F. 1979. The Influence of Waves on the Low Frequency Hydrodynamic Coefficients of Moored Vessels. *Proc. Offshore Technology Conference*, Houston, Paper No. OTC 3625, pp. 2313-2319.

Appendix A

Green's Function Representation

The Green's function which satisfies the Laplace equation and the boundary conditions on the free surface, seabed, and radiation surface was originally derived by John (1950). It can either be expressed in an integral form or as an infinite series. The integral representation is given by

$$\begin{aligned} G(\mathbf{x};\mathbf{x}') &= \frac{1}{R} + \frac{1}{R'} \\ &+ 2\,\mathrm{PV}\int_0^\infty \frac{(\mu+\nu)\cosh[\mu(z'+d)]\cosh[\mu(z+d)]}{(\mu\tanh\mu d-\nu)\cosh(\mu d)}\exp(-\mu d)J_0(\mu r)\,d\mu \\ &+ i\frac{2\pi(k^2-\nu^2}{(k^2-\nu^2)d+\nu}\cosh[k(z'+d)]\cosh[k(z+d)]J_0(kr) \end{aligned} \tag{A.1}$$

where PV denotes the principal value of the integral, and

$$\begin{aligned} R &= \sqrt{(x-x')^2+(y-y')^2+(z-z')^2} \\ R' &= \sqrt{(x-x')^2+(y-y')^2+(z+2d+z')^2} \\ r &= \sqrt{(x-x')^2+(y-y')^2} \end{aligned}$$

J_0 is the Bessel function of the first kind of order zero, while ν is given by

$$\nu = k\tanh kd = \frac{\omega^2}{g} \tag{A.2}$$

The series representation of the Green's function is given by

$$G(\mathbf{x};\mathbf{x}') = i\frac{2\pi(k^2-\nu^2)}{(k^2-\nu^2)d+\nu}\cosh[k(z'+d)]\cosh[k(z+d)]H_0^{(1)}(kr)$$

$$+ \quad 4 \sum_{n=1}^{\infty} \frac{\mu_n^2 + \nu^2}{(\mu_n^2 + \nu^2)d - \nu} \cos[\mu_n(z' + d)] \cos[\mu_n(z + d)] K_0(\mu_n r) \tag{A.3}$$

where μ_n are the real positive roots of the equation

$$\mu_n \tan(\mu_n d) + \nu = 0 \tag{A.4}$$

$H_0^{(1)}$ is the Hankel function of the first kind of order zero, and K_0 is the modified Bessel function of the second kind of order zero.

Appendix B

Estimation of Moments of Inertia

When the mass distribution of a floating structure model is not exactly known, the moments of inertia can alternatively be determined from tests on a swing frame. The swing frame is a support structure for the model which is allowed to rotate about a knife edge as shown in figure B.1. The swing frame can also be used to determine the vertical position of the centre of gravity of the model. The experimental procedure used to determine the vertical location of the centre of gravity and the moments of inertia of the floating box is now described.

B.1 Determination of the Vertical Position of the Centre of Gravity

The vertical position of the centre of gravity is determined by applying a known moment PL to the swing frame and measuring the angle of tilt α produced by the applied moment. Figure B.2 shows the forces acting on such a rotated body. Taking moments about the knife edge (see figure B.2) results in

$$PL \cos\alpha = mga \sin\alpha \tag{B.1}$$

where m is the mass of the body, g is the gravitational acceleration, and a is the vertical distance between its centre of gravity and the knife edge. For a system consisting of the swing frame and the box model, the above equation can be expressed as

$$PL = (m_f g a_f + m_b g a_b) \tan\alpha \tag{B.2}$$

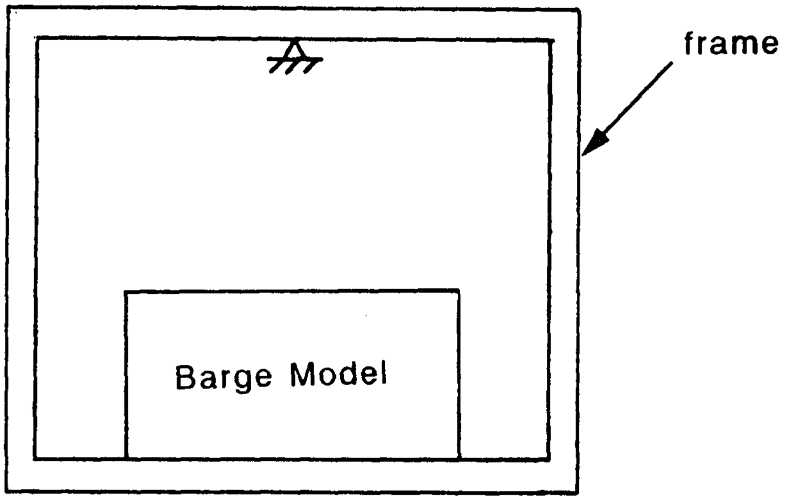

Figure B.1: Sketch of swing frame

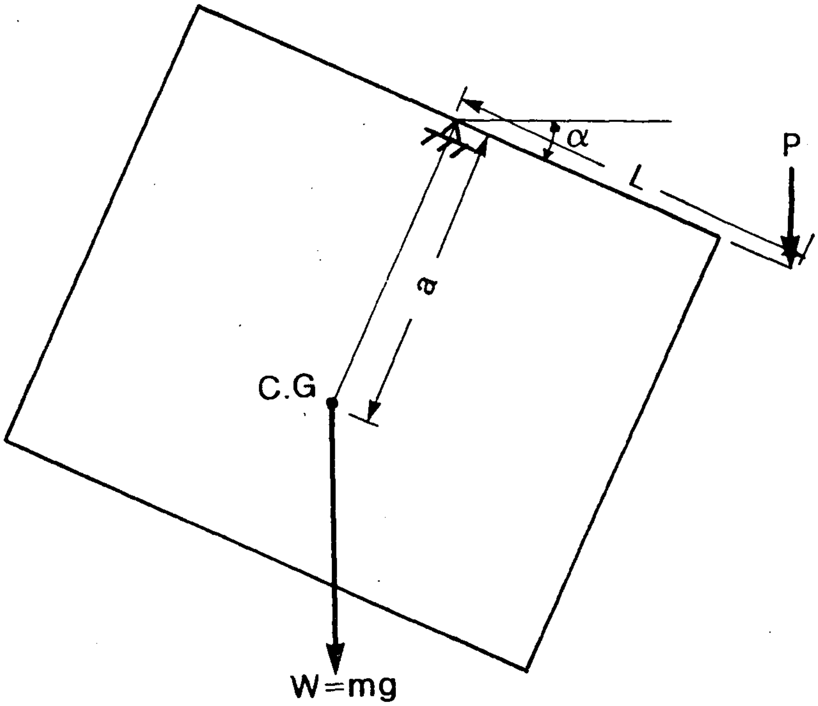

Figure B.2: Free body diagram of rotated body

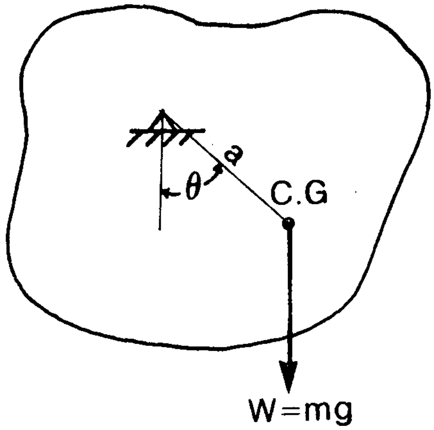

Figure B.3: Sketch showing forces acting on compound pendulum

where the subscripts f and b denote the frame and box model respectively. By initially determining the vertical location of the centre of gravity of the swing frame, the vertical position of the centre of gravity of the box model can be estimated from equation (B.2).

B.2 Estimation of Moments of Inertia

The moments of inertia of the box for the roll, pitch, and yaw motions can be estimated by measuring the period of the angular motions of the box - swing frame system. The box - swing frame system can be considered to act as a compound pendulum and the equations governing the motions of a compound pendulum is thus used to relate the moment of inertia to the period of the angular oscillations. Consider a compound pendulum (see figure B.3) with total mass m, and polar moment of inertia I about the axis of rotation (knife edge). The differential equation of motion can be expressed as

$$I\ddot{\theta} = -mga\sin\theta \tag{B.3}$$

For small angles of rotation, $\sin\theta \approx \theta$ and the above equation reduces to

$$I\ddot{\theta} = -mga\theta \tag{B.4}$$

The periodic angular motions of a pendulum with frequency ω_o can be expressed as

$$\theta = \theta_a \sin \omega_o t \tag{B.5}$$

where θ_a is the amplitude of the angular rotation. Subsitution of equation (B.5) into equation(B.4) results in the following relationship between the moment of inertia and the period of the angular oscillations

$$I = \frac{mga}{\omega_o^2} \tag{B.6}$$

The moment of inertia of the body about its centre of gravity I_G can then be obtained from the transfer of axis equation

$$I = I_G + ma^2 \tag{B.7}$$

For a system consisting of the box model and the swing frame, the moments of inertia of the box and frame about the knife edge, I_b, and I_f, are related to the period of oscillation by

$$I_b + I_f = \frac{1}{\omega_o^2}(m_b g a_b + m_f g a_f) \tag{B.8}$$

The moment of inertia of the swing frame is initially estimated by timing the free angular oscillations of the swing frame. The moments of inertia of the box for the different motions can then be determined from equation (B.8) after measuring the period of the angular motions of the box - swing frame system.

Appendix C

Estimation of Damping from Free Oscillation Tests

In determining the amplitudes of motions of large floating structures in waves, it is important to estimate accurately the amount of damping present in the system. In addition to the damping associated with waves radiated away from the body, there is also additional damping associated with viscosity effects. Viscous damping is primarily due to skin friction and flow separation effects and is difficult to estimate analytically. Experimental methods involving free oscillation tests in still water are thus often used to estimate the damping coefficient. The tests involve applying an initial displacement to the body and recording the time history of the free oscillations of the body. The amount of damping present can be estimated from the rate of decrease of the motion amplitudes.

Consider a single degree of freedom motion $x(t)$ of a linear system described by the following differential equation

$$m\ddot{x}(t) + b\dot{x}(t) + cx(t) = 0 \tag{C.1}$$

where m is the mass of the body including the added mass, b is the viscous damping coefficient, and c is the spring stiffness coefficient. The solution of the above differential equation can be found in any standard textbook on dynamics (see for example Clough and Penzien, 1975), and is given by

$$x(t) = x_o \exp(-\zeta\omega_n t)\cos(\omega_d t) \tag{C.2}$$

where x_o is the initial displacement of the body, $\zeta = b/2m\omega_n$ is the viscous damping ratio, $\omega_n = \sqrt{c/m}$ is the undamped natural frequency, and $\omega_d = \omega_n\sqrt{1-\zeta^2}$ is the damped natural frequency. Consider any two positive peaks, m cycles apart. The ratio of the amplitudes is given by

$$\ln \frac{x_n}{x_{n+m}} = 2m\pi\zeta\frac{\omega_n}{\omega_d} \simeq 2m\pi\zeta \tag{C.3}$$

The above equation implies that the logarithmic decrement $\ln x_n/x_{n+m}$ is independent of the x_n since the damping was assumed linear. Numerous experimental and theoretical analysis have however shown that the fluid viscous damping is in general nonlinear and can suitably be modelled by quadratic damping term. The total damping force, F_D can thus be expressed as

$$F_D(t) = b_1\dot{x}(t) + b_2\dot{x}(t)|\dot{x}(t)| \tag{C.4}$$

where b_1 and b_2 are the linear and quadratic damping coefficients respectively. Consider an equivalent linear coefficient, b^*, defined by

$$b^*\dot{x} \simeq b_2\dot{x}|\dot{x}| \tag{C.5}$$

For periodic motions, the coefficient which minimizes the error introduced by the linearization in a least squares sense is given by

$$b^* = \frac{8}{3\pi}\dot{x}_a b_2 \tag{C.6}$$

where $\dot{x}_a$ is the amplitude of the velocity. The logarithmic decrement can thus be expressed as

$$\ln\left(\frac{x_{n-1}}{x_{n+1}}\right) = \frac{\pi b_1}{m\omega_n} + \frac{8b_2}{3m}x_n \tag{C.7}$$

The logarithmic decrement is now linearly dependent on the amplitude. x_{n-1} and x_{n+1} are one cycle apart while x_n is the amplitude at midcycle. The coefficients b_1 and b_2 can be determined by plotting $\ln x_{n-1}/x_{n+1}$ versus x_n and fitting the data points with a straight line.

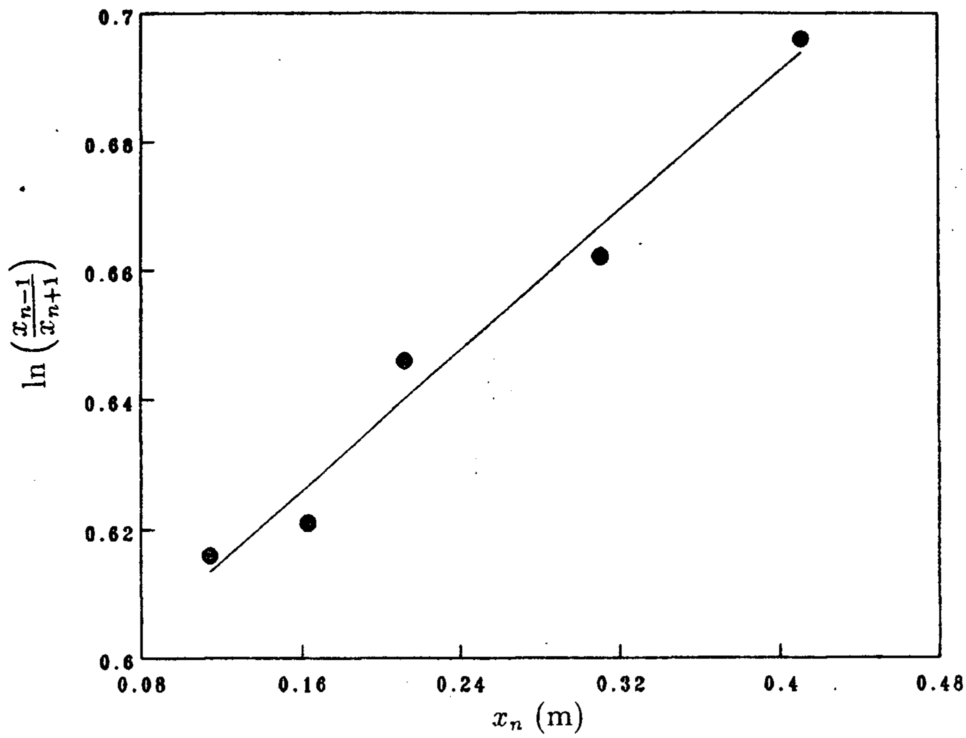

Figure C.1: Variation of log-decrement with amplitude of motion (surge)

Experimental free oscillation data were obtained for the surge, sway, roll, and pitch motions of the floating box. Typical time histories are shown in figure 5.21. Figure C.1 to C.4 show plots of the logarithmic decrement versus amplitude of motion for the four motions. The correlation coefficients for the surge and sway motions were around 0.99, indicating that the damping for the low frequency surge and sway motions is accurately modelled by quadratic damping. It can be observed from figures C.1 and C.2 that surge damping increases with amplitude of motion while the sway damping decreases. The damping ratio ζ for the surge and sway motions was quite high with values of 10.6% and 14.4% respectively, at a displacement of 0.3m.

There was more variability in the fit of the quadratic model to the roll and pitch data. The correlation coefficients were around 0.97 but the figures show that the fit was not as good as that for the surge and sway motions. At an amplitude of 3°, the damping ratio is 4% for the pitch motions and 5.2% for the roll motions.

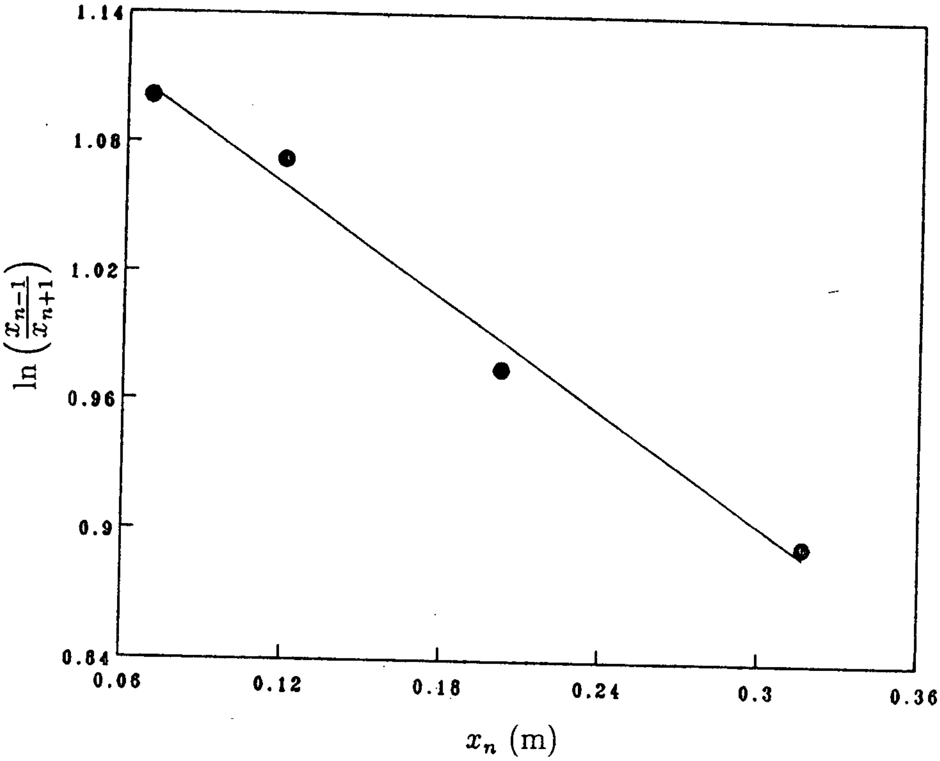

Figure C.2: Variation of log-decrement with amplitude of motion (sway)

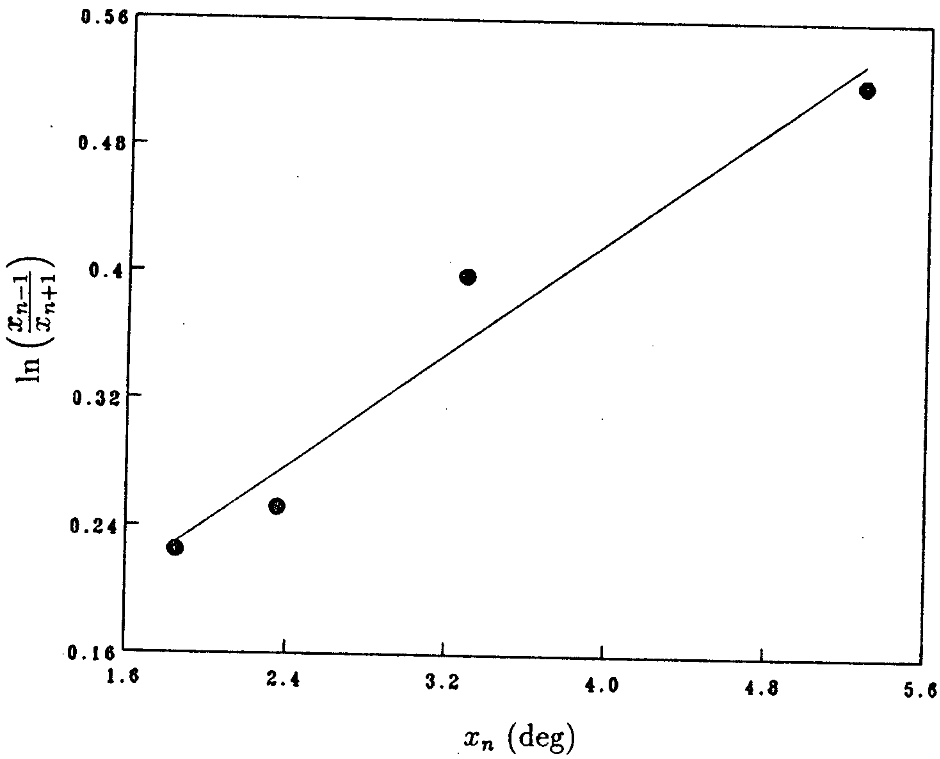

Figure C.3: Variation of log-decrement with amplitude of motion (roll)

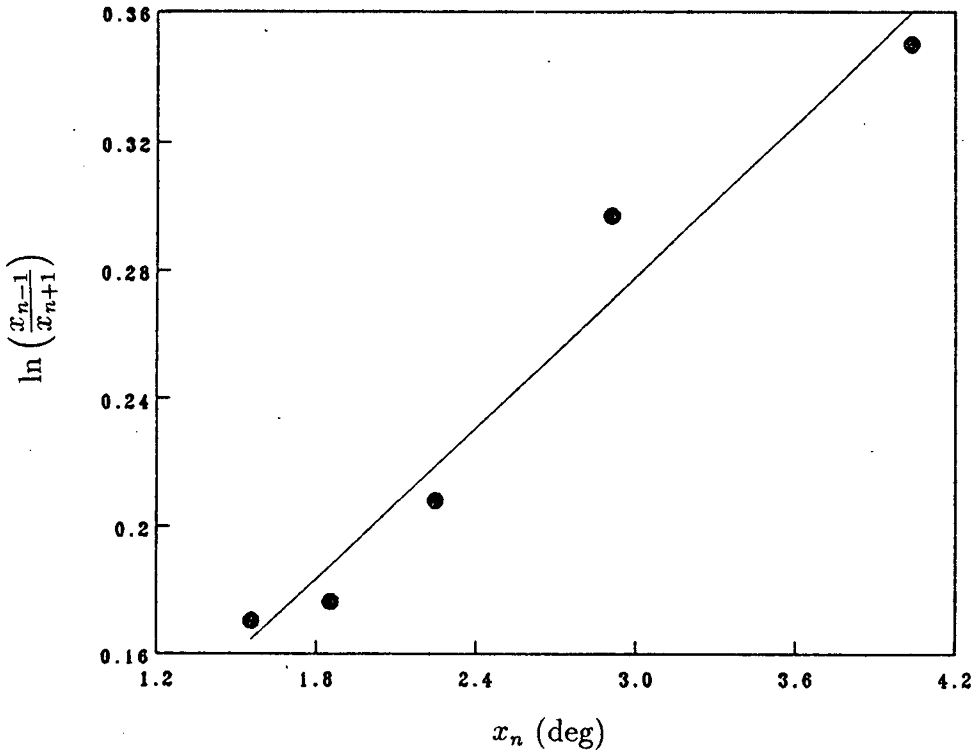

Figure C.4: Variation of log-decrement with amplitude of motion (pitch)